Cytoskeletal organization in biomimetic liposomes

Feng-Ching Tsai

This thesis was reviewed by:
dr. Yves Bollen (Vrije Universiteit, Amsterdam, the Netherlands)
dr. Armağan Koçer (Rijksuniversiteit Groningen, Groningen, the Netherlands)
prof.dr. Cécile Sykes (Institut Curie, Paris, France)
prof.dr. Thomas Schmidt (Universiteit Leiden, Leiden, the Netherlands)
prof.dr. Gijs Wuite (Vrije Universiteit, Amsterdam, the Netherlands)

The work described in this thesis was performed at the FOM Institute AMOLF, Science Park 104, 1098 XG Amsterdam, The Netherlands. This work is part of the research programme of the Foundation for Fundamental Research on Matter (FOM), which is financially supported by the Netherlands Organisation for Scientific Research (NWO).

ISBN/EAN: 978-90-77209-78-3

A digital version of this thesis is available at www.ubvu.vu.nl/dissertations and www.amolf.nl/publications/theses. Printed copies can be obtained by request to the library at FOM Institute AMOLF, library@amolf.nl.

VRIJE UNIVERSITEIT

Cytoskeletal organization in biomimetic liposomes

ACADEMISCH PROEFSCHRIFT

ter verkrijging van de graad Doctor aan
de Vrije Universiteit Amsterdam,
op gezag van de rector magnificus
prof.dr. F.A. van der Duyn Schouten,
in het openbaar te verdedigen
ten overstaan van de promotiecommissie
van de Faculteit der Exacte Wetenschappen
op woensdag 15 januari 2014 om 15.45 uur
in de aula van de universiteit,
De Boelelaan 1105

door

Feng-Ching Tsai

geboren te Taichung, Taiwan

promotor: prof.dr. G.H. Koenderink

To my parents

Publications covered in this thesis:

Tsai, F.-C., Stuhrmann, B., and Koenderink, G. H. (2011). Encapsulation of active cytoskeletal protein networks in cell-sized liposomes. *Langmuir*, 27:10061–10071.

Weinberger, A., **Tsai, F.-C**., Koenderink, G. H., Schmidt, T. F., Itri, R., Meier, W., Schmatko, T., Schröder, A. and Marques, C. (2013). Gel-assisted formation of giant unilamellar vesicles. *Biophysical journal*, 105:154–164.

Carvalho, K.*, **Tsai, F.-C.***, Lees, E., Voituriez, R., Koenderink, G. H. and Sykes, C. (2013). Cell-sized liposomes reveal how actomyosin cortical tension drives shape change. *Proceedings of the National Academy of Sciences*, 14: 16456-16461. *joint first author

Tsai, F.-C. and Koenderink, G. H. (Manuscript in preparation)
Cell-sized liposomes reveal the mechanical interplay of membrane and actin bundles on liposome shape determination.

Mavrakis, M., Azou-Gros, Y., **Tsai, F.-C.***, Alvarado, J.*, Bertin, A.*, Iv, F., Kress, A., Brasselet, S., Koenderink, G. H. and Lecuit, T. (Manuscript under review)
Septins promote F-actin ring formation by cross-linking actin filaments into curved bundles. *authors contributed equally

Alvarado, J.*, **Tsai, F.-C.***, Bertin, A., Iv, F., Lecuit, T., Koenderink, G. H. and Mavrakis, M. (Manuscript in preparation)
Mechanistic insights into actin filament bending and bundling by septins. *authors contributed equally

Other publications by the same author:

Tsai, **F.-C.,** Tai, L.-A., Wang, Y.-J., Xiao, J.-L., Hsu, T.-H. , Yang, C.-S. and Lee, C.-H. (2010). Three-dimensional tracking and temporal analysis of liposomal transport in live cells using bright-field imaging, *Microscopy Research and Technique*, 74: 531-538

Chen, C.-H., **Tsai**, **F.-C.,** Wang, C.-C. and Lee, C.-H. (2009). Three-dimensional characterization of active membrane waves on living cells. *Physical Review Letters*, 103: 238101

Tsai, F.-C. and Chen, H.-Y. (2008). Adsorption-induced vesicle fission. *Physical Review E***, 78:** 051906

Content

CHAPTER 1. Introduction

Precisely controlled shape changes are vital for cells to fulfill key processes such as growth, division and movement. For an animal cell, shape changes are determined by interactions of the cell with its extracellular tissue environment and by intracellular forces exerted on the plasma membrane by the cytoskeleton. The plasma membrane defines the cell boundary, separating the intracellular components from the extracellular environment. Since the plasma membrane is a fluid and highly deformable material, cells rely on the relatively rigid cytoskeleton to provide shape and mechanical stability to the plasma membrane. The area of the plasma membrane for most animal cells is much larger than needed to enclose their volume. This excess area allows cells to adopt a variety of shapes required for different cellular functions. The main cytoskeletal component that determines cell shape is the actin cytoskeleton, which actively pushes the membrane outwards by polymerization or pulls the membrane inwards by means of contractile forces applied by myosin II motors. It has been recognized that a precise cell shape control relies on the balance of these myosin- and polymerization-driven active forces with passive forces provided by the elasticity of the plasma membrane and the underlying actin network and by actin-membrane anchors. However, due to the vast molecular complexity of living cells, it remains elusive how the interplay of the actin cytoskeleton and the plasma membrane determines cell shape. In this thesis, we address this question by performing a bottom-up approach in which we utilize a biomimetic model system based on cell-sized liposomes encapsulating active actin-myosin networks. This approach allows us to dissect the contribution of the active actin-myosin network, the liposome membrane, and actin-membrane anchors on liposome shape determination. Finally, we investigate how actin filaments are organized by septins, a family of GTP-binding proteins, which have been shown to intimately interact with the actin cytoskeleton as well as the plasma membrane during cell division and motility. In Chapter 1, we provide some background on the plasma membrane and the cytoskeleton, with a focus on the actin cytoskeleton. We give an overview of the direct and indirect interactions that couple actin filaments to the plasma membrane. We also briefly review the state of the art in methods to obtain cell-sized liposomes encapsulating actin filaments and myosin motors. Finally, we present an outline of this thesis.

1.1 The plasma membrane

The basic structure of the plasma membrane is a thin sheet of 4-5 nm in thickness, composed of two leaflets of lipids. In most animal cells, the major lipids are glycerophospholipids, sphingolipids and sterols (Fig. 1A) [1] [2] [3] [4] [5]. Glycerophospholipids have the carboxyl groups of two fatty acid chains esterified to the two hydroxyl groups of a glycerol and a phosphoric acid esterified to the third hydroxyl group of the glycerol. The phosphate is in turn esterified to the hydroxyl group of one of several alcohols. The most common glycerophospholipids are phosphatidylcholine (PC), phosphatidylethanolamine (PE), phosphatidylserine (PS) and phosphatidylinositol (PI) lipids, with choline, ethanolamine, serine and inositol as the alcohol component, respectively. The basic building block of sphingolipids is a sphingoid base that links to a fatty acid via an amide bond. A common sphingolipid is sphingomyelin (SM), in which the sphingoid base, sphingosine, is esterified to a phosphorylcholine. Finally, the main sterol in the plasma membrane of animal cells is cholesterol. The hydroxyl group of cholesterol interacts with the polar head groups of the phospholipids, while the bulky steroid and the hydrocarbon chains are alongside the nonpolar fatty acid chains of the phospholipids.

Glycerophospholipids account for ca. 50 mole% of the total lipid content of the plasma membrane of animal cells, while cholesterol and sphingolipids make up about 30 mole% and 20 mole%, respectively [2] [6] [5]. The plasma membrane is asymmetric, with the majority of the PC and SM enriched in the outer (exoplasmic) leaflet, whereas PS, PE, PI and cholesterol are concentrated mainly in the inner (cytoplasmic) leaflet [7] [6].

Phospholipids have an inherent propensity to self-assemble into bilayers [4] [3], which arises from their amphiphilic architecture (Fig. 1B): a hydrophilic head group attached to one or two hydrophobic fatty acid chains. When dispersed in water, the hydrophobic effect promotes lipid self-assembly into supramolecular structures in which the head groups are in contact with the water, whereas the hydrophobic chains turn away from the water. For a long time, the plasma membrane was thought of in terms of the “fluid mosaic model”, which pictures the membrane as a two-dimensional fluid sheet of lipids forming a matrix in which proteins are dissolved [8]. However, there is growing experimental evidence that membranes contain ordered domains of lipids associated with membrane proteins [9]. The dimensions of these domains can vary from nanometer to micrometer scales [10]. These lipid rafts are thought to have important functions in signal transduction processes [11].

The plasma membrane contains a large number of membrane-associated proteins, which participate in mechanical integration during cell morphogenesis, force generation and transmission and signal transduction [12] [13]. Membrane-

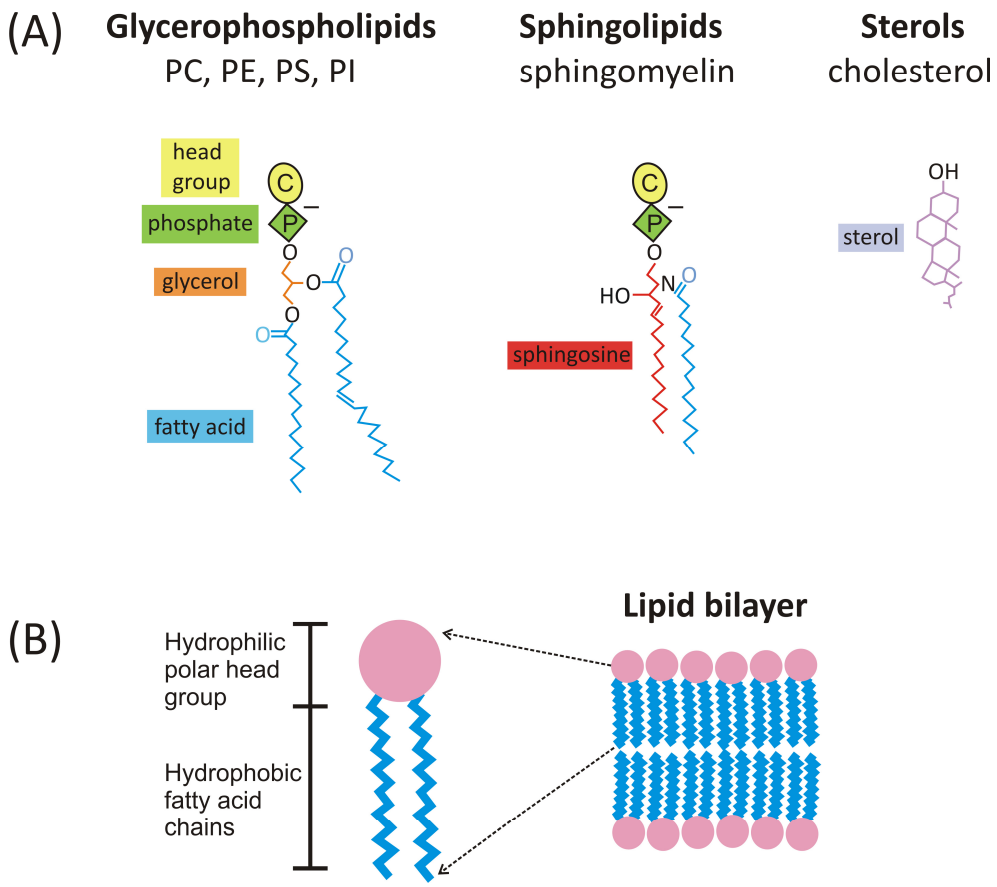

Figure 1. (A) Schematic illustrations of the main lipids of the plasma membrane of animal cells: glycerophospholipids, sphingolipids and sterols. Note that for glycerophospholipids, the kink resulting from the *cis*-double bond is exaggerated for clarity. (B) Schematic illustration of the amphiphilic architecture of lipids (*Left panel*) and their packing into a bilayer (*Right panel*).

associated proteins are often classified into (1) transmembrane proteins embedded in the bilayer by a hydrophobic transmembrane domain, (2) proteins that are anchored to the cytosolic surface by an amphipathic α-helix that partitions into the cytosolic monolayer of the membrane through the hydrophobic face of the helix, (3) proteins attached to the membrane via a lipid anchor, and (4) peripheral proteins that bind either specifically or nonspecifically to certain lipids or other membrane proteins. On average, the protein-to-lipid number ratio is around 1:50 [14], but this number varies among cell types and can dynamically

vary. Several membrane-associated proteins have the ability to locally deform the plasma membrane [15] [16]. For instance, dynamin and proteins that contain the Bin, amphiphysin and Rvs (BAR) domain can promote the formation of cylindrical membrane regions [15]. There is growing evidence that lipids and proteins do not diffuse freely within the plasma membrane, as a result of protein crowding [17] [18] [19] [20] (ca. 50% of the membrane mass is taken up by proteins [12]), interactions with the cortical cytoskeleton [21] [22], and in special cases cortical diffusion barriers associated with septins [23] [24] [25].

1.2 The cytoskeleton

The cytoskeleton is composed of biopolymers that extend throughout the cytoplasm [12]. The cytoskeleton maintains cell shape and mechanically protects cells from damage by external forces, but at the same time, the cytoskeleton also actively generates forces to change cell shape. The dynamics and architecture of the cytoskeleton are regulated by a multitude of accessory proteins. There are primarily three types of biopolymers, microtubules, actin filaments and intermediate filaments (Fig. 2), which differ markedly in bending rigidity. The bending stiffness of a semiflexible biopolymer is usually quantified in terms of the persistence length, which can be roughly defined as the length scale over which the polymer backbone remains straight under thermal undulations.

Microtubules (MTs) are the stiffest cytoskeletal polymers, with a persistence length of millimeters [26], much larger than the typical size (20-50 μm) of an animal cell. During interphase, MTs assemble into radial arrays that facilitate positioning of the centrosome in the cell center [27]. During mitosis, MTs re-organize into the mitotic spindle, which separates the chromosomes [28]. Intracellular cargo transport by molecular motors such as dyneins and kinesins relies on the cellular tracks provided by the MTs, which span across the cytoplasm from the nucleus to the cell periphery [29] [30] [31].

Intermediate filaments (IFs), with a persistence length of 0.5-1 μm [32], are the most flexible cytoskeletal biopolymers. In interphase animal cells, there are two distinct IF structures [33]. One is a mesh-like network of lamins formed underneath the inner nuclear membrane of the cell nucleus. The other one is a cytosolic network that extends from the outer nuclear membrane to the plasma membrane. There are at least 65 different types of IFs that are expressed in a tissue-type dependent manner. In fibroblasts, for instance, the main IF type is vimentin, while in keratinocytes the main IF type is keratin [33].

Actin filaments, with a persistence length of 9-18 μm [34] [26], have a rigidity that is intermediate between that of IFs and MTs. Actin filaments are the main determinant of cell shape, although the spatial arrangement of MTs and IFs and

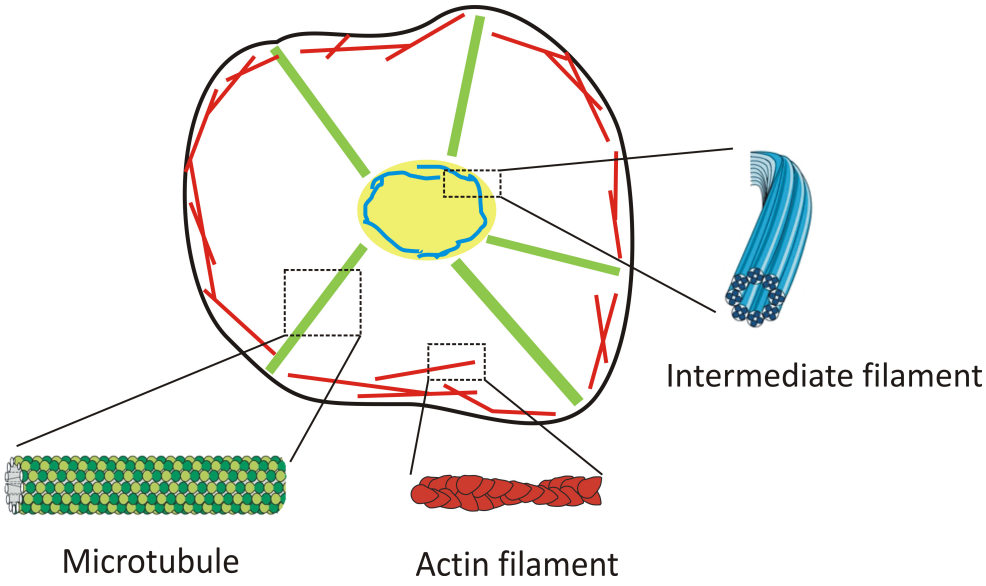

Figure 2. Schematic illustration of a cell and its three major cytoskeletal filaments: microtubules, actin filaments and intermediate filaments. A microtubule is built from 13 protofilaments, each composed of two types of tubulin molecules (α and β tubulins as shown by light and dark green circles, respectively), which are laterally associated to form a hollow cylinder. An actin filament is assembled by globular actin monomers that are arranged into a double-helical filament. Intermediate filaments, which are present at the nuclear lamina as sketched here but also in the cytosol, are built of fibrous oligomers that are packed together into a helical array. (Schematic illustrations of the microtubules and the intermediate filaments are from © Garland Science.)

interactions between the three cytoskeletal biopolymers are certainly also important. Actin filaments assemble into various architectures, including branched networks, bundles and contractile stress fibers (Fig. 3) [35] [36] [37]. In cytokinesis, actin filaments form a ring-like structure at the cell division site that facilitates cell division. In the front of a cell crawling on a flat substrate, actin filaments assemble into a branched network that drives a flat membrane protrusion known as the lamellipodium forward [38] [39] [40] [41] [42]. Bundles composed of actin filaments assemble in the cell front to form cylindrical membrane protrusions, called filopodia, that are important for sensing the extracellular environment [43] [44] [45]. In addition, actin networks form a thin mesh-like cortex (0.1 – 0.2 μm) underneath the plasma membrane [46] [47] [48], which provides mechanical support and protection to the membrane [49] [50].

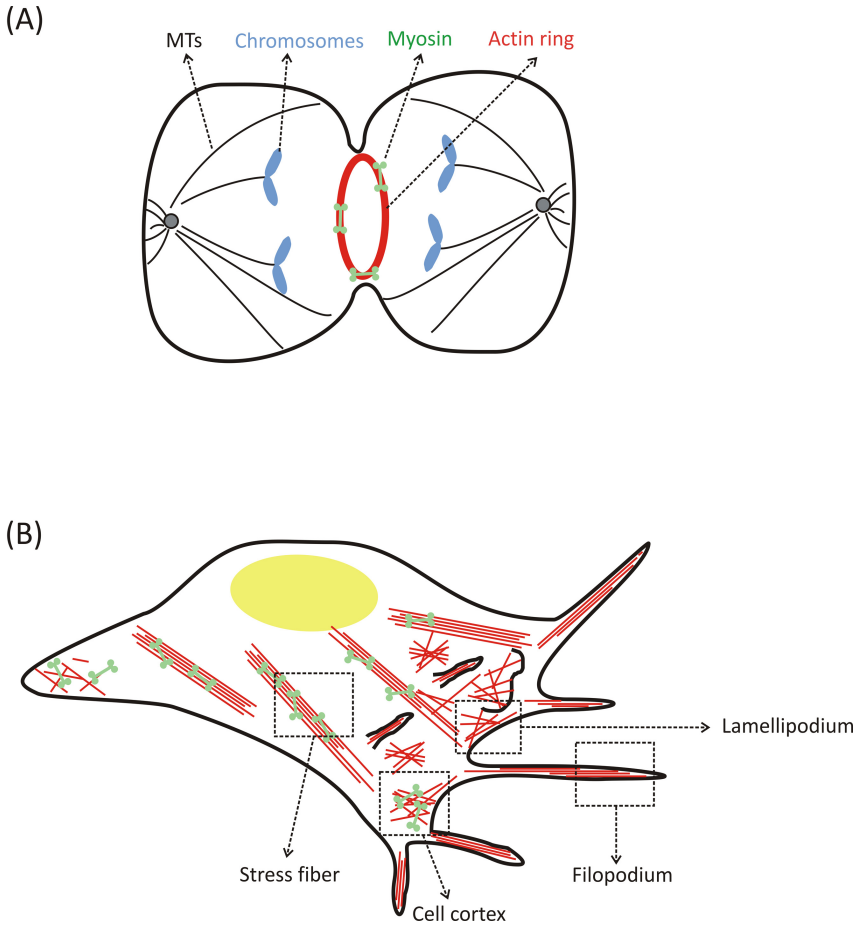

Figure 3. Schematic illustrations of the actin-myosin cytoskeleton in a typical animal cell such as a fibroblast during cell division (A) and cell locomotion (B). (A) In cell division, actin filaments and myosin motors form a contractile ring that physically constricts the membrane in the middle of the cell. (B) Cell locomotion is driven by the pushing forces exerted by actin filaments in the lamellipodium and the pulling force exerted by the myosin motors in the cell rear. Myosin-driven contraction detaches the rear end of the cell from the substrate, facilitating its movement. Also, in the cell front, membrane protrusions filled with actin bundles (called filopodia) act as environmental sensors for the cell to determine its direction. Besides, in the cell cortex, myosin-driven contractile forces generate cortical tension and sometimes induce cortical flows that can cause cell shape change. Stress fibers assembled by actin bundles and myosin motors are connected to extracellular matrix adhesion sites of the cell to ensure a proper communication between the cell and the substrate during cell movement.

To drive membrane protrusions, polymerization of actin filaments occurs mostly, perhaps even exclusively, adjacent to the plasma membrane [12] [40] [51]. An important set of actin binding proteins initiates the formation of new actin filaments by a process called nucleation. Since spontaneous nucleation of actin filaments is unfavorable, membrane-bound nucleators are required to initiate assembly of actin-based structures [52] [53] [54] [55] [35] [41] [56]. There are three types of actin nucleators: the actin-related protein-2/3 (Arp2/3) complex [57] [58], formin [59] and spire [60]. For instance, actin filaments in lamellipodia form branched arrays [41] [61] [62] that arise by dendritic nucleation mediated by the Arp2/3 complex [63] [64] (Fig. 4A). When activated at the plasma membrane by binding to nucleation promoting factors (NPFs) such as the Wiskott−Aldrich syndrome protein (WASP) family and WASP-family verprolin-homologous (WAVE) protein (Fig. 4A, *Left panel*) [65], the Arp2/3 complex initiates the formation of a new (daughter) filament that emerges from an existing (mother) filament in a Y-branch configuration (Fig. 4A, *Right panel*) [57]. The NPFs are themselves regulated by Rho-family GTPase and the lipid secondary messengers $PI(4,5)P_2$ and $PI(3,4,5)P_3$, which have been implicated in the recruitment of the NPFs to the plasma membrane [66]. Actin filaments within filopodia can be initiated by formins located at the tip of the filopodia [67] [68] [69] [70] [71] (Fig. 4B), though also other mechanisms have been proposed involving a transition from dendritic to bundled actin arrays at the base of the filopodia [44] [41]. An *in vitro* study of dendritic actin filaments growing on the outer surface of liposomes showed that membrane tension can also drive the spontaneous emergence of bundled actin filaments [72]. It has been shown that formin is regulated by the Rho GTPases such as Cdc42, RhoA and RhoC [73] [74] [75].

It remains elusive how actin filaments forming the thin cortex underneath the membrane are nucleated [76] [77] [78] [49]. A few candidate nucleators have been identified by live-cell microscopy observations of the recruitment of actin and actin-binding proteins to the plasma membrane of retracting membrane blebs [76] [77]. Membrane blebs initially appear to be devoid of filamentous actin and myosin motors. However, over time, actin filaments are recruited underneath the bleb membrane, forming a cortex, followed by the recruitment of myosin motors. The contractile forces applied by the myosin motors on the newly formed actin cortex then retract the bleb. It is conceivable that actin nucleators are present on the bleb membrane to promote rapid actin polymerization. Both the Arp2/3 complex and mDia1 of the formin family were not observed at the bleb membrane by GFP staining and immunofluorescence. However, since RhoA plays a role in the regulation of blebbing, formins likely do play a role in actin nucleation [77]. Based on indirect evidence, several nucleators of the formin family, Fhod1 [79], mDia2 [80] and Fmnl1 [81], have been suggested to play a role in the nucleation/assembly of cortical actin.

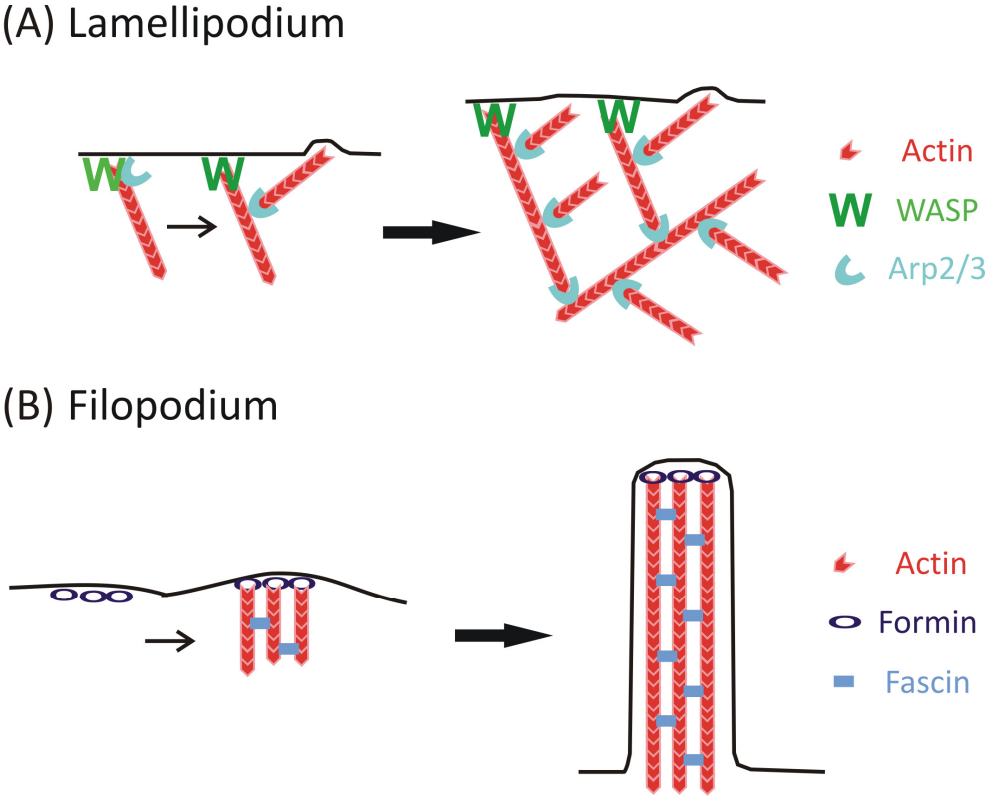

Figure 4. Organization of actin networks underneath the plasma membrane nucleated by the Arp2/3 complex (A) or by formin (B). (A) In lamellipodia, the Arp2/3 complex that is activated by membrane-bound nucleation promoting factors such as WASP (A, *Left Panel*) nucleates new actin filaments from the side of an existing filament, promoting the formation of a branched actin network (A, *Right panel*). (B) Formin has been suggested to nucleate actin filaments at the tip of filopodia. Activated formin that is recruited to the plasma membrane nucleates actin filaments and maintains their elongation (B, *Left Panel*). Elongating filaments are crosslinked by fascin to form a unipolar actin bundle (B, *Right Panel*).

Interactions of actin filaments with myosin II molecular motors, which apply contractile forces, are especially important for driving cell shape changes [82] [83] [84]. Myosin motors generate cortical tension, which can drive tangential flows of the cortex in the plane of the plasma membrane, resulting in cortical polarization or cell shape change [49] [85]. Myosin-driven cortical tension also contributes to the formation of the contractile ring in some cell types and to various morphogenetic processes in developing embryos [82] [83] [86] [87] [88]. During

cell division, actin and myosin form a contractile ring at the division site that physically constricts the plasma membrane (Fig. 3A) [89] [90]. During cell crawling, myosin-driven contraction in the cell rear causes cell body retraction and detachment from the substrate, facilitating directional cell movement [61] [91]. Contractile stress fibers composed of actin bundles and myosin motors that connect to focal adhesion complexes situated in the plasma membrane ensure a proper communication between the cell and the extracellular matrix during cell migration (Fig. 3B) [92] [93] [94] [95].

Recently, septins have been recognized as a fourth component of the cytoskeleton [96]. In animal cells as well as in budding yeast cells, septins form rings in the cell division site that act as scaffolds to recruit specific proteins to the division site and to promote functional interactions of these proteins [97] [98] [99] [100] [101] [102] [89]. A similar ring structure of septins has been found at the base of cilia [103] [104], dendritic spines [105] [106] and the annulus of the sperm tail [107] [108], where septin rings are thought to form a diffusion barrier. In addition to these functions, septins also influence the cortical elasticity of cells by locating at the plasma membrane, where they interact with phospholipids and the actin cytoskeleton [109] [96].

1.3 The interaction between the plasma membrane and the actin cytoskeleton

A key factor that influences cell shape control by the actin cytoskeleton is the interaction between the actin cytoskeleton and the plasma membrane [21] [110] [111] [112] [84]. Actin-membrane anchoring can be realized in three ways (and combinations thereof) [21]: (1) direct binding of actin to lipids, (2) direct binding of actin to transmembrane proteins, or indirect binding through adapter proteins, and (3) binding of actin to the membrane through peripheral membrane proteins. Some cortical proteins can have more than one type of interaction with the membrane. For example, spectrin is linked to the anion exchange protein band 3 through ankyrin, but spectrin can directly link to membrane phospholipids as well [113] [114] [21].

Nonspecific, direct actin-lipid interactions

In addition to the specific interactions mentioned above, it is also possible that actin may interact with positively charged lipids through electrostatic interactions since actin is an acidic globular protein (G-actin) with an isoelectric point of about 5.3 [115] [116]. Thus, both G-actin and filamentous (F-)actin are negatively charged in a physiological pH environment [110] [117]. *In vitro* experiments with reconstituted model systems indeed showed that a positively charged lipid layer composed of PC and sterylamine induces actin polymerization in low salt (2 mM

Tris-HCl pH 8.0, 0.2 mM NaATP and 0.2 mM $CaCl_2$) conditions, where actin is normally in its monomeric state [118] [119]. Under the same buffer condition, no actin polymerization was observed on lipid layers composed of neutral or negatively charged lipids, indeed suggesting that the interaction is electrostatic in nature. It was suggested that the high surface charges of lipid head groups may shield the net charge of actin monomers, facilitating monomer-monomer contact and promoting G-actin polymerization [119]. At high enough density, actin filaments adopt a nematic liquid crystalline arrangement on positively charged lipid layers [118]. In the presence of millimolar concentrations of divalent cations (2-10 mM Mg^{2+}), F-actin forms paracrystalline or net-like patterns on layers composed of zwitterionic lipids, PC and PE [120] [121] [122] [123] [124] [125]. Surprisingly, actin filament adsorption can also occur on lipid layers containing negatively charged lipids, such as PS, by increasing the divalent cation concentration (6 – 12 mM Mg^{2+}) [124]. In this case, the attraction was argued to be caused by the enhanced translational entropy of the counterions released upon adsorption of F-actin to the lipid layer [124]. The electrostatic interaction between actin and lipids is likely to be weak and dependent on the ionic strength of the buffer. Indeed, the interaction was shown to be reversible through addition of a high ionic strength buffer (> 65 mM KCl) [126] [123]. A Fourier analysis of thermally fluctuating lipid bilayers with adsorbed actin filaments indicated that the filaments are separated from the membrane by a distance of approximately 0.5 μm [127].

It is not clear if the electrostatic attractions between actin and lipids observed in cell-free systems are relevant for living cells. However, it is certainly conceivable that electrostatic interactions contribute to actin-membrane interactions, given that the experimental salt conditions were close to physiological conditions (1 - 8 mM Mg^{2+} and K^+ around 100 mM) [121].

There is evidence from experiments with model lipid bilayers that actin adsorption can alter the lateral distribution of lipids. For instance, adsorption of actin filaments to a PS/cholesterol containing membrane was shown to alter the size of cholesterol-based lipid domains [128]. Branched actin networks mediated by the Arp2/3 complex polymerizing on the outer surface of liposomes containing the phosphatidylinositol lipid $PI(4,5)P_2$ were also shown to induce lipid domain formation [129]. It is not clear to what extent these effects contribute to lipid domain formation in cells, but many of the structural and functional properties of lipid rafts do appear to require an intact actin cytoskeleton [130].

Binding of actin filaments to the plasma membrane through accessory proteins

Regulation of actin-membrane attachments is essential to allow controlled and reproducible shape changes during cellular processes such as cell motility and division [131] [132]. The plasma membrane plays an important role in the

regulation of actin assembly. Many actin binding proteins are for instance activated by binding to phosphatidylinositol (PI) lipids [132] [111] [133] [134] [135]. PI is a lipid with a charged inositol headgroup, from which 7 distinct species with distinct cellular roles are generated by phosphorylation. Phosphorylation can occur at three positions denoted as D-3, D-4 and D-5, leading to monophosphates [PI(3)P, PI(4)P, PI(5)P], diphosphates [PI(3,4)P_2, PI(3,5)P_2, PI(4,5)P_2], and one triphosphate species [PI(3,4,5)P_3]. These species are reversibly interconvertable by kinases and phosphatases. Although PIPs constitute only a small fraction of cellular lipids (0.3-1.5 mole% for the most abundant PIP, PI(4,5)P_2 [136] [2] [21] [137] [138] [139]), they are critical regulators of the actin cytoskeleton by binding and regulating actin binding proteins [135] [132] [21] [140] [134]. Examples include proteins of the WASP family, which activate the actin nucleator Arp2/3 complex; the actin depolymerizing factor ADF/cofilin, which promotes actin turnover by causing depolymerization; and the gelsolin superfamily, which severs and caps actin filaments. Regulation is achieved by specialized enzymes, which can adopt different spatial distributions during the cell cycle. During cytokinesis [141] [142] [143], for instance, cells concentrate PI(3,4,5)P_3 in the poles, where it activates actin polymerization, and PI(4,5)P_2 in the cleavage furrow, where it regulates actomyosin ring constriction.

Several accessory proteins have been identified that bridge F-actin to the plasma membrane [144] [133] [111] [132]. For instance, α-actinin can bind to palmitic acid (PA) and diacylglycerol (DAG) [145]. While bound to lipids, α-actinin can still bind to actin filaments [146]. At cell-cell and cell-matrix adhesions, actin-membrane linkages comprise large junctional complexes composed of many proteins, which are regulated by biochemical as well as mechanical signals [147] [148]. These adhesions are strong, but discrete. Accessory proteins such as members of the ezrin, radixin and moesin (ERM) family provide weaker, but continuous adhesion of the actin cortex to the plasma membrane [131] [149] [132] [150].

1.4 A bottom-up approach to investigate cell shape control: a cell-free model system

Having a physical description of a cell is critical to understand which mechanical properties are essential, and how these properties interact with each other, for cell shape determination [88] [151] [152] [36] [153] [82] [87] [49] [154]. Understanding how the actin cytoskeleton together with the plasma membrane determines cell shape can be achieved by two major experimental approaches [155] [87] [156], a “top-down” approach where biophysical measurements are performed in living cells or organisms [40] [157] [83] [158] [159], and a “bottom-up” approach where minimal components are put together to mimic cellular

events [21] [160] [161] [162] [163] [164] [165]. The top-down approach has provided key knowledge on cell shape control by the reciprocal interactions of the actin cortex and the plasma membrane [82] [49] [158] [83] [166]. However, due to the enormously complex biochemical composition of cells, it is rather challenging to distinguish various cellular contributions to cell shape change. This challenge may be addressed by complementing the top-down approach with a bottom-up approach based on simplified cell-free model systems. Given that such cell-free systems have a limited number of components with a well-controlled stoichiometry, they can reveal the minimal requirements for cellular functions and provide quantitative measurements as a basis for theoretical modeling. Here we briefly describe current bottom-up systems for studying actin-membrane interactions as well as actin-based membrane shape changes.

Solid-supported flat lipid bilayers (Fig. 5A) provide a suitable platform to study actin-membrane interactions [167] [156] [164]. Supported bilayers mimic the structure of the plasma membrane and allow for lateral diffusion of lipids within the plane of the bilayer. Planar lipid bilayers can be obtained by fusing small lipid liposomes onto glass coverslips. Functional membrane proteins can be incorporated in the bilayer using proteoliposomes [168]. For instance, a minimal actin cytoskeletal system has been reconstituted by binding actin filaments to a planar lipid bilayer using the transmembrane protein ponticulin [169] [170] and ezrin [171]. Filopodia-like actin structures were recently obtained by incubating frog egg extracts on lipid bilayers containing $PI(4,5)P_2$ in the presence of purified actin, cell division control protein 42 homolog (Cdc42), Neural Wiskott-Aldrich syndrome protein (N-WASP), transducer of Cdc42-dependent actin assembly-1 (toca-1) and the Arp2/3 complex [172]. Active actin-myosin networks have also been studied on supported lipid bilayers [173] [174].

To preserve the curvature of the plasma membrane, a supported lipid bilayer can be formed on a glass microsphere instead of on planar glass (Fig. 5B) [156] [165]. This approach has been developed intensively to study many aspects of actin assembly, based on a biomimetic system modeling motile, dendritic actin networks that propel certain bacteria [175]. A propulsive actin motility assay reconstituted on a lipid-coated glass bead revealed how N-WASP attaches actively polymerizing actin networks to the bead [176] and uncovered that the small GTPase Rac1 and Arf1 act synergistically to stimulate the actin nucleation promoting activity of the WAVE complex [177]. Actin assembly has also been achieved on the outer surface of water-in-oil emulsion droplets [178] [179] and on lipid bilayer liposomes [162] [156] [165]. Anchoring of actin to curved membrane layers was achieved by (1) electrostatic interactions between actin filaments and cationic lipids [180], (2) using succinimide-functionalized lipids that are able to react with lysine and cysteine residues in actin [180], (3) utilizing biotinylated lipids that connect to actin filaments containing biotinylated actin via streptavidin

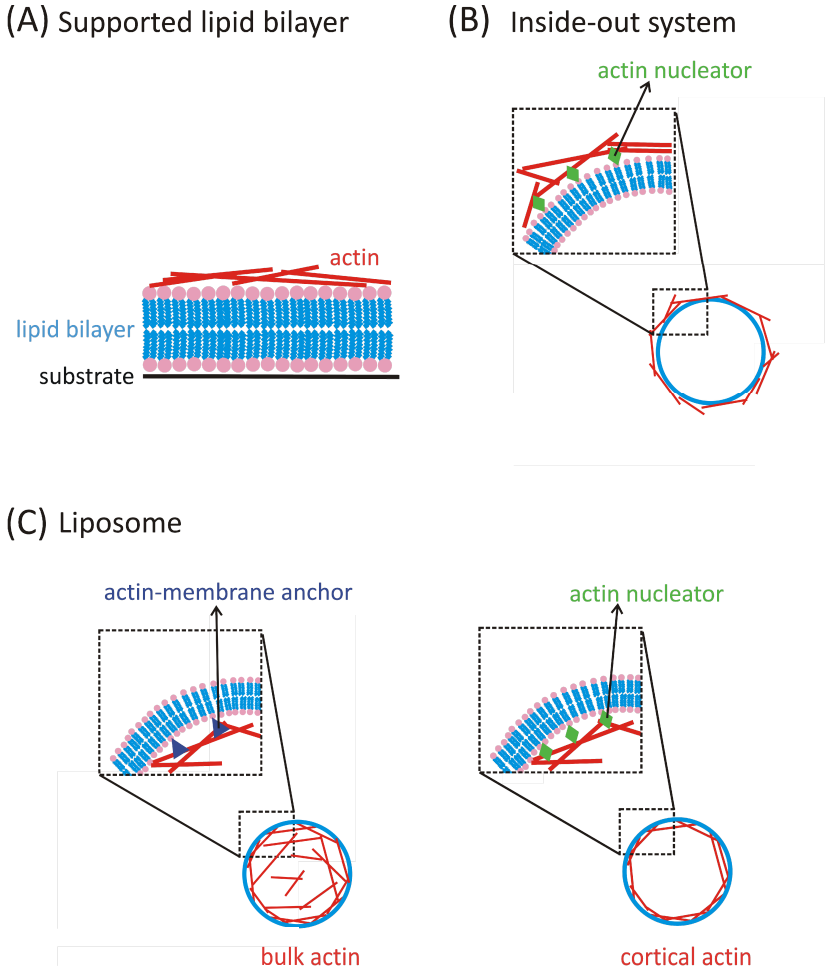

Figure 5. Bottom-up model systems to study actin-membrane interactions and the mechanisms of cell shape determination by the actin cytoskeleton. A supported lipid bilayer (A) is a suitable platform for studying actin-membrane interactions using high-resolution imaging. To mimic the curvature of the plasma membrane, one can use an inside-out model system (B) based either on a lipid bilayer-coated microsphere or on a liposome. In this system, actin nucleators can be used to promote actin polymerization from the lipid bilayer. Alternatively, one can use liposomes encapsulating actin filaments (C), which is an especially powerful model system to study how the actin cytoskeleton deforms the plasma membrane, since it mimics the confinement and geometrical characteristics of animal cells. In general, there are two types of actin organization inside liposomes: bulk actin networks with or without anchoring to the inner surface of the liposomes (*Left panel*) or a thin cortical actin network assembling from the liposome membrane that mimics the cellular cortex (*Right panel*).

or neutravidin [181] [182] [178] [183] [179], (4) through PIP_2, which transiently binds to N-WASP that activates the Arp2/3 complex to initiate growth of a dendritic actin network at the outer surface of a liposome [129] or a lipid-coated microsphere [176], (5) using His-tagged human N-WASP that links to Ni-NTA chelating lipids [184] and (6) linking of actin nucleating protein His-tagged ActA to Ni-NTA chelating lipids [185] [186]. In cells, to efficiently drive membrane protrusions, actin polymerization mostly, perhaps even exclusively, occurs on the plasma membrane. Thus, it is important to develop model systems where actin nucleators are bound to the lipid membrane, as in the last three scenarios, where lipid bound N-WASP or ActA was present to promote actin nucleation at the liposome membrane. A more physiological anchoring was achieved with spectrin/ankyrin proteins that anchor to the outer surface of liposomes composed of membranes extracted from human red blood cells [187].

The aforementioned model systems enable measurements of the viscoelastic properties of actin-membrane composites [183] [179], and have provided insights in actin-membrane interactions, the roles of actin binding proteins and their corresponding activators on actin filament growth. For instance, dendritic actin networks growing on the outer surface of liposomes containing PIP_2 lipids were found to stabilize PIP_2-rich membrane domains against temperature-induced mixing with other lipids [129]. The deformable character of liposomes further provides an ideal tool to study force generation by actin networks anchored on the liposome outer surface [180] [183] [185] [186] [184] [188] as well as the role of membrane tension on the organization of actin filaments growing from the liposome outer surface [72]. Recently, active actin-myosin networks have been reconstituted on the outer surface of liposomes, which revealed how myosin-driven contractile tension drives liposome shape changes [181] [182] (see Chapter 4).

Cell-sized liposomes (also called giant unilamellar vesicles, GUVs) encapsulating purified proteins, such as actin (Fig. 5C) [162] [164] [156] [163] [189] [190] [165], or minimal gene expression systems [191] [192] [193] [194] have been recognized as a powerful tool for modeling living cells. These liposomes preserve three key factors of the plasma membrane of living cells: (1) the compartmentalization of the membrane, which encloses cellular components in a small volume on the order of a pL, (2) the curvature and unilamellarity of the membrane, and (3) the fluid and deformable nature of the membrane. Cell-sized liposomes are thus an ideal model system to study how actin-membrane interactions determine cell shape. Unilamellar liposomes are composed of a single closed bilayer. For a liposome with a diameter of 50 μm composed of a single bilayer of POPC, there are around 2.2×10^{10} POPC lipids in the bilayer and the enclosed volume is around 65pL [195]. Thus far, three major methods have been used to obtain cell-sized liposomes encapsulating actin cytoskeletal systems: a lipid hydration method [196]

[197] [198] [199] [200] [201] [123] [202] [127], an inverted emulsion method [203] [204] [205] [206] [207] [208] [209] [210], and a jet-blowing method [163].

Briefly, in lipid hydration methods, a lipid mixture dissolved in an organic solvent is first deposited on a substrate and dried; then, an aqueous solution is applied upon the dry lipid layer to induce lipid hydration [211]. During hydration, lipid layers detach and swell to form liposomes. Applying an electric field to lipids deposited upon a conductive glass surface (a procedure known as electroformation [212]) promotes liposome formation, but only in a low ionic strength buffer in which actin remains monomeric. In this case, salt solutions needed for actin polymerization can be introduced into the liposomes by means of electroporation [198] or incorporation of transmembrane ion pores [123] [202] [127]. Alternatively, special electroformation protocols can be used to allow formation at high salt condition [213] [214] [215] [216]. As demonstrated in this thesis (Chapter 2), liposome formation can also be promoted by the use of partially dried hybrid films composed of lipids and an agarose gel (or a polyvinyl alcohol gel, PVA gel). This method has the advantage that liposomes can be formed using buffers of physiological ionic strength and for a wide range of lipid types [217] [218]. The resulting liposomes are unilamellar [219] with a symmetric lipid composition. The average protein encapsulation efficiency is around 50% [219].

The inverted emulsion technique of forming liposomes is a two-step procedure. First, water-in-oil emulsion droplets stabilized by a lipid monolayer are formed, and second the emulsion droplets are transferred into an aqueous phase through a lipid monolayer, so that a bilayer assembles [220]. Microfluidics-based methods to produce emulsion droplets can increase the liposome yield and ensure a monodisperse and controllable liposome size [221] [222] [223] [206]. An alternative method to create liposomes from emulsion droplets is the double emulsion method, where water droplets with an oil shell are formed in water, with both water/oil interfaces stabilized by lipids. To form liposomes, the oil is extracted from the oil shell by adding a volatile organic solvent into the outer aqueous phase, resulting in lipid self-assembly into a bilayer [224] [225]. Although oil remains trapped in the liposome membrane [205], emulsion-based methods have the advantage that one can obtain unilamellar liposomes with an asymmetric lipid composition [220] and with a reliable protein encapsulation efficiency under physiological buffer conditions.

In the jet-blowing strategy, a planar lipid bilayer is first formed and then deformed by injecting an actin solution using a microfluidic device [226] [227] [228]. Although this method requires a complicated experimental set up, it allows one to obtain unilamellar liposomes with an asymmetric lipid composition and a reliable protein encapsulation efficiency in a physiological buffer.

In cells, to drive membrane protrusions, actin polymerization is mostly initiated on the plasma membrane. To mimic actin nucleation at the membrane, Pontani et al. [203] [204] [205] used the inverted emulsion technique and introduced Ni-NTA chelating lipids in the membrane to recruit His-tagged N-WASP, which activates the actin nucleator Arp2/3 complex. They were thus able to nucleate actin filaments at the inner surface of the liposomes, resulting in a thin cortical actin network with a shell thickness around 0.2-0.4 μm (Fig. 5C, *Right panel*). In all other aforementioned liposome systems, actin polymerization occurred everywhere in the liposome interior, resulting in a bulk actin network (Fig. 5C, *Left panel*). However, in some cases, these bulk actin networks were anchored to the inner surface of the liposome utilizing the electrostatic interaction of actin filaments and cationic lipids [123], or biotinylated lipids that link to actin filaments having biotinylated actin through streptavidin or neutravidin (see this thesis, and references [182] [219]). More physiological anchoring has thus far only been achieved with spectrin/ankyrin proteins that anchor to the inner surface of liposomes composed of porcine brain membrane extracts [201].

1.5 Thesis outline

The central goal of this thesis is to reveal physical mechanisms by which the actin cytoskeleton and the plasma membrane may jointly determine cell shape. We address this question by performing *in vitro* experiments using a cell-free model system based on liposomes encapsulating active actin-myosin networks. We also study configurations of actin filaments mediated by the GTPase protein septins, which closely interact with the actin cytoskeleton and the plasma membrane in many cellular processes that involve cell shape change.

In Chapter 2, we develop a method to obtain liposomes encapsulating active actin-myosin networks. This method is based on the gentle hydration method assisted by an agarose or PVA hydrogel. We demonstrate that specific actin-membrane anchors can be introduced by immobilizing neutravidin on the surface of the liposomes and encapsulating biotinylated actin. In Chapter 3, we use the gentle hydration method facilitated by an agarose hydrogel to prepare liposomes encapsulating rigid actin-fascin bundles. By using confocal microscopy, we find that the liposome shape is controlled by a reciprocal interplay of actin bundle stiffness and membrane elasticity. Inside a flaccid liposome, where the membrane is deformable, actin bundles generate finger-like membrane protrusions, reminiscent of cellular filopodia. In contrast, when the liposome membrane is under high tension or has a large bending rigidity, confinement by the membrane forces the bundles to organize into cortical rings to reduce the energy cost associated with filament bending. In Chapter 4, we investigate the influence of actin-membrane anchoring on myosin-driven contractility of actin networks

encapsulated inside liposomes. We show that the myosin molecules form a single dense cluster that contracts the surrounding actin network, provided that the actin network is crosslinked to allow stress build-up. We demonstrate that when actin-membrane anchors are present, contraction is directed towards the membrane, whereas in the absence of anchors, actomyosin networks contract inwards, away from the membrane. When fascin is added to create actin bundles, the liposomes are less protrusive in the presence of myosin motors than in their absence, suggesting that the myosin motors may disassemble the bundles.

In Chapter 5 and 6, we investigate the structural properties of septins, which are indispensable for cell shape control in animal cells. Septins intimately interact with the plasma membrane and the actin cytoskeleton, for instance in the actin-myosin contractile ring assembled in the middle of a dividing animal cell. Unlike other more well-known actin crosslinkers, septins have the ability to form filaments and other higher order structures, including bundles and rings. In Chapter 5, we investigate the assembly of septins under different assembly conditions by using purified fly, human and budding yeast septins. We show that fly septins as well as their human counterparts assemble into rod-like hexamers containing three septins, each of which is present in two copies, and budding yeast septins assemble into rod-like octamers containing four septins, each of which is present in two copies. In buffers promoting septin polymerization, the fly and human septins assemble into bundles composed of aligned filaments, whereas the budding yeast septins form paired filaments. In Chapter 6, we investigate the ability of septins to organize actin filaments. Although a close interaction between septin and actin has been proposed based on their colocalization in diverse cell types and in different organisms, little is known about the nature of this interaction. We show that both fly and human septins bind directly to actin filaments. Furthermore, fly and human septins assemble actin filaments into bundles whose morphology depends on the polymerization state of the septins. Septin complexes assemble actin filaments into curved bundles and rings, whereas septin bundles mediate the formation of straight actin bundles. Budding yeast septins do not appear to interact with actin filaments. Our observations reveal that fly and mammalian septins may potentially both stabilize and help form the contractile ring that powers cell division.

CHAPTER 2. Building a cell-free model system: liposomes encapsulating active actomyosin networks

We demonstrate that cytoskeletal actin networks can be encapsulated in cell-sized liposomes by hydration of lipid layers in either an agarose hydrogel or a polyvinyl alcohol hydrogel. We show that liposomes formed using an agarose hydrogel have cell-like diameters of 10 to 20 μm, a high actin encapsulation efficiency, and a rather uniform actin content. We show by measurements of membrane fluorescence intensity and bending rigidity that the majority of liposomes are unilamellar. We further demonstrate that the actin network can be specifically anchored to the membrane by biotin-streptavidin linkages. Finally, we show that active actin networks containing contractile myosin II motor filaments can be encapsulated as well. We find that the myosin filaments form multiple foci at low myosin density, while condensing into a single dense focus that contracts actin filaments towards it at higher myosin density. The cell-sized actomyosin-filled liposomes prepared in this study are useful model systems for quantitative studies of the physical mechanisms by which the cytoskeleton actively controls cell shape and mechanics. In a broader context, this new preparation method should be widely applicable to encapsulation of proteins and polymers, for instance to create polymer-reinforced liposomes for drug delivery. Moreover, actomyosin-filled liposomes may possibly evolve into artificial cells in combination with minimal gene expression systems that enable self-reproduction using synthetic genetic information.

The contents of this chapter are based on:

Tsai, F.-C., Stuhrmann, B., and Koenderink, G. H. (2011). Encapsulation of active cytoskeletal protein networks in cell-sized liposomes. *Langmuir*, 27(16):10061–10071.

Weinberger, A., **Tsai, F.-C**., Koenderink, G. H., Schmidt, T. F., Itri, R., Meier, W., Schmatko, T., Schröder, A. and Marques, C. (2013). Gel-assisted formation of giant unilamellar vesicles. *Biophysical journal*, 105(1):154–164.

2.1 Introduction

The shape of animal cells is jointly determined by the plasma membrane and the cytoskeleton [12]. The plasma membrane defines the cell's autonomy, separating the cytoplasm from the external environment. Since the main structural component of the plasma membrane is a lipid bilayer, the membrane is fluid and highly deformable. Thus, to maintain a stable shape, cells rely on the cytoskeleton to provide mechanical support. The main cytoskeletal component to support the membrane is the actin cytoskeleton. Actin is a globular protein that polymerizes to form double-helical filaments with two structurally distinct ends. In the presence of a chemical fuel (adenosine 5'-triphosphate, ATP), actin filaments can generate pushing forces by growing with their fast-growing plus ends against the membrane [42]. These pushing forces contribute to cell locomotion [40] and the formation of membrane protrusions such as lamellipodia, thin (0.1 - 0.2 μm) and flat sheet-like protrusions [41] [39], and filopodia, thin (0.1 – 0.3 μm), finger-like protrusions [43] [44] [45]. To facilitate cell shape change, the actin cytoskeleton forms a mesh-like cortex with a thickness of 100 – 190 nm underneath the plasma membrane [46] [47] [48]. The actin cortex is actively tensed by myosin II motors, which hydrolyze ATP to contract the actin network [229]. Part of the myosin-based tension in the actin cytoskeleton is transmitted to the extracellular matrix or to adjacent cells across transmembrane adhesion receptors [84]. This force transmission enables cells to actively sense and respond to changes in tissue stiffness and to participate in tissue morphogenesis [84] [83].

The molecular composition of the cytoskeleton and the associated plasma membrane are complex and highly regulated [230]. Thus, it is difficult to unravel the interplay of physical and biochemical mechanisms that is responsible for the shape, mechanical properties, and mechanosensitivity of cells [230]. *In vitro* studies of model cytoskeletal networks, reconstituted from purified actin [231] [163] [156] [165], and of model membranes, reconstituted from synthetic/cell-extracted lipids [232] [9] [11], have provided many quantitative insights into the material properties of these components in isolation. There have also been *in vitro* studies of interactions of actin networks with membranes [162] [164], based on assays where actin filaments were coupled to flat lipid monolayers [233] [234] and supported lipid bilayers [169] [170], and onto the outer surface of water-in-oil droplets [178] and liposomes [180] [183] [129] [188] [185] [186] [184] [181] [72]. These model systems have enabled measurements of the viscoelastic properties of actin-membrane composites, and have provided insights in the role of actin filament growth in driving membrane deformation. More recently, active actin networks containing myosin motors were reconstituted on supported lipid bilayers [174] [173], and on the outer surface of water-in-oil droplets [179] and liposomes [182] [181]. However, these model systems cannot account for the

confinement effect that the actin cytoskeleton experiences *in vivo*. Moreover, they cannot be used to model transmembrane transmission of forces generated by myosin contractility. Accordingly, there have also been several efforts to encapsulate actin-myosin networks inside cell-sized liposomes [208] [189] [162] [164]. However, encapsulation of actin (or other cytoskeletal proteins, such as tubulin [213]) and myosin motors under physiological buffer conditions, necessary to promote actin polymerization and mechanochemical activity of motor proteins, is difficult. There is currently no facile and robust method to achieve this encapsulation.

There are two main factors hampering the encapsulation of active cytoskeletal systems into cell-sized liposomes. First, the high salt levels in physiological buffers generally cause a low, or even zero, yield of liposomes [195]. Second, the encapsulation procedure should preserve the biological activity of the proteins, which requires a fast procedure. The widely used electroformation method requires low salt concentrations [235] [195] [236] [237], though special protocols can be used to allow formation at high salt [213] [214] [215] [216], or salt can be introduced afterwards by means of electroporation [198] or incorporation of ion channels in the membrane [202] [123] [238] [239] [240]. However, liposome formation is slow, typically taking a few hours. Also, the electric field applied during electroformation can cause peroxidation of unsaturated lipids [241] [242], and may be potentially harmful to the proteins that are to be encapsulated.

Several alternative approaches have been developed for encapsulating high-salt solutions, including gentle hydration [243] [244], freeze-thaw extrusion [245], solvent evaporation [246], inkjet or pulsed jet flow formation [247] [227] [248] [224] [228] [226], heat-induced formation [249] and an inverted emulsion method [250] [220] [251]. Several methods have been specifically developed to obtain liposomes containing actin in a physiological buffer that promotes actin polymerization, such as gentle hydration [199], inkjet formation [163], and the inverted emulsion method [203] [210] [205] [204]. Yet, each of these methods has its drawbacks. Gentle hydration usually gives variable protein encapsulation efficiencies [195]. The microfluidic inkjetting technique is a fast method that can produce liposomes in high yield, but it requires specialized equipments. The inverted emulsion method is fast (20 minutes) but requires multiple steps. Two of these steps, the creation of a water-in-oil emulsion and centrifugation of the emulsion droplets through a lipid monolayer to obtain liposomes, are particularly difficult to reproduce [195], though recent studies show that microfluidics-based methods can improve the reproducibility [206] [223]. Another concern with these techniques is that oil is trapped in the bilayer, which changes the rheology of the membrane [205].

To mimic actin nucleation at the plasma membrane as it occurs in cells, Pontani et al. [203] [204] [205] used the inverted emulsion technique and introduced Ni-

NTA chelating lipids in the liposome membrane to recruit His-tagged N-WASP, which activates the actin nucleator Arp2/3 complex [57]. Combined with profilin co-encapsulation to suppress bulk nucleation, actin filaments exclusively nucleate at the inner surface of the liposomes, forming a thin (0.2-0.4 μm) cortical actin network [203]. To mimic anchoring of actin filaments to the plasma membrane, several types of actin-membrane interactions have been utilized. One method relies on the electrostatic interaction of negatively charged actin filaments with cationic lipids [123]. More physiological anchoring of actin filaments inside liposomes has so far only been reported with spectrin/ankyrin proteins combined with liposomes composed of porcine brain membrane extracts [201].

Here we propose a new method to prepare giant liposomes filled with an active actin-myosin cytoskeleton. Our method is facile, quick and reproducible, and permits control over actin-membrane anchoring. Our method is inspired by a recent study of Horger and coworkers [217], who showed that liposomes containing high-salt buffers can be obtained by gentle hydration of an agarose hydrogel film infiltrated with lipids. They proposed that the agarose hydrogel promotes multiple factors that are essential for liposome formation, including self-assembly of the dried lipids into lamellae, swelling of the lamellae, and fusion of adjacent liposomes into giant liposomes. In this chapter, we show that actin-filled liposomes are obtained in high yield when hybrid agarose/lipid films are hydrated in a physiological buffer solution of skeletal muscle actin and myosin II. Actin polymerization occurs everywhere inside the liposomes, resulting in bulk actin networks. The required conditions – spin-coated agarose/lipid films and the presence of PEGylated lipids – are more restrictive than those for empty liposomes. We characterize the liposome size distribution, membrane lamellarity, and the efficiency of protein encapsulation. We demonstrate that our method affords control over the anchoring of the actin-myosin network to the inner leaflet of the liposome membrane by utilizing biotin-streptavidin linkers. We further show that polyvinyl alcohol (PVA) gels can be used instead of agarose gel, with the advantage that PVA, in contrast to agarose, does not associate with the membrane. Finally, we show that neutravidin can be specifically immobilized on the membrane by combining the gel-assisted method with an inverted precursor method [252]. This method allows us to place specific membrane anchors on the membrane to anchor biotinylated actin filaments without needing to add neutravidin to the liposome inner buffer, which would cause network crosslinking.

2.2 Results and Discussion

Encapsulation of cytoskeletal proteins in cell-sized liposomes presents a long-standing technical challenge. High liposome yield is generally incompatible with physiological salt levels, and the yield is even further reduced with inclusion of

proteins. Though several strategies have been described which overcome these difficulties, there is currently no facile and robust method to achieve this encapsulation. We present a new approach based on gentle hydration of hybrid lipid-agarose films in solutions of cytoskeletal proteins, inspired by a recent study of Horger and coworkers [217], where liposomes were prepared from a variety of lipids under physiological ionic conditions. Our method proceeds in three stages, as sketched in Fig. 1A. First, a uniform layer of ultralow gelling agarose is spin-coated on a glass slide and partially dried (*panel i*). In contrast to the standard gelling temperature agarose that forms a fibrous, cross-linked gel, ultralow gelling agarose forms loose meshes of agarose molecules that partially dissolve upon hydration [217]. Second, a lipid solution is spin-coated on the agarose layer and dried under vacuum (*panel ii*). Third, the hybrid film is hydrated in a buffer solution containing monomeric (G-actin) and (optionally) myosin II (*panel iii*). It was proposed in the paper of Horger et al. [217] that swelling and partial dissolution of the agarose film upon hydration promote liposome formation. The large contact area of the lipids with the porous agarose film and the prehydration of the lipids by residual water may facilitate lipid self-assembly into bilayers. Swelling of the agarose gel may generate forces normal to the lipid bilayers that promote bilayer separation. The dissolved agarose molecules may further enhance water influx into the lipid film by generating hyperosmotic conditions. Furthermore, it was proposed that crowding of the liposomes that grow out from the porous agarose film promotes their fusion into cell-sized liposomes. Dissolved agarose molecules were shown to associate with the lipid membranes after liposome formation, and it was proposed that they may promote liposome formation in a similar fashion as PEGylated lipids [243].

Liposome formation and protein encapsulation

Figure 1B shows cell-sized liposomes containing F-actin that form spontaneously when films of agarose and lipids are hydrated in a physiological buffer ("I-buffer"). The I-buffer contains 4 mg/mL G-actin, at a pH value of 7.4 and ionic condition (50 mM KCl and 2 mM $MgCl_2$) that promote polymerization of G-actin into filaments. The filaments form homogeneous, entangled solutions inside the liposomes as well as in the external "O-buffer" solution (the liposome suspension was diluted about 5-fold with 255 mM glucose). However, we can digest the external F-actin by supplementing the O-buffer with DNAseI, which complexes G-actin [127]. The liposome yield is high: we typically find 50-100 liposomes in the observation chamber with a chamber volume of around 120 – 300 μl after around four times dilution. Most liposomes are spherical and freely floating, while some attach to the bottom surface of the observation chamber. Strikingly, all liposomes in the observation chamber contain actin. In the presence

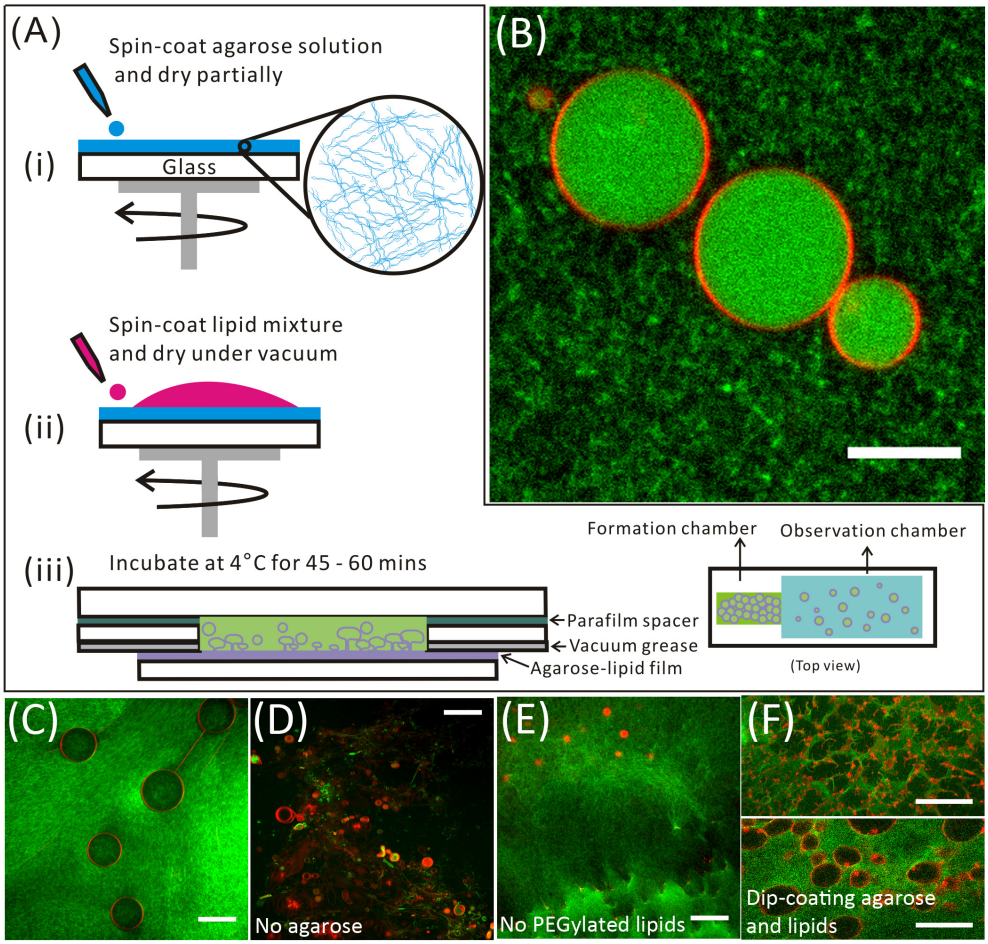

Figure 1. (A) Schematic overview of the liposome preparation procedure, which consists of three steps: (i) an ultralow gelling agarose solution is spin-coated onto a glass slide and partially dried, (ii) lipids are spin-coated on top and dried under vacuum, and (iii) liposomes are formed by hydration in a solution of actin and myosin in I-buffer at 4°C. The liposomes are flown from the formation chamber into an adjacent observation chamber by injection of O-buffer. Actin polymerization is initiated by heating the sample to room temperature. (B) – (F) Confocal fluorescence micrographs of actin-filled liposomes formed within one hour by gentle hydration of agarose/lipid films. Red represents rhodamine-lipid fluorescence and green represents AlexaFluor 488-actin fluorescence (10 mole% in (B)-(D) and 20 mole% in (E) and (F)). The following lipid compositions were used (in mole%): (B, C, D, F) DOPC/PEG-DOPE/Rhodamine-DOPE = 94.8:5:0.2. (E) DOPC/Rhodamine-DOPE = 99.8:0.2. Observation conditions: (B) liposomes were diluted 5-fold with O-buffer and observed in the observation chamber; (C) – (F) liposomes were observed inside the formation chamber. (B) Liposomes filled with actin (4 mg/mL) are obtained with high yield

using hybrid films of agarose and 5 mole% PEGylated lipids. Scale bar: 10 μm. (C) Liposomes filled with actin (1 mg/mL) in the formation chamber. Scale bar: 50 μm. (D) In the absence of agarose, virtually no liposomes are formed. Scale bar: 50 μm. (E) No liposomes are formed in the absence of PEGylated lipids. Scale bar: 50 μm. (F) Liposomes formed on hybrid agarose-lipid films prepared by dip-coating [217] rarely contain actin, and liposomes are absent in most areas of the formation chamber (*top panel*) except for a few locations (*bottom panel*). Scale bars: 30 μm.

of myosin II, 85% of the liposomes (out of 60) contain actin and myosin II. The remainder 15% contains only actin.

For comparison, we also make actin-filled liposomes with the inverted emulsion technique [203]. In our hands, the liposome yield is high (in the hundreds) when we encapsulate sucrose in water, but low when we encapsulate actin in I-buffer. We find a maximum of 15 actin-filled liposomes per sample, much less than with the agarose swelling method. It is unclear what factors determine liposome yield. There are examples of encapsulation of proteins in high salt solutions that do give high yields [253]. We also observe that liposomes obtained by the inverted emulsion technique tend to have attached oil droplets or lipid aggregates that complicate measurements of membrane fluctuations by video microscopy (Supplementary Fig. 2A). In contrast, a larger fraction of the liposomes obtained by swelling of agarose/lipid films have cleaner contours (around 50% of a total of 60 liposomes, determined by phase contrast images, see Supplementary Fig. 2B).

The presence of an agarose film is essential for the formation of liposomes in the presence of proteins and salts. Lipid films deposited directly on glass substrates do not form cell-sized liposomes, as shown in Figure 1D. The few liposomes that do form are smaller than 20 μm, do not contain actin, and are predominantly multilamellar. This looks strikingly different from the formation chamber in the presence of an agarose film, where large liposomes containing actin are found (Fig. 1C). The reason why high salt concentrations hamper liposome formation from lipids coated on bare glass is uncertain. Although some mechanisms for liposome formation have been proposed [254], the exact molecular mechanism remains uncertain. It is thought that solutions of high ionic strength hinder in particular the first step of separation of lipid lamellae due to electrostatic screening of charges on the lipid head groups. We dope the membranes with 5 mole% PEG-PE lipids bearing a 2 kDa polyethylene glycol (PEG) tail to prevent nonspecific membrane adsorption of actin and to reduce aggregation of liposomes [123] [217]. We find that PEG-PE is also indispensable to obtain actin-filled liposomes in high yield. In the absence of PEGylated lipids, liposomes are rarely formed and they do not contain actin, as shown in Fig. 1E.

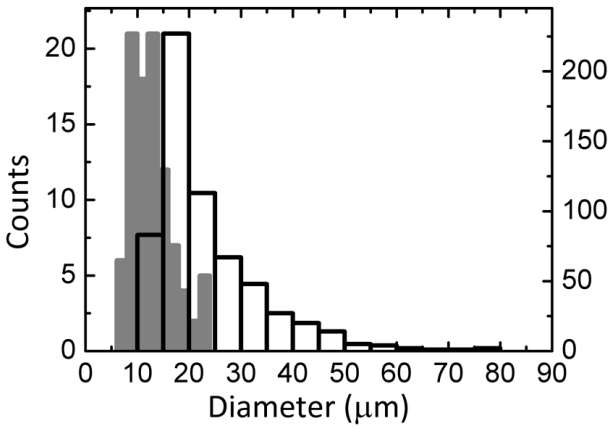

Figure 2. Size distribution of actin-filled liposomes determined from confocal fluorescence images of equatorial cross-sections. Empty bars correspond to liposomes in the formation chamber measured within four hours after formation (*right-hand* y-axis, 614 liposomes counted), while gray bars correspond to liposomes harvested from the formation chamber by injection of O-buffer (*left-hand* y-axis, 96 liposomes counted).

This suggests that steric repulsions of the PEGylated lipids may contribute to liposome formation by promoting initial bilayer orientation and separation, similar to their proposed role in gentle swelling on bare glass [243] [255]. In the study of Horger et al. [217], liposomes did form with high yield from pure POPC, but PEGylated lipids increased the yield. This difference may be caused by different buffer conditions (such as the presence of Mg^{2+} in the actin buffer) or by the presence of actin during formation. In addition to agarose and PEGylated lipids, the spin-coating step is also crucial to obtain a good liposome yield and efficient actin encapsulation. When the agarose and lipid layers are dip-coated [217] instead of spin-coated, most regions of the formation chamber do not have liposomes (*upper panel* of Fig. 1F); liposomes are present in a few regions of the formation chamber but they do not contain detectable actin (*bottom panel* of Fig. 1F)). We suspect that spin-coating improves the uniformity of the agarose and lipid films, which is apparently beneficial for liposome formation. Similar effects

have been observed with lipid mixtures on indium tin oxide plates in the electroformation method [256].

To test whether dissolved agarose enters the liposomes, we formed liposomes using an agarose gel containing 0.1 % (w/w) FITC labeled agarose. We measured the fluorescence intensities of FITC- agarose inside and outside the liposomes right after formation using confocal microscopy (Supplementary Fig. 3A, D). Interestingly, we observe that actin-filled liposomes do not contain agarose at a detectable level (Supplementary Fig. 3B), whereas liposomes devoid of actin do contain agarose (Supplementary Fig. 3C).

Size distribution and membrane lamellarity

We measure liposome size distributions by imaging their equatorial cross-sections with a confocal laser scanning microscope, using identical laser and detector settings for all images. Liposomes adhering to the agarose film in the formation chamber display a wide distribution of diameters, ranging from 14 to 76 μm with an average diameter of 24 ± 10 μm, as shown in Figure 2 (empty bars). Liposomes removed from the chamber and suspended in O-buffer are almost twofold smaller, with an average diameter of 13 ± 4 μm (gray bars in Fig. 2). The larger size of the liposomes in the formation chamber may be caused by fusion of adjacent liposomes within the four hour time span required for image recording. In addition, large liposomes are more likely to break when they are flown into the observation chamber. The liposome sizes are comparable with sizes of actin-filled liposomes obtained by electroformation [123] and the inverted emulsion method [203]. In our hands, liposomes containing actin in I-buffer prepared with the inverted emulsion method have diameters of approximately 10 μm, comparable to liposomes prepared with the new agarose method. However, the agarose method produces around tenfold more liposomes per sample and also generates actin-filled liposomes with diameters larger than 10 μm that are rarely found with the inverted emulsion method.

In order for the liposomes to serve as a faithful model of the plasma membrane, it is important that the membrane be unilamellar. Liposomes containing 5 mole% PEGylated lipids are expected to be unilamellar [243]. To confirm unilamellarity, we measure the mechanical properties of the membranes by video tracking of the thermally driven membrane undulations. We form liposomes with an inner solution of 0.016 % (w/w) sucrose in water and dilute them in an aqueous solution of 330 mM glucose with slightly higher osmolarity (by 20 mOsmol/kg) to reduce the membrane surface tension [257]. Free-floating, spherical liposomes are observed by phase contrast microscopy and spectra of transverse bending undulations are extracted by image analysis. Figure 3A shows a typical fluctuation spectrum of a liposome encapsulating a sucrose solution (black squares). The

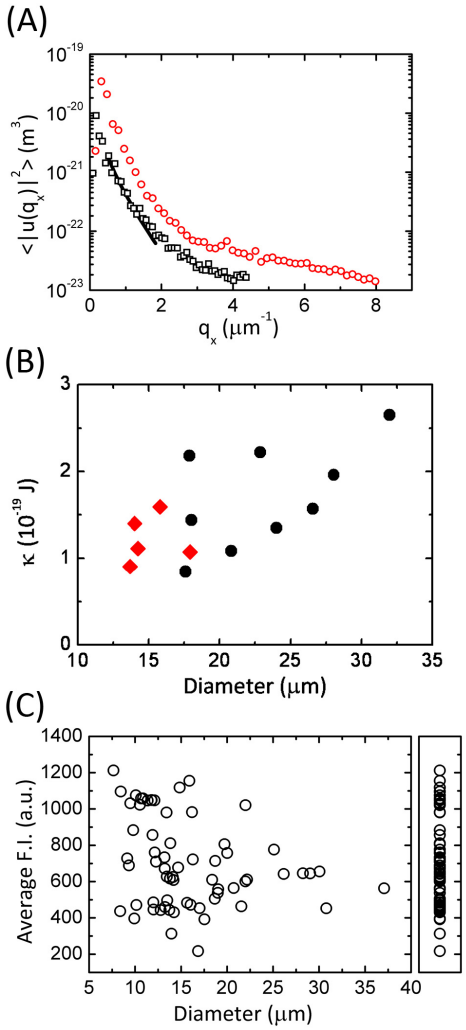

Figure 3. Analysis of liposome lamellarity by membrane bending modulus measurements and by fluorimetric estimation. (A) Representative membrane fluctuation spectra of liposomes encapsulating a sucrose solution (black squares) or 1 mg/mL F-actin (red circles). The spectrum of the sucrose-filled liposome is fitted to a modified Helfrich model [258] [257], taking into account the influence of camera integration time (black straight line). (B) Elastic bending modulus of empty liposomes as a function of liposome diameter. Each symbol corresponds to one liposome (black circles, agarose-swelling method; red diamonds, electroformation). (C) *Left panel*: the average fluorescence intensity (F.I.) of liposome membranes as a function of liposome diameter (65 liposomes measured). *Right panel*: projection of data points in the left panel to their corresponding average fluorescence intensities.

bending rigidity and membrane tension are determined from the spectrum by fitting to a modified Helfrich model (black line), taking into account the effect of the finite camera integration time [257] [258].

Figure 3B shows the bending modulus, κ, of various liposomes with different diameters (black circles). We find values between 0.8×10^{-19} J and 2.7×10^{-19} J with an average value of 1.7×10^{-19} J (corresponding to 42.5 k_BT, where k_BT is the thermal energy). The large spread in the data is typical when determining bending moduli of liposomes by contour analysis [259]. The average membrane tension is 3.6×10^{-7} N/m, comparable to prior reports [257]. The average κ-value is two-fold larger than that of liposomes composed exclusively of DOPC [260]. However, that value was obtained by micropipette aspiration, which is known to yield smaller values for κ than contour analysis [261]. Furthermore, the PEGylated lipids used in our lipid formulation are expected to increase κ compared to pure DOPC membranes, since they increase the membrane thickness [262] and κ scales as membrane thickness squared [263]. However, we cannot exclude a contribution from residual agarose molecules associated with the lipid layer [217].

To test whether residual agarose contributes to the bending modulus, we measure bending moduli for liposomes of the exact same lipid composition but prepared by electroformation. The electro-formed liposomes have a similar range of κ-values (red diamonds in Fig. 3B) and a similar average κ-value (1.1×10^{-19} J) as the liposomes prepared by gentle swelling. The membrane tension (mean value 2×10^{-7} N/m) is also comparable to that of liposomes obtained by gentle swelling. This observation suggests that residual agarose has no measurable influence on membrane stiffness or tension.

We also measure membrane fluctuation spectra for a few actin-filled liposomes, as exemplified in Figure 3A by the red circles. These spectra can in principle be fitted to the Helfrich relation, but this fit returns an unphysical tension of 4×10^{-21} N/m. This is probably a signature of the viscoelastic material properties of the encapsulated actin network, which is not captured in the Helfrich model that assumes a viscous liquid interior. In follow-up work, we plan to extend membrane fluctuation models, taking into account the viscoelastic nature of the actin network [264] [265] [266] and, in case of encapsulated actin-myosin networks, the contractile activity of myosin [267].

The close correspondence of the mechanical behavior of the liposomes prepared by gentle swelling to that of electroformed liposomes also suggests that the liposomes are predominantly unilamellar [236]. To independently assess membrane lamellarity, we analyzed the fluorescent intensity of the membranes of actin-filled liposomes. Figure 3C (*left panel*) shows the average fluorescence intensity (F.I.) of liposome membranes as a function of liposome diameter, measured for 65 freely suspended liposomes in the observation chamber. The distribution of intensities is rather broad with no clear peak(s), and there is no

apparent dependence on liposome diameter. However, when we project the data to their corresponding average fluorescence intensity (Fig. 3C, *right panel*), there appear to be two groups of liposomes: one group with a membrane intensity of 400 – 800 a.u. (63% of the liposomes), and another group with an intensity of 1000 – 1200 a.u. (20% of the liposomes). This suggests that a small fraction of the liposomes may be multilamellar.

Encapsulation efficiency

An important application of actin-filled liposomes is as cell-mimetic systems for quantitative measurements of the influence of the actin cortex on membrane mechanics and force generation. To fulfill this promise, it is desirable that the encapsulated amount of actin be close to the target concentration with low variance among liposomes. To estimate the encapsulation efficiency, we measure the average fluorescence signal for F-actin inside liposomes (I_i) and outside liposomes (I_o) in the formation chamber. For a bulk actin concentration of 1 mg/mL, the encapsulation ratio, defined as I_i/I_o, is on average 56% $\pm$ 26%, as shown in Figure 4A. This is comparable with other studies [268], which report typical solute encapsulation efficiencies below 50%. Some liposomes have apparent encapsulation ratios larger than 100%. This could be due to non-homogeneities in the highly viscous actin solution outside the liposomes. However, encapsulation efficiencies higher than 100% were also reported for encapsulation of several other macromolecular solutes [269] [270]. The underlying mechanism of this phenomenon, which has been termed “spontaneous protein crowding” [270] [271] [272], is unclear. It was suggested that nonspecific solute/lipid interactions may increase the amount of solute entering between the lipid lamella during hydration [269].

To test whether the encapsulation efficiency depends on actin concentration, we compare the encapsulation efficiency for 1 mg/mL and 0.25 mg/mL actin, as shown in Figure 4A. We observe a slightly lower encapsulation efficiency for 1 mg/mL actin than for 0.25 mg/mL actin, which may be due to the higher solution viscosity at 1 mg/mL actin that may hinder encapsulation. In the future, the encapsulation efficiency may potentially be enhanced by using lipids with a functional group to bind the proteins [268] or by adding a crowding agent [273] [274].

The encapsulation variance among liposomes was estimated by comparing the average fluorescence signal of F-actin in liposomes flown from the formation chamber into the observation chamber by injecting O-buffer. Figure 4B shows that the average fluorescent intensity is independent of liposome diameter (left) and well-described by a Gaussian distribution (red line) with a peak at a fluorescence intensity of 421 $\pm$ 33 arbitrary unit. This narrow distribution indicates a low variance in the encapsulated amount of actin among liposomes.

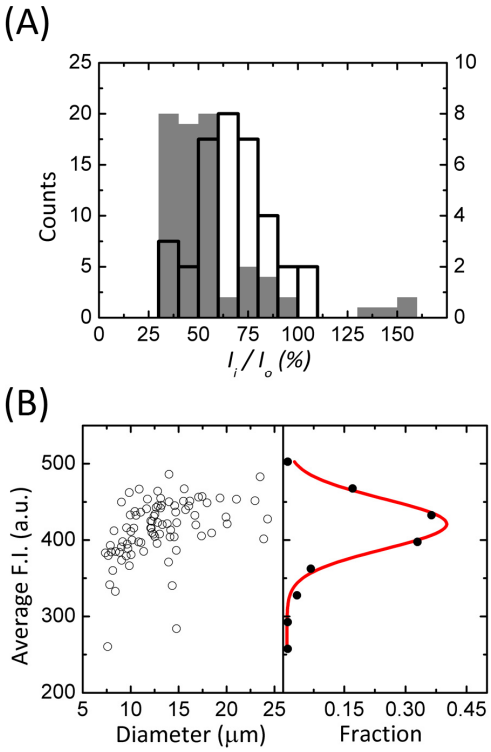

Figure 4. Encapsulation efficiency of liposomes determined from confocal fluorescence images. (A) Histogram of F-actin encapsulation ratio defined as average fluorescent intensity inside a liposome (I_i) divided by the average fluorescent intensity outside the liposomes (I_o). Filled bars: 1 mg/mL F-actin, *left-hand y-axis*, 76 liposomes counted. Empty bars: 0.25 mg/mL F-actin, *right-hand y-axis*, 35 liposomes counted. (B) *Left panel*: encapsulated F-actin (1 mg/mL) concentration, measured as average fluorescence intensity (F.I.), plotted as a function of liposome diameter (88 liposomes counted). *Right panel*: histogram of F-actin content of liposomes fitted by a Gaussian distribution (red line).

Actin-membrane interaction

In order for the liposomes to faithfully mimic the mechanics of biological cells, it is important that the actin network can be attached to the membrane by specific anchors of controlled surface density. To prevent non-specific membrane adhesion of actin, we include 5 mole% PEGylated lipids in the lipid mixture, which act as a steric brush. The membranes are indeed passivated successfully, as shown by confocal imaging (Fig. 5A): while the actin network (green) is homogeneous throughout the liposome, near the membrane (red) an empty depletion zone devoid of actin is observed, as expected for rigid actin filaments near nonbinding

surfaces [275]. The depletion of actin close to the membrane is also clearly visible in a fluorescence intensity cross-section of the liposome, as shown in Figure 5B. To create well-defined actin-membrane anchoring, we use biotin-streptavidin bonds [234], which are nearly permanent. When actin is doped with biotinylated G-actin in a 1:400 molar ratio (ca. 1 biotin per 1 μm length of filament) but the membrane is free of biotin, inclusion of streptavidin (1:25 molar ratio to G-actin) in the I-buffer causes the formation of actin bundles which do not adhere to the membrane, as shown in Figure 5C. However, upon inclusion of biotinylated lipids in the membrane, the biotinylated actin network adheres to the inner surface of the membrane and forms a cortex-like structure, leaving a depleted zone in the liposome center, as shown in Figure 5D. This structure is reminiscent of cortical actin structures observed in electroformed liposomes where actin filaments self-organized underneath the liposome membrane to reduce their bending energy [123]. However, with a thickness of around 2 μm, it is thicker than actin cortices adhered to membranes of electroformed liposomes through electrostatic interaction, where the thickness was ~1 μm [123]. It is also thicker than actin cortices obtained by the Arp2/3 complex nucleated growth from the inner membrane of a liposome, whose thickness was 0.2 – 0.4 μm [203].

Encapsulation of active actin-myosin networks

The actin cytoskeleton *in vivo* actively exerts contractile forces on the membrane by the activity of myosin motors that assemble into bipolar filaments and slide actin filaments past each other. To the best of our knowledge, the only prior myosin encapsulation into liposomes was done with heavy meromyosin (HMM), a double-headed derivative of myosin II motors [209] [276] [207] [210]. HMM is nonprocessive, with a duty ratio of only a few percent [277]. Nevertheless, HMM motors can collectively generate contraction of actin filament networks and bundles [278]. However, bipolar filaments are likely more effective since they are more processive, and they more closely mimic the cytoskeleton of nonmuscle cells, in which nonmuscle myosin II self-assembles into bipolar minifilaments composed of 10-20 myosins [279] [61]. We use large bipolar filaments of skeletal muscle myosin II motors with a length of around 0.69 μm, as shown in Figure 6A. These filaments contain about 100 myosins per filament [280]. These filaments are capable of generating contraction of entangled and crosslinked actin networks *in vitro* [281] [282] [280] [283].

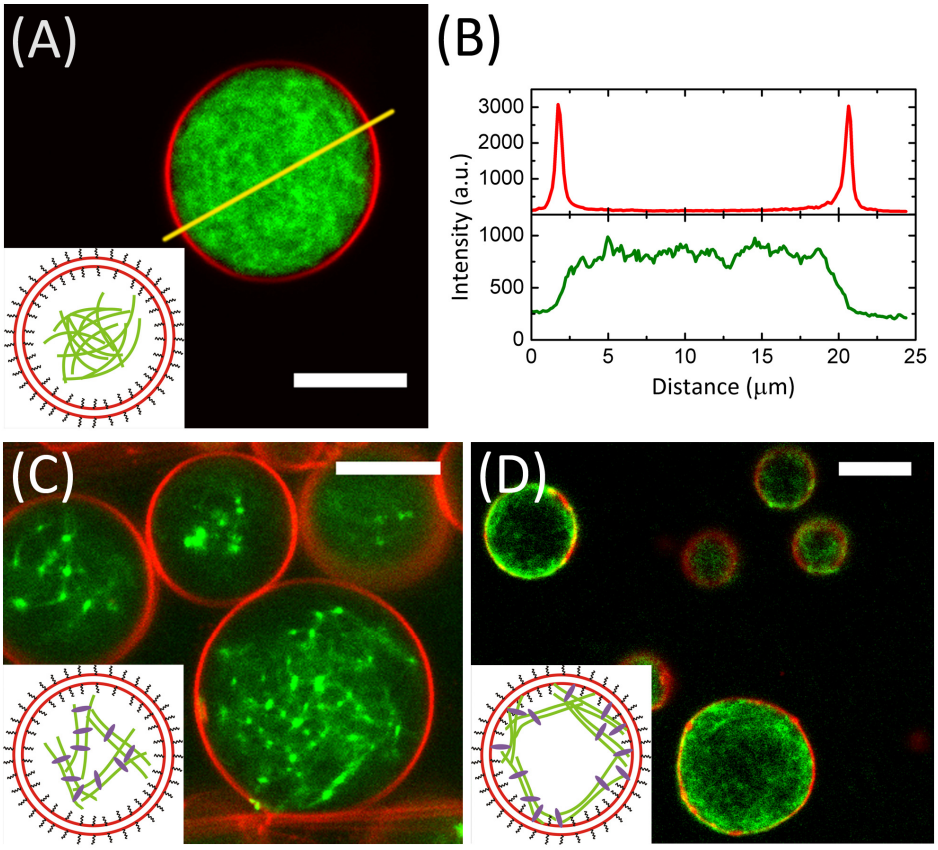

Figure 5. (A), (C) and (D) Confocal fluorescence micrographs of actin-filled liposomes. Lipid membranes are labeled with rhodamine (red); actin is labeled with AlexaFluor 488 (green). The actin concentration in the I-buffer before encapsulation was 1 mg/mL. Insets indicate the nature of the actin-membrane interaction. (A) F-actin solution inside a liposome with an inert membrane (containing PEG-lipids) is homogeneous and displays a depletion zone underneath the membrane. (B) Fluorescence intensity profiles along the yellow line across the liposome in (A). *Upper panel*: membrane fluorescence intensity along the line scan. *Bottom panel*: actin fluorescence intensity along the line scan. (C) F-actin network crosslinked by biotin-streptavidin inside a liposome with an inert membrane is inhomogeneous and bundled, and does not attach to the membrane. (D) Liposomes containing biotinylated lipids encapsulate networks of biotinylated actin filaments that are coupled to the membranes via biotin-streptavidin bonds. Scale bars: 10 μm. Biotinylated G-actin to G-actin molar ratio = 1:400.

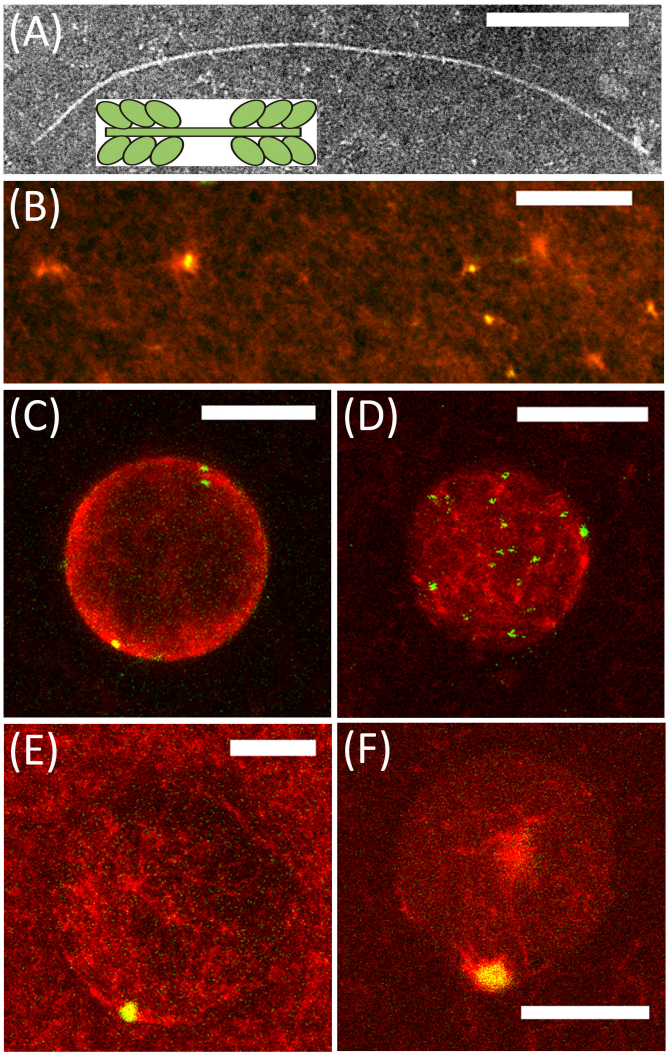

Figure 6. (A) Typical electron micrograph of a reconstituted bipolar skeletal muscle myosin II filament. Scale bar: 200 nm. (B) – (F) Confocal fluorescence micrographs of bulk F-actin solutions containing active myosin II filaments (B) (scale bar: 20 μm), and of actomyosin solutions inside liposomes (C) - (F) (scale bars: 10 μm). Actin (concentration 1 mg/mL) is labeled with AlexaFluor 488 (shown in red); myosin is labeled with DyLight 594 (shown in green). The F-actin network adheres to the membrane by biotin-streptavidin bonds. Biotinylated G-actin to G-actin molar ratio = 1:400. Myosin II to G-actin molar ratio: (C) and (D) 1: 200; (E) 1 : 100 and (F) 1 : 50.

Bulk networks of actin filaments and myosin bipolar filaments are initially homogeneous, but within 5 minutes the motor filaments self-assemble into large clusters [280] (shown in green in Fig. 6B) within the actin network (shown in red). Using the agarose-swelling method, we are able to encapsulate myosin filaments together with actin into liposomes, as shown in Fig. 6C and D. The myosin:actin molar ratio is 1:200 and the membrane contains biotinylated lipids that bind to the biotinylated actin filaments. Similar to their organization in bulk networks, myosin molecules form clusters (shown in green) within the entangled F-actin network. Interestingly, there are two classes of liposomes. Half of the liposomes (out of 63) contain a cortex-like actin-myosin structure (Fig. 6C), whereas the other half contains a homogeneous actomyosin network (Fig. 6D). We suspect that this variability is related to a variable myosin encapsulation efficiency. We are unable to quantify the encapsulation efficiency for myosin, since myosin is not homogeneously distributed in the encapsulated actin networks, but concentrated in dense foci. However, we expect that it is less efficiently encapsulated than actin, since the hydrodynamic radius of myosin (45 nm [284]) is much larger than that of actin (2 nm [285]). Prior studies showed that solutes with hydrodynamic radii above 10 nm are encapsulated much less efficiently than smaller ones [269] [274]. Also, it is possible that the homogeneous networks contain more myosin, and are therefore more contractile, leading to disruption of the actin-membrane anchoring. To test this possibility, we encapsulate actin-myosin networks with higher myosin/actin ratios, of 1:100 (Fig. 6E) and 1:50 (Fig. 6F). We find that at higher myosin densities, the myosin filaments usually condense into a single focus, which contracts actin filaments towards it. We do not find any cortex-like structures at these high myosin/actin ratios. There are a few possible explanations. First, motor-driven forces may disrupt actin-membrane attachments. Second, motor-driven forces may rupture the actin cortex, resulting in cortex detachment from the membrane. Third, lipid/streptavidin anchors may be dragged in the plane of the membrane by the myosin-driven force [286]. Fifth, myosin-driven forces may possibly pull out the lipids from the membrane instead of rupturing the biotin-streptavidin bonds, given that biotin-streptavidin bonds are stronger than lipid-membrane bonds [287].

The cell-sized actomyosin-filled liposomes prepared in this study provide an experimental model system to guide future quantitative studies of physical mechanisms that determine cellular processes such as cell spreading/adhesion [189] [288] [204], contraction and blebbing [289] [76], and myosin-based mechanosensing [84]. Ultimately, such systems may evolve into artificial cells in combination with minimal gene expression systems that enable self-reproduction using synthetic genetic information [192].

To enhance the physiological relevance of the model system, it would be interesting to increase the actin concentration. The actin concentrations used

here (~0.6 mg/mL inside the liposomes) are at the low end of the range reported for mammalian, non-muscle cells. Concentrations of actin *in vivo* depend on organism and cell type, actin has an inhomogeneous spatial distribution in cells, and this distribution changes during the cell cycle. Global estimates of F-actin concentrations in non-muscle cells range from 12 to 300 μM (0.5-12 mg/mL) [52]. However, locally, the F-actin concentration can be higher, for instance 500 μM (20 mg/mL) was reported in the lamellipodium of migrating cells [290]. The myosin:actin molar ratios used in our work are well within the range reported for nonmuscle cells, which ranges from 1:10 to 1:100 depending on cell type [291] [292].

In the future, it would also be interesting to couple the actomyosin networks to the membrane through physiological linker proteins such as ezrin, radixin and moesin (the ERM protein family) [131] [150], spectrin/ankyrin proteins [201], or septins (see Chapters 5 and 6 of this thesis). Many of these cortical proteins specifically bind to phosphatidylinositol 4,5-bisphosphate (PIP_2) [135] [129] [132]. As a first step, we show that liposomes containing 2.5 mole% or 5 mole% of PIP_2 lipids can be obtained by using the agarose swelling method (Fig. 7).

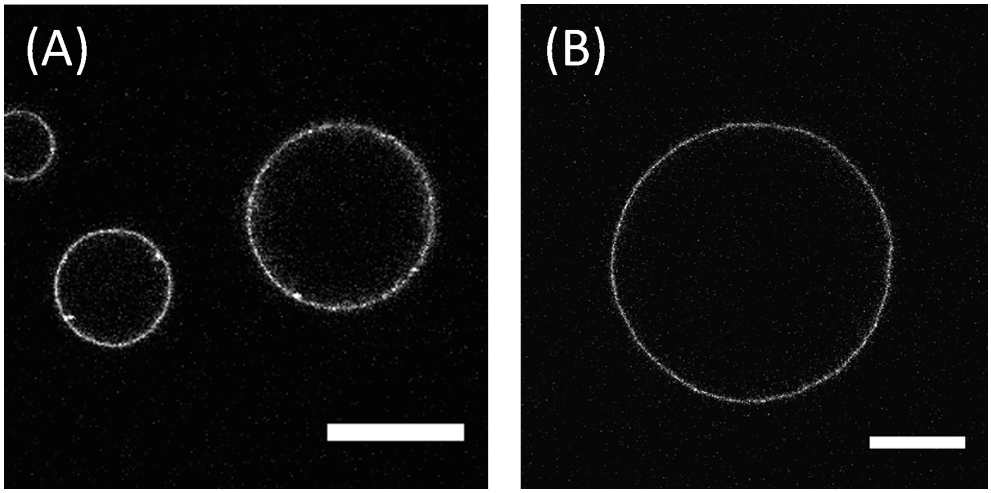

Figure 7. Confocal fluorescence micrographs of liposomes containing PIP_2 at 2.5 mole% (A) and 5 mole% (B) visualized by fluorescently labeled PIP_2. Liposome membranes are composed of DOPC, 5 mole% PEG-PE, 0.1 mole% rhodamine-PE and 2.5 mole% (or 5 mole%) PIP_2 including 0.1 mole% TopFluor-PIP_2. The inner and outer buffer of the liposomes is sucrose (290 mM) and glucose (308 mM), respectively. Scale bars: 20 μm.

Polyvinyl alcohol (PVA)-assisted liposome formation

A potential disadvantage of the agarose swelling method is the contaminating agarose on the liposome membranes, which may hamper the inclusion of transmembrane or peripheral membrane proteins. To overcome this issue, we utilize a PVA gel instead of an agarose gel to assist lipid swelling, because PVA gels are expected to be much less prone to dissolution upon swelling than other hydrophilic gels [293][294]. Indeed, we find that liposomes obtained by swelling of PVA/lipid gels have no detectable PVA fluorescence signal (Fig. 8) [218]. Furthermore, we can achieve actin encapsulation by the PVA-swelling method (Fig. 9) [218].

To test whether actin can be anchored to the membrane, we again use biotinylated lipids and actin, which we couple by neutravidin. However, rather than co-encapsulating neutravidin with actin, as described above, we develop a hybrid method combining the PVA swelling method with an inverted precursor method [252] to bind neutravidin to the lipids before the swelling procedure. This method should make crosslinking of actin filaments with each other independent from anchoring of actin filaments to the membrane. We note that neutravidin molecules immobilized on the liposome membrane still contribute to actin filament crosslinking near the membrane, since one neutravidin molecule has four biotin binding sties. We confirm that neutravidin molecules introduced by the inverted precursor method are functional by assessing their biotin binding ability (Fig. 10). In Chapter 4, we will use the hybrid method to obtain liposomes encapsulating membrane-anchored actin-myosin cortical shells.

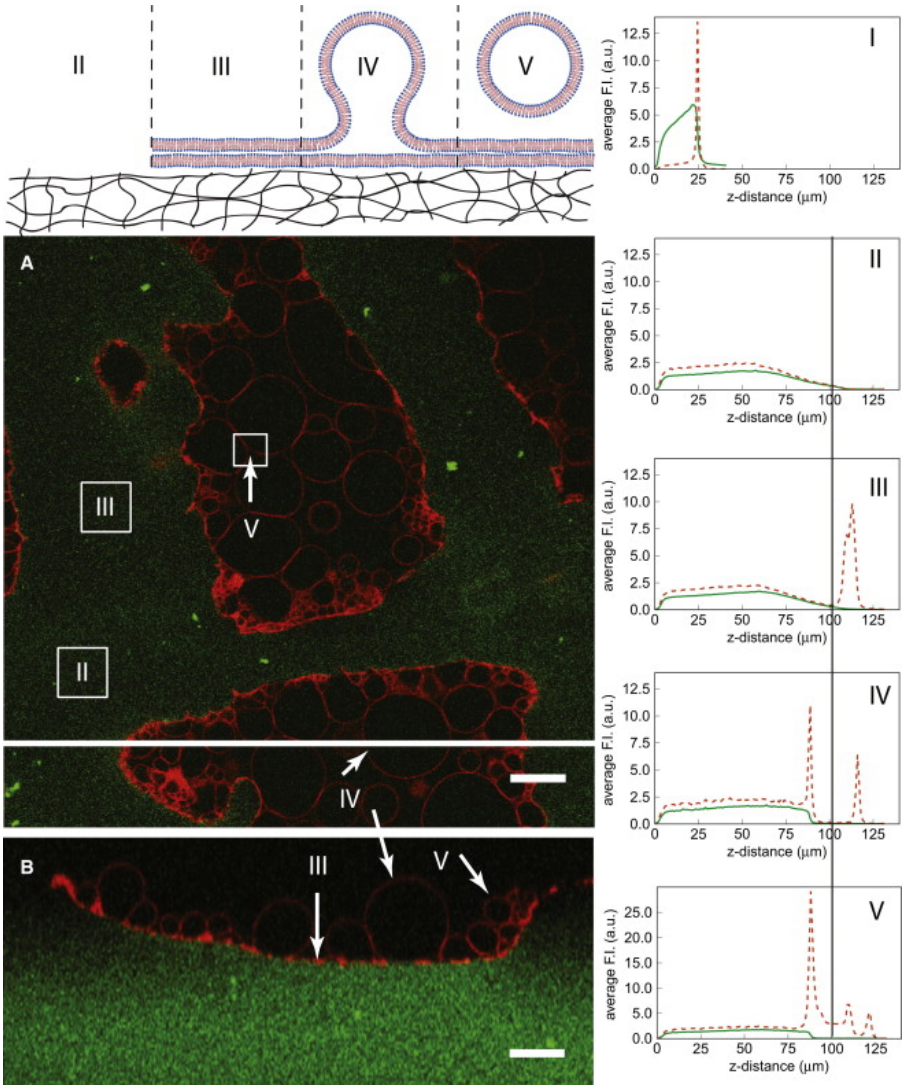

Figure 8. Quantification of PVA content of liposomes formed by gentle swelling of PVA-lipid films (see sketch in *Top panel*). *Left panel* (A) Confocal fluorescence micrograph of DTAF-labeled PVA gel (shown in green) and liposomes labeled with 0.2 mole% rhodamine-PE (shown in red) recorded at the equatorial cross-sectional plane (x-y view). (B) X-z view of the horizontal white line in (A). *Right panel* Graph I is a *z*-profile of the sample shown in panel (A) before hydration, while the other graphs correspond to different regions of the sample indicated by roman numerals in (A). Pixel-averaged fluorescence intensity (average F.I.) of a given *z* position is determined within a 20 μm × 20 μm area. The scan was performed starting from the top of the sample. Note that *z* = 0 in the right panels corresponds to the bottom of the sample. Scale bars: 20 μm.

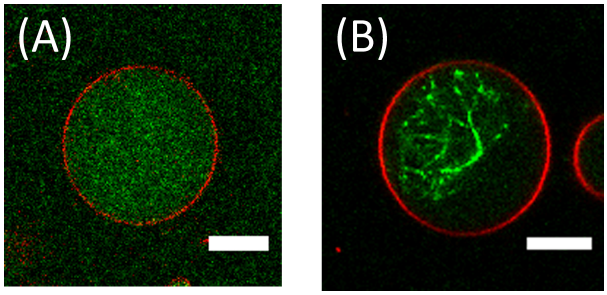

Figure 9. Confocal fluorescence micrographs of liposomes formed by gentle swelling of PVA-lipid films, encapsulating actin filaments (A) and actin bundles mediated by biotin-streptavidin linkers (B). Liposome membranes are composed of DOPC, 5 mole% PEG-PE and 0.2 mole% rhodamine-PE. Scale bars: (A) 10 μm and (B) 20 μm.

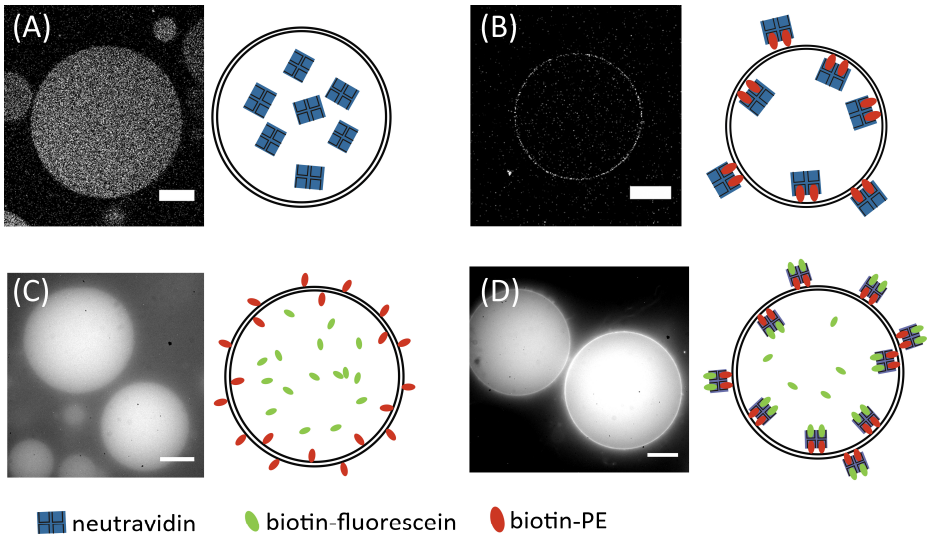

Figure 10. Fluorescence micrographs of liposomes obtained by the PVA-precursor swelling method, with corresponding schematic diagrams explaining the experimental conditions. To assess the specificity of membrane binding of neutravidin to biotinylated lipids, neutravidin labeled with AlexaFluor 350 was incorporated into the inverse phase precursor micelles either in the absence (A) or presence (B) of biotin-PE lipids. To verify that neutravidin is still functionally active after the inverse phase precursor procedure, biotin-fluorescein (500 nM) is encapsulated in the liposomes in the absence (C) or presence (D) of neutravidin on the membrane. Images in (A) and (B) are taken by confocal fluorescence microscopy, whereas images in (C) and (D) were taken by fluorescence microscopy. Scale bars: 20 μm.

2.3 Conclusion

We demonstrate a new preparation method for liposomes containing active actomyosin networks in physiological buffers by gentle swelling of lipid layers upon an agarose hydrogel. This method is facile and fast, taking under one hour for liposome formation. We show that this method gives high yield (typically 50-100 liposomes per preparation) and leads to rather uniform encapsulation of actin among liposomes with an average efficiency of 56%. Moreover, the encapsulated networks can be selectively anchored to the inner leaflet of the membrane via biotin-streptavidin (or, equivalently, biotin-neutravidin) linkages. The membranes are unilamellar and have a similar bending rigidity as membranes of liposomes prepared by electroformation. We show that the disadvantage of the contaminating agarose on the liposome membranes obtained by using the agarose swelling method can be overcome by using a PVA hydrogel. We further combine the PVA swelling method with an inverted precursor method to disentangle the crosslinking of actin filaments from the actin-membrane anchoring. Taken together, the new gentle swelling method developed here opens the way for quantitative studies of physical mechanisms by which the actin cytoskeleton and the plasma membrane jointly control cell shape and mechanics. In Chapter 3 of this thesis, we use the method to study membrane deformation by actin-fascin bundles, and in Chapter 4 we use the method to study the influence of actin-membrane anchoring on active actomyosin cortex contractility.

2.4 Supplementary Figures

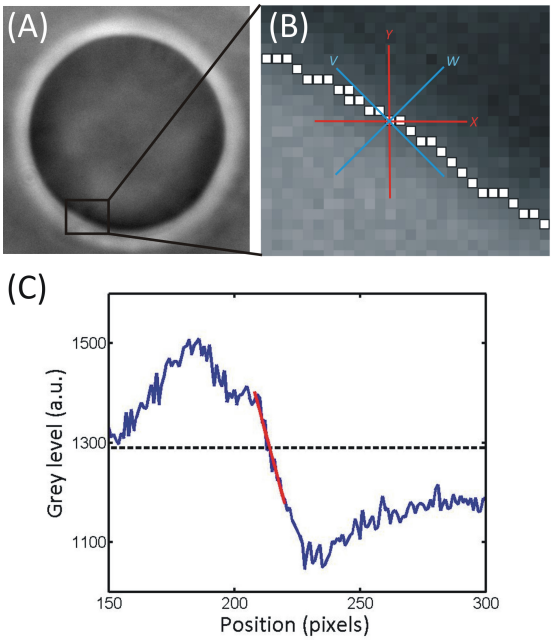

Supplementary Figure 1. Principle of automated liposome contour detection. (A) Image of a liposome in phase contrast. (B) Detected contour of the liposome edge. Pixels marked with white squares are detected positions of the liposome contour. Red lines represent detection directions along horizontal and vertical axes, denoted *x* and *y*, respectively; blue lines represent detection directions along the diagonal axes, denoted *v* and *w*. (C) Gray level profile along the *x*-direction spanning a length of 150 pixels centered near the liposome edge. The profile is locally fitted by a straight line (red line) centered at the detection position; the dashed line corresponds to the mean gray level within 24 pixels centered at the detection position. The intersection of these two lines gives an estimate of the membrane edge position in the *x*-direction. This procedure is repeated along the *y*-, *v*- and *w*-directions; all four positions, weighted by the corresponding slope of the intensity profiles, are averaged to obtain the liposome position with subpixel accuracy.

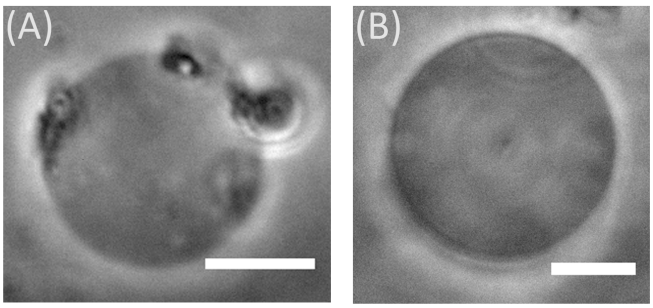

Supplementary Figure 2. Representative phase contrast images of liposomes encapsulating an actomyosin network, produced with the inverted emulsion method (A) and with the agarose-swelling method (B). Inside both liposomes, the biotinylated F-actin network adheres to biotinylated lipids within the inner surface of the membrane. Actin concentration is 1 mg/mL; myosin II to G-actin molar ratio is 1:200; biotinylated G-actin to G-actin molar ratio is 1:400. Small spherical objects (oil droplets or lipid agglomerates) are attached on the outer surface of the liposome in (A), which is characteristic of the majority of liposomes obtained by the inverted emulsion method. By contrast, the liposome obtained by the agarose swelling method has a cleaner surface. Scale bars: 5 μm.

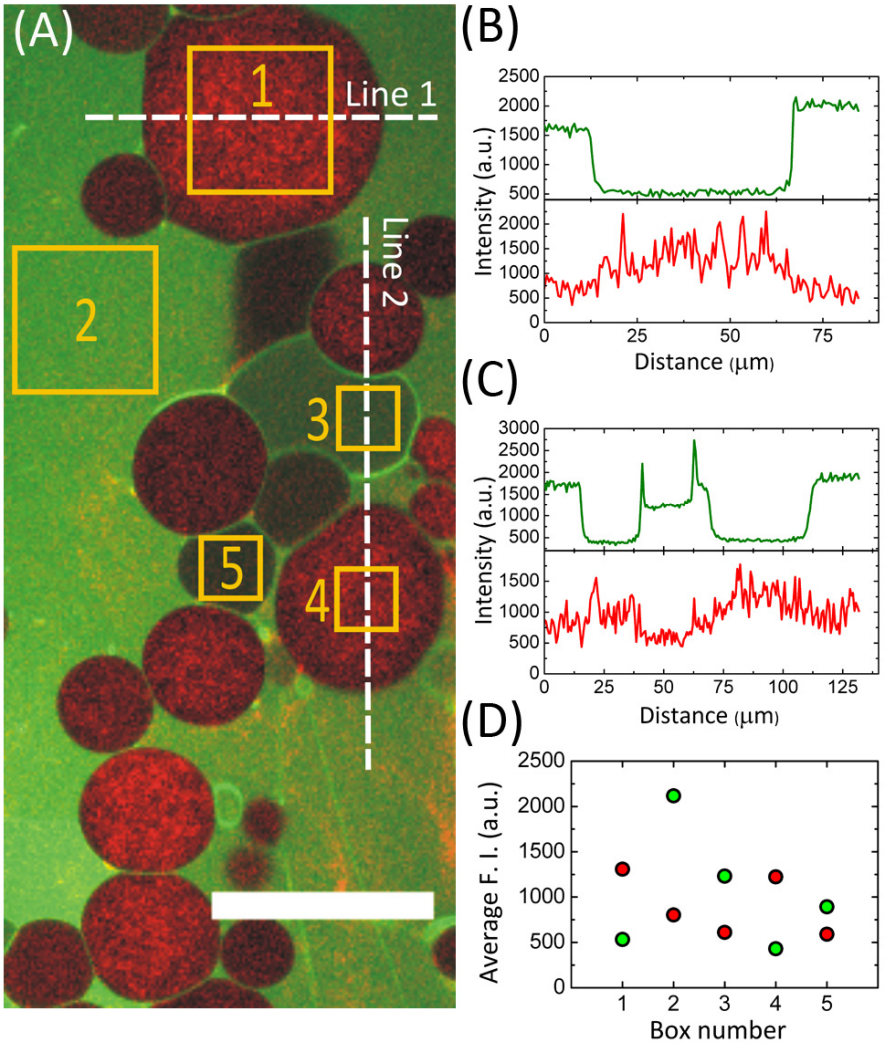

Supplementary Figure 3. Quantification of agarose content of liposomes using confocal fluorescence images of equatorial cross-sections. (A) Liposomes formed from a hybrid film of lipids and 0.1% (w/w) FITC labeled agarose (green) were observed inside the formation chamber; F-actin (1 mg/mL) is labeled with 10% mole% AlexaFluor 568-actin (red). Scale bar: 50 μm. (B) and (C): Fluorescence intensity profiles along line 1 and line 2 in (A), respectively. *Upper panels*: FITC-agarose fluorescence intensity along the line scan. *Bottom panels*: AlexaFluor 568-actin fluorescence intensity along the line scan. (D) Average fluorescence intensities of FITC labeled agarose (green circles) and AlexaFluor 568 labeled actin (red circles) inside numbered boxes in (A).

2.5 Materials and Methods

Lipids and chemicals

Lipids were purchased from Avanti Polar Lipids (Alabaster, AL, USA). These included 1,2-dioleoyl-sn-glycero-3-phosphocholine (DOPC), 1,2-dipalmitoyl-sn-glycero-3-phosphoethanolamine-N-[methoxy(polyethylene glycol)-2000] or 1,2-dioleoyl-*sn*-glycero-3-phosphoethanolamine-N-[methoxy(polyethylene glycol)-2000] (PEG-PE with a 2 kDa polyethylene glycol tail), the fluorescently labeled lipids 1,2-dioleoyl-sn-glycero-3-phosphoethanolamine-N-(lissamine rhodamine B sulfonyl) (rhodamine-DOPE) and 1-oleoyl-2-{6-[4-(dipyrromethene boron difluoride)butanoyl]amino}hexanoyl-*sn*-glycero-3-phosphoinositol-4,5-bisphosphate (TopFluor-PIP_2), the biotinylated lipid 1,2-dipalmitoyl-sn-glycero-3-phosphoethanolamine-N-(cap biotinyl) (biotin-PE), and brain phosphatidylinositol 4,5-bisphosphate (PIP_2). We investigated the formation of liposomes on films of type IX-A ultralow gelling agarose (gel point T_g ≤17 ^oC) from Sigma-Aldrich (St. Louis, MO, USA). We chose this type of agarose because it has the lowest gelling temperature on the market, which we need for gentle swelling at 4^oC. We also tested ultra-low gelling temperature agarose from Fluka, but this agarose type gave a markedly reduced liposome yield and encapsulation efficiency. To test for association of agarose with the liposome membrane, agarose was fluorescently labeled [217] with fluorescein isothiocyanate (FITC) from Sigma-Aldrich (St. Louis, MO). Polyvinyl alcohol (PVA, MW 145000, Merck KGaA, Darmstadt, Germany) was purchased from VWR International (Amsterdam, the Netherlands). Neutravidin and AlexaFluor 350 labeled neutravidin were purchased from Invitrogen (Breda, The Netherlands). Streptavidin was obtained from Thermo Scientific (Breda, The Netherlands), creatine phosphate and creatine kinase were obtained from Roche Diagnostics (Almere, The Netherlands). Other chemicals were purchased from Sigma Aldrich (St. Louis, MO, USA). ATP was prepared as a 100 mM MgATP stock solution using equimolar amounts of Na_2ATP and $MgCl_2$ in 10 mM imidazole-HCl buffer (pH 7.4).

Proteins

G-actin and myosin II were purified from rabbit skeletal muscle including a gel filtration of actin on a Sephacryl S-200 high-resolution column (GE Healthcare, Munich, Germany) to remove residual capping proteins, crosslinkers, and actin oligomers [295] [296]. G-actin was stored at -80^oC in G-buffer (2 mM Tris-HCl, 0.2 mM Na_2ATP, 0.2 mM $CaCl_2$, 0.2 mM dithiothreitol (DTT), 0.5 mM NaN_3, pH 8.0). Myosin II was stored at -20^oC in a high salt buffer with glycerol (0.6 M KCl, 25 mM KH_2PO_4, 10 mM EDTA, 1 mM DTT, pH 6.5, 50% w/w glycerol). Fresh myosin solutions were prepared daily by dialysis against AB300 buffer (300 mM KCl, 4 mM $MgCl_2$, 1 mM DTT, 25 mM imidazole, pH 7.4). Protein concentrations were

determined by absorption measurements at 280 nm using extinction coefficients of 0.53 cm^2/mg for myosin and 1.1 cm^2/mg for actin [295]. Fluorescent myosin with a dye/protein ratio of 1.7 was prepared by labeling amine groups with DyLight 594 NHS Ester [297]. G-actin labeled with AlexaFluor 488 or AlexaFluor 568 or with biotin was purchased from Invitrogen (Breda, The Netherlands) and Tebu Bio (Heerhugowaard, The Netherlands), respectively. The polymerization activity of actin was checked by fluorescence microscopy and by measurements of rheological properties with video particle tracking microrheology and macroscopic shear rheometry [280]. The motor activity of myosin was checked by standard motility assays and by bulk self-organization assays [280], and in the same way we confirmed that DyLight 594 labeling did not influence motor activity. To test the filament assembly capability of myosin II in I- buffer (25 mM imidazole-HCl (pH 7.4), 1 mM DTT, 0.1 mM MgATP, 50 mM KCl, 2 mM $MgCl_2$, 1 mM tris(hydroxymethyl)aminomethane (Tris), 280 mM sucrose) [282], we obtained transmission electron micrographs of myosin filaments assembled at a concentration of 0.24 μM. After incubation in I-buffer for three minutes at room temperature, 4 μL of sample was pipetted on a glow-discharged 300 meshes carbon-coated grid (Agar Scientific, Stansted, UK) and negatively stained with 2% methylamine tungstate (Nanoprobes, New York, USA). The sample was examined with a transmission electron microscope CM12 (Philips Electronic Instrument, Eindhoven, the Netherlands) operated at 120 kV.

Fluorescence labeled PVA preparation

PVA was labeled with 5-(4,6-dichlorotriazinyl)aminofluorescein (DTAF) by elimination of hydrochloride using protocols as previously described [298] [299]. DTAF covalently couples to the alcohol groups of PVA at pH levels above 9. DTAF-labeled PVA was separated from free DTAF molecules by dialyzing against Milli-Q water using a cellulose membrane with a molecular weight cut-off of 4000-6000 Dalton.

Liposome preparation (agarose-swelling method)

The liposome preparation method was adapted from a recently published procedure where liposomes, either empty or dextran-filled, were formed by hydrating mixed films of agarose and lipids in buffer solutions [217]. The main modifications are the inclusion of cytoskeletal proteins and the use of buffer conditions that promote actin polymerization and myosin activity. In addition, we found that the formation conditions were more restrictive, as explained below. Lipid mixtures of DOPC/PEG-PE/Rhodamine-DOPE/Biotin-PE with molar ratios of 94.8:5:0.2:0 or 93.8:5:0.2:1 were dissolved in 95:5 v/v chloroform/methanol at a total concentration of 3.75 mg/mL. We also tested lipid solutions of 0.87 mg/mL and other chloroform:methanol ratios (100:0 and 6:4), but this gave poorer

liposome yield. Agarose was dissolved in deionized water at a concentration of 1% (w/w) and boiled for 30-50 seconds in a microwave oven immediately before spin-coating 300 μL on 24x24 mm glass coverslips (pre-cleaned by rinsing with H_2O, ethanol and methanol, and drying after each rinse under a stream of nitrogen) at a speed of 1200 rpm for 30 seconds (DELTA 10BM, SUSS MicroTec). We also tested spin speeds of 200, 600, and 800 rpm and agarose solution volumes of 50, 100, 600 and 800 μL, but this resulted in a poorer liposome yield and quality. The spin-coating procedure was essential for high liposome yield and protein encapsulation. The originally described dip-coating procedure gave low yield and poor encapsulation efficiency (see Fig. 1F). The coated slide was dried for 30 minutes at 37°C, yielding a partially dried agarose film that retains ~15% water [217]. Lipid solution was deposited onto this film by spin-coating 150 μL at a speed of 1200 rpm for 5 minutes. Not as good results were obtained with a speed of 600 rpm and/or lipid solution volumes of 20, 30, 50, 100, or 200 μL. The coated slide was then placed under vacuum for 1 hour at room temperature to remove residual chloroform and methanol. A glass chamber was constructed by placing a glass slide on top of the coated slide using glass and parafilm spacers sealed with vacuum grease, as sketched in Fig. 1A. I-buffer (30 μl) was injected into the formation chamber and the chamber was incubated for 45–60 minutes to form liposomes containing I-buffer. We performed the incubation at 4^oC to prevent premature actin (and myosin) filament formation. Prior to use, the glass slides were passivated by 2 mg/mL casein to prevent liposome adhesion and rupture.

The composition of the I-buffer was chosen to promote actin polymerization and myosin II motor activity (25 mM imidazole-HCl (pH 7.4), 1 mM DTT, 0.1 mM MgATP, 50 mM KCl, 2 mM $MgCl_2$, 1 mM Tris, 280 mM sucrose) [282]. If myosin motors were present, an enzymatic system composed of 1.33 mM creatine phosphate and 2.48 mg/mL creatine phosphokinase was included to regenerate ATP. We used actin concentrations between 1 and 4 mg/mL, with or without myosin II (in a molar ratio of 1:200, 1:100 and 1:50 with G-actin), biotinylated G-actin (in a molar ratio of 1:400 with G-actin), and streptavidin (in a molar ratio of 1:25 to G-actin). After incubation, the liposomes were flown from the formation chamber into the adjacent observation chamber and diluted by injecting 120 - 300 μl O-buffer with 500 mM glucose. The osmolarity of the O-buffer (Osmomat 030, Gonotec GmbH) was adjusted to 20 mOsmol/kg higher than that of the I-buffer to make the liposomes sufficiently floppy for contour fluctuation analysis by video microscopy [257]. Sucrose and glucose provide sufficient optical contrast for visualization of the membranes by phase-contrast microscopy; moreover, the slight difference in mass density causes liposome sedimentation to the bottom of the observation chamber.

Liposome preparation (PVA-swelling method)

PVA in powder form was dissolved at 5% w/w in a sucrose solution (280 mM sucrose) by continuous stirring at 90^{o}C for at least 1 hour. The PVA coated glass slide was prepared by following the same procedure as described above. The remaining steps are also the same as in the agarose-swelling method, except that we used either an open-top formation chamber where a 0.12 mm thick spacer (secure-seal spacer, Invitrogen) was placed on the coated slide or a closed formation chamber in which a 0.5 mm thick spacer (Coverwell, Invitrogen) was placed on the coated slide and closed by another glass coverslip. To harvest liposomes from the open-top formation chamber, we pipetted at least 4 chamber volumes of a glucose solution (O-buffer) into the formation chamber, to flow the liposomes into an open-top observation chamber. The open-top observation chamber was assembled by placing a 0.5 mm thick spacer upon a 76 x 26 mm glass slide and closed by a 24 x 24 mm coverslip.

Preparation of neutravidin-coated liposomes (PVA-swelling and inverse phase precursor method)

We combined the PVA swelling method with an inverse phase precursor method [252], in which neutravidin molecules bind to the lipids before membrane swelling in a buffer containing actin. This method should disentangle the crosslinking of actin filaments and actin-membrane anchors, when both of them are achieved by using biotin-neutravidin (or, equivalently, biotin-streptavidin) linkages. A PVA-coated glass slide was prepared by following the same procedure as described in the PVA-swelling method. A volume of 2 μl neutravidin solution (48 mg/mL) in PBS was added into 60 μl of lipid mixture. In experiments without biotin-PE lipids, we added 2 μl of PBS without neutravidin. The mixtures were pipetted up and down several times by a 500 μl glass syringe until the mixtures become opalescent to create inverted micelle precursors [252]. A volume of 40 μl precursors was spin-coated upon the PVA coated slide at 100 rpm for 100 sec, followed by drying under vacuum for 100 min at room temperature. The remaining steps were the same as in the PVA-swelling method, except that the lipid swelling time was 90 min instead of 45 min.

Microscopy and image analysis

We observed liposomes with a confocal laser scanning microscope using a Nikon C1 scanhead on a Nikon Eclipse Ti inverted microscope with 100x/NA1.4, 60x/NA1.2, 40x/NA1.0 or 40x/NA0.06 Plan Apo objectives. Images were captured using EZ-C1 software (Nikon, version 3.10). AlexaFluor 488 was excited using a diode-pumped solid state laser with a wavelength of 488 nm (Melles-Griot); rhodamine, DyLight 594 and AlexaFluor 568 were excited using a helium-neon laser with a wavelength of 543 nm (Melles-Griot). Liposome diameter, lamellarity,

and encapsulation efficiency were analyzed from fluorescence images of equatorial cross-sections of liposomes. Sizes of liposomes before harvesting (in the formation chamber) and after harvesting (in the observation chamber), were determined by detecting the center of mass position and diameter of each liposome. Since the liposomes were densely packed, especially in the formation chamber, we used a method based on the Hough transform, which can distinguish liposomes even when they are in contact. This method groups edge points into object candidates by performing an explicit voting procedure over a set of parameterized image objects [300] [301] [302]. Fluorescence intensities of membranes for lamellarity analysis were measured from confocal images of liposomes in the observation chamber. For these dilute and well-separated liposomes, we used a custom-written MatLab program based on Canny edge detection [300]. Two concentric circles were centered on the liposome to create a ring-shaped area enclosing the fluorescent membrane contour; the width of the ring was fixed for all liposomes. The image was thresholded to eliminate pixel intensity values below the noise level. To obtain the average pixel intensity for each membrane, the intensity values of pixels along the membrane contour were summed and normalized by the total number of pixels.

To compare the F-actin content inside liposomes to the original actin content of the hydration buffer, confocal images of liposomes in the formation chamber were recorded. The average fluorescent intensity of F-actin inside a liposome (I_i) was obtained as follows. First, since F-actin was present both inside and outside of liposomes, we identified the liposome boundaries from fluorescence images of rhodamine-labeled membranes. Then, we summed the pixel intensities in the AlexaFluor 488-actin channel of all pixels within the boundary, and finally divided the total intensity by the total number of pixels. To quantify the F-actin density outside the liposomes, we obtained the average fluorescence intensity (I_o) of the entire field of view excluding areas of liposomes. The encapsulation ratio was defined as I_i/I_o.

To measure the variance in actin encapsulation among liposomes, we used confocal images of liposomes harvested from the formation chamber by flowing them into the observation chamber with O-buffer. We identified liposomes by thresholding fluorescence images of AlexaFluor 488-actin. To ensure that only pixels inside liposomes were measured, each liposome image was first dilated and then eroded by a 5-pixel sized circle structure element [300]. We then summed up the intensities of all measured pixels and divided the total intensity by the number of pixels to obtain the average fluorescence intensity.

Liposome contour analysis

Membrane fluctuation spectra were measured by phase contrast microscopy using a Nikon Eclipse Ti inverted microscope with a 100x/NA1.4 Plan Apo objective. At least 500 consecutive images of the equatorial cross-section of a liposome were recorded with a digital CCD camera (CoolSNAP HQ2, Nikon). Membrane edge detection with sub-pixel resolution was achieved with a custom-written MatLab program based on a published method [257]. Due to the refractive index difference between the buffers inside and outside the liposome, the liposome's edge is silhouetted dark against the surrounding background in phase contrast, with a bright halo on the outside, as shown in Supplementary Fig. 1A. We detected the edge positions of a liposome contour in four directions: horizontal, vertical, and two diagonal directions, as shown in Supplementary Fig. 1B. Supplementary Fig. 1C exemplifies the edge finding procedure for the horizontal direction. A gray level profile along a line of 20-24 pixels across the membrane in the horizontal direction was constructed, and a straight line was fitted to the portion of the profile having the maximum slope over a range of 8-12 pixels. The edge position was defined as the intersection of this line with a line corresponding to $I = I_{\text{avg}}$, where I_{avg} is the average gray level of the gray level profile. The membrane position was calculated as the average of the positions obtained from the four directions weighted by the corresponding slopes of the intensity profiles. This edge detection procedure provides a high spatial resolution of 0.1 pixels (6 nm with our setup). The detected positions in Cartesian coordinates (x and y) were transformed to polar coordinates (r and θ). The contours were projected to a Fourier series with 50 modes,

$$r(\theta) = R\left(1 + \sum_{n=1}^{50} a_n \cos(n\theta) + b_n \sin(n\theta)\right), \quad (1)$$

where R is the liposome radius and *n* is the mode number. The power spectrum of the transverse thermal fluctuations, *u*, of the membrane is defined as

$$\left\langle \left|u(q_x)\right|^2 \right\rangle = \frac{\pi \left\langle R \right\rangle^3}{2}\left(\left\langle \left|c_n\right|^2 \right\rangle - \left\langle \left|c_n\right| \right\rangle^2\right), \quad (2)$$

where $c_n = \sqrt{{a_n}^2 + {b_n}^2}$, $\left\langle R \right\rangle$ is the time-averaged liposome radius, and the wave vector $q_x = \dfrac{n}{\left\langle R \right\rangle}$. According to the classical Helfrich model of fluctuating two-dimensional membranes [257] [258], the time-averaged fluctuation spectrum decays with wave vector $\mathbf{q}$ as

$$\left\langle \left| u(\mathbf{q}) \right|^2 \right\rangle = \frac{k_{\mathrm{B}}T}{\sigma \mathbf{q}^2 + \kappa \mathbf{q}^4} \ , \tag{3}$$

where $\mathbf{q} = \left(q_x, q_y \right)$, the thermal energy $k_{\mathrm{B}}T = 4 \times 10^{-21} J$, σ is the membrane tension and κ is the membrane bending rigidity. This general expression needs to be modified since we only observed the equatorial plane of each liposome and so the spectrum is one-dimensional. Moreover, we need to account for smearing of fluctuations whose life time is shorter than the camera integration time. Taking these two factors into account, the measured membrane fluctuation spectrum can be described by a modified Helfrich model [257],

$$\left\langle \left| u(q_x) \right|^2 \right\rangle = \frac{1}{\pi} \int_{-\infty}^{\infty} \frac{k_{\mathrm{B}}T}{4\eta \mathbf{q}} \tau_{\mathrm{m}} \frac{{\tau_{\mathrm{m}}}^2}{\tau^2} \left(\frac{\tau}{\tau_{\mathrm{m}}} + \exp\left(-\frac{\tau}{\tau_{\mathrm{m}}} \right) - 1 \right) \mathrm{d}q_y \tag{4}$$

where η is the buffer viscosity, τ_{m} is the fluctuation lifetime, $\tau_{\mathrm{m}}(\mathbf{q})^{-1} = \left(\frac{1}{4\eta \mathbf{q}} \right) \left(\sigma \mathbf{q}^2 + \kappa \mathbf{q}^4 \right)$, and τ is the camera integration time (10 - 20 ms with our camera setting). We excluded the first 5 modes from the fit, which was necessary due to the closed topology of the membrane, and we also excluded modes with wave vectors above 2 μm^{-1}, since these modes have a wavelength less than the pixel size (60 nm) and a spectral density in the noise floor [257]. We note that to reduce the camera integration time, several approaches have been reported. One approach is to record images by an ultrafast camera [303]. Alternatively, one can utilize a xenon flash lamp [304] or a mercury lamp [305] to increase the illumination light intensity, thus allowing one to reduce the camera integration time. Another approach is to record bright field image by using a 430 nm laser combined with a fast resonant scanning confocal microscope [306].

2.6 Acknowledgements

Part of this work was performed in collaboration with Björn Stuhrmann (AMOLF, Amsterdam) and with Andreas Weinberger, André Schröder and Carlos Marques from the Institut Charles Sadron (Strasbourg). We thank Kévin Carvalho and Cécile Sykes from the Institut Curie (Paris) for advice on the inverted emulsion technique and for insightful discussions. We further thank Aurélie Bertin (Institut Curie, Paris) for taking the electron micrographs of myosin filaments. We thank Marjolein Kuit-Vinkenoog (AMOLF, Amsterdam) for protein purification. We benefited from helpful discussions with Baldomero Alonso-Latorre (AMOLF, Amsterdam) regarding image analysis, and Nils Becker (University of Heidelberg), Stefan Semrau (Massachusetts Institute of Technology, Cambridge), Jacques Pécréaux (CNRS, Rennes), Ruddi Rodríguez-García (CNRS, Rennes), Michael Mell

(Complutense University, Madrid) and Iván López-Montero (Complutense University, Madrid) regarding analysis of liposome fluctuation spectra.

CHAPTER 3. Cell-sized liposomes reveal the reciprocal interplay of membrane and actin bundle mechanical properties on liposome shape change

Here we reconstitute a cell-free model system based on cell-sized liposomes encapsulating actin filaments bundled by fascin to elucidate how the reciprocal interplay of the lipid bilayer membrane and of cytoskeletal actin bundles determines liposome shape. Our results clearly demonstrate that the mechanical properties of the membrane and of the actin bundles jointly determine liposome shape, and furthermore that the membrane and the bundles influence each other's configuration. Inside a flaccid liposome, where the membrane is deformable, actin bundles generate finger-like membrane protrusions, reminiscent of filopodia in living cells. In contrast, when the liposome membrane is under high tension or has a large bending rigidity, the membrane forces the bundles to organize into cortical rings, an arrangement that minimizes the energy cost associated with bending of the bundles inside the cell-sized confinement. We find that membrane protrusions can reach impressive lengths of up to 60 μm, confirming recent theoretical predictions that actin bundles enclosed in narrow membrane tubes are stabilized against buckling due to the elasticity of the membrane. Our results highlight the importance of taking into account the physical characteristics of the cytoskeleton and the plasma membrane besides factors such as biochemical signaling to understand cell shape control. On the one hand actin filaments exert forces on the membrane and deform it. On the other hand, the membrane itself is under tension and will therefore also exert forces on the cytoskeleton, thus constraining and influencing its organization. Our cell-free system provides a platform for future quantitative studies of how other molecular factors, such as myosin motors, actin nucleators such as formins, or the membrane curvature promoting BAR family proteins influence the interplay of the membrane and the actin cytoskeleton.

The contents of this chapter are based on:

Tsai, F.-C. and Koenderink, G. H. (Manuscript in preparation)
Cell-sized liposomes reveal the mechanical interplay of membrane and actin bundles on liposome shape determination.

3.1 Introduction

Animal cells can take on a rich variety of shapes to fulfill functions such as division and migration [12]. Cell shape changes are primarily determined by an interplay of the deformable plasma membrane and the viscoelastic cytoskeleton. The plasma membrane defines the cell boundary, separating intracellular components from the extracellular environment. The main structural component of the plasma membrane is a lipid bilayer, making the plasma membrane fluid and highly deformable. Thus, to maintain a stable cell shape and prevent mechanical damage, cells rely on the cytoskeleton for providing mechanical support to the plasma membrane. At the same time, the cytoskeleton drives cell shape change, by actively exerting forces to deform the membrane and form protrusions. In migrating cells, there are two main types of cellular protrusions at the leading edge: the lamellipodium and filopodia. The lamellipodium is a thin (0.1 - 0.2 μm) and flat sheet-like protrusion filled with diagonally oriented actin filaments forming a branched network [61] [41] [39]. Filopodia are thin (0.1 – 0.3 μm), finger-like protrusions filled with tightly packed parallel actin filaments arranged into a bundle [43] [44] [45]. To efficiently generate these protrusions, actin nucleation mostly occurs adjacent to the plasma membrane [12] [40] [51]. For instance, branched actin arrays in lamellipodia are mediated by the actin nucleator Arp2/3 complex that is activated by membrane bound nucleation promoting factors, such as WASP and WAVE [57]. The formation of these protrusions also requires actin assembly by addition of actin subunits to the barbed ends of the filaments that are oriented towards the membrane [307] [308] [309] [40] [310]. The key role of actin filaments in maintaining protrusions is illustrated by the effect of actin disruption by the actin-depolymerizing drug latrunculin B, which causes a drastic reduction of the number of filopodia [311].

Experiments with simplified cell-free model systems support the idea that growing cytoskeletal filaments can deform the plasma membrane to form protrusions. For instance, reconstituted dendritic actin networks mimicking the actin networks found in the lamellipodium can deform spherical liquid drops [178] and liposomes [185] [186] into a teardrop shape by active growth. Actin bundles encapsulated inside cell-sized liposomes are able to deform the liposomes into various shapes in the absence [196] [198] [239] [312] and presence of polycations [200] and physiological actin crosslinking proteins [199] [202]. Similar membrane deformations have been demonstrated in case of liposomes containing microtubules [313] [314] [315] [316] [317] [318] [319].

Notably, in the aforementioned cellular protrusions, the actin cytoskeleton is highly confined by the plasma membrane in either a two-dimensional geometry (for the lamellipodium) or a quasi-one-dimensional geometry (for filopodia). Since actin filaments have micrometer lengths and are rather rigid, with a persistence

length of 9 – 18 μm [34] [26], they experience a strong confinement effect inside cellular protrusions. Several biophysical studies of cell-free model systems have addressed the influence of spatial confinement on actin filament organization. In quasi-two-dimensional cell-sized hard microchambers with a depth of 5 μm [320], actin filaments were shown to spontaneously form aligned bundle-like arrangements instead of homogeneous networks observed in unconfined bulk solutions at the same filament density. Inside cell-sized liposomes, actin filaments were shown to arrange spontaneously into a cortical shell to reduce the enthalpic energy cost associated with filament bending [123] [127]. In this case, no liposome deformation was observed, presumably since the force that single actin filaments apply (a few pN) [321] is insufficient to overcome the membrane elastic resistance [322] [323] [324]. Only when bundled, actin filaments were shown to be able to cause the formation of thin membrane protrusions resembling filopodia [196] [198] [199]. These observations point to an interesting feedback between the effects of membrane-enclosed confinement on actin organization and, conversely, actin filament-induced membrane deformation.

Besides confining the cytoskeleton, the plasma membrane also coordinates the cytoskeleton by altering membrane tension and rigidity [50] [325] [159] [158]. In *Caenorhabditis elegans* sperm cells, it was shown that a higher membrane tension orients major sperm protein filaments towards the direction of cell movement [326]. In motile keratocytes, the lower membrane tension at the leading edge allows the polymerization of actin filaments to generate protrusions, while the higher membrane tension in the cell rear suppresses the polymerization of filaments, resulting in a collapse of the actin network [310]. Finally, a recent *in vitro* study demonstrates that membrane tension gathers actin filaments that grow from the outer surface of a liposome, resulting in the formation of filopodia-like protrusions [72].

Taken together, it is clear that cell shape changes are determined by a reciprocal interplay of the plasma membrane and the actin cytoskeleton [159] [50] [327] [49] [158] [327]. However, owing to the molecular complexity of the interactions among cellular components, it is difficult to clearly distinguish the contributions of the plasma membrane and the cytoskeleton to changes in cell shape [230] [163].

Here, to dissect the reciprocal (mechanical) interplay of the plasma membrane and the actin cytoskeleton in determining membrane shape, we use a controlled model system based on cell-sized liposomes encapsulating actin filaments and fascin. Fascin is a physiologically important actin crosslinking protein [328] that is particularly prevalent in filopodia [329] [44]. Its ability to bundle actin filaments and form elastic bundle networks *in vitro* has been demonstrated in bulk mixtures of purified actin and fascin [330] [331]. By varying the tension and bending rigidity of the liposomal membrane as well as the rigidity of the actin-fascin bundles, we

disentangle the contributions of membrane mechanics and the mechanics of the actin bundles to liposome shape control. We show that actin bundles deform liposomes into a rich set of different morphologies, including lollipop-shaped liposomes exhibiting thin, finger-like membrane protrusions that are reminiscent of filopodia in living cells. We demonstrate that the formation of membrane protrusions is determined by a competition between membrane elastic resistance and actin bundle stiffness. High membrane tension and bending rigidity suppress the formation of protrusions, and softer bundles are less efficient at deforming the membrane than stiffer bundles. Conversely, we find that the configuration of the actin bundles is also determined by a competition between membrane and bundle elasticity: stiffer actin bundles remain straight and cause membrane deformation, whereas softer bundles are forced to kink or buckle, leaving the membrane undeformed.

3.2 Results

Morphologies of liposomes encapsulating actin-fascin bundles

In unconfined bulk solution, actin filaments at a concentration of 12 μM (corresponding to 0.5 mg/mL) form an isotropic entangled network with an average mesh size of about 0.4 μm [332]. Since this mesh size is close to the optical diffraction limit, confocal micrographs show homogeneous networks whose constituent filaments cannot be discerned (Fig. 1C). When confined within a cell-sized liposome in a physiological buffer that promotes actin polymerization [219], the filaments often spontaneously rearrange into a thick cortical shell underneath the liposome membrane (Fig. 1F). Although this arrangement reduces the conformational entropy of the filaments, it still minimizes the total free energy since it reduces the enthalpic cost associated with filament bending [123] [182]. This cortex configuration is particularly prominent in liposomes with a diameter below 8 μm (ca. 59% of the cases), whereas in larger liposomes the actin networks always homogeneously fill the entire liposome (Supplementary Fig. 1A and B). In all cases, the liposomes retain a spherical shape with no obvious signs of membrane deformation, consistent with prior observations [123] [182].

When actin polymerization is initiated in the presence of fascin in bulk solution, an isotropic network of F-actin bundles forms (Fig. 1D and E, R_F denotes the molar ratio of fascin to actin), consistent with prior reports [333]. These bundles are composed of tightly packed actin filaments (Fig. 1A) and have been shown to be unipolar (Fig. 1B) [334] [335] [336] [337]. When confined in cell-sized liposomes, the actin-fascin bundles cause dramatic membrane deformation (Fig. 1G and H). Many liposomes have long, finger-like protrusions and the shape of the main body is often deformed into an ellipsoidal shape.

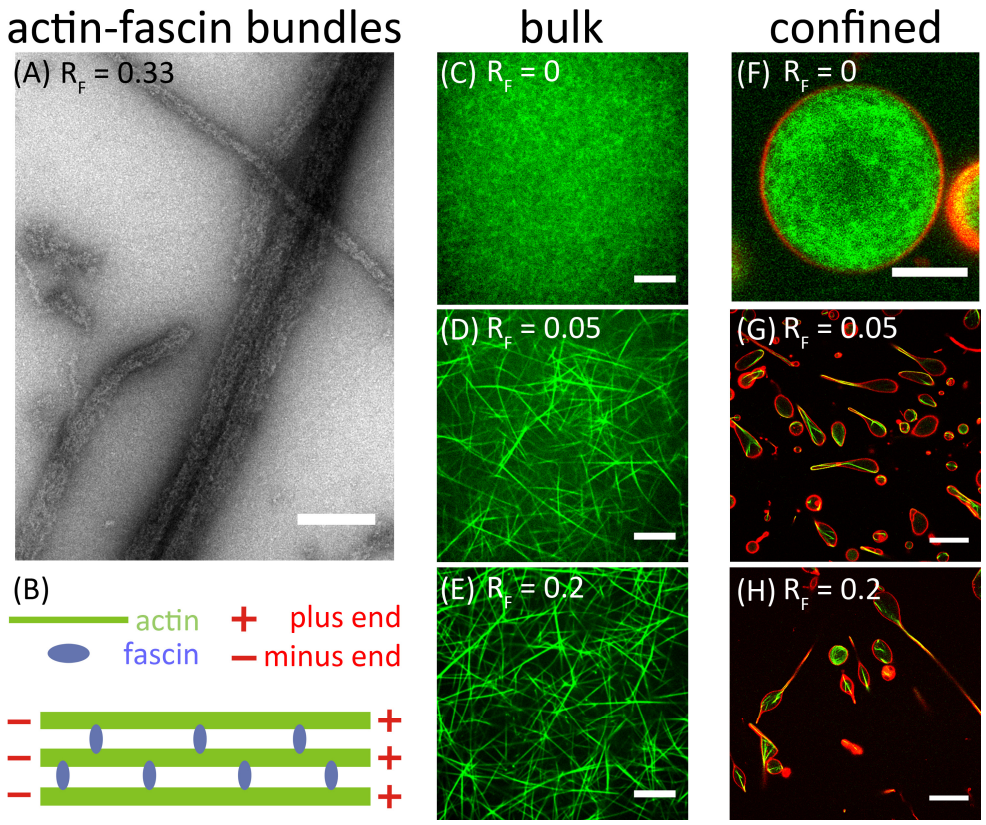

Figure 1. Characterization of actin networks polymerized in bulk solution (A, C - E) and confined inside cell-sized liposomes (F – H). (A) Electron micrograph of fascin-mediated actin bundles. (B) Schematic representation of a unipolar fascin-mediated actin bundle. (C – E) Confocal fluorescence micrographs of bulk actin networks formed in the absence (C) and presence (D, E) of fascin. (F - H) Confocal fluorescence micrographs of actin networks inside liposomes formed in the absence (F) and presence (G, H) of fascin. R_F indicates the molar ratio of fascin to actin. Actin concentrations: (A) 3 μM, (C – E) 12 μM and (F – H) 23.8 μM in the swelling solution (after encapsulation, ca. 12 μM is present inside the liposomes, see Chapter 2). Actin is shown in green and lipid membranes in red. Scale bars: (A) 200 nm, (C – E) 10 μm, (F) 5 μm, (G, H) 20 μm.

To systematically characterize the diversity of liposome shapes for different sample conditions, we observe a large population of liposomes (usually on the order of 50 per liposome preparation). For liposomes filled with actin-fascin bundles at R_F = 0.05, we find many liposomes with a "lollipop" shape with an ellipsoidal main body containing multiple actin-fascin bundles and a single long and narrow protrusion at one pole, reminiscent of filopodia in living cells (Fig. 2A and Fig. 3A *left-most panel*). Occasionally we find ϕ-shaped liposomes with two narrow actin-filled protrusions at two opposite poles, or even liposomes with more than two actin-filled protrusions (Fig. 3A, *middle and right panels*). Also, some liposomes have a shape that is close to spherical, tube-like, pear-shaped, or irregular (Fig. 2B). To distinguish these non-protruded liposomes from protruded ones, which is especially difficult for the pear-shaped liposomes, we compare the width of the finger or tongue-like part of the liposome with that of the main body. We classify a liposome to be protruded when its protrusion width is at least 3 times smaller than its body width (Fig. 2C *right panel* and Supplementary Fig. 2). Based on this criterion, we find that more than half of the liposomes are protruded (60% of a total of 104 liposomes). Most of these protruded liposomes have a single protrusion, while a minority has two or even more protrusions (Table 1). There is no obvious difference between the total surface area of the equatorial plane of non-protruded and protruded liposomes (Supplementary Fig. 3). For the protruded liposomes, up to 25% of the surface area contributes to the protrusion (Supplementary Fig. 4).

To characterize the distribution of liposome shapes, we describe the geometrical properties of each liposome (observed in the equatorial plane) by its circularity and solidity (Fig. 2D) [338]. Here, the circularity quantifies the deviation of a 2-D shape from a circle, which has a circularity of 1, while the solidity quantifies the degree of indentation as compared to a convex shape, which has a solidity of 1 (Fig. 2C *left panel*). The circularity and solidity of the liposome shapes clearly correlate with the classification of protruded versus non-protruded liposomes: protruded liposomes (black symbols in Fig. 2D) tend to have smaller values of both circularity and solidity than non-protruded liposomes (red symbols). The circularity of protruded liposomes is usually below 0.4 (Fig. 2E) and their solidity is inversely correlated with the protrusion length, reaching values close to 0.5 for the longest protrusion lengths of 35 μm (Fig. 2F).

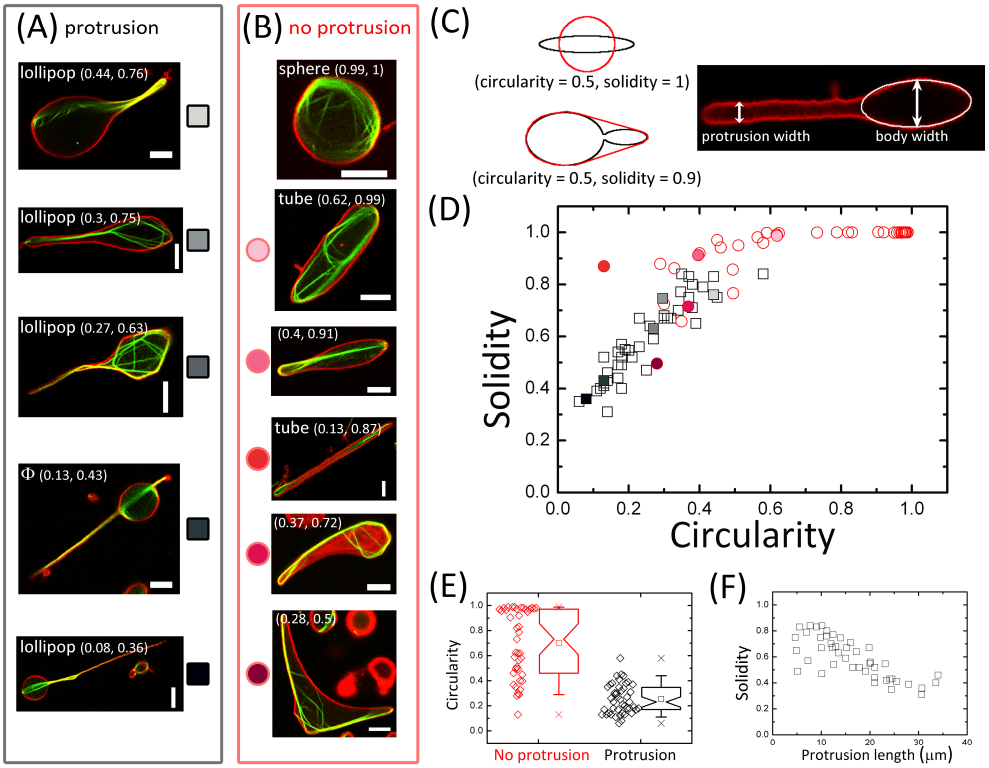

Figure 2. Morphological characterization of a population of 87 liposomes encapsulating actin-fascin bundles (R_F = 0.05). (A, B) Confocal fluorescence micrographs of typical liposomes sorted by their extent of deformation (increasing from *top* to *bottom*). Images represent single confocal planes, recorded at the equatorial plane, except for the liposome with (circularity, solidity) = (0.37, 0.72) in (B), which is a maximum intensity projection of 11 planes over a total z-range of 5 μm. Red: membrane, green: actin. Scale bars: 5 μm. (C) *Top left panel*: circularity quantifies the deviation of a liposome shape from a circle. The red line demonstrates a circle having the same perimeter as the elongated liposome (shown by the black ellipse). *Bottom left panel*: solidity quantifies the degree of concavity of a liposome shape by comparing its area to that of the smallest convex hull enclosing the shape, shown by the red line. *Right panel*: confocal fluorescence image of a deformed liposome with its protrusion width and main body width indicated by white arrows. The main body contour is fitted to an ellipse (white line). (D) State space of liposome shapes in terms of circularity and solidity. Reddish symbols represent liposomes having no protrusion (42 liposomes) and black/grayish symbols are liposomes with (at least 1) protrusion(s) (45 liposomes). Color-coded solid symbols correspond to the confocal images shown in (A) and (B). (E) Comparison of circularities of liposomes with and without protrusions. (F) The liposome solidity is inversely correlated with the protrusion length (correlation coefficient = -0.772, $p < 0.001$).

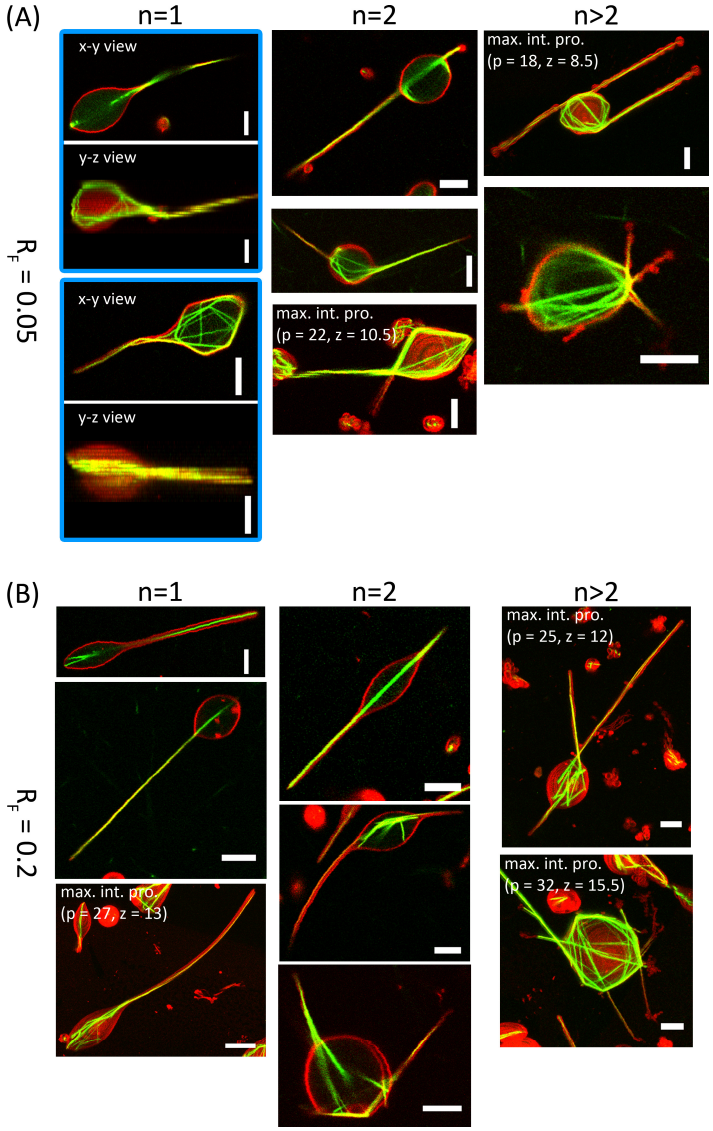

Figure 3. Confocal fluorescence micrographs of liposomes exhibiting single (n = 1) and multiple (n = 2 and n > 2) protrusions at low (A) and high (B) fascin concentration. Images are single confocal sections recorded at the equatorial plane of the liposomes, except for the middle image in (A) n = 2 and the bottom image in (B) n = 2, where 2 confocal images are summed to show the entire shape, and for images specified by "max. int. pro." that represent maximum intensity projections constructed from *p* planes over a total z-range denoted as *z* (in μm). Scale bars: 5 μm, except for the bottom image in (B) n = 1 where the scale bar is 10 μm. Red: membrane, green: actin.

	R_F = 0.05 (total 62 liposomes)	R_F = 0.2 (total 40 liposomes)
single protrusion (n = 1)	82%	65%
multiple protrusions (n > 1)	18%	35%
two protrusions (n = 2)	13%	28%
ϕ–shaped protrusions	8%	18%

Table 1. Percentage of protruded liposomes having *n* protrusions (see the first column) for two actin-fascin molar ratios, R_F = 0.05 and R_F = 0.2.

Configurations of fascin-mediated actin bundles inside protruded liposomes

When viewed in 3-D, there is rarely a single bundle (1 of a total of 21 liposomes) inside the main body of the protruded liposomes. Rather, we observe multiple bundles, regardless of the numbers of protrusions (Fig. 3A). These bundles often arrange into a ring-like structure or a sparse web located in the equatorial plane (Fig. 3A, *n* = 1) or another cross-sectional plane (Supplementary Fig. 5A) of a liposome. Only two out of the total of 21 liposomes have bundles located in different planes (Supplementary Fig. 5B).

Strikingly, bundles often show sharp kinks underneath the membrane within the liposome main body (Fig. 4A) or within the protrusions (Fig. 4 A and B), suggesting that their configuration is strongly affected by the spatial confinement within the liposome. If the bundles would simply buckle, we would expect a smoothly curved contour, as we observed at the end of some protrusions (Fig. 4C). The sharp kinks thus suggest that some bundles have weak spots due to structural defects. One possibility is side-branching of actin filaments mediated by fascin, which could potentially result in weaker actin bundles compared to non-branched ones [339]. Another possibility is that such defects may arise if the bundles are composed of actin filaments that do not run along the entire length of the bundles. Indeed, based on length measurements of actin filaments assembled in bulk solution, we expect a broad filament length distribution with only few filaments long enough to span the entire liposome length [182] (see Chapter 4).

The influence of actin-fascin bundle stiffness

We observe a broad range of protrusion lengths, spanning from 5 to 35 μm (Fig. 2F). An important question is what physical factors limit the maximal length. It has been shown that the force applied by a single actin filament (on the order of 1 pN) [321] is insufficient to protrude a lipid bilayer membrane [322] [323] [324]. To overcome the resistance from membrane elasticity and tension, actin filaments thus need to form bundles [196] [198] [72]. However, the length of the resulting

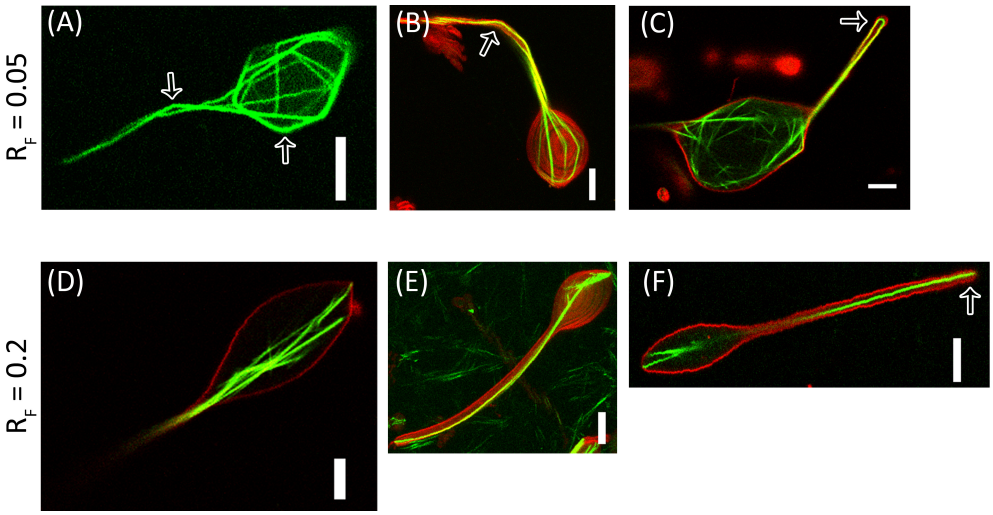

Figure 4. Characterization of actin-fascin bundles inside liposomes at low (A – C, R_F = 0.05) and high (D – E, R_F = 0.2) fascin concentration. At low fascin concentration, actin bundles tend to kink inside the liposome main body (A) or inside the protrusions (A, B), and they sometimes buckle at the end of the protrusions (C), as indicated by the white arrows. At high fascin concentration, actin bundles are straight inside the liposome main body (D), only occasionally gently curved along a protrusion (E), and always straight at the end of a protrusion (F, indicated by the white arrow). Images are single confocal sections recorded at the equatorial plane of the liposomes, except for (B) and (E) where maximum intensity projections are assembled from 25 planes over a total z-range of 12 μm in (B) and 21 planes over a total z-range of 10 μm in (E). Red: membrane, green: actin. Scale bars: 5 μm.

protrusions is limited by the buckling instability of the actin bundles under the compressive load applied at the bundle tip by the membrane [323] [322] [324]. For liposomes with protrusions, we observe that 25% (total 24 liposomes) of the actin-fascin bundles in the protrusions are buckled at the tip (Fig. 4C). This suggests that the protrusion length is indeed limited by the maximum compressive load (the Euler buckling force) that the bundles can sustain.

To test this hypothesis, we increase the fascin-actin molar ratio R_F, which is expected to increase the bundle stiffness [340] and consequently the corresponding Euler buckling force, which is proportional to the bending stiffness of a bundle [341]. Strikingly, we now observe that the protrusions can reach two-fold longer lengths, of up to 60 μm (Fig. 5A). Moreover, the actin-fascin bundles now always remain straight at the tip of the protrusions (Fig. 4F), clearly indicating that the rigidity of the actin bundles is an important determinant of protrusion length. Another interesting change is that protrusions formed at low R_F are

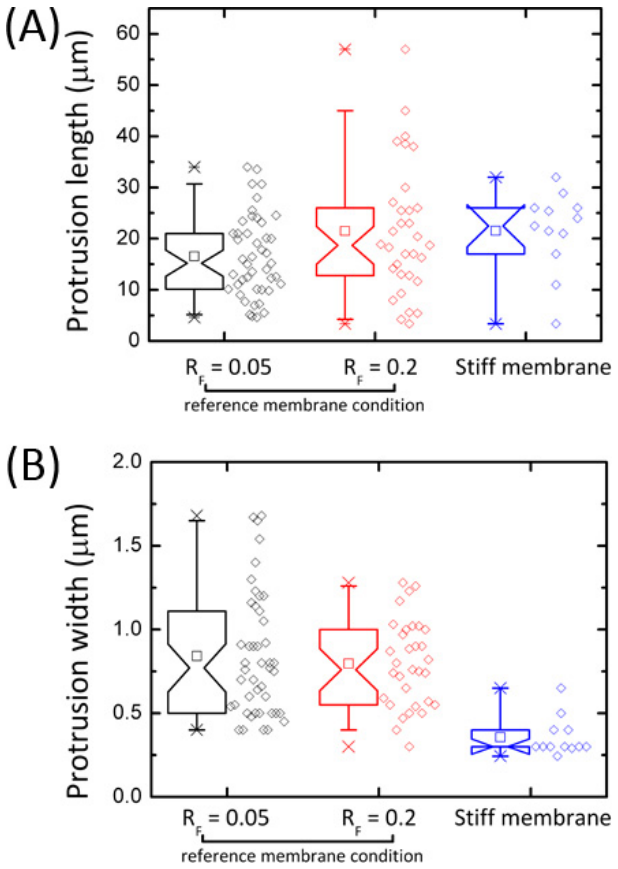

Figure 5. Influence of actin bundle stiffness (modulated by R_F) and membrane stiffness (modulated by decorating the membrane with neutravidin) on liposome protrusion length (A) and width (B). Liposome population sizes from left to right: 45, 32 and 12.

sometimes sharply bent due to a kink in the supporting actin bundle (16% out of 44 protruded liposomes; Fig. 4B), whereas protrusions formed at high R_F less often exhibit kinks (9% out of 32 protruded liposomes) and are instead straight (Fig. 3B and 4F) or sometimes (12.5% out of 32 protruded liposomes) gently curved (Fig. 3B and 4E).

The arrangement of the actin bundles in the main body of the liposomes is also significantly altered when R_F is increased: most of the bundles are straight and, instead of forming a ring-like structure with kinks, the bundles align along the long axis of the liposome body (90% out of 28 protruded liposomes, Fig. 3B and 4D). Only a few liposomes (the other 10%) have ring-like or web-like network structures resembling the structures seen at low R_F. Furthermore, the shape of

the body of liposomes having a single protrusion is more elongated, with a smaller body circularity, than the body shapes observed at low R_F (Supplementary Fig. 6). Collectively, these observations suggest that the morphology of the actin-filled liposomes is controlled by a balance between the mechanical energy associated with the membrane and the bundle elasticity. Softer bundles are forced to conform to the confinement provided by the membrane and buckle or kink, whereas more rigid bundles instead cause a deformation of the membrane.

The global liposome morphologies at high fascin concentration are similar to the morphologies at low R_F, ranging from liposomes with protrusions that have a lollipop or ϕ shape (Fig. 6A) to non-protruded liposomes that are spherical, tube-like, lemon-shaped, or pear-shaped (Fig. 6B). Also, we observe liposomes with multiple protrusions (Fig. 3B). The fraction of protruded liposomes is around 60% at both high and low R_F (Fig. 7), but the fraction of liposomes with more than one protrusion is higher at high R_F than at low R_F (see Table 1). Similar to the liposomes formed at low R_F, there is no apparent difference between the total surface area of the equatorial plane of non-protruded and protruded liposomes (Supplementary Fig. 3). For the protruded liposomes, up to 40% of the surface area contributes to the protrusion (Supplementary Fig. 4), which is slightly higher than for liposomes at low R_F. The broad range of liposome shapes can again be summarized in terms of a circularity/solidity shape space (Fig. 6C). Similar to the liposomes formed at low R_F, protruded liposomes have a lower circularity than (most) non-protruded liposomes (Fig. 6D), and the solidity of the protruded liposomes is inversely correlated with the protrusion length (Fig. 6E).

The fascin concentration can modulate actin bundle stiffness in two distinct ways. First, a higher fascin concentration can increase the number of filaments per bundle up to a maximum of 20 [331]. Second, a higher fascin concentration can also enhance the degree of coupling between the actin filaments within the bundles, from a decoupled regime where filaments bend independently under an applied load to a fully coupled regime where filaments are tightly glued and bend together [340]. To compare the bundle thickness obtained at low and high R_F, we compare the fluorescence intensity of the bundles. By normalizing this intensity by the intensity measured in between bundles in the liposome body, and assuming that this intensity represents the intensity of single actin filaments, we obtain an estimate of the number of actin filaments per actin bundle. Actin bundles within the protrusions contain 10 - 60 filaments with an average value of 30, at both R_F = 0.05 and 0.2 (Fig. 8A, black symbols). This observation suggests that the apparently increased rigidity of the bundles at high R_F reflects a tighter coupling of the filaments rather than an increased bundle thickness.

Line profiles along the bundles reveal that the actin fluorescence intensity is sometimes rather homogeneous (Fig. 8B right), whereas at other times there is a

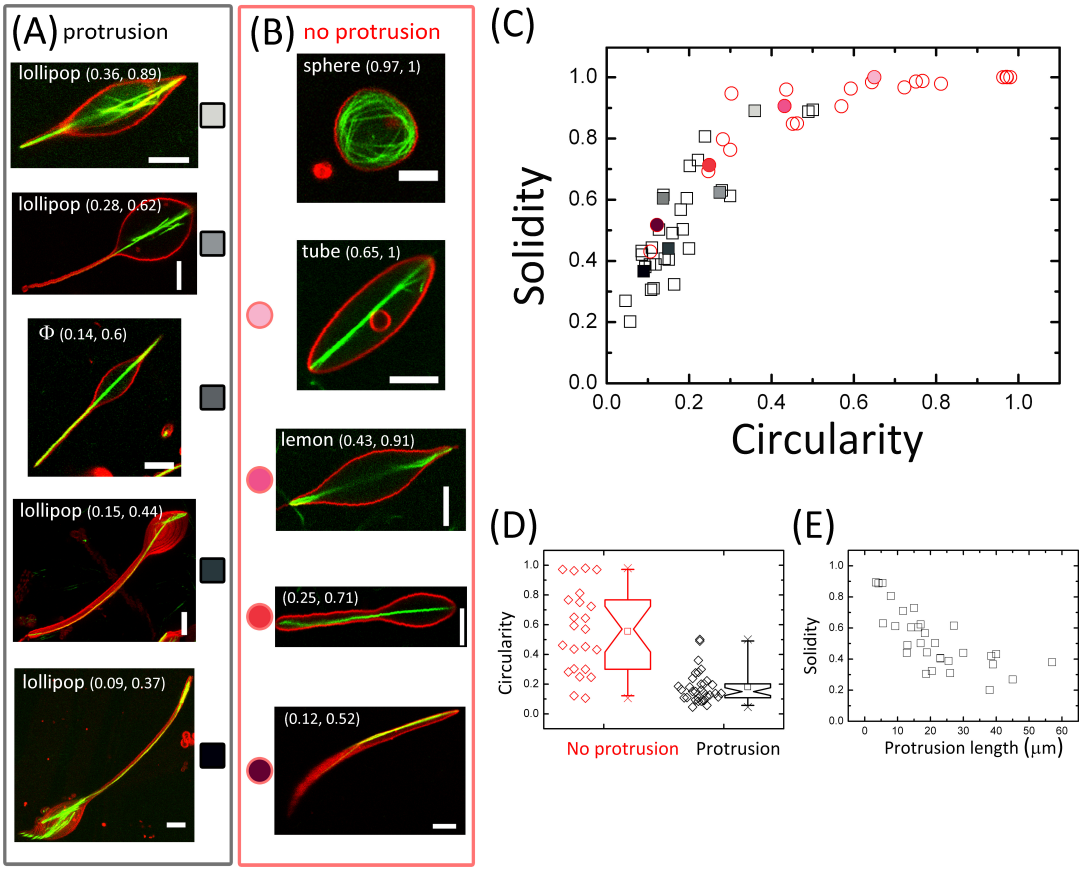

Figure 6. Morphological characterization of a population of 55 liposomes encapsulating actin-fascin bundles (R_F = 0.2). (A, B) Confocal micrographs of liposomes that are increasingly deformed (*top* to *bottom*). Images are single confocal sections recorded at the equatorial plane of the liposomes, except for the lollipop (0.36, 0.89), where 2 confocal images are summed to show the entire shape, and for the lollipop (0.15, 0.44) and (0.09, 0.37), where maximum intensity projections are shown composed of *p* planes over a total z-range (*z* in μm) of (*p* = 21, *z* = 10) and (*p* = 22, *z* = 10.5), respectively. Red: membrane, green: actin. Scale bars: 5 μm. (C) State space of liposome shapes in terms of circularity and solidity. Reddish symbols represent liposomes having no protrusion (23 liposomes) and black/grayish symbols represent liposomes with protrusions (32 liposomes). Color-coded solid symbols correspond to images of liposomes in (A) and (B). (D) Circularities of liposomes with and without protrusions. (E) The solidity is inversely correlated with the protrusion length (correlation coefficient = -0.724, $p < 0.001$).

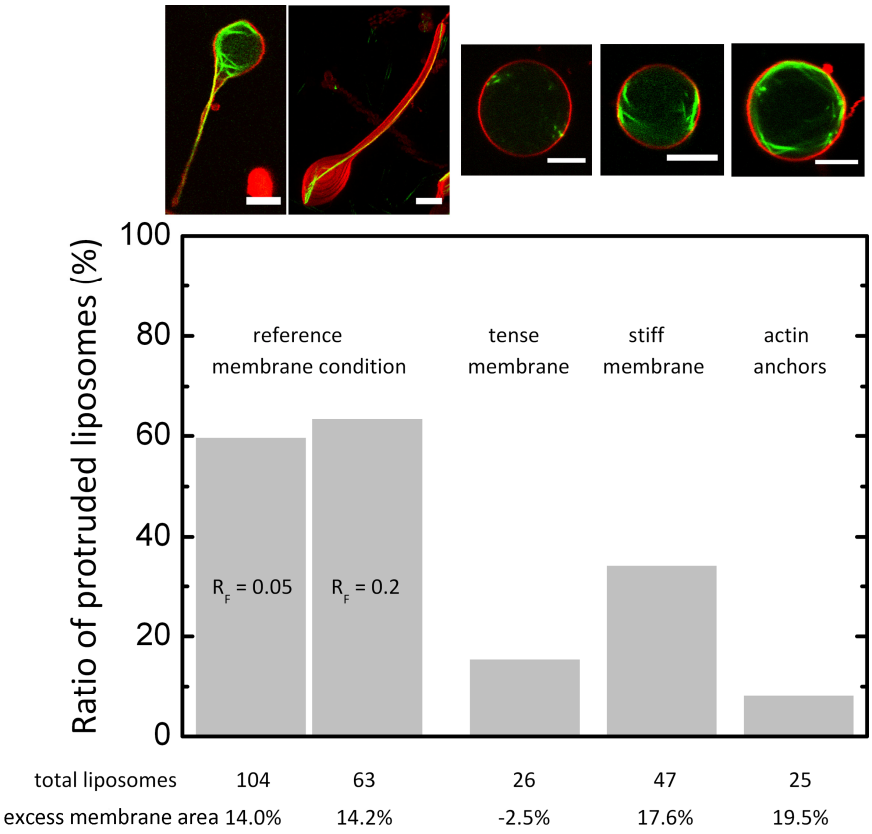

Figure 7. Membrane tension and bending rigidity affect the likelihood of protruded liposomes. *Top row*: confocal fluorescence images of liposomes corresponding to different membrane conditions indicated in the bottom graph. Images are confocal sections recorded at the equatorial plane of the liposomes, except for the second liposome from the left, where a maximum intensity projection of 21 planes over a total z-range of 10 μm is shown. Red: membrane, green: actin. Scale bars: 5 μm. *Bottom*: for all conditions, floppy membranes are obtained by placing liposomes in a hypertonic environment, except in the "tense membrane" condition, where liposomes are swollen in a hypotonic environment. In both "stiff membrane" and "actin anchors" conditions, neutravidin molecules are bound to biotinylated lipids within the membrane. Only in the "actin anchors" condition, biotinylated actin (1/400 molar ratio to the total actin concentration) is introduced to produce actin-membrane binding. The population sizes of liposomes and the excess membrane area in each condition are indicated below the graph.

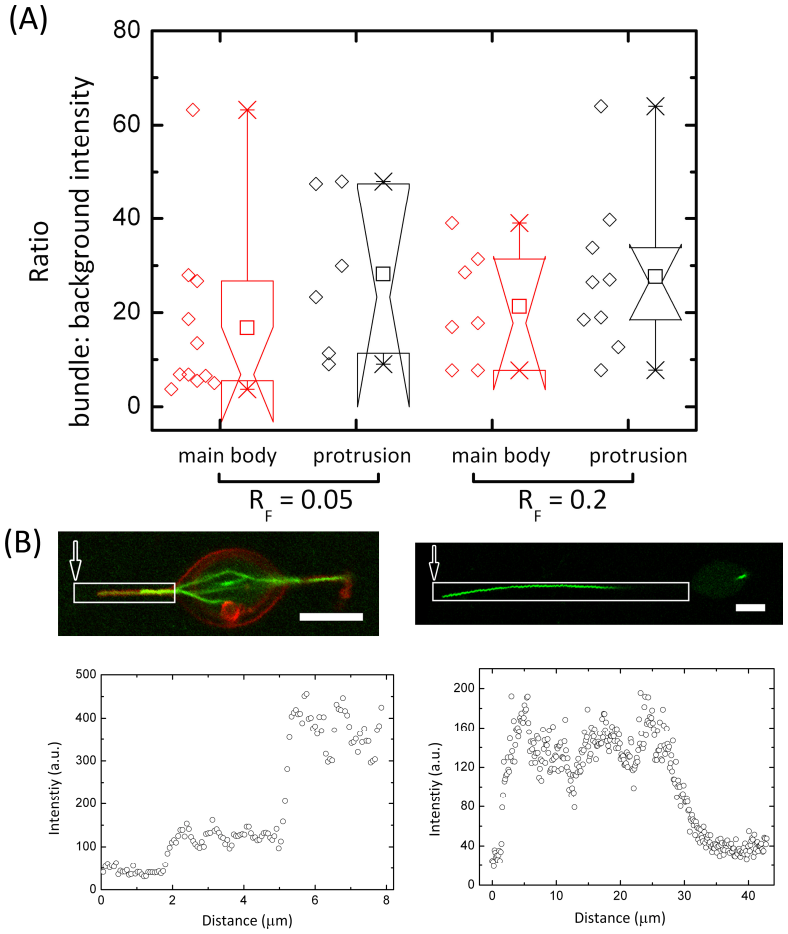

Figure 8. Estimation of actin-fascin bundle width inside the main body and the protrusion of protruded liposomes from the fluorescence intensity. (A) Ratio between fluorescence intensity of an actin bundle inside either the main body or the protrusion to the background fluorescence intensity of unbundled actin in the main body. This ratio provides a lower bound on the number of actin filaments per bundle. Liposome population sizes from left to right: 11, 6, 7, 9. (B) *Top row*: confocal fluorescence images of liposomes at R_F = 0.2. In the left image, 2 confocal images are summed to show the entire shape while in the right image a single confocal image is shown. Red: membrane, green: actin. Scale bars: 5 μm. *Bottom row*: actin fluorescence intensities are calculated within a selected rectangular region, as indicated by the white boxes in the corresponding images in the top row. The x-axis represents the horizontal distance, starting on the left (see white arrow in the top image); the y-axis shows intensities obtained by integrating intensities over the vertical direction followed by averaging by the vertical length (in pixels).

stepwise change in intensity (Fig. 8B left). In the example shown, it appears that bundles emanating from the main body are gathered when they enter the protrusion. It is not clear what the mechanism for filament gathering is. One possibility is that an increase in membrane tension accompanying the growth of the bundles against the membrane facilitates the recruitment of bundles, similar to prior observations of membrane tension driving spontaneous bundling of actin filaments growing from the outer surface of a liposome membrane [72]. A second possibility is that, once an actin bundle initiates a protrusion, subsequently formed bundles align themselves in parallel to the pre-existing bundle to reduce bending energy [318]. A third possibility is that these stepwise intensity changes indicate that bundles are composed of actin filaments that do not span along the entire bundle length, reflecting the wide length distribution of the filaments [182]. However, due to lacking kinetic observations of the bundle formation pathway or higher-resolution images, we currently cannot distinguish between these mechanisms.

The bundles within the liposome bodies are on average thinner than the bundles in the protrusions, with around 10 - 30 filaments per bundle (Fig. 8A, red symbols). Again there is no significant difference between the average bundle size at R_F = 0.05 and 0.2, suggesting that the higher stiffness of the bundles formed at R_F = 0.2 reflects a tighter filament coupling rather than a bundle thickening. We emphasize that these numbers provide a good relative comparison between different conditions, but only a rough estimate of the absolute number of filaments per bundle, given that the fluorescence intensity in the main body likely reflects both filamentous and monomeric actin.

The influence of membrane mechanical properties on liposome shape

The experiments with varying fascin concentration indicate that the formation of membrane protrusions is determined by a balance between bundle rigidity and membrane elasticity. We can independently test this interpretation by varying the elastic properties of the membrane. The elastic energy of a liposomal membrane is a sum of the energy cost to stretch the liposome membrane and the energy cost to bend the membrane [258]. The resistance to stretching can be experimentally adjusted by osmotically changing the in-plane membrane tension. In the experimental conditions discussed so far, the liposomes are in a hypertonic environment, which we refer to as the "*reference membrane condition*". In a hypertonic environment, the liposomes are shrunk by placing them in a solution with a higher osmolarity compared to the inner buffer. The osmolarity mismatch across the membrane sets up an outward flow of water which continues until osmotic equilibrium is reached. Assuming the surface area of the liposome remains constant, the liposome thus gains "excess membrane area" compared to

a sphere having the final volume of the liposome after water has flown out [342]. In the buffer used here, the liposomes gain 14% excess area (Fig. 7).

To increase the membrane resistance to stretch, we transfer the liposomes to a hypotonic environment, where the liposomes swell by uptake of water from the outer buffer. The membrane area stored in thermally driven undulations is smoothed out due to the volume increase, resulting in a "*tense membrane condition*" (-2.5% excess membrane area). Strikingly, much fewer liposomes (15% out of 26) are protruded, compared to 60% at the reference membrane condition (Fig. 7, R_F = 0.05). The non-protruded tense liposomes are mostly spherical (Supplementary Fig. 7 and 8). Similar to the liposomes in the reference membrane condition, we observe that both protruded and non-protruded liposomes are filled with actin bundles forming ring-like structures with sharp kinks (Supplementary Fig. 8). We note that tense membrane conditions are difficult to achieve experimentally, due to the low lysis tension of lipid bilayers. Depending on lipid composition, bilayers can be expanded by only 4 - 9% of their original surface area [343] [342]. In our hands, when the excess membrane area of the liposomes is reduced to -4.8% instead of -2.5% (the tense membrane condition), we observe a higher fraction of protruded liposomes (37% out of 62 liposomes). However, we suspect that the membranes are leaky due to transient opening of membrane pores [343] [344], since the membranes look flaccid. When we further reduce the excess membrane area to -14%, we observe only very few liposomes, presumably due to membrane lysis.

To further test the influence of membrane elastic properties on liposome morphology, we increase the membrane bending stiffness (referred to as the "*stiff membrane condition*"). This is achieved by doping the membrane with biotinylated lipids and decorating these lipids with neutravidin, which binds nearly permanently to biotin groups. The bending rigidity of a protein-coated liposome is about 10 times higher than that of a bare liposome [345]. We observe a marked reduction of the percentage of protruded liposomes, from 60% to ca. 30% (Fig. 7), consistent with an increased elastic energy cost for membrane protrusion. The liposomes that are protruded have only a single protrusion with a length up to 30 μm (Supplementary Fig. 9A and E). Similar to the liposomes formed under the reference membrane condition, the protrusion length is inversely correlated with the solidity of the liposomes (Supplementary Fig. 9E). Interestingly, the main body of the protruded liposomes is more circular than that of the liposomes formed under the reference membrane condition (Supplementary Fig. 6 and 7). Furthermore, unlike liposomes formed under the reference membrane condition, where there are various shapes of non-protruded liposomes, here we observe mainly circular shapes for the non-protruded liposomes (Supplementary Fig. 9B-D). Liposome size is unlikely to play a role here, since the cross-sectional areas of the liposomes are comparable to those formed under the reference membrane

condition (Supplementary Fig. 3). Taken together, our observations confirm our hypothesis that a higher bending energy cost to deform a stiffer membranes limits liposome deformation.

Interestingly, the protrusions of the stiff liposomes are significantly narrower than the protrusions formed in liposomes at the same R_F but at the reference membrane condition (Fig. 5B). It is surprising that membranes with a higher bending energy can develop narrower tubes, given that the higher curvature of narrow tubes is associated with a higher bending energy cost [258][346][347]. It is possible that narrow protrusions form due to an uneven decoration of neutravidin on the liposome membrane, such that the actin bundles only deform parts of the membrane that are not decorated by neutravidin. Alternatively, lipid flow from the main body of the liposome to the protrusion, which is required for elongation of the protrusion [348] [349] [350], may be hindered by the neutravidin decoration, thus restricting the available membrane area for the protrusion. Consistent with the latter idea, the membrane surface area contributed to the protrusions is lower than for liposomes formed under the reference membrane condition (up to 20%, compared to up to 25%, see Supplementary Fig. 4). The organization of the actin bundles within the protruded stiff liposomes is similar to that observed in liposomes under the reference membrane condition. Half of the liposomes have a planar ring-like bundle structure with sharp kinks in the main body, and the other half has multiple distorted rings located in multiple planes.

The influence of actin-membrane coupling

In cells, the plasma membrane tightly conforms to the architecture of the cytoskeleton, suggesting the presence of adhesive interactions between the membrane and the cytoskeleton. Indeed, a host of actin-binding proteins has been identified that can physically connect actin filaments to the plasma membrane [110] [131] [111]. It has been proposed that actin-membrane attachments may stabilize protrusions supported by actin bundles, including filopodia, microvilli and stereocilia [351] [322] [352]. However, actin-membrane coupling can also effectively make the cell surface more resistant to deformation [353] [349] [354] [348] [355]. To resolve the effect of actin-membrane anchoring on liposome morphology, we encapsulate sparsely biotinylated actin filaments which are linked to the inner neutravidin-decorated surface of the liposome via neutravidin crosslinks. Similar to the stiff (but non-adhesive) membrane condition, we observe only a small fraction of protruded liposomes (8%, see Fig. 7) and most of the non-protruded liposomes are spherical (Supplementary Fig. 10 B-D). The actin bundles form rings with kinks underneath the membrane (Supplementary Fig. 10 A and B).

Confinement-induced deformation of actin-fascin bundles in non-protruded liposomes

In non-protruded liposomes, actin-fascin bundles formed at low fascin concentration (R_F = 0.05) form ring-like structures and sometimes exhibit sharp kinks and buckles, similar to the bundles observed in the body of protruded liposomes (Fig. 9A and B, *i*). In about half of the cases, the bundles pack into a single cortical ring (which we refer to as a planar actin structure, Fig. 9A and B, *i*), whereas in the other half, the bundles form multiple cortical rings and/or bundles that are not focused into a single plane (which we refer to as a non-planar actin structure, Fig. 9A and B, *ii*). The difference between planar and nonplanar ring-like structures is clearly visible when plotting the average intensity of each confocal slice as a function of distance along the z-axis (Fig. 9A, *iii*). The organization of the bundles in the liposomes does not appear to depend on the liposome radius in the experimentally accessible range of radii, from 2 to 9 μm (Fig. 9C). Changes in membrane tension, bending rigidity, or presence of actin-membrane anchors also do not obviously influence the occurrence of planar versus non-planar actin structures.

Since even the largest liposomes examined have a diameter that is comparable to the persistence length of single actin filaments [26] [34], and much smaller than the persistence length of the bundles, we anticipate that under all conditions the bundles are strongly confined. For strongly confined semiflexible filaments, it has been suggested that the filaments will be forced to adopt a peripheral localization and bend underneath the liposome surface to minimize their bending energy [127]. This prediction has been verified by the observations of cortical actin shells inside liposomes [123] [182]. Ring-like structures similar to the ones we observe were reported for actin filaments polymerized in the presence of actin-binding crosslinking proteins in liposomes [202] and water-in-oil droplets [340]. Furthermore, ring-like configurations of microtubules and/or microtubule bundles inside liposomes have been observed previously [313]. Our observations of cortical actin rings also qualitatively agree with theoretical predictions for semiflexible polymers confined within a rigid spherical confinement [356] [357] [358] or a soft liposome [359] [360]. Interestingly, we occasionally observe distorted ring-like bundles inside spherical liposomes (Fig. 9D and E), which are qualitatively similar to theoretical predictions that polymer rings can buckle into a banana-like shape when enclosed by a spherical hard confinement [357] [358].

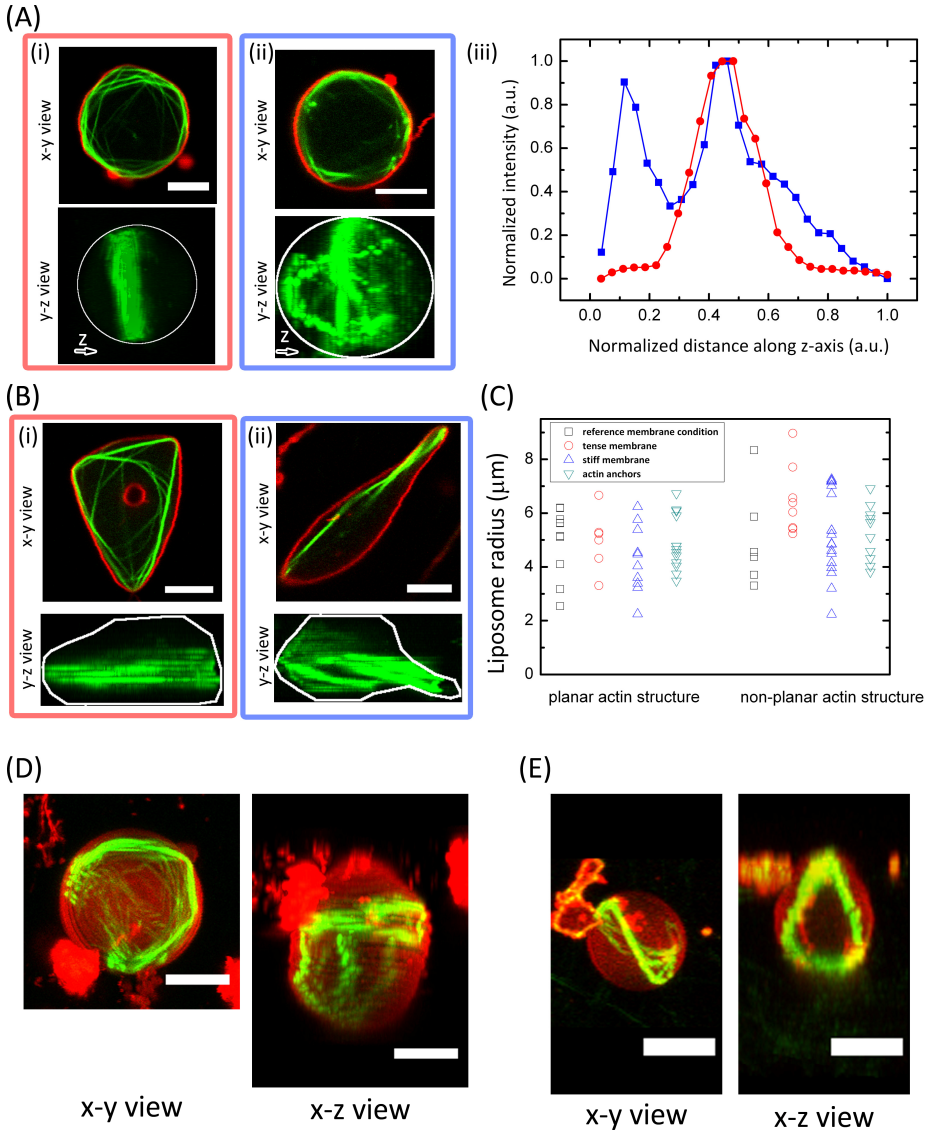

Figure 9. Organization of actin-fascin bundles inside non-protruded liposomes. (A) Confocal fluorescence micrographs of two "actin anchors" liposomes exhibiting a packed cortical ring composed of actin bundles (i) (denoted as planar actin structure) and a distorted cortical actin bundle structure (ii) (denoted as non-planar actin structure). Images in the bottom row show the 3D reconstructions of the liposomes in the top row, with the white circles indicating the outer edges. *Bottom left*: 27 planes over a total z-range of 13 μm; *bottom right*: 26 planes over a total z-range of 12.5 μm. (iii) Pixel-averaged actin fluorescence intensity in each confocal x-y plane as a function of distance along the z-axis, where the red curve corresponds to the liposome in (i) and the blue curve

to the liposome in (ii). For each curve, the normalized intensities are obtained by subtracting the minimum value followed by normalizing by the difference between the minimum and the maximum values. (B) Irregularly shaped liposomes containing planar (*left*) and non-planar (*right*) actin structures. The bottom images show the 3D reconstructions of the liposomes: 25 planes over a total z-range of 12 μm (*left*) and 31 planes over a total z-range of 9 μm (*right*). The white lines indicate liposome edges. Liposomes are formed at the reference membrane conditions and with R_F = 0.05. (C) Radius of liposomes containing planar or non-planar actin bundle structures. Radii represent the equivalent radius of a circle having the same cross-sectional area measured at the equatorial plane of the corresponding liposome. Liposome population sizes from left to right: 11, 6, 10, 13, 6, 8, 18 and 10. (D) and (E) Confocal fluorescence micrographs of liposomes having distorted ring-like structures of actin bundles: a bent actin ring (D) and a twisted actin ring (E). Liposomes were formed with the stiff membrane condition. Red: membrane, green: actin. Scale bars: 5 μm.

3.3 Discussion

Morphological diversity

The plasma membrane of animal cells can deform both globally and locally under the influence of interactions with the cytoskeleton. Understanding the mechanisms that determine membrane shape is challenging due to the numerous molecular components involved and the complexity of their interactions. Here, we specifically focus on the physical aspects involved in the formation of thin membrane protrusions by cytoskeletal actin bundles. By using a cell-free, well-controlled model system based on cell-sized liposomes encapsulating actin-fascin bundles, we demonstrate that protrusion formation is governed by the interplay between the elastic properties of the lipid bilayer membrane and the rigidity of the actin-fascin bundles (see schematic summary in Fig. 10). Actin bundles are needed to drive membrane protrusion. Protruded liposomes are favored when the membrane is flaccid and soft, whereas high membrane tension and/or high membrane rigidity prevent membrane deformation.

Our findings are qualitatively consistent with earlier studies of liposomes deformed by encapsulated actin bundles and microtubules (see below). However, we performed a more complete and quantitative analysis of liposome shapes across a large population, involving 25-100 different liposomes for each experimental condition. This analysis enabled us to reveal a wide variety of liposome shapes with different degrees of membrane deformation and different spatial arrangements of actin bundles. It is possible that some of the shapes are in non-equilibrium/metastable states. The ϕ–shaped liposomes with two protrusions are for instance expected to be energetically slightly less favorable than lollipop-

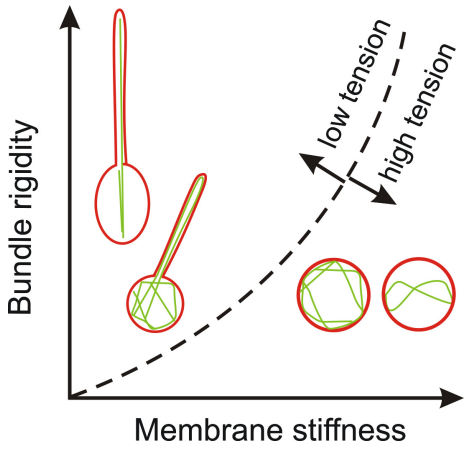

Figure 10. Schematic shape space of liposomes encapsulating actin-fascin bundles in terms of the mechanical properties of the membrane and the stiffness of the actin bundles. When confined within flaccid liposomes, actin bundles generate membrane protrusions. Actin bundles with a high bending rigidity tend to align along the long axis of the protruded liposomes whereas bundles with a low bending rigidity are forced by the membrane to kink or buckle inside the liposome body and/or at the end of a protrusion. A higher membrane bending stiffness or membrane tension suppresses membrane deformation and under these conditions membrane confinement forces the actin bundles to form cortical rings to reduce the enthalpic cost associated with bundle bending.

shaped liposomes with one protrusion, due to the energy barrier involved in initiating a protrusion [346] [361] [362]. Consistent with this expectation, we do observe ϕ-shaped liposomes, but with a lower probability than lollipop-shaped liposomes with a single protrusion (see Table 1). The morphological diversity we observe may also be related to a variability in membrane elastic properties within a given liposome preparation, which is quite common [363] [345] [219]. Alternatively, variations in actin content may contribute to the morphological diversity. Within a given liposome preparation, the actin encapsulation efficiency typically varies between 25 and 100% (see Chapter 2) [219]. In the future, it will be interesting to test whether alternative encapsulation methods based on water-in-oil emulsions [203] [206] [220] or inkjet printing [227] can reduce the variability. However, there is also an advantage to the diversity of morphologies we obtain: it enables us to correlate membrane shape and actin bundle organization over a wide range of morphologies.

Formation and stability of membrane protrusions

Our results clearly show that membrane protrusions are only formed if the actin filaments are bundled. This conclusion is consistent with earlier, more qualitative, reports of changes in liposome morphology induced by encapsulated actin filaments. At a low actin concentration (2 - 24 μM), actin filaments inside liposomes arranged into a cortical shell to reduce their bending energy and the liposomes remained close to spherical [123] [182]. At a higher actin concentration (48 – 200 μM), actin filaments arranged into bundle-like structures that induced liposome deformation [196] [198] [239] [199]. These bundle-like structures were suggested to occur due to a liquid crystalline phase transition of the actin filaments [364]. Both physiological actin-binding proteins [199] [202] and polycations [200] can bundle actin filaments inside liposomes and give rise to actin-filled membrane protrusions. In this work, we focus on the crosslinking protein fascin, since this protein is known to be important for forming stable filopodia in animal cells [329] [44].

The energy required to generate a cylindrical thin membrane protrusion from a flat membrane surface arises from the elastic energy associated with stretching as well as bending of the membrane. Considering a membrane tube with length L and radius R, the total energy associated with the tube follows from the Helfrich equation, $E = 2\pi RL(\sigma + \kappa/(2R^2)) - fL$, in which κ is the bending rigidity, σ is the surface tension, and f is the equilibrium point force required to maintain the tube [258]. Thus, to minimize the total free energy, the bending rigidity acts to increase the radius whereas the surface tension works to reduce it. The balance between these two factors gives the equilibrium tube radius and equilibrium force: $R = (\kappa/2\sigma)^{0.5}$ and $f = 2\pi(2\kappa\sigma)^{0.5}$, respectively [349] [365] [347] [366]. For typical values of bending rigidity (a few tens of pN nm) and tension (0.001 – 0.1 pN/nm), the protrusion radius is expected to range from 10 nm to 200 nm, and the force from 1 pN to 50 pN [366] [260] [257]. However, to initiate a protrusion, theoretical models predict that the applied force has to be around 13% higher than the equilibrium force required for maintaining the protrusion, due to the formation of a half-catenoid shape connecting the cylindrical protrusion to the flat membrane [367] [365]. This force barrier (also known as overshoot force) has been experimentally verified by pulling membrane tubes from liposomes [368] [369] as well as cells [370] [371].

Thermodynamic models [372] [361] predicts that the force generated by actin polymerization can be expressed by $f_{poly} = (k_BT/\delta)\ln(C/C_{crit})$, where $k_BT \approx 4.1$ pN nm is the thermal energy, $\delta \approx 2.7$ nm is the elongation distance for adding a single actin monomer, C is the actin monomer concentration, and $C_{crit} \approx 0.12$ μM [373] is the critical concentration for polymerization. Considering typical actin concentrations in cells (around 10 - 100 μM) [374] [52], the maximum force

generated by a single actin filament is around 9 pN [321]. Since this force is close to the minimum force for generating and maintaining a membrane protrusion, protrusions can only be formed if the actin filaments form bundles [321] [322] [362].

The maximum length of a membrane protrusion generated by an actin bundle is limited by the mechanical stability of the bundle against the compressive load imposed at its tip by the membrane [324] [362] [322] [361] [323]. Naively, the length of a protrusion is limited by the Euler buckling instability of the bare actin bundle. An elastic filament with length L_{fil} and persistence length l_p will buckle for loads given by the Euler buckling force, $f_b = l_p k_B T \pi^2 / 4 L_{fil}^2$ [341] [323]. Under fixed compressive load, filaments will buckle if they are longer than the buckling length $l_b = (l_p k_B T \pi^2 / 4 f_b)^{0.5}$. Thus, for a typical membrane resistive force of 10 - 50 pN associated with a thin membrane protrusion, single actin filaments with a persistence length l_p ~ 10 μm have a buckling length of only 40 – 100 nm. Actin bundles have an effective persistence length that scales with the number of actin filaments in the bundle N as $N^{\alpha} l_p$, where α can range from 1 in case of weak bundling to 2 in case of tight bundling [340]. For fascin-mediated actin bundles, a higher fascin concentration was shown to cause both an increase of N and an increase of α up to a limiting value of 2 [340]. In bulk solution, the maximum bundle size is 20 due to internal stress associated with an overtwist of the bundle [331] [375] [376], which is comparable to the bundle size observed in filopodia (N = 10 – 20) [44] [377]. From our fluorescence data, we estimate N-values that are indeed in this range. Thus, the naive Euler buckling stability criterion suggests that the actin-fascin bundles can support protrusions of 1 - 2 μm long. However, it was recently shown by combined theoretical modeling and computer simulations that the tight enclosure of bundles within a narrow membrane tube can prevent filament buckling, even for bundles that are composed of only 4 weakly coupled actin filaments (corresponding to a persistence length of ~40 μm) [378] [323]. Our findings experimentally confirm this picture, since we observe protrusions of up to 30 μm (average length of 16.6±7.9 μm) at low R_F and even 60 μm (average length of 21.5±12.8 μm) at high R_F. This finding is consistent with measurements of filopodial lengths in cells. Depending on cell type, a broad distribution of filopodial lengths has been reported (0.4 – 50 μm) [379] and filopodia can sometimes be extremely long, with lengths of up to 100 μm [379] [380] [381].

The observed protrusion lengths are longer than the previously reported protrusion length of liposomes deformed by microtubules (5 – 14 μm) [313] [314] [315] [316] [317] [318] [319] and actin bundles (3 - 12 μm) [200] [196] [198] [312] [199]. The difference may be due to differences in membrane composition and excess area, as well as differences in actin bundle stiffness, which depends on actin and crosslinker concentration, and the type of crosslinker used.

The theoretical models for filopodium stability based on a combination of bundle and membrane elasticity assume that the bundles adopt a helical contour [323]. We cannot observe this in our experiments. At low fascin concentration, we observe localized buckling of the bundle at the tip of the protrusion, suggesting that buckling does impose a limit on filopodium stability. The maximum length observed at low R_F, independent of membrane stiffness, is around 30 μm. Stiffening the bundles by increasing R_F prevents buckling of bundles at the tips and increases the maximum protrusion length to 60 μm. These very long protrusions are often gently curved, consistent with the theoretical predictions that the membrane bends together with the enclosed bundle and thus stabilizes the protrusion [323].

The theoretical models assume that the actin filaments in the bundle run along the entire length of the membrane protrusion [324] [322] [382]. In our cell-free liposome system, we expect a broad distribution of filament lengths, since we did not include length-regulatory factors such as capping protein or profilin. This can explain why we sometimes observe uneven numbers of actin filaments along a bundle and frequent kinks in actin bundles in protrusions as well as in the main body of the liposomes. It is likely that the filament packing in the bundles is uneven, leading to structural defects where the bundles exhibit kinks. The bundles appear to be more homogeneous at high fascin-to-actin ratio, since there we observe mainly straight bundles. Our findings may be relevant to interpret differences between the properties of slow-growing and fast-growing filopodia. For slow-growing filopodia in mouse melanoma cells, bundles of continuous actin filaments were observed [44], whereas fast-growing filopodia in *Dictyostelium* cells were shown to contain many short, contiguous actin filaments [377].

According to the abovementioned purely energetic considerations, filopodia can grow to arbitrary lengths [323]. However, other factors such as monomer diffusion to the growing tip may limit the protrusion length [324] [322] [361]. In our experimental assay, we are unable to observe the kinetics of bundle growth and therefore cannot directly verify whether monomer diffusion is limiting. In the future, it will be interesting to measure filament growth kinetics by triggering actin polymerization in the microscope, for instance by injecting polymerization buffer with the help of membrane channels [123] [202] or by microinjection [383] [384] [385]. Furthermore, the liposomes provide an ideal test bed to test the contribution of other putative length regulatory mechanisms, such as capping protein activity [386] and myosin-X-driven transport of the actin elongation mediator Enabled/vasodilator-stimulated phosphoprotein (Ena/VASP) [387] and actin monomers [388].

The observed membrane morphologies of protruded liposomes are consistent with theoretical models of the shape transitions of liposomes subject to an axial load imposed by a growing rod whose ends push against the membrane [346]

[389] [390] [391]. These models predict that growing rods can deform liposomes into tubes, lemons, lollipops and ϕ-shaped liposomes, depending mainly on the axial force and the rod length. To a lesser degree, the relative area difference between the two leaflets of the membrane under stretching and the osmotic pressure also govern the protrusion width and the kinetics of liposome shape transitions from a lemon to a lollipop shape. We observe all the theoretically predicted shapes for liposomes containing actin-fascin bundles. Previous studies showed similar shapes for liposomes containing microtubules [313] [314] [315] [316] [317] [318] [319]. As mentioned above, lollipop shapes with a single protrusion at one pole are predicted to be energetically more favorable than ϕ–shaped liposomes with two protrusions, due to the energy cost to initiate a protrusion [346] [362] [361]. Furthermore, it has been predicted that the main body of a ϕ-shaped liposome does not need to be in the center of the two opposing protrusions; the exact locations are energetically indifferent as long as a small membrane protrusive part remains on either side of the body. Indeed, it has been reported that the main body of a ϕ-shaped liposome can freely move along the long axis of a microtubule-deformed liposome and eventually move towards one of the ends, forming a lollipop-shaped liposome [318]. In agreement with the models, we observe a higher proportion of lollipop-shaped liposomes compared to ϕ-shaped ones: at the reference membrane condition, 9% out of 56 protruded liposomes (the sum of the lollipop and ϕ-shaped liposomes) are ϕ-shaped at R_F = 0.05 and 21% out of 33 are ϕ-shaped at R_F = 0.2.

Our observations show similarities to previous observations for liposomes deformed by growing microtubules, which also revealed a majority of lollipops and a minority of ϕ-shaped liposomes [318]. Notably, ϕ-shaped liposomes were shown to transform into a pointed prolate-shape maintained by a single microtubule when reducing the number of microtubules inside the liposome by lowering the temperature [314]. Thus, although individual microtubules have a sufficiently large persistence length (~ 5 mm), bundles of microtubules may be required to protrude a liposome. Indeed, assembly of bundles in the protruded liposomes has been documented [314] [316] [317] [318]. Interestingly, ϕ-shapes supported by microtubules have also been observed for cells subjected to treatment with an actin depolymerization drug [392].

We find that the liposome shapes are sensitive to the fascin-to-actin molar ratio, which sets the stiffness of the bundles. At low R_F, the actin filaments form multiple bundles arranged in a ring-like structure in a liposome body. Often, single protrusions are formed by two or more bundles that emanate from the liposome body and are gathered in the protrusion. A few liposomes have two or more protrusions when different bundles protrude the membrane at different spots. At high R_F, the bundles align along the long axis of the liposomes, indicating that the

bundles are stiffer. Assuming a fascin-mediated bundle composed of 20 filaments in the tightly coupled region, the estimated persistence length ($N^2 l_p$) is around 4 mm. Thus, in mechanical terms, these stiffer actin bundles are more comparable to microtubules than the bundles formed at low R_F.

The theoretical models effectively assume that the filament that imposes an axial load on the liposome membrane has an infinitely high bending stiffness that prevents buckling. In our experiments, the actin-fascin bundles have a finite bending stiffness and buckled and kinked bundles are observed. Furthermore, it is important to note that the width of the actin-filled protrusions is not determined just by the membrane rigidity and tension, in contrast to empty membrane tubes [366]. The width of the actin bundles inside the protrusion likely impacts the protrusion width [366]. It will be interesting to include the structural and mechanical properties of actin-fascin bundles, including potential defects in filament packing, in the future theoretical modeling of filopodium formation and liposome deformation.

Influence of membrane tension and bending rigidity

We observe a strong influence of the membrane tension on the occurrence of membrane protrusions. At the reference membrane condition, corresponding to low membrane tension, the liposomes are flaccid and more than half of the liposomes form protrusions, whereas at the tense membrane condition achieved by osmotically swelling the liposomes, the majority of the liposomes retain a quasi-spherical shape and the actin-fascin bundles form a single or multiple circular bands. Intriguingly, variations in membrane tension induced by osmotic stress were shown to cause similar global shape transitions in earthworm cells: these cells underwent transitions between spherical shapes at high tension and protruded shapes at low tension [393]. Similar shape transitions were also observed for liposomes with encapsulated microtubules, where the membrane tension was controlled by micropipette aspiration. When an initially flaccid, ϕ–shaped liposome was subjected to increasing membrane tension, it underwent an irreversible shape transition into a discoid shape due to buckling and collapse of the microtubules [314] [316].

Our observations are also consistent with predictions of theoretical models that the force required to generate membrane protrusions is higher for a tense membrane [367] [349] [365] [347]. Membrane tension affects the stability and formation of protrusions in two ways. First, a higher membrane tension exerts a higher load on growing filaments, disallowing them to generate protrusions [310]. Second, the Brownian ratchet model predicts that growth of bundles perpendicular to the membrane is only possible if there are thermal undulations of the membrane or the actin filament end, such that sufficient space remains between the membrane and the filament end to add actin monomers to the

bundle tip [361] [322] [394]. There is growing evidence that membrane tension in cells acts as a global mechanical regulator that influences many processes involving membrane deformation, including cell motility and cell morphology [50] [325] [158] [159]. In motile cells, membrane tension for instance regulates the dynamics of cytoskeletal actin filaments and major sperm protein filaments [326] [310] [395].

Theoretical models of membrane tether formation predict that actin-driven membrane protrusion depends not only on membrane tension, but also on the membrane bending stiffness. To initiate a membrane protrusion, the energy barrier is higher when deforming a membrane with a higher bending modulus and once a protrusion is formed, a higher bending modulus acts to generate a wider membrane protrusion [367] [365] [347] [362] [361]. We observe that the membrane bending stiffness, although it does not influence the protrusion length, has a remarkable effect on the protrusion width. In contrast to the theoretical predictions, we find wider protrusions at a lower membrane stiffness (corresponding to liposomes with naked membranes) and much narrower protrusions when decorating the membrane with neutravidin. However, as discussed before, we suspect that the neutravidin decoration on the liposome membrane may be uneven, such that only parts of the membrane that are not decorated by neutravidin are deformed by the actin bundles. Furthermore, since the protrusions are not empty, as assumed in the theoretical calculations, the protrusion width is likely determined by the enclosed actin bundle structures as well as the membrane stiffness [366]. We observe that the membrane stiffness has a substantial effect on the occurrence of membrane protrusions: around half of the liposomes exhibit single protrusions while the others are close to spherical with actin-fascin bundles arranged into cortical rings. A similar result was reported previously for microtubule-containing liposomes where the membrane rigidity was modulated by adjusting the amount of cholesterol within the membrane: when the rigidity was increased, less protruded liposomes were found [313].

Confinement effects on actin bundle organization

Interestingly, our results reveal a reciprocal influence of the membrane and the actin bundles on each other's organization. The organization of the actin bundles in the non-protruded liposomes as well as in the body of the protruded liposomes shows clear evidence of confinement effects. In bulk solution, configurational entropy favors a random spatial and orientational organization of the actin bundles. However, the liposomes strongly confine the bundles, since the liposome diameter is much smaller than the persistence length of the bundles, and the bundle lengths are comparable to, or larger than, the liposome diameter. Bundles formed at low fascin concentration, which are probably (somewhat) weakly coupled, arrange in ring-like structures underneath the membrane, which are

packed into a single tight band. In contrast, stiffer bundles formed at high fascin concentration remain straight and align with the longest axis of the liposomes. The peripheral ring configuration avoids membrane deformation at the cost of filament bending, whereas the bundle alignment along the long axis avoids filament bending at the cost of membrane stretching.

In agreement with our observations, theoretical models have predicted that when confined within a rigid (non-compliant) spherical confinement, a ring polymer is buckled into a distorted ring [357] and a semiflexible linear polymer is organized into a cortical ring [356]. Models of deformable liposomes containing a single semi-flexible polymer find that the stiffness of the polymer and the liposome membrane influence each other's configuration reciprocally [359] [360]. While a stiff polymer remains straight and deforms the liposome into a prolate shape, a soft polymer forms a toroidal structure that deforms the liposome into an oblate shape [360]. We note that in our experiments the liposomes are freely floating inside the observation chamber, hampering a full 3D-reconstruction of liposome shape. Thus, we could not determine whether the spherical-like liposomes actually had a prolate or oblate shape. Nevertheless, our observations are qualitatively in good agreement with the predictions of the theoretical models. Interestingly, it has been shown that several microtubules form a strongly bent peripheral ring at the circumference of an activated blood platelet [396] [397] and in erythrocytes [398], similar to our observations of cortical actin rings inside liposomes.

Influence of actin-membrane attachment

In cells, actin filaments are anchored to the membrane by a host of cortical linker proteins [131] [144] [117] [133] [111]. A highly conserved and important link is for instance provided by proteins from the ezrin-radixin-moesin (ERM) family, which individually form weak bonds but collectively provide strong and continuous adhesion of actin filaments to the membrane [131] [149] [399]. To test how actin-membrane linkage may influence membrane protrusion formation, we introduce artificial actin-membrane links to our cell-free system based on biotin-neutravidin bonds. We observe a strong suppression of membrane deformation and of protrusion formation. This observation is in contrast with the previously reported increase of protrusions on liposomes deformed by microtubules in the presence of microtubule associated proteins that mediate microtubule-membrane binding [318]. In our experiments, the suppression of protrusions may stem from the high bending rigidity of the neutravidin decorated membrane [345]. It will therefore be interesting to repeat our experiments with a more physiological actin-membrane linker that does not rigidify the membrane. However, it is possible that attachment of a cortical actin layer to the plasma membrane hampers protrusion formation by increasing the stiffness of the

membrane [349] [400] [325] [355]. In addition, myosin-II motor activity in the actin cortex generates contractile stress that acts to increase the effective surface tension of cells [310] [401] [49], which likely also hampers protrusion formation. It is therefore important for cells to employ highly dynamic actin-membrane linkers, different from the virtually permanent biotin-neutravidin bonds used in our model system. Cells dynamically regulate actin-membrane anchoring by enzymes, actin associated proteins and lipids [110] [402] [52]. The signaling lipid phosphatidylinositol 4,5-bisphosphate (PIP_2) for instance regulates the adhesion energy between the cytoskeleton and the plasma membrane, consequently controlling cell shape [403]. Our cell-free model system provides a new assay to study the influence of more physiological linkers in the future.

In addition, our model system can be used to disentangle the different mechanisms that have been proposed to contribute to filopodium formation. Filaments in the dendritic actin array in the lamellipodium of migrating cells can converge into bundle precursors [44]. The dendritic actin array is nucleated by the Arp2/3 complex [56], which is itself activated by membrane-bound actin nucleation promoting factors such as the WASP and WAVE family proteins [57]. An approach based on water-in-oil emulsions has been used to obtain thin (0.2 – 0.4 μm) actin shells nucleated by the Arp2/3 complex on the inner surface of a liposome membrane [203] [204]. It would be interesting in the future to introduce the Arp2/3 complex nucleation machinery in our model system. Alternatively, formins in the so-called tip complex can help the elongation and have been suggested to initiate filopodia formation [68] [404] [71]. Ena/VASP proteins also localize at the tip of filopodia and are thought to facilitate elongation and possibly bundling of actin filaments in filopodia [405] [44] [406] [407]. Myosin-X motors has been reported to transport VASP to the filopodia tip [408] [409]. Moreover, there is evidence that proteins of the Bin-amphiphysin-Rvs (BAR) superfamily sense and/or induce membrane curvature to facilitate filopodium formation [112] [311] [15]. The liposome-based model system can be used to introduce formins to nucleate linear bundle arrays and length-regulatory factors such as VASP and capping protein, and also to study a possible synergy with curvature-promoting proteins such as members of the BAR family.

3.4 Conclusion

The shape of animal cells is determined by a reciprocal interplay between the plasma membrane and the enclosed cytoskeleton. An important contributor to cell shape change is the actin cytoskeleton, which can generate protrusive membrane structures such as extended flat lamellipodia and thin cylindrical filopodia and microspikes. Here, we reconstitute a minimal cell-free model system based on liposomes containing actin-fascin bundles to elucidate how the

membrane and the actin cytoskeleton can influence each other's organization through physical interactions. We find that the mechanical properties of the membrane and the rigidity of the actin-fascin bundles jointly determine liposome shape as well as actin organization. When the liposomes are sufficiently flaccid and deformable, the actin-fascin bundles can deform the membrane to form finger-like membrane protrusions reminiscent of filopodia in living cells. In contrast, liposomes with a membrane under high tension or with a large bending rigidity remain predominantly spherical and force the actin-fascin bundles to form cortical rings to minimize membrane stretching as well as bending energy in the highly confined environment of the liposomes. We find that membrane protrusions can reach lengths of up to 60 μm, confirming recent theoretical predictions that an actin bundle enclosed in a narrow membrane tube is stabilized against buckling due to the elasticity of the membrane. Our results highlight the importance of taking into account the physical properties of the cytoskeleton and the plasma membrane besides factors such as biochemical signaling for understanding cell shape control. On the one hand actin filaments/bundles exert forces on the membrane and deform it. On the other hand, the membrane itself is under tension and will exert forces on the actin cytoskeleton, thus constraining and influencing its organization. Our cell-free model system provides a powerful platform to dissect how other molecular factors such as actin-binding proteins and membrane association proteins influence this interplay.

3.5 Supplementary Figures

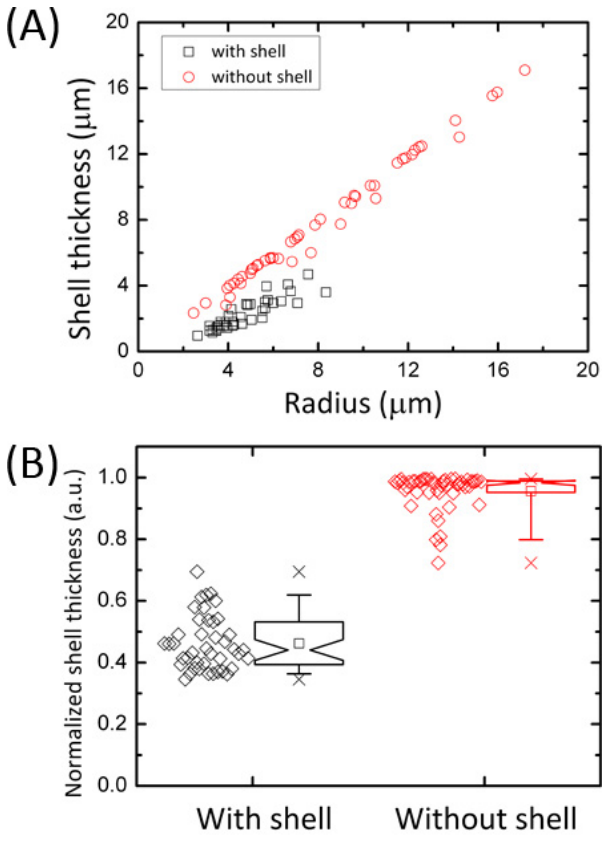

Supplementary Figure 1. Characterization of confinement-induced self-organization of actin filaments in liposomes into cortical shells in the absence of fascin. (A) Dependence of thickness of the actin cortical shell on liposome radius. Black symbols denote liposomes exhibiting a cortical actin shell and red symbols denote liposomes having a bulk actin network that fills the entire liposome interior. Note that actin shells are only found in liposomes with a radius below ~ 8 μm, indicating that spatial confinement promotes shell formation. (B) Actin shell thickness normalized by the corresponding liposomes radius. Note that a liposome is classified as exhibiting an actin shell if its normalized shell thickness is below 0.7, otherwise it is classified as "without shell". Liposome population sizes: 42 (with shell) and 50 (without shell).

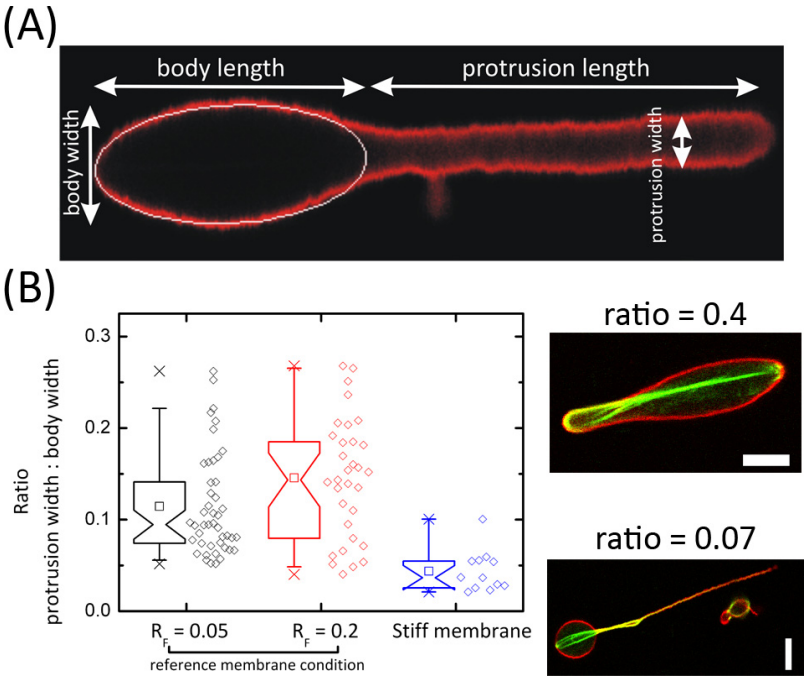

Supplementary Figure 2. (A) A confocal micrograph of a deformed liposome in which the white ellipse presents the result of fitting the liposome main body contour to an ellipse. (B) *Left*: The ratio of the protrusion width of a liposome and the width of its main body. Note that only liposomes having a protrusion-to-body width below 0.3 are classified as "protruded liposomes" and shown here. Liposome population sizes from left to right: 45, 32 and 12. *Right*: Confocal fluorescence images show a liposome classified as having no protrusion (*top panel*, protrusion width/body width = 0.4) and a liposome classified as having a protrusion (*bottom panel*, protrusion width/body width = 0.07). Red: membrane, green: actin. Scale bars: 5 μm.

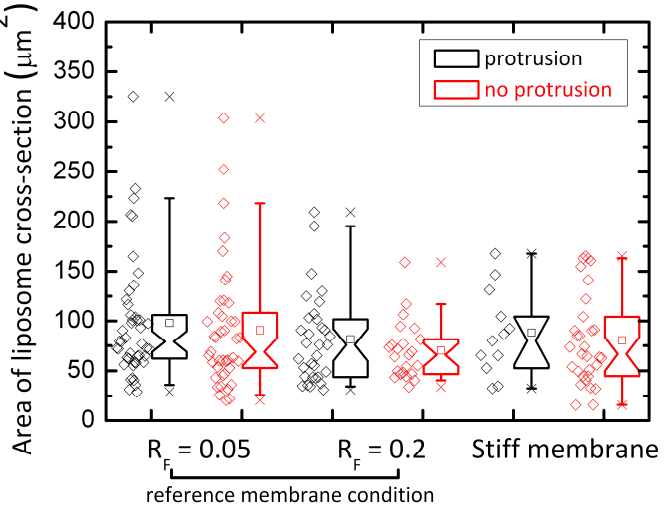

Supplementary Figure 3. Cross-sectional surface area measured from images of the equatorial plane of liposomes with and without protrusions, for three different sample conditions. Note that for some liposomes with protrusions that extended out of the equatorial plane, areas were computed from a projected image obtained by summing up several confocal images to present the entire shape. Liposome population sizes, from left to right: 45, 42, 32, 23, 12 and 31.

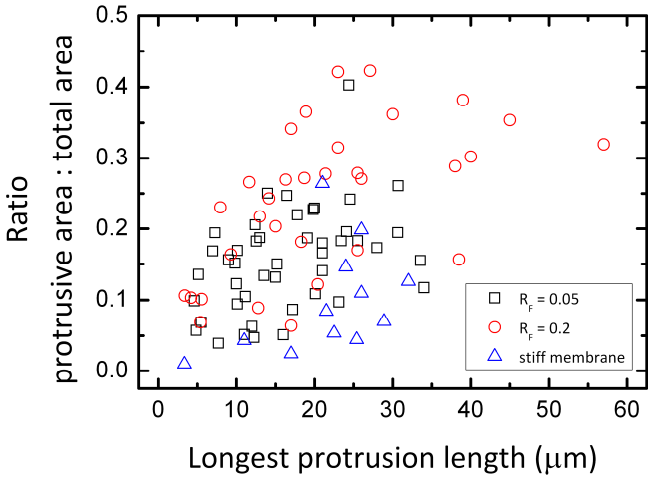

Supplementary Figure 4. Ratio of the protrusive area and the total surface area of a liposome versus the protrusion length. A protrusive area can take up to 40% of the total area of a liposome.

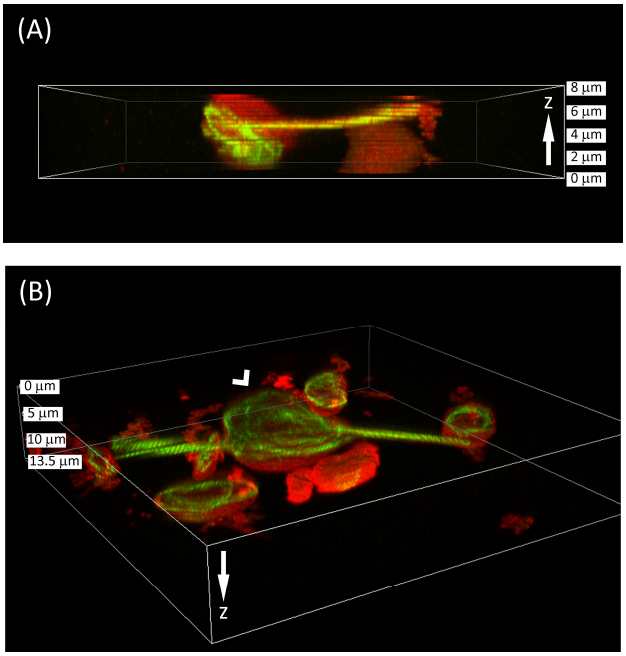

Supplementary Figure 5. 3-D reconstruction of liposomes encapsulating fascin-mediated actin bundles. (A) A planar ring-like structure of actin bundles in a protruded liposome. (B) Multiple ring-like structures of actin bundles (indicated by the white arrow head) inside a protruded liposome with two protrusions. Liposomes are formed with the reference membrane condition and with R_F = 0.05. Red: membrane, green: actin.

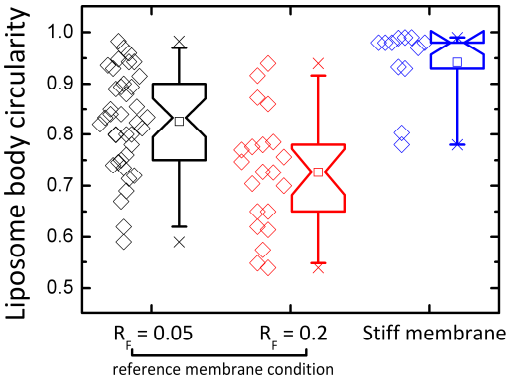

Supplementary Figure 6. Circularity of the main body of liposomes exhibiting a single protrusion for different sample conditions. Liposome population sizes from left to right: 39, 21 and 12.

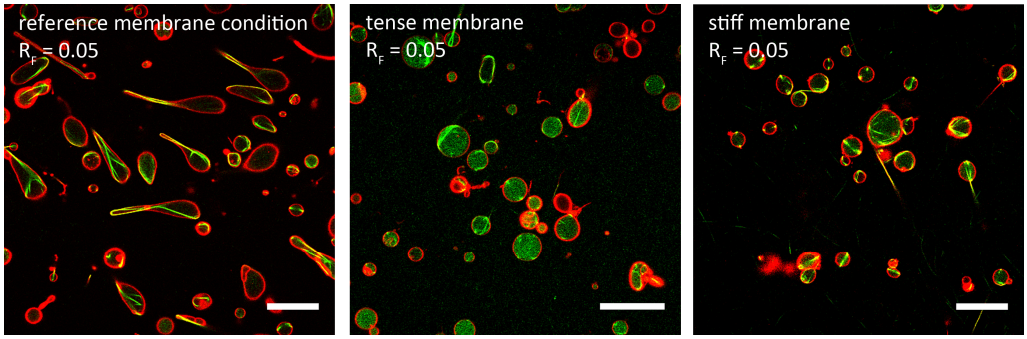

Supplementary Figure 7. Low-magnification overview images (confocal fluorescence) of liposomes obtained at different membrane conditions. Actin is shown in green and membranes in red. Scale bars: 20 μm.

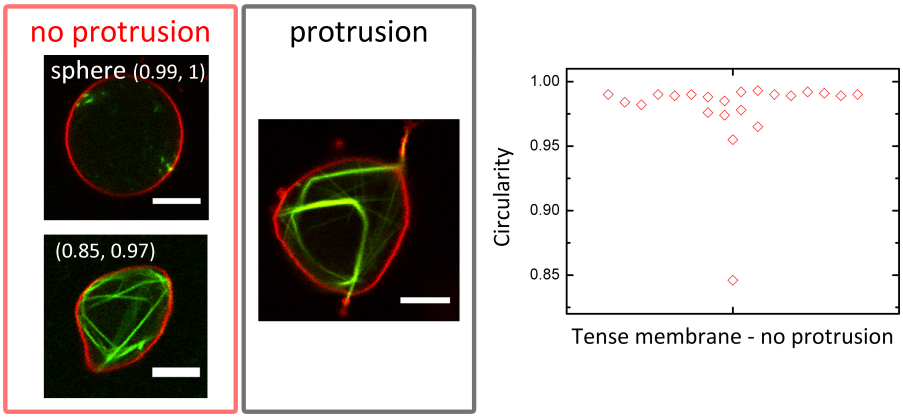

Supplementary Figure 8. *Left*: Confocal fluorescence micrographs of liposomes encapsulating actin-fascin bundles in the "tense membrane" condition, where the liposomes are swollen in a hypotonic environment. Only 4 liposomes out of a total 26 liposomes have protrusions. *Right*: circularities of non-protruded liposomes (22 liposomes). Note that only one non-protruded liposome is significantly non-spherical (circularity 0.85, see image *bottom-left*). R_F = 0.05. Red: membrane, green: actin. Scale bars: 5 μm.

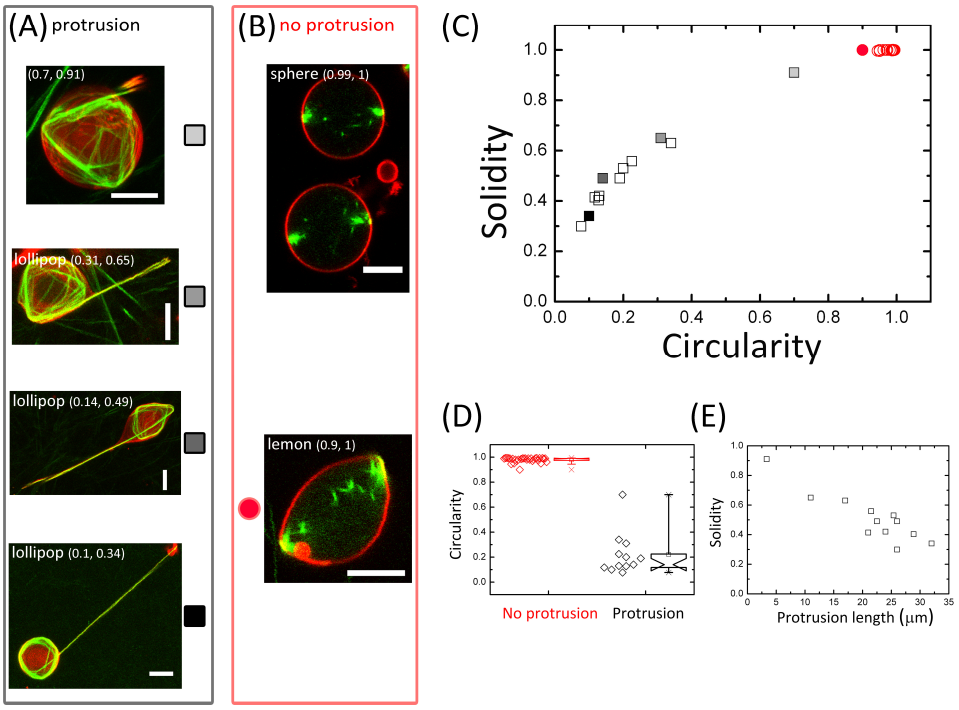

Supplementary Figure 9. Morphological characterization of a population of 43 liposomes encapsulating actin-fascin bundles (R_F = 0.05) in the "stiff membrane" condition, where neutravidin molecules are bound to the liposome membrane via biotinylated lipids. (A, B) Confocal micrographs of liposomes that are increasingly deformed (*top* to *bottom*). In (A), maximum intensity projections of confocal sections of liposomes are shown where the number of planes (p) over a total z-range (z, in μm) are (p = 30, z = 14.5), (p = 17, z = 8), (p = 19, z = 9), (p = 24, z = 11.5) from *top* to *bottom*. In (B), images are confocal sections recorded at the equatorial plane of the liposomes. Red: membrane, green: actin. Scale bars: 5 μm. (C) State space of liposome shapes in terms of circularity and solidity. Reddish symbols represent liposomes having no protrusion (31 liposomes) and black/grayish symbols represent liposomes with one protrusion (12 liposomes). Color-coded solid symbols correspond to images of liposomes in (A) and (B). (D) Circularities of liposomes with and without protrusions. (E) The solidity is inversely correlated with the protrusion length (correlation coefficient = -0.9057, $p < 0.001$).

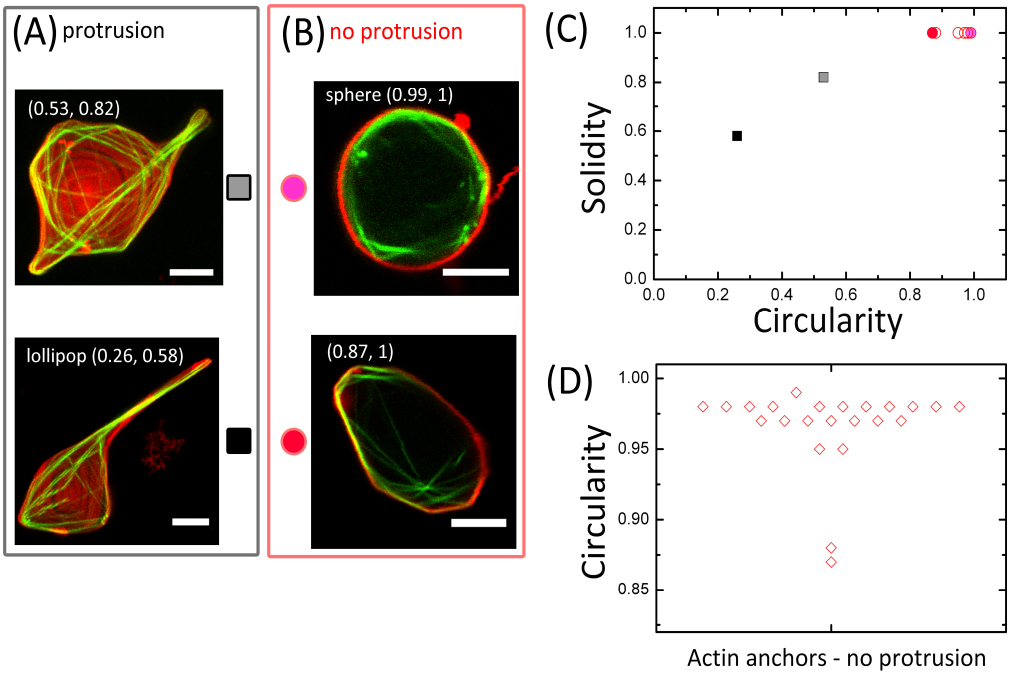

Supplementary Figure 10. Morphological characterization of a population of 25 liposomes encapsulating actin-fascin bundles (R_F = 0.05) in the "actin anchors" condition, in which actin is anchored to the membrane via biotin-neutravidin linkers. (A, B) Confocal micrographs of liposomes that are increasingly deformed (*top* to *bottom*). In (A), maximum intensity projections of liposomes are shown where the number of planes (p) over a total z-range (z, in μm) are (p = 29, z = 14), (p = 24, z = 11.5) from *top* to *bottom*. In (B), images are sections recorded at the equatorial plane of the liposomes. Red: membrane, green: actin. Scale bars: 5 μm. (C) State space of liposome shapes in terms of circularity and solidity. Reddish symbols represent liposomes having no protrusion (23 liposomes) and black/grayish symbols represent liposomes exhibiting protrusions (2 liposomes). Color-coded solid symbols correspond to images of liposomes in (A) and (B). (D) Circularities of non-protruded liposomes.

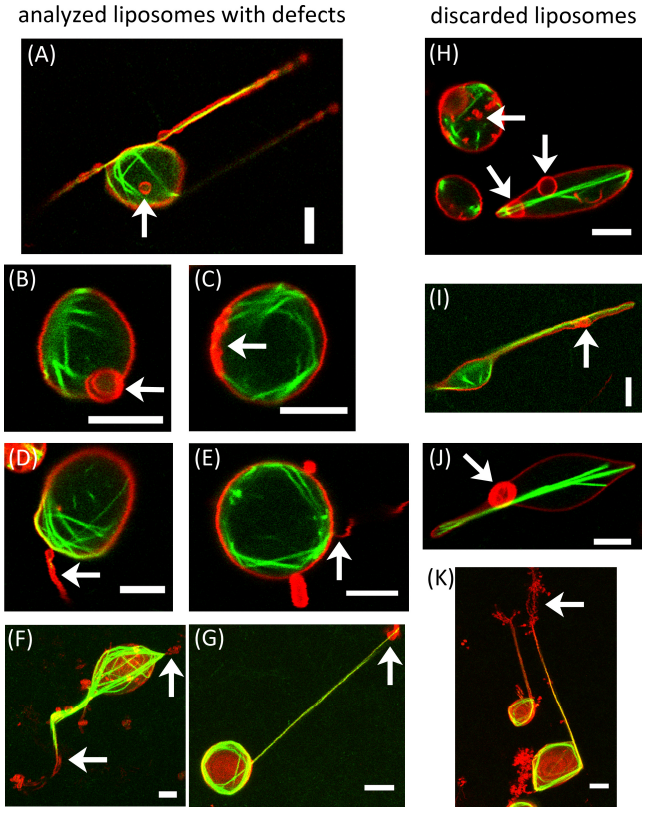

Supplementary Figure 11. (A) – (G) Confocal fluorescence micrographs of liposomes having defects that are deemed sufficiently minor to include in the morphological analysis (around 5% of a total of 70 liposomes and 30% of a total of 45 liposomes with the reference membrane condition and actin anchor condition, respectively). Defects included: (A) a smaller liposome inside a larger liposome, (B, C) smaller liposomes adhered on the inside of liposome main bodies, (D, E) membrane tubes adhered to the outside of liposomes, and (F, G) membrane aggregations or tubes adhered to the end of of a protrusion or to the main body of liposomes. (H) – (J) Confocal fluorescence micrographs of liposomes that are not considered in the analysis given that the shape of the liposomes or the actin structures are potentially affected by the encapsulated membrane tubes or aggregates, as indicated by the white arrows (around 30% of a total of 70 and 45 liposomes with the reference membrane condition and actin anchor condition, respectively). Images are single confocal sections recorded at the equatorial plane of the liposomes, except for (F), (G) and (K), where maximum intensity projections are assembled from 31 planes over a total z-range of 15 μm in (F), 24 planes over a total z-range of 11.5 μm in (G) and 20 planes over a total z-range of 9.5 μm in (K). Red: membrane, green: actin. Scale bars: 5 μm.

3.6 Materials

Chemicals were purchased from Sigma Aldrich (St. Louis, MO, USA) unless specified otherwise. All lipids were purchased from Avanti Polar Lipids (Alabaster, AL, USA). Liposomes were based on 1,2-dioleoyl-sn-glycero-3-phosphocholine (DOPC), which has a melting temperature of -20^{o}C. To prevent liposome aggregation or protein adhesion, we added 1,2-dipalmitoyl-sn-glycero-3-phosphoethanolamine-N-[methoxy(polyethylene glycol)-2000] (PEG-PE with a 2 kDa polyethylene glycol tail). For fluorescence imaging, we used 1,2-dioleoyl-sn-glycero-3-phosphoethanolamine-N-(lissamine rhodamine B sulfonyl) (rhodamine-PE). For specific coupling of actin filaments, we used the biotinylated lipid 1,2-dipalmitoyl-sn-glycero-3-phosphoethanolamine-N-(cap biotinyl) (biotin-PE). ATP was prepared as a 100 mM MgATP stock solution using equimolar amounts of Na_2ATP and $MgCl_2$ in 10 mM imidazole-HCl buffer, pH 7.4. Neutravidin was purchased from Invitrogen (Breda, The Netherlands) and reconstituted in PBS (10 mM phosphate buffer, 2.7 mM KCl and 137 mM NaCl, pH 7.4) at either 10 or 48 mg/mL.

Rabbit skeletal muscle G-actin, with and without biotin-label, was purchased from Cytoskeleton (Tebu Bio, Heerhugowaard, The Netherlands). Fluorescent actin with a dye/protein molar ratio of 0.6 was prepared by labeling amine groups with AlexaFluor 488 carboxylic acid succinimidyl ester [410]. G-actin was stored in G-buffer (2 mM Tris-HCl, 0.2 mM Na_2ATP, 0.2 mM $CaCl_2$, 1 mM dithiothreitol (DTT), pH 7.8) at 0^{o}C for up to 1 week or at -80^{o}C for long-term storage. Before use, frozen aliquots were always quickly thawed and 4 mM DTT was added to reduce any oxidized sulfhydryl groups [411] [412]. The G-actin solution was centrifuged at 120,000g for 30 min to remove aggregated proteins, followed by sonication for 5 min to disrupt actin dimers [413]. Recombinant mouse fascin was prepared from T7 pGEX *E. coli* as described in [410], with the only difference that gel filtration was performed on a high-resolution Superdex 200 column (GE Healthcare, Munich, Germany). Fascin was stored at -80^{o}C in 50 mM Tris-HCl pH 7.5, 150 mM KCl, 5 mM DTT, 10% (v/v) glycerol. Before use, fascin stock solutions were clarified by centrifuging at 120,000g for 5 min and used within a week. Protein concentrations were determined by optical absorption measurements at a wavelength of 280 nm, using extinction coefficients of 66300 $M^{-1} \cdot cm^{-1}$ for fascin [414] and 46218 $M^{-1} \cdot cm^{-1}$ for G-actin [295].

3.7 Methods

Agarose lipid swelling method

Liposomes at the "*reference membrane condition*" and the "*tense membrane*" condition were prepared by swelling lipids dried on top of an agarose film [217]

[219]. The agarose film was prepared by spin-coating a 1% (w/w) agarose solution (300 μl; Type IX-A ultralow gelling point, $T_g \leq 17^oC$) on a 24 x 24 mm microscope coverslip at 1200 rpm for 30 sec (DELTA 10BM, SUSS MicroTec), followed by drying at 37^oC for 30 min. A volume of 150 μl lipid mixture was spin-coated on the agarose-coated slide at 1200 rpm for 300 sec, followed by drying under vacuum for 60 min at room temperature. The lipid mixture contained DOPC, 0.2 mole% rhodamine-PE and 5 mole% PEG-PE dissolved in 95:5 (v/v) chloroform/methanol at a total lipid concentration of 3.75 mg/mL. Liposomes having membranes decorated by neutravidin (the "*stiff membrane*" condition and the "*actin anchors*" condition) were prepared by a slightly modified procedure, which involved swelling of inverse phase precursor micelles dried on an agarose film [252] [218]. In this case, a lipid mixture of 95.3 mole% DOPC, 0.2 mole% rhodamine-PE, 2 mole% biotin-PE, and 2.5 mole% PEG-PE was dissolved in 95:5 (v/v) chloroform/methanol at a total lipid concentration of 3.75 mg/mL, and inverse phase precursor micelles were formed by adding 3.5 μl (17 μl) neutravidin solution at 48 mg/mL (10 mg/mL) to 60 μl of the lipid mixture and pipetting up and down with a 500 μl glass syringe until the mixture became opalescent. The precursor solution (40 μl) was spin-coated on the agarose-coated slide at 100 rpm for 100 sec, followed by drying under vacuum for 100 min at room temperature. An open-top liposome formation chamber was assembled by placing a 0.12 mm thick spacer (secure-seal spacer, Invitrogen) on the agarose-lipid coated slide. Lipid swelling was initiated by pipetting 40 – 50 μl of an inner buffer (I-buffer) containing proteins into the formation chamber. The lipid swelling time was 45 min for lipids-agarose sample, and 90 min for the precursor-agarose sample. Swelling was performed at low temperature (4^oC) to slow actin polymerization and in a humid environment to prevent I-buffer evaporation. To collect liposomes, 65 μl of a glucose solution (O-buffer) was pipetted into the formation slide to flow the liposomes into an open-top observation chamber by gently tilting the slide. We repeated this process 2 times. The actin remaining outside the liposomes was diluted at least 2.6-fold. We note that sometimes actin bundles appeared outside of liposomes due to the low dilution factor used. The open-top observation chamber was assembled by placing a 0.5 mm thick spacer (Coverwell, 13 mm in diameter, Invitrogen) on a 76 x 26 mm glass slide. After liposome collection, the observation chamber was closed by a 24 x 24 mm coverslip. Prior to use, the glass slides were passivated by a casein solution at 2 mg/mL to prevent liposome adhesion and rupture. The liposomes were kept at 4^oC for 5 – 10 min to ensure osmotic equilibrium between the interior and exterior of the liposomes. Actin polymerization was initiated by bringing the observation chamber to room temperature. We observed liposomes after at least 45 min incubation at room temperature, to ensure complete actin polymerization. Liposomes encapsulating

only actin filaments were prepared with the precursor method, using a PBS solution to create precursors in a lipid mixture containing DOPC, 0.2 mole% rhodamine-PE and 5 mole% PEG-PE.

I-buffer and O-buffer osmolarity adjustment

The osmolarities of I-buffer and O-buffer were measured in the absence of proteins (Osmomat 030, Gonotec GmbH). The osmolarity difference between I- and O-buffers was controlled by adjusting the glucose concentration in the O-buffer. In the I-buffer, there was around 1.5 – 3.5% (v/v) of glycerol (contributed by the fascin and protocatechuate 3,4-dioxygenase storage buffers, 0.5 – 2.5% and 1% (v/v), respectively). Since glycerol is membrane permeable, but with a lower permeability rate than water [343], we sometimes included 0.5 – 2.5% (v/v) of glycerol in the O-buffer to expedite the osmotic equilibrium between the inside and the outside of liposomes. No obvious differences in liposome morphologies were observed when 2.5% (v/v) glycerol was present in the O-buffer; however liposome yield decreased when the O-buffer contained 3.5% (v/v) glycerol. In a hypertonic environment, the mismatch of the osmolarity inside/outside of a liposome determines how much water the liposome has to lose before reaching osmotic equilibrium. Assuming the membrane area of a liposome is constant, the liposome gains excess membrane area in a hypertonic environment as it loses water. The excess area of the liposome compared to a sphere having the same final volume as the liposome after the loss of water can be calculated as,

$$\frac{\Delta A}{A} = 1 - \left(\frac{C_0}{C_0 + \Delta C} \right)^{\frac{2}{3}}, \qquad (1)$$

where A is the surface area of the liposome, ΔA is the surface area difference between the liposome and the sphere, C_0 is the osmolarity of the I-buffer and ΔC is the osmotic gradient over the liposome membrane [342]. We note that the excess membrane area was calculated by assuming liposomes are suspended in pure O-buffer, meaning that the contribution of the I-buffer that remained outside the liposomes after liposome collection was not taken into account.

Reconstitution of actin networks

The I-buffer was composed of actin polymerization buffer (F-buffer: 25 mM imidazole-HCl (pH 7.4), 50 mM KCl, 2 mM $MgCl_2$, 1 mM DTT, 0.1 mM MgATP) with 280 mM sucrose, 2 mM trolox to prevent blinking, and an oxygen scavenging mixture of 2 mM protocatechuic acid and 0.1 μM protocatechuate 3,4-dioxygenase to minimize photobleaching [415]. The bulk actin concentration was 23.8 μM (equivalent to 1 mg/mL), including 20 - 30 mole% of AlexaFluor 488-actin and, if present, 0.25 mole% of biotinylated actin (on average ca. 1 biotin per 1 μm-

length of F-actin). The average encapsulation efficiency is ca. 50% (see Chapter 2) [219].

Confocal fluorescence microscopy and phase contrast microscopy

Confocal fluorescence images and phase contrast images were taken on a Nikon Eclipse Ti inverted microscope equipped with a Nikon C1 confocal scanhead using a 100x/NA1.4 Plan Apo objective. Images were captured using NIS Elements software (Nikon, version 4). AlexaFluor 488 was excited using a laser with a wavelength of 488 nm; rhodamine was excited using a laser with a wavelength of 543 nm.

Transmission electron microscopy

Commercial carbon coated copper grids (CF300-Cu, Electron Microscopy Sciences) were glow discharged (EMS 500 sputter coater, Electron microscopy sciences) before the protein solutions were adsorbed onto the grids. Samples were incubated for at least 30 minutes on grids in a humid environment to make sure enough material was adsorbed onto the grids. The samples were stained with commercial Nano-W (Nanoprobes) or uranyl acetate (Nanoprobes) and examined with a FEI Tecnai Spirit (120 kV) electron microscope (Institut Curie, France).

Characterization of actin filaments inside liposomes

The actin shell thickness of a liposome was determined as previously described [182] by integrating the fluorescence intensity around concentric circles and repeating this for radial distances from the liposome center to the liposome edge. By normalizing all values by the corresponding circumference (in pixels), we obtained a profile of integrated intensities along the liposome radius. To compare the integrated intensities of the liposome, we normalized integrated intensities by subtracting the minimum integrated intensity and then dividing by the difference between the maximum and minimum integrated intensities. The actin shell thickness is defined as the distance between the liposome edge and the radial position from the center of the liposome where the normalized integrated intensity is greater than 0.5. The shell thickness is finally divided by the liposome radius to obtain a normalized shell thickness. For a homogeneously filled liposome we expect a normalized shell thickness of 1. Since thick actin shells are in practice difficult to distinguish from homogeneous networks, we define liposomes with a normalized shell thickness above 0.7 as “bulk” and liposomes with normalized shell thicknesses below 0.7 as exhibiting a cortical actin shell. We excluded liposomes from the analyses which contained lipid structures such as tubes, lipid aggregates, or small liposomes (typically present in around 50% of all liposomes).

Shape characterization of liposomes

Image analysis was performed with Fiji software [416]. 2D-contours of liposomes were detected manually by using phase contrast images or confocal fluorescence images of membrane fluorescence signals recorded at the equatorial plane of each liposome. For some liposomes with a long membrane protrusion that projected out of the plane, we determined the shape from an image obtained by summing up a few images along the direction of the protrusion from 3D-confocal z-stacks or phase contrast images. The area (*A*), perimeter (*l*), circularity and solidity of each liposome were extracted from the detected contour [338]. The *circularity* of a given 2D-contour is defined as $4\pi A/l^2$, which is the ratio of the area of the contour and the area of a circle having the same perimeter as this contour. The circularity is 1 for a circle and is reduced as the 2D-contour gets increasingly elongated. The *solidity* of a 2D-contour quantifies the extent to which the shape is concave. It is defined as the ratio of the area of the object to the area of the minimum convex boundary circumscribing it. The solidity is 1 for a convex shape, and is smaller than 1 when concavities are present. Note that we included some liposomes with minor defects, but not liposomes that enclosed, or had adhered small liposomes or membrane aggregates that could potentially affect liposome/actin bundle morphology (see examples in Supplementary figure 11).

Classification of protruded and non-protruded liposomes

For a liposome with finger-like membrane tubes, we measured the width and length of its main body by fitting the body shape to an ellipse [416]. The major (minor) axis length of the ellipse was assigned to the body length (width) of the liposome (Supplementary Fig. 2). The protrusion width was measured as an average of $2-3$ width values measured at different locations along the protrusion. We classified a liposome as a protruded liposome if the ratio of its protrusion width to its body width was below 0.3. We note that if liposomes exhibit multiple protrusions (n > 1), we only present the length of the longest protrusion in Fig. 2F, 5A and 6E, and Supplementary Fig. 9E. For protruded liposomes, we determined the total surface area by adding the surface area of the main body (approximated as a prolate spheroid) and that of the protrusion(s) (approximated as a cylinder) [346].

Actin-fascin bundle intensity

The pixel averaged intensity of actin bundles was determined by averaging line profiles constructed by drawing lines along bundles with a width of 1 pixel (0.05 – 0.22 μm/pixel) and length of at least 1.3 μm. The intensity was corrected for dark background noise by subtracting the average intensity measured outside of liposomes. To estimate the number of actin filaments per bundle from the average bundle intensity, we calculated the ratio of the bundle intensity

(corrected for background) and the actin fluorescence intensity inside the main body of the liposomes (corrected for background). The actin fluorescence intensity inside the liposome main body was always significantly larger than the dark background intensity ((actin – background)/actin = 74 ± 15%), indicating the presence of actin that was not incorporated in bundles. We could not distinguish between F-actin and G-actin, meaning that the number of filaments per bundle estimated in this way provides a lower bound.

Statistics

Scatter plots show measurements obtained for individual liposomes. Liposomes encapsulating actin bundles were collected from 2 independent experiments, except for the "*actin anchors*" condition where liposomes were obtained from 2 separate swelling experiments using the same stock solutions of lipid and protein mixtures. All notched boxes show mean value (small squares), maximum and minimum values (crosses), and the 5th and 95th (with whiskers) and 25th and 75th percentile. The notches that extend to $\pm 1.58 \times IQR / \sqrt{N}$ (*IQR* is the interquartile range and *N* is the sample size) represent the 95% confidence level of the median value [417]. Statistical tests were performed by Pearson's linear correlation coefficient and the *p*-value was obtained by using a Student's t-distribution.

3.8 Acknowledgements

We thank Björn Stuhrmann, Sophie Roth, Ioana Garlea and Bela Mulder (AMOLF, Amsterdam) for insightful discussions. We thank Marjolein Kuit-Vinkenoog (AMOLF, Amsterdam), José Alvarado (AMOLF, Amsterdam), Magdalena Preciado López (AMOLF, Amsterdam), Said Omar and Liselotte Oppel for protein purification. We further thank Omar Mertins and Carlos Marques (Institut Charles Sadron, Strasbourg) for advice on the inverse phase precursor technique. Mouse fascin plasmid was a kind gift from Scott Hansen and R. Dyche Mullins (UC San Francisco).

CHAPTER 4. Active actin-myosin networks inside cell-sized liposomes

Animal cells actively generate contractile forces in the actin cortex, a thin actin network lying beneath the plasma membrane, to facilitate cell shape change during processes such as cytokinesis and motility. On a microscopic scale, this force is generated by myosin motors that bind to the actin cytoskeleton and use chemical energy to exert pulling forces. To resolve how these forces can generate cortex and membrane shape changes, we reconstitute active actin-myosin networks inside cell-sized liposomes to mimic the geometry of a cell. We focus on the interplay between myosin activity with actin-membrane anchoring and actin cortex crosslinking, both provided by biotin-neutravidin links. We show that actin cortex crosslinking is required for myosin motors to contract the cortex. In contractile cortices, the myosin motors always form a single dense focus. When actin-membrane anchors are present, myosin foci are restricted towards the liposome membrane while in the absence of the anchors, myosin foci are randomly positioned. When fascin is added to create actin bundles, the liposomes are less protrusive in the presence of myosin motors than in their absence, suggesting that the myosin motors may disassemble the bundles. Taken together, our findings show how actin-membrane anchors and actin network connectivity physically regulate actin network remodeling, which is relevant for understanding how the actin cortex may drive cell polarization.

The contents of this chapter are based on:

Carvalho, K.*, **Tsai, F.-C.***, Lees, E., Voituriez, R., Koenderink, G. H. and Sykes, C. (2013). Cell-sized liposomes reveal how actomyosin cortical tension drives shape change. *Proceedings of the National Academy of Sciences*, 14: 16456-16461. *joint first author

4.1 Introduction

Animal cells constantly change their shape to fulfill tasks including locomotion and division. Cell shape changes require remodeling of the actin cytoskeleton as well as the plasma membrane [418] [419]. To reorganize the actin cytoskeleton, cells rely on subcellular contractility, an emergent property of the actin cytoskeleton interacting with myosin II motors [82]. Myosin II motors assemble into bipolar filaments [61] and hydrolyze adenosine triphosphate (ATP) to exert pulling forces on the actin cytoskeleton [420]. To facilitate cell shape change, the actin cytoskeleton and myosin forms a thin actomyosin cortex with a thickness of 100 – 190 nm that is tightly coupled to the plasma membrane [46] [47] [48]. Contraction of the actomyosin cortex creates a cortical tension that can stiffen the cell surface [421] and has been suggested to play a role during mitotic cell rounding [422] [423] [421]. Also, actomyosin contraction can cause membrane constriction [89], global cortical flows [424] [86] [82], membrane blebbing [82] [49], and global cell shape oscillations [425].

One of the key factors determining cell shape change is the anchoring of the actin cytoskeleton to the plasma membrane, which is needed to mechanically stabilize cell shape, but also to change it. Examples of cortical linkers are ezrin, radixin and moesin (members of the ERM protein family), which are enriched at the cleavage furrow during cytokinesis and at the trailing edge of motile cells to facilitate cell shape change [131] [426] [421] [427] [428] [86]. Actin-membrane anchors have been shown to strongly influence contractile processes. For instance, cellular blebbing, which is critical for the stability of cleavage furrow positioning in cell division [166], is driven by local detachment of the actin cortex from the membrane at the cell poles to release excess cortical tension generated by the contractile cortex [289] [77]. During epithelial morphogenesis, the actin-myosin network is mechanically coupled to the cell junctions, which governs the direction of cortical flows [429]. In meiotic mouse oocytes, the meiotic spindle is transported by a contractile actin-myosin network that is connected to the cell cortex to ensure a directional relocation of the spindle [430].

It is well recognized that cortex remodeling and cell shape changes depend on a balance between active forces from myosin contractility and passive forces originating from cortex viscoelasticity and actin-membrane anchoring [49]. However, elucidating the force balance *in vivo* is hindered by the complexity of living cells. To overcome this difficulty, studies using cell-free extracts [431] [281] [432] [433] and reconstituted model systems based on purified proteins [434] [283] [280] [282] [435] [281] have been performed. These alternative approaches have shown that contraction of bulk actin-myosin networks occurs only above a threshold motor concentration and within a window of crosslinker concentrations [280] [282] [281]. Crosslinking is required to establish contractile stress [436] [280]

[437] [291]. Various theoretical models have been proposed to explain these experimental observations [283] [438] [439] [440] [441] [442]. To mimic the two-dimensional constraint of the cellular cortex, several studies have been performed where actin-myosin networks were anchored to an oil-water interface [179] or a supported lipid bilayer [173] [174]. For instance, a recent study of actin-myosin networks anchored to a supported lipid bilayer revealed that actin-membrane anchors influence the long-range transmission of stresses necessary for network contractility [174]. However, while this type of model system can address actin-membrane anchoring, it cannot account for the geometry of a cell, for the confinement that the plasma membrane imposes on the actin-myosin cytoskeleton, nor for the deformability of the membrane.

Here, we reconstitute a cell-free model system based on cell-sized liposomes encapsulating active actin-myosin networks that are anchored to the inner membrane surface. We reveal the impact of actin-membrane anchors on myosin organization and myosin-driven actin remodeling. We show that myosin motors form a single dense focus provided that the actin network is crosslinked. In the presence of actin-membrane anchors, myosin foci are restricted towards the liposome membrane while in the absence of the anchors, myosin foci adopt random positions. Finally, we show that active myosin filaments limit protrusion formation of liposomes that encapsulate actin-fascin bundles. Our model system provides a powerful platform to further dissect how different types of actin crosslinkers or physiological actin-membrane anchors such as the ERM family influence the contractility of actin-myosin networks as well as cell shape change.

4.2 Results

Formation of cortical actin shells inside liposomes

In unconfined bulk solution, actin filaments polymerized at 23.8 μM (equivalent to 1 mg/mL) form an isotropic entangled network with a pore size of about 0.3 μm [332]. Confocal micrographs show homogeneous networks whose constituent filaments cannot be discerned since the pore size is close to the optical diffraction limit (Supplementary Fig. 1, panel "*actin only*"). In cells, actin filaments are often crosslinked by actin crosslinking proteins, giving rise to various cytoskeletal architectures such as actin bundles assembled by fascin in filopodia, branched actin networks organized by the actin-related protein 2 and 3 complex (Arp2/3) in lamellipodia [443] [43] [444] [445], and randomly crosslinked cortical shells with a thickness around 100 - 190 nm beneath the plasma membrane [46] [48] [47]. This actin cortex attaches to the plasma membrane through various actin-membrane anchors, including the ezrin, radixin and moesin (ERM) proteins [446].

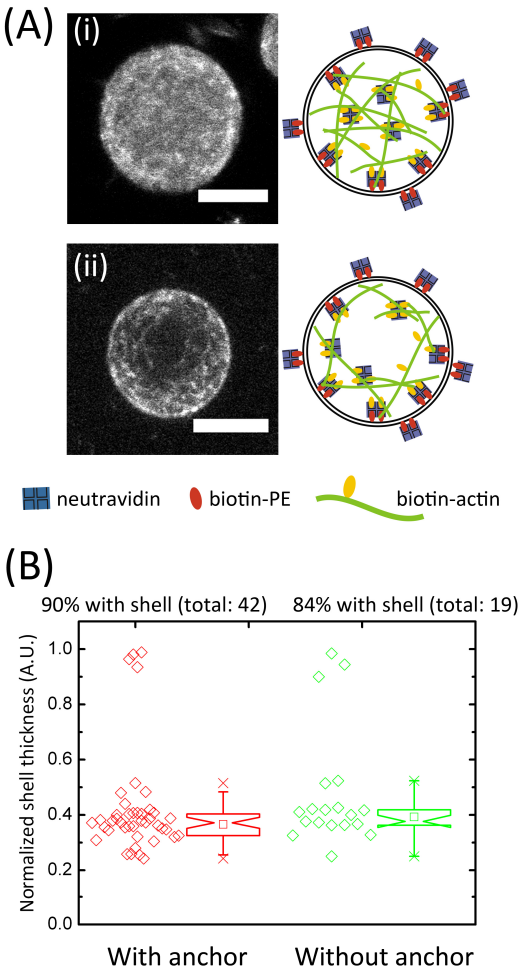

Figure 1. Characterization of actin networks inside liposomes. (A) Confocal fluorescence micrographs (*left*) and corresponding schematic diagrams (*right*) of liposomes filled with a bulk actin network (i) or having a cortical actin shell (ii). Actin-membrane anchors (biotin-neutravidin crosslinkers) are present in both cases, and the networks themselves are crosslinked. Scale bars: 5 μm. (B) Thickness of actin shell inside liposomes (normalized by liposome radius) in the presence (red symbols) and absence (green symbols) of actin-membrane anchors. We classify liposomes as having a bulk actin network when their normalized shell thickness is above 0.7. Box plots are computed only for the liposomes that exhibit a shell, i.e. with a normalized shell thickness below 0.7.

To reconstitute a crosslinked actin network in our cell-free model system, we introduce non-physiological biotin-neutravidin crosslinkers. By doping actin filaments with biotinylated actin at a molar ratio of 1:400 to actin, which results in about one biotinylated actin for every 1 μm of actin filament, crosslinked homogeneous networks are obtained in the presence of neutravidin (Supplementary Fig. 1, panel "*actin+Xlinker*"). To mimic the cellular cortex, we utilize neutravidin-decorated liposome membranes to anchor the crosslinked actin networks to the inner leaflet of the liposome membrane (Fig. 1A and 2A) (see Chapter 2 as well) [182] [219]. When confined in a cell-sized liposome, the crosslinked actin networks often spontaneously rearrange into a thick cortical shell underneath the liposome membrane (Fig. 1B). It has been argued that, even though this cortical configuration reduces the conformational entropy of the filaments, it minimizes the total free energy by reducing the enthalpic cost associated with filament bending [123] [127] [182] [203]. Notably, incorporation of actin-membrane anchors does not change the percentage of liposomes exhibiting a cortical shell (Fig. 1B). Furthermore, the thickness of the shell (around 1 - 2 μm, Fig. 2B), the liposome radius (Fig. 2C), and the actin encapsulation efficiency (Fig. 2D) are comparable for liposomes with and without actin-membrane anchors. However, it appears as if the homogeneity of encapsulation is slightly improved in the presence of the anchors (Fig. 2D).

Active actin-myosin networks inside liposomes

The cellular cortex is able to contract owing to non-muscle myosin II motors organized into bipolar filaments that exert pulling forces on the actin network. Actomyosin contraction builds up a cortical tension, which increases cell surface stiffening [421] and has been suggested to play a role in mitotic cell rounding [422] [423] [421] [447]. Gradients in contractility can cause global flows of the actomyosin cortex tangential to the plasma membrane, which contribute to cytokinesis and to various morphogenetic events in developing embryos [85] [86] [49] [448] [429] [449] [447]. To elucidate the role of myosin motors in contractility of the actin cortex, we introduce skeletal muscle myosin II into liposomes encapsulating actin networks. Under our experimental conditions, myosin II motors assemble into bipolar filaments with motor heads at each end. The myosin filaments have an average length of 0.69 μm, which corresponds to approximately 100 myosin motors [280]. This size is larger than that of myosin filaments in non-muscle cells, which typically consist of 10-30 motors [419]. However, skeletal muscle myosins are less processive than non-muscle myosins, and therefore need to operate in larger clusters [279] [450] [451].

Experiments on bulk (unconfined) actin-myosin networks have revealed that myosin filaments can only cause macroscopic network contraction if there is a certain minimal connectivity of the network to propagate the contractile forces

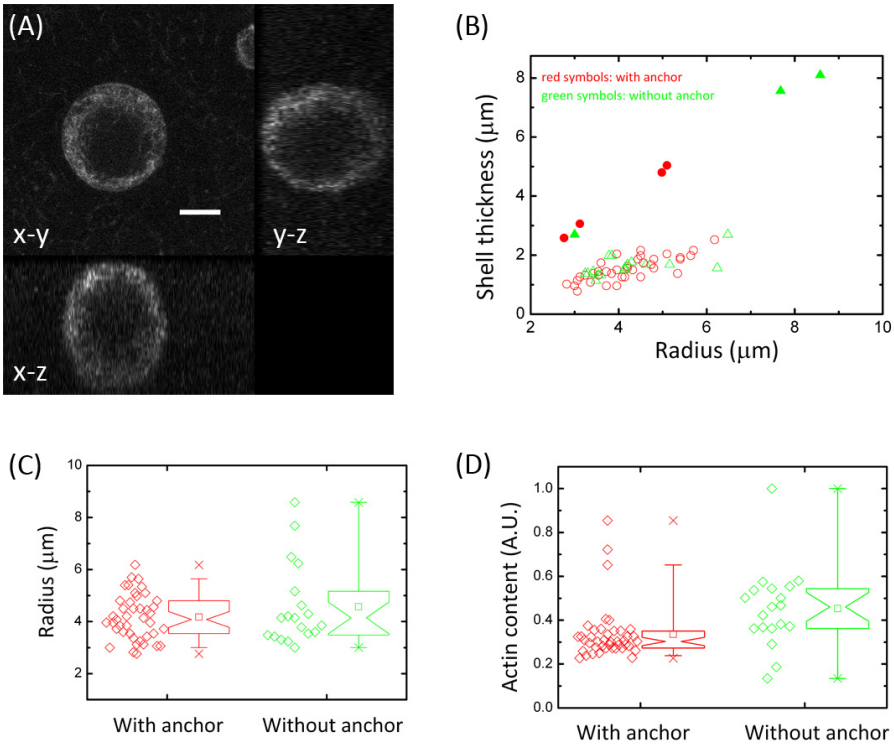

Figure 2. Characterization of the actin content of the liposomes. (A) 3-D views (in the form of three orthogonal confocal sections) of a liposome with an actin shell anchored to the inner leaflet of the membrane by biotin-neutravidin anchors. Note that the actin shell is rather homogeneous (the y-z and x-z slices are distorted due to optical effects). Scale bar: 5 μm. (B) Dependence of actin shell thickness on liposome radius. Empty symbols denote liposomes exhibiting actin shells, while solid symbols denote liposomes filled with a bulk actin network. (C) and (D) Notched box plots of liposome radius and actin content, respectively, in the presence or absence of actin-membrane anchors. Liposome population sizes: 42 (with anchor) and 19 (without anchor).

[281] [283] [434]. We confirm this finding here: in the presence of biotin-neutravidin crosslinkers, myosin motors form clusters (often termed foci) surrounded by compacted actin filaments (Supplementary Fig. 1, panel "*actin+myosin+Xlinkers*"). In contrast, when biotin-neutravidin crosslinkers are absent, we observe clusters of myosin filaments embedded in the filamentous actin solution with no sign of macroscopic contraction (Supplementary Fig. 1, panel "*actin+myosin*"). Similarly, inside liposomes, myosin filaments embedded in a bulk actin network (Fig. 3, *left*) or a cortical actin shell (*right*) cause no obvious

contraction in the absence of network crosslinkers. In striking contrast, the myosin filaments form a single dense focus that is surrounded by a compacted actin network in the presence of biotin-neutravidin crosslinkers (Fig. 4A). We note that typically only about 10% of a total of around 50 liposomes contain enough myosin to be detected by confocal microscopy. The myosin foci appear to be randomly positioned inside the liposomes (Fig. 4D). There is no obvious correlation between myosin foci position and liposome radius over the examined range of liposome radii of 4 – 16 μm (Fig. 4E).

In cells, the contractile actin-myosin cortex is anchored to the membrane through actin-membrane anchors. To mimic this anchoring in our cell-free system, we utilize liposomes with their membranes decorated by neutravidin. Strikingly, we observe that actin-membrane anchoring biases cortex contraction towards the membrane. Both in the presence of weak anchoring (1% biotinylated lipids and 5% PEGylated lipids) and strong anchoring (2% biotinylated lipids and 2.5% PEGylated lipids), we observe a single myosin focus located close to the membrane (Fig. 4B-D). Apparently, myosin-driven contraction is insufficiently strong to completely disrupt actin-membrane binding. We observe myosin foci close to the membrane even in large liposomes with a radius of 16 μm (Fig. 4E). Given that these liposomes are likely to exert at most a weak confinement effect and are therefore not expected to induce a cortical actomyosin arrangement, this observation further supports our conclusion that myosin contraction is not able to disrupt the actin-membrane anchoring.

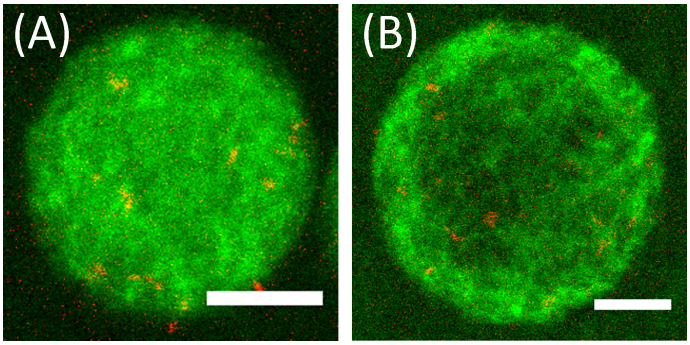

Figure 3. Confocal fluorescence micrographs of liposomes encapsulating actin-myosin networks in the absence of crosslinks between actin filaments. The actin network (green) is rather homogeneous in (A) and forms a cortical shell in (B). Myosin (red) is randomly dispersed in the liposomes in both cases. Scale bars: 5 μm.

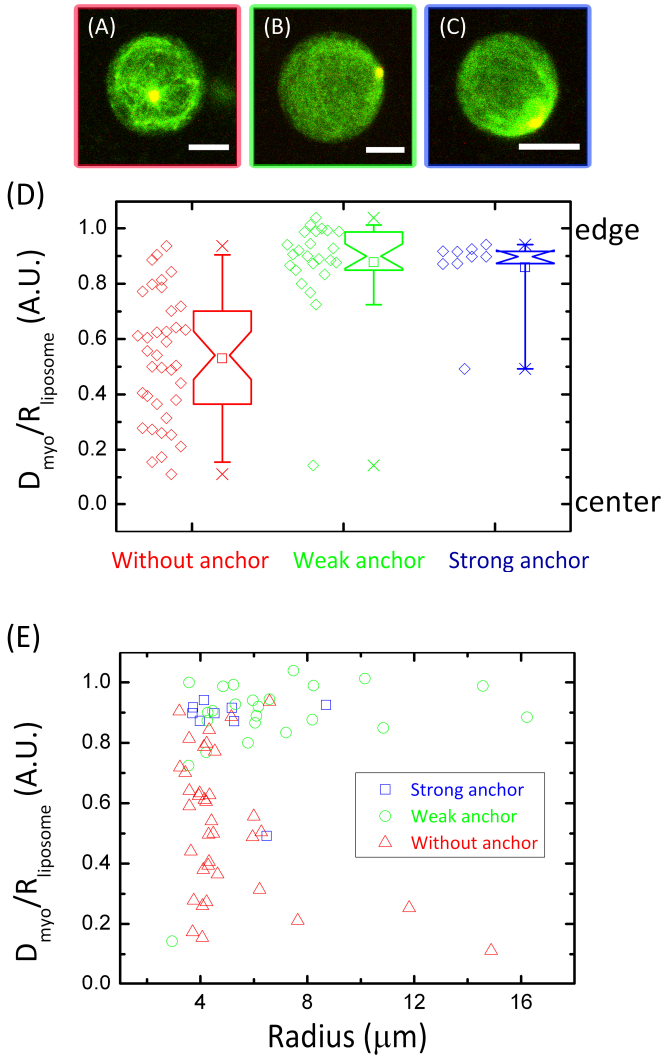

Figure 4. Effect of membrane anchoring on the positioning of myosin foci and directionality of active contraction. Images represent the steady-state situation observed after contraction. (A) - (C) Confocal fluorescence micrographs of actin (green) and myosin (red) inside liposomes in the absence (A) or presence (B: weak anchor, C: strong anchor) of actin-membrane anchors. Green: actin, red: myosin. Scale bars: 5 µm. (D) Distance of the myosin cluster from the center of the liposome (D_{myo}) normalized by the liposome radius, $R_{liposome}$, for liposomes with and without actin-membrane anchors. (E) Normalized myosin foci distance with respect to the corresponding liposome radius. Liposome population sizes: 37 (without anchor), 24 (weak anchor) and 9 (strong anchor).

The observations shown in Fig. 4 are made after at least 45 minutes incubation of the liposomes at room temperature. To assess the kinetics of myosin-driven cortex contraction, we trigger actin polymerization and myosin activity on the microscope stage by raising the sample temperature from 4°C to 20°C [452] [453] using a custom-built temperature control system (Supplementary Fig. 2). Confocal time-lapse imaging reveals that myosin contraction occurs within one minute (Fig. 5), making it very difficult to observe the contraction process in detail.

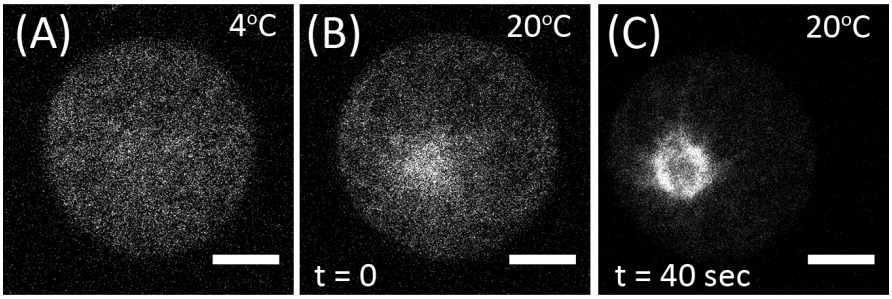

Figure 5. Kinetics of myosin-driven actin network contraction inside a liposome observed by confocal fluorescence microscopy. To permit immediate visualization of contraction upon myosin activation, we heat the sample on the microscope stage from 4 to 20°C using a dedicated temperature stage. At 4°C, actin is homogeneously distributed inside the liposome and not yet forming a clear network structure (A). Directly upon heating to 20°C, which takes about 30 seconds, signatures of network contraction are already visible (B). After 40 seconds at 20°C, the actin network has already contracted inwards, away from the membrane (C). Scale bars 5 μm.

Biotin-neutravidin crosslinkers assemble actin filaments into random networks having no preferred filament orientations. In this respect, these networks resemble networks formed by physiological actin binding proteins (ABPs) such as α-actinin [454] [455], fimbrin [456] and rigor-heavy meromyosin [457], though these ABPs form much more transient crosslinks than biotin-neutravidin. However, in cells there are also many unipolar arrangements of actin filaments created by small bundling ABPs such as fascin [331] and espin [458]. It remains an open question how the supramolecular actin architectures tune myosin contractility. In the absence of actin crosslinkers, myosin motors contract only filaments of opposite polarity [459]. However, several studies have revealed that myosin motors can contract not only isotropic, non-polar actin networks

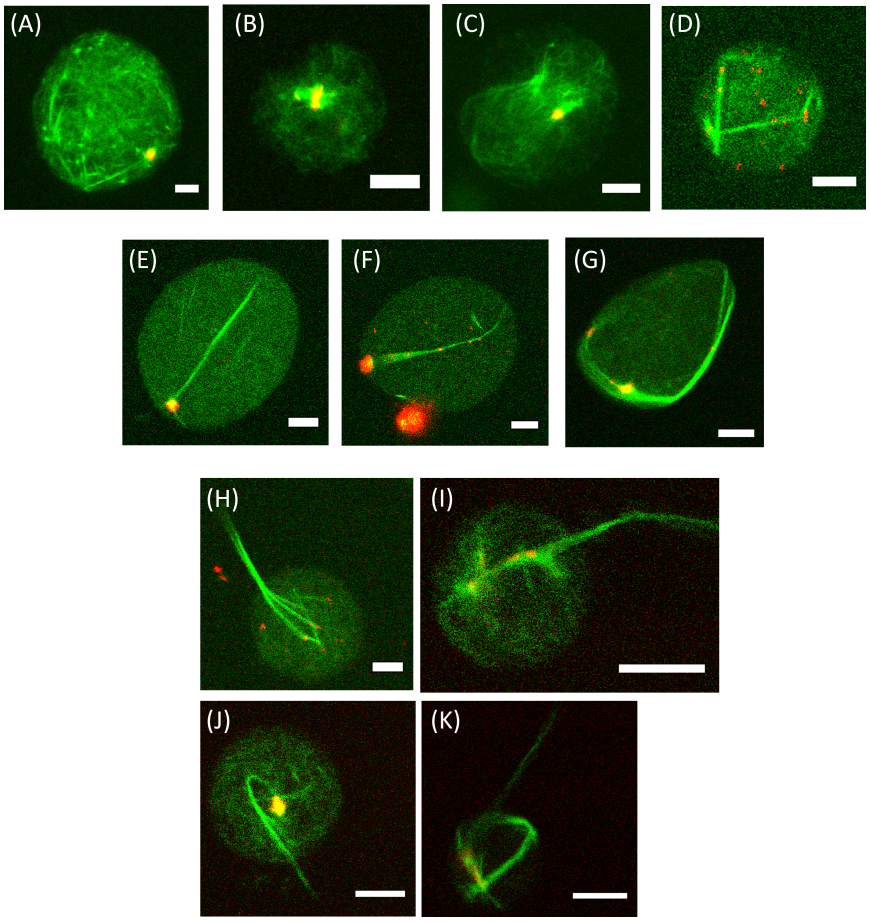

Figure 6. Confocal fluorescence micrographs of liposomes containing actin networks bundled by fascin in the presence of myosin bipolar filaments. Green: actin, red: myosin. Scale bars: 5μm.

assembled by biotin-streptavidin linkers [280], filamin [282] or cortexillin [434], but also networks of polar actin bundles assembled by fascin [283] [434].

To assess how actin network architecture influences myosin contraction inside liposomes, we introduce the physiological actin crosslinker, fascin. *In vivo*, fascin is prevalent in filopodia [329] [44]. Fascin assembles actin filaments into a network of needle-like bundles composed of parallel actin filaments (see Fig. 1 in Chapter 3) [330] [331]. Inside liposomes, in the absence of myosin filaments, fascin-mediated actin bundles deform liposomes into various shapes, ranging from liposomes with

protrusions that have a lollipop or ϕ-shape to non-protruded liposomes that are spherical, tube-like, lemon-shaped, or pear-shaped (see Fig. 2 in Chapter 3). Interestingly, in the presence of myosin filaments, we observe mostly non-protruded liposomes that are either spherical (50% of total 50 liposomes, Fig. 6A-D) or ellipsoid (28%, Fig. 6E-G). Sometimes, we observe liposomes with a single membrane protrusion enclosing bundles of actin filaments (22%, Fig. 6H-K).

In the spherical liposomes, around half of a total of 25 liposomes have myosin filaments form a single focus that is surrounded by a compacted actin network, which is a clear signature of myosin-driven contraction (Fig. 6A-C). The other half of the liposomes has multiple myosin foci (Fig. 6D). In some cases there is clear evidence of myosin-driven contraction (Fig. 6 B, C), but it is not always clear if any contraction has occurred (Fig. 6A). All in all, these actin network configurations are drastically different from the buckled bundles observed in spherical liposomes when myosin filaments are absent (see Fig. 2 in Chapter 3). In the ellipsoidal liposomes, single actin bundles are always decorated by myosin foci, either at one end of the bundles (Fig. 6E) or along the bundles (Fig. 6F, G). In these cases, the influence of myosin-driven contraction on the configuration of the actin networks is not as clear as in the case of the spherical liposomes (see Fig. 6B, C).

In the absence of myosin filaments, actin bundles organize into a ring-like structure inside the main body of a protruded liposome (see Fig. 4A in Chapter 3). Strikingly, when myosin filaments are present, we mainly observe straight (Fig. 6H-J) actin bundles decorated by a single (Fig. 6J) or multiple myosin foci (Fig. 6H, I). Only few liposomes (3 of the total 11 protrusive liposomes) have a ring-like actin bundle configuration inside their main body (Fig. 6K). Occasionally, we observe that actin filaments split at the base of actin bundles that enter the protrusive portion of the liposome (Fig. 6H). This observation is reminiscent of previous observations of actin bundle splitting by myosin II motors in gliding assays [337] and in bulk solution [460] [283], which have been taken to signify that myosin forces can cause forced fascin unbinding.

4.3 Discussions

Actin-membrane anchoring controls the directionality of actomyosin contraction

In animal cells, contractile forces applied by myosin motors play a key role in changing cell shape during vital cellular processes such as cell division and tissue morphogenesis [155]. In the past few years, several *in vitro* studies have addressed the question how myosin motors and crosslinking proteins together control actin network contraction in unconfined bulk solution [434] [283] [280] [282] [435] [281]. Recently, contractile networks have been reconstituted on 2-D surfaces, specifically supported lipid bilayers [173] [174] and an oil-water interface [179]. However, it remains poorly understood how confinement within the

plasma membrane combined with physical anchorage of the cortex to the membrane influence myosin-driven actin remodeling. Here, we reconstitute active actin-myosin networks inside cell-sized liposomes to mimic the geometry of a cell and reveal the role of actin-membrane anchors [219] [182]. We show that in the absence of myosin filaments, actin networks spontaneously form cortical shells underneath the liposome membrane to reduce their bending energy. When myosin filaments are present, they apply contractile forces that cause actin network reorganization. The myosin filaments gather into a single dense focus at a random position within the liposome. Strikingly, in the presence of actin-membrane anchors, myosin foci always locate close to the liposome membrane. Thus, our results reveal the impact of actin-membrane anchors on myosin focus positioning and consequently on the organization of actin networks (Fig. 7, *lower panel*).

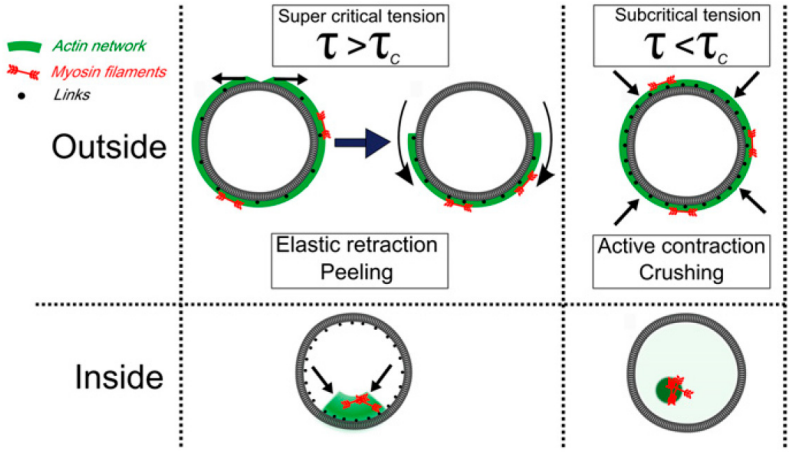

Figure 7. Summary of the outcome of myosin-driven contraction of actin-myosin cortices anchored to the outside (*upper panel*) or inside (*lower panel*) of a liposome membrane. (*Upper panel*) In the outside geometry, myosin filaments (red) build up a cortical tension, τ. When τ exceeds a critical level, τ_C, the cortex ruptures and elastically retracts, resulting in cortex peeling towards one side of the liposome. If the cortex is strongly anchored to the membrane or strongly crosslinked internally, the tension remains subcritical and the myosin contractile force actively compresses the liposome, resulting in liposome crushing. (*Lower panel*) In the inside geometry, myosin filaments contract the membrane anchored cortex towards the membrane, whereas they contract and consequently detach the cortex from the membrane if the cortex is not anchored to the membrane.

Interestingly, after myosin-driven contraction, not all of the actin is gathered towards the myosin foci. Instead, we observe that a portion of the actin network either remains close to the membrane (see Fig. 4A, C) or distributed throughout the entire liposome (see Fig. 4B). These observations likely reflect that the amount of encapsulated myosin filaments (~3000 myosin filaments in a liposome having a radius of 10 μm, given a 50% encapsulation efficiency [219] and 100 myosin motors per filament [280]), is not enough to pull the whole actin network towards the foci. In bulk solution, by coalescing of multiple myosin foci, the foci can reach sizes up to 15 μm at high myosin concentrations [280], which is close to, or even larger than, the diameter of the liposomes. We suspect that the limited amount of available myosin filaments in the liposomes results in the formation of smaller foci. It is also possible that during myosin contraction, rupturing of the actin network decreases the connectivity of the network, resulting in smaller foci [174] [283].

Relevance to biological systems

Several studies performed in live cells or with cell extracts have revealed an influence of actin-membrane anchors on contractile actin networks. By encapsulating *Xenopus* meiotic extracts in water-in-oil emulsion droplets, it was shown that actin-surface anchors direct myosin-driven actin flows [433]. In the absence of actin-surface anchors, actin flow was mainly directed radially inward, reminiscent of our observation of randomly positioned myosin foci in liposomes in the absence of actin-membrane anchors. In starfish oocytes, it was shown that a contractile actin network transports chromosomes to one side of the oocyte [461] [462]. When the actin network is not anchored to the cell cortex, chromosomes are transported to the center of the oocyte with no preferred direction. In contrast, when the actin network is anchored to the cell cortex, a directional transport of chromosomes towards the anchoring point occurs [461]. These observations are reminiscent of our observation of myosin foci that are always close to the membrane when actin-membrane anchors are present. We note that it remains unclear if myosin II motors are responsible for chromosome congression [462]. In meiotic mouse oocytes, it was shown that myosin-II motor driven contraction of the actin network, which is connected to the cell cortex, directionally relocates the spindle [463] [430] [464] [465]. Recent evidence suggests that cell junction coupling plays a key role in controlling the direction of myosin-driven actin flows during epithelial morphogenesis. Uncoupling of the anchors between cell junctions and the actin-myosin cortex in developing fly embryos results in a random direction of the flows [429]. Thus, although our system based on liposomes encapsulating purified proteins lacks biochemical regulators, it does possess an inherent capacity for mimicking certain cellular events.

In cells, myosin contractility helps control cell shape by generating cortical tension [49] [85] [424] [86]. Contractility gradients can result in either a tangential cortical flow in the plane of the membrane or a force normal to the membrane that drives cell deformation [49] [449]. In our model system, we do not observe obvious membrane shape changes induced by myosin contraction. Instead, we observe that actin is partly peeled or torn away from the membrane. These observations most likely reflect dragging of lipid-neutravidin anchors in the plane of the membrane [286]. Alternatively, pulling the lipids out of the membrane may contribute to cortex detachment, given that biotin-streptavidin bonds are stronger than lipid-membrane bonds [287]. Besides, rupturing of actin filaments may occur, which would prevent transmission of the myosin contractile force to the membrane [174]. Also, neutravidin decoration is known to rigidify lipid bilayer membranes about 10-fold [345], increasing the resistance of the membrane to shape change given that the required energy to deform a membrane is proportional to its bending modulus [258].

In cells, a local increase of cortical tension can disrupt actin-membrane interactions by either weakening/rupturing cortex-membrane attachment or rupturing the cortex itself [466] [467]. This local disruption, combined with the presence of an intracellular hydrostatic pressure that drives cytoplasmic fluid to the weak spot, can induce the formation of spherical membrane protrusions known as blebs [76] [289] [77]. We observe no bleb formation in our model system, possibly due to insufficient intracellular pressure or too strong actin-membrane anchoring by the nearly permanent biotin-neutravidin bonds.

Anchoring an active actin cortex on the outer leaflet of liposome membranes

To facilitate membrane deformation by the contractile actin cortex, cells restrict myosin contractile forces within a thin cortex with a thickness of only 100 - 190 nm [46] [48] [47]. In contrast, inside our model liposomes, the cortical actin shell has a thickness of around 1 - 2 μm. Thus, myosin contractile force may dissipate within the thick actin networks and be inefficiently transmitted to the membrane. Interestingly, by anchoring actin-myosin networks to the outer leaflet of liposome membranes to form a thinner (0.2 - 0.5 μm) cortex (Fig. 8A, B), our collaborators Kévin Carvalho and Cécile Sykes observed that myosin motors are able to crush liposomes [182]. It was shown that myosin motors generate cortical tension, which, if it exceeds a critical level, causes cortex rupture followed by an elastic retraction of the cortex toward one side of the liposome (Fig. 8C, a2 and b2, and Fig. 7, *upper panel*). However, when the cortex is strongly anchored to the membrane or strongly crosslinked (by adjusting the number of actin-membrane anchors or of the crosslinkers, respectively), the cortical tension remains subcritical. In this case, the force applied by myosin filaments compresses the

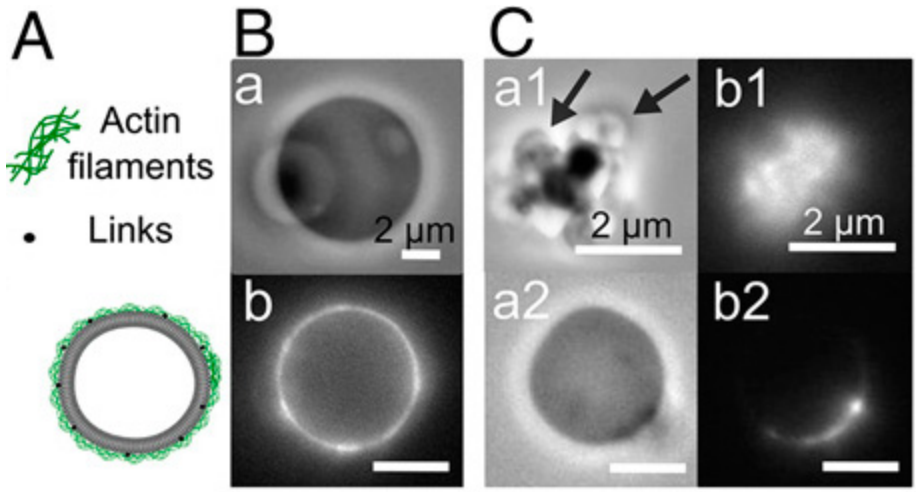

Figure 8. (A) Schematic drawing of a liposome having actin filaments anchored to the outer leaflet of the membrane by actin-membrane linkers. (B, C) Phase contrast images (a, a1 and a2) and actin fluorescence images (b, b1 and b2) of liposomes containing actin-membrane linkers. In the absence of myosin (panel B), actin forms a homogeneous shell on the outer leaflet of the liposome membrane. In the presence of myosin (panel C), the cortices are contracted. In panels a1 and b1, myosin contraction crushes the liposome, which results in the appearance of bulges (see arrows). In panels a2 and b2, the contractile force applied by myosin filaments peels the actin cortex towards one side of the liposome. Scale bars are 2 μm in the top panels and 5 μm in the bottom panels.

liposome, resulting in liposome crushing (Fig. 8C, a1 and b1 and Fig. 7, *upper panel*) [182].

Myosin motors inhibit shape change of liposomes encapsulating actin-fascin bundles

Intriguingly, we find that myosin motors have a marked influence on liposome deformation by actin-fascin bundles. Whereas in the absence of myosin, actin-fascin bundles cause protrusion formation in a large percentage of liposomes, in the presence of myosin, liposomes stay mostly spherical or ellipsoidal. To deform a liposome membrane, actin bundles have to apply forces perpendicular to the membrane. Given that myosin II motors apply contractile rather than extensile forces to actin networks [434] [283] [280] [282] [435] [281], it is possible that myosin contraction “pulls” actin bundles away from the membrane, inhibiting liposome deformation. Alternatively, myosin contractile forces may disassemble the actin bundles by causing forced fascin unbinding, consequently preventing liposome deformation. Indeed, we occasionally observe that actin filaments split

at the base of actin bundles that enter protrusions (see Fig. 6H). Disassembly of actin bundles by myosin II motors has previously been observed in case of bundles immobilized on a substrate [337] and also in bulk solution [460] [283]. Also, myosin has been shown to cause rupture of individual actin filaments within contractile networks upon a supported lipid bilayer [174] [173]. *In vivo*, myosin II has been demonstrated to cause disassembly of actin networks in crawling keratocytes [468]. It has been suggested that myosin-II driven contractility also severs actin bundles in filopodia of neuronal growth cones near their minus ends, which are located in the transition zone between the lamellipodium and the central domain of the growth cone [469]. This suggestion was based on the observation that an elongation of filopodia enclosing actin bundles was observed upon inhibition of myosin II activity. Taken together, our finding reveals the potential ability of myosin motors to disassemble actin-fascin bundles inside liposomes. However, a more detailed time-lapse imaging of the process of bundle (dis)assembly will be needed to draw firm conclusions.

Towards time-lapse observations of the process of myosin contraction

To understand the mechanism of how myosin filaments reorganize actin networks inside liposomes, it will be crucial to observe the kinetics of myosin contraction. However, some practical issues in the current experimental system hamper such measurements. Here we discuss these issues and give suggestions for improvements.

(1) Triggering myosin contraction on the microscope. To facilitate the kinetic observation of myosin contraction, it would be helpful to trigger myosin activity on the microscope. Although we are able to trigger myosin activity by raising the temperature of the sample, this does not allow us to trigger myosin activity selectively in a single liposome. Given that we usually obtain only 10% out of a total of 50 liposomes with a detectable myosin fluorescence signal, together with the fact that we need to observe liposomes by a 100x objective to have sufficient spatial resolution, it is not optimal to trigger myosin contraction in all liposomes simultaneously. Furthermore, when raising the temperature from 4^{o}C to 20^{o}C, the condensation of water on the observation glass chamber interferes with the imaging. This requires a manual readjustment of the focus of the objective during image recording. To overcome these issues, it would be interesting to trigger myosin activity in a selected liposome by supplying ATP through a well-controlled caged-ATP system by using stepwise UV-pulse sequences of varying intensity [470]. Alternatively, one could introduce myosin filaments into liposomes by microinjection [383] [384] [385] or by fusion with a second liposome containing myosin filaments [228].

(2) Observing myosin contraction at a high temporal resolution. Given that myosin contraction takes place within a minute inside the liposomes, it is essential to perform image recording at a higher temporal resolution to obtain more detailed information on the contraction process, using a minimum of 10-30 frames per second. However, when obtaining fluorescence images, photobleaching of fluorescent dyes is unavoidable, especially when recording at a high frame rate for a long period of time. To overcome this issue, one can encapsulate inert microspheres inside the liposomes as tracers for indirectly detecting the movement of the myosin filaments as well as the reorganization of the actin network by bright field or phase contrast microscopy [471] [472].

(3) Immobilizing liposomes. Although the temperature control chamber enables us to observe myosin-driven contraction, the fact that the liposomes are suspended impedes the possibility to record 3-D time-lapse images to extract the movement of the foci. Thus, it is essential to immobilize liposomes during image recording. To achieve this goal, there are many well developed methods including holding a liposome by using a micropipette, anchoring it to a substrate or a supported lipid bilayer via poly-l-lysine, polyethylenimine [473] [474] or biotin-streptavidin linkages [475], or embedding it inside a hydrogel [476].

(4) Improving myosin encapsulation efficiency. Although the yield of actin-containing liposomes is reasonable (around 50 liposomes in each experimental trial), the yield of myosin-containing liposomes is rather low (~10%). Thus, it will be interesting to test whether alternative encapsulation methods based on water-in-oil emulsions [203] [206] or inkjet printing [227] can improve the encapsulation efficiency.

4.4 Conclusion

During cell shape changes, the actin cortex is not merely a passive, adaptive structure, but it actively participates in plasma membrane deformation in a wide range of cellular phenomena, including cell migration and cytokinesis. Active forces generated by the actin-myosin cortex are transmitted to the plasma membrane and to the extracellular matrix through actin-membrane anchors. This force transmission enables cells to change shape and also to actively sense and respond to the extracellular environment during cell morphogenesis. Here, we use a minimal cell-free model system based on liposomes containing active actin-myosin networks to elucidate how myosin-driven contractile forces and actin-membrane anchors combine to control actin network remodeling. We show that when the actin networks are crosslinked, myosin motors form a single focus surrounded by a compacted actin network. We furthermore find that actin-

membrane anchoring controls the directionality of actin-myosin contraction. When the anchors are present, myosin motors contract towards the liposome membrane, while in the absence of the anchors, myosin motors contract away from the membrane. Also, we find that myosin-driven contractile forces are able to reorganize polar fascin-actin bundles and prevent deformation of the liposomes by these bundles. It is possible that the myosin motors disassemble the bundles, which would be reminiscent of the severing of actin bundles in filopodia of neuronal growth cones. However, more detailed time-lapse imaging of the process of bundle formation will be needed to draw firm conclusions. Given that in cells actin-membrane adhesion is spatiotemporally modulated to allow cell shape changes while maintaining cortical integrity, it would be interesting to study in the future how physiological actin-membrane anchors such as the ERM proteins or septins (see Chapter 5) combined with their membrane binding partner, the phosphatidylinositol lipids, influence myosin-driven contractility and liposome shape change.

4.5 Supplementary Figures

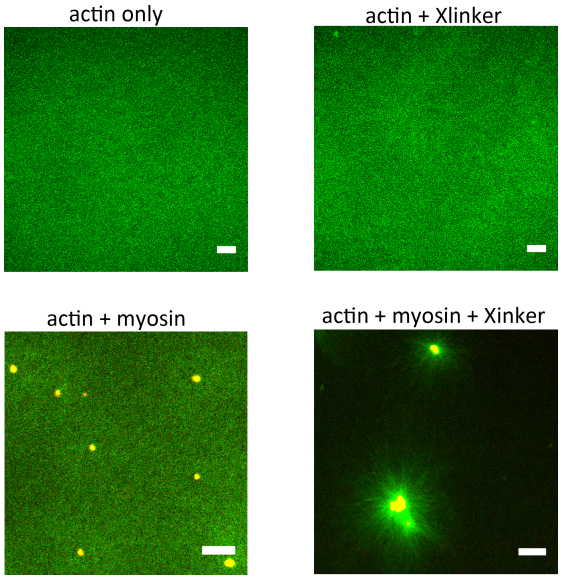

Supplementary Figure 1. Confocal fluorescence micrographs of a solution of 1 mg/mL actin filaments (*actin only*), a cross-linked actin network (*actin + Xlinker*), a solution of actin filaments in the presence of myosin filaments (*actin + myosin*), and a cross-linked actin network in the presence of myosin filaments (*actin + myosin + Xlinker*). Actin is shown in green and myosin in red. Scale bars: 10 μm

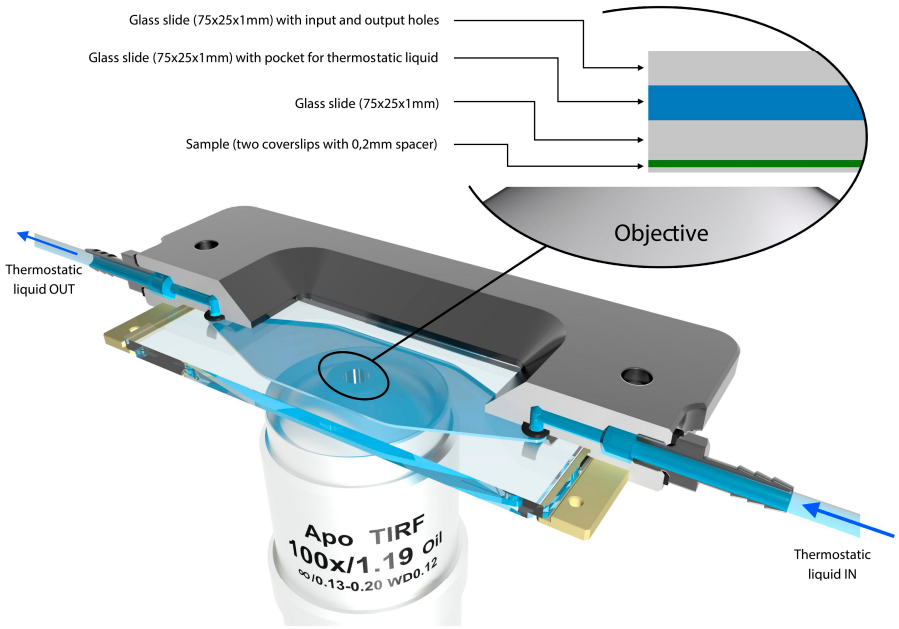

Supplementary Figure 2. Schematic representation of the custom-made temperature control system, which is designed by Henk-Jan Boluijt and manufactured in the workshop of the FOM institute AMOLF.

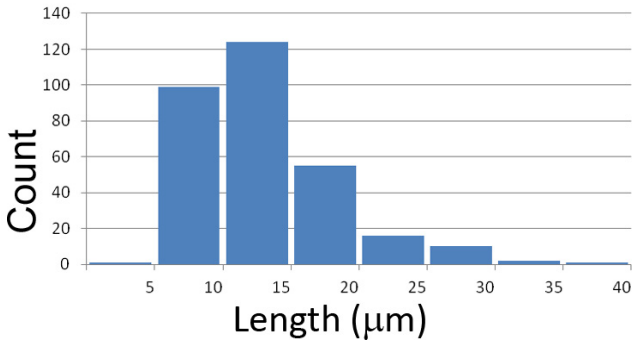

Supplementary Figure 3. Length distribution of actin filaments polymerized in bulk solution measured by total internal reflection fluorescence (TIRF) microscopy. Actin filaments are obtained by polymerizing actin at 1.5 μM (including 5 mole% AlexaFluor 488 labeled actin) with phalloidin (1:1 molar ratio to actin) to stabilize the filaments and further diluting to 10 nM for TIRF imaging. The average length is 13 ± 5 μm. Total number of analyzed filaments is 307.

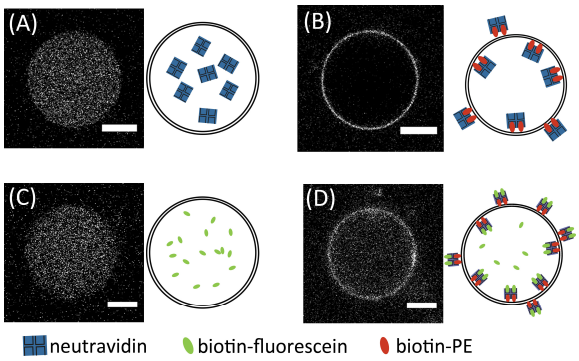

Supplementary Figure 4. Confocal fluorescence micrographs of liposomes obtained by the agarose-precursor swelling method. To assess the specificity of neutravidin binding to biotinylated lipids, neutravidin labeled with AlexaFluor 350 was incorporated into the inverse phase precursor micelles either in the absence (A) or presence (B) of biotinylated lipids. To verify that neutravidin is still functionally active after the inverse phase precursor procedure, biotin-fluorescein was encapsulated in the liposomes in the absence (C) or presence (D) of neutravidin on the membrane. Concentrations of biotin-fluorescein are 50 nM and 500 nM for liposomes in (C) and (D), respectively. The schematic diagrams explain the corresponding experimental conditions. Scale bars: 5 μm.

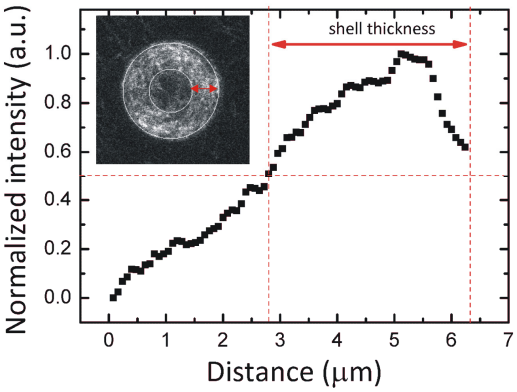

Supplementary Figure 5. Normalized actin intensity as a function of radial distance going from the center (at zero) to the edge of a liposome. Actin shell thickness is defined as the radial distance from the liposome edge to a position where the normalized intensity is greater than 0.5. The inset image shows an example liposome in which the shell thickness is indicated by the red arrow; the outer and inner circles show the inner edge of the shell and the liposome edge, respectively.

4.6 Materials

Chemicals were purchased from Sigma Aldrich (St. Louis, MO, USA) unless specified otherwise. Lipids were purchased from Avanti Polar Lipids (Alabaster, AL, USA) unless specified otherwise. Liposomes were based on 1,2-dioleoyl-sn-glycero-3-phosphocholine (DOPC), which has a melting temperature of -20^{o}C. To prevent liposome aggregation and nonspecific protein adhesion, we added 1,2-dipalmitoyl-sn-glycero-3-phosphoethanolamine-N-[methoxy(polyethylene glycol)-2000] (PEG-PE with a 2 kDa polyethylene glycol tail). For fluorescence imaging, we used 1,2-dioleoyl-sn-glycero-3-phosphoethanolamine-N-(lissamine rhodamine B sulfonyl) (rhodamine-PE) or fluorescently labeled Marina blue 1,2-Dihexadecanoyl-*sn*-Glycero-3-Phosphoethanolamine (Marina blue-PE) and Pacific Blue 1,2-ditetradecanoyl-sn-glycero-3-phosphoethanolamine (Pacific blue-PE). The N-((6-(Biotinoyl)amino)hexanoyl)-1,2-Dihexadecanoyl-sn-Glycero-3-Phosphoethanolamine (Biotin-x-PE), Marina blue-PE and Pacific blue-PE lipids were purchased from Invitrogen (Breda, The Netherlands). For specific coupling of actin filaments, we used the biotinylated lipid 1,2-dipalmitoyl-sn-glycero-3-phosphoethanolamine-N-(cap biotinyl) (biotin-PE). ATP was prepared as a 100 mM MgATP stock solution using equimolar amounts of Na_2ATP and $MgCl_2$ in 10 mM imidazole-HCl buffer, pH 7.4. Neutravidin and AlexaFluor 350 labeled neutravidin were purchased from Invitrogen (Breda, The Netherlands).

Rabbit skeletal muscle monomeric (G-) actin and myosin II motors were purchased from Cytoskeleton (Tebu Bio, Heerhugowaard, The Netherlands) or purified by standard procedures including a gel filtration on a Sephacryl S-200 26/60 high-resolution column (GE Healthcare, Munich, Germany) to remove residual capping proteins, cross-linkers, and actin oligomers [295] [296]. Fluorescent actin with a dye/protein molar ratio of 0.6 was prepared by labeling amine groups with AlexaFluor 488 carboxylic acid succinimidyl ester [410]. Fluorescent myosin with a dye/protein ratio of 1.7 was prepared by labeling amine groups with DyLight 594 NHS Ester [297]. G-actin was stored in G-buffer (2 mM Tris-HCl, 0.2 mM Na_2ATP, 0.2 mM $CaCl_2$, 1 mM dithiothreitol (DTT), pH 7.8) at 0^{o}C for up to 1 week or at -80^{o}C for long-term storage. Before use, frozen aliquots were always quickly thawed and 4 mM DTT was added to reduce any oxidized sulfhydryl groups [411] [412]. The G-actin solution was centrifuged at 120,000g for 30 min to remove aggregated proteins, followed by sonication for 5 min to disrupt actin dimers [413]. Myosin II was stored at -20^{o}C in a high salt buffer with glycerol (0.6 M KCl, 25 mM KH_2PO_4, 10 mM EDTA, 1 mM DTT, pH 6.5, 50% w/w glycerol). Fresh myosin solutions were prepared daily by dialysis against a buffer containing 300 mM KCl, 4 mM $MgCl_2$, 1 mM DTT, 25 mM imidazole, pH 7.4. Recombinant mouse fascin was prepared from T7 pGEX *E. coli* as described in [410], with the only difference that gel filtration was performed on a high-

resolution Superdex 200 column (GE Healthcare, Munich, Germany). Fascin was stored at -80°C in 50 mM Tris-HCl pH 7.5, 150 mM KCl, 5 mM DTT, 10% (v/v) glycerol. Before use, fascin stock solutions were clarified by centrifuging at 120,000g for 5 min and used within a week. Protein concentrations were determined by optical absorption measurements at a wavelength of 280 nm, using extinction coefficients of 66300 $M^{-1} \cdot cm^{-1}$ for fascin [414], 46218 $M^{-1} \cdot cm^{-1}$ for G-actin [295], and 248826 $M^{-1} \cdot cm^{-1}$ for myosin [296]. G-actin with biotin-label was purchased from Cytoskeleton (Tebu Bio, Heerhugowaard, The Netherlands).

4.7 Methods

Reconstitution of actin networks and actin-myosin networks inside liposomes

G-actin was polymerized in the I-buffer (25 mM imidazole-HCl (pH 7.4), 1 mM DTT, 0.1 mM MgATP, 50 mM KCl, 2 mM $MgCl_2$, 280 mM sucrose, 0.5% (v/v) glycerol, 2 mM trolox, 2 mM protocatechuic acid and 0.1 μM protocatechuate 3,4-dioxygenase). When myosin motors are present in the I-buffer, an enzymatic system was included to regenerate ATP, composed of 1.33 mM creatine phosphate and 766 unit/mL creatine phosphokinase. We note that for the I-buffer containing fascin, the concentration of KCl is 66 or 55 mM due to the salt contributed from the fascin storage solution. Actin concentration is 23.8 μM, including 20 or 30 mole% of AlexaFluor 488 labeled actin and if present, 0.25 % mole of biotinylated actin. If present, we use 120 nM of neutravidin and either 238 nM or 476 nM myosin, including 10 mole% fluorescently labeled myosin (the results were similar for both myosin concentrations). The average length of the actin filaments is 13 μm, as measured by the total internal reflection fluorescence microscopy (Supplementary Fig. 3).

Agarose precursor swelling method

Liposomes were prepared using a hybrid procedure that combines an agarose hydrogel swelling method [219] (see Chapter 2) and an inverse phase precursor method [252]. The agarose film was prepared by spin-coating a 1% (w/w) agarose solution in water (300 μl; Type IX-A ultralow gelling point, $T_g \leq 17°C$) on a 24 x 24 mm microscope coverslip at 1200 rpm (DELTA 10BM, SUSS MicroTec) for 30 sec, followed by drying at 37°C for 30 min. Membranes were composed of DOPC and always doped with 2.5 or 5 mole% PEG-PE to prevent non-specific protein adhesion. For the actin shell characterization, the "*without anchor*" condition corresponds to 0 mole% biotin-PE and 2.5 mole% PEG-PE, and the "*with anchor*" condition corresponds to 2 mole% biotin-PE and 2.5 mole% PEG-PE. For the examination of myosin foci, the lipid compositions were 0 mole% biotin-PE and 5 mole% PEG-PE for the "*without anchor*" condition, 1 mole% biotin-PE and 5

mole% PEG-PE for the "*weak anchor*" condition, and 2 mole% biotin-PE and 2.5 mole% PEG-PE for the "*strong anchor*" condition. Membranes were sometimes doped with either 0.2 mole% rhodamine-PE, for fluorescence imaging in the absence of myosin, or 0.2 mole% Pacific blue-PE or Marina blue-PE, for imaging in the presence of myosin. Lipids were dissolved in 95:5 (v/v) chloroform/methanol at 3.75 mg/mL. An inverted phase of water droplets in the lipid solution was formed by adding 3.5 μl (for lipid mixtures containing 2 mole% biotin-PE) or 1.6 μl (for lipid mixtures containing 1 mole% biotin-PE) of a neutravidin solution (48 mg/mL in PBS) or just PBS to 60 μl of the lipid mixture. The mixture was pipetted up and down until opalescence, indicating that inverted micelle precursors had formed. The micelles (40 μl) were spin-coated at 100 rpm for 100 sec on agarose slides and dried under vacuum for 100 min at room temperature. An open-top formation chamber was assembled by placing a 0.12 mm thick spacer (secure-seal spacer, Invitrogen) on the lipid-coated slide. A volume of 40 μl inner buffer (I-buffer) containing actin and myosin proteins was pipetted on top of the formation chamber and incubated for 90 min at 4°C to form liposomes. Liposomes were collected (and diluted) by pipetting 65 μl of O-buffer (glucose solution) into the formation chamber and tilting the slide to flow the liposomes into an open-top observation chamber assembled from a glass slide with a 0.5 mm thick spacer (Coverwell, 13 mm in diameter, Invitrogen). We repeated this process 2 times. The actin remaining outside the liposomes was diluted at least 2.6-fold. Finally, the observation chamber was closed by a glass coverslip to avoid evaporation. Glass slides were passivated by 2 mg/mL casein before use. The O-buffer osmolarity was adjusted be 15 mOsmol higher than the I-buffer osmolarity to prevent liposome rupture (Osmomat 030, Gonotec GmbH). Actin polymerization was initiated by bringing the observation chamber to room temperature. We observed liposomes after at least 45 min incubation at room temperature, to ensure complete actin polymerization. We confirmed the functionality of neutravidin by two observations: (i) fluorescent neutravidin localizes to the membrane only when biotinylated lipids are present (compare Supplementary Fig. 4A, B) and (ii) fluorescent biotin only binds to the inner leaflet of the membrane when neutravidin is bound to the membrane (compare Supplementary Fig. 4C, D).

Agarose swelling method

Liposomes encapsulating actin, fascin (1.2 μM) and myosin (238 nM) were obtained by using the agarose swelling method (without inverse phase precursor micelles) as described in Chapter 2. Membranes were composed of DOPC and 5 mole% PEG-PE. For some samples, 2 mole% biotin-x-PE was included. Membranes were sometimes doped with 0.2 mole% Pacific blue-PE or Marina blue-PE for fluorescence imaging.

Confocal fluorescence microscopy and phase contrast microscopy

Confocal fluorescence images and phase contrast images were taken on a Nikon Eclipse Ti inverted microscope equipped with a Nikon C1 confocal scanhead using a 100x/NA1.4 Plan Apo objective. Images were captured using NIS Elements software (Nikon, version 4). AlexaFluor 350, Pacific blue-PE and Marina blue-PE were excited using a laser with a wavelength of 408 nm. AlexaFluor 488 was excited using a laser with a wavelength of 488 nm. Rhodamine and DyLight 594 were excited using a laser with a wavelength of 543 nm.

Image analysis

The actin shell thickness of a liposome was determined by integrating the fluorescence intensity around concentric circles and repeating this for radial distances from the liposome center to the liposome edge. By normalizing all values by the corresponding circumference (in pixels), we obtained a profile of integrated intensities along the liposome radius. To compare the integrated intensities of a liposome, we normalized integrated intensities by subtracting the minimum integrated intensity and then dividing by the difference between the maximum and minimum integrated intensities. The actin shell thickness is defined as the distance between the liposome edge and the radial position from the center of the liposome where the normalized integrated intensity is greater than 0.5 (Supplementary Fig. 5). The shell thickness is finally divided by the liposome radius to obtain a normalized shell thickness. For a homogeneously filled liposome we expect a normalized shell thickness of 1. Since thick actin shells are in practice difficult to distinguish from homogeneous networks, we classify liposomes with a normalized shell thickness above 0.7 as “bulk” and liposomes with normalized shell thicknesses below 0.7 as exhibiting a cortical actin shell.

The average actin intensity was obtained by summing fluorescence intensities of all pixels inside the liposome and dividing the sum by the total number of pixels. To compare encapsulation efficiencies for a population of liposomes examined under identical illumination conditions, we normalize the average intensity for each liposome by the maximum value of the distribution. We excluded liposomes from the analyses which contained lipid structures such as tubes, lipid aggregates, or small liposomes (typically present in around 50% of all liposomes).

To quantify the position of myosin foci after active cortex contraction, we used confocal fluorescence z-stacks of the actin and myosin signals inside the liposomes. To determine the 3D-contour of the liposomes, we fitted the actin signal in each plane of the z-stack to an ellipse. The resulting stack of ellipses was then fitted to an ellipsoid and its center position and radius were determined. We then manually located the position of the myosin cluster and measured its distance from the center of the ellipsoid (D_{myo}). Finally, we calculated the relative

distance of the myosin cluster normalized by the radius of the liposome as $D_{myo}/R_{liposome}$.

Statistics

All notched boxes show mean value (small squares), maximum and minimum values (crosses), and the 5th and 95th (with whiskers) and 25th and 75th percentile. The notches that extend to $\pm 1.58 \times IQR/\sqrt{N}$ (*IQR* is the interquartile range and *N* is the sample size) represent the 95% confidence level of the median value [417].

4.8 Acknowledgements

Part of this work was performed in collaboration with Kévin Carvalho and Cécile Sykes (Institut Curie, Paris). We benefited from insightful discussions with Nils Becker (University of Heidelberg) and Björn Stuhrmann (AMOLF, Amsterdam). We thank Henk-Jan Boluijt (AMOLF, Amsterdam) for designing the temperature control chamber for observing myosin contraction. We thank Sophie Roth (AMOLF, Amsterdam) for writing image analysis software for 3D detection of myosin cluster positions in liposomes. We further thank Omar Mertins and Carlos Marques (Institut Charles Sadron, Strasbourg) for advice on the inverse phase precursor technique.

CHAPTER 5. Septin assembly: a comparative study of fly, human and budding yeast septins

Septins are guanine nucleotide binding proteins that are conserved from fungi to humans. Septins have important roles in various cellular functions, in which they assemble into hetero-oligomeric complexes and higher order structures such as filaments, rings, or gauzes. The mechanisms by which septin assembly is regulated remain elusive. Also, it is unclear whether higher-order structures of septins from different kingdoms share a common organization at the molecular level. Here, we purified recombinant fly, human and budding yeast septins from Escherichia coli, and study the process of septin assembly in different assembly conditions by combining electron microscopy with time-lapse fluorescence microscopy. We show that fly septins as well as their human counterparts assemble into rod-like hexamers containing three septins, each of which is present in two copies, and budding yeast septins assemble into rod-like octamers containing four septins, each of which is present in two copies. We further show that in the same assembly conditions, fly and human assemble into bundles composed of aligned filaments, whereas budding yeast septins form paired filaments. By assessing a broad range of septin concentrations, we estimate the critical concentration for septin filament formation. We do not observe any formation of septin rings or spirals, in contrast to previous findings for bacteria-derived budding yeast septins and insect cell-derived human septins. It will be important to test whether factors such as posttranslational modifications or the presence of septin binding partners such as PIP_2 lipids can promote the formation of these alternative, highly curved structures.

The contents of this chapter are based on:
Mavrakis, M., Azou-Gros, Y., **Tsai, F.-C.***, Alvarado, J.*, Bertin, A.*, Iv, F., Kress, A., Brasselet, S., Koenderink, G. H. and Lecuit, T. (Manuscript under review)
Septins promote F-actin ring formation by cross-linking actin filaments into curved bundles. *authors contributed equally

Alvarado, J.*, **Tsai, F.-C.***, Bertin, A., Iv, F., Lecuit, T., Koenderink, G. H. and Mavrakis, M. (Manuscript in preparation)
Mechanistic insights into actin filament bending and bundling by septins. *authors contributed equally

5.1 Introduction

Septins are guanine nucleotide (GTP)-binding proteins that are conserved from fungi to man [477]. They were first discovered in the budding yeast *Saccharomyces cerevisiae*, where they localize to the bud neck and are crucial for cell division [478] [479]. Since then, it has been demonstrated that septins are responsible for a vast number of cellular functions [96]. In budding yeast as well as in mammalian cells, septins form rings that act as scaffolds to recruit proteins to the division site that are important for cytokinesis and to promote their functional interactions [97] [98] [99] [100] [101] [102]. There is also evidence that septin rings function as diffusion barriers in budding yeast cells and dividing mammalian cells by tight association with the plasma membrane, controlling the exchange of molecules between the two daughter cells [24] [480] [25]. A similar ring structure and function of septins have been found at the base of cilia [103] [104], dendritic spines [105] [106] and the annulus of the sperm tail [107] [108]. However, septins also associate with flat regions of the cell cortex, where they interact with phospholipids and the cytoskeleton [109]. In this way they for instance control the cortical elasticity of T lymphocytes [481]. Septins have been shown to interact with both the actin and the microtubule (MT) cytoskeleton during various cellular processes [480] [482]. In human epithelial cells, for instance, septins guide the direction of growing MTs by suppressing MT catastrophes [483]. Septins localize to various actomyosin structures, including stress fibers [484] [485] [486] [487], contractile rings [486] [102] and around actomyosin-covered bacteria in infected cells [488].

It has been suggested that septins need to form filaments and higher-order structures to fulfill these functions [489] [490]. Septin filament formation has indeed been shown to be essential in budding yeast [489]. Also, several observations demonstrate that septins are present in a filamentous form at the bud neck in budding yeast. Paired, hourglass-shaped and ring-like assemblies of septin filaments have been demonstrated in budding yeast cells by polarized fluorescence microscopy [491] [492]. An ordered array of septin filaments forming a gauze-like septin organization wrapped around the mother-bud neck in budding yeast [493] [494] [495] as well as in *Candida albicans* [496] has been shown by electron microscopy. Nevertheless, direct evidence that septins need to form filaments to fulfill their functions in other organisms is still lacking.

Septin assembly into filaments begins with their incorporation into core unit complexes. The primary structure of all septins is a variable N-terminal region, a polybasic region that binds to phospholipids, a septin unique element, and a conserved GTP-binding domain (Fig. 1A). Most septins have a C-terminal extension (CTE) that is predicted to form a coiled-coil [497] [498]. Septins hetero-oligomerize to form rod-shaped complexes containing two, three or four distinct

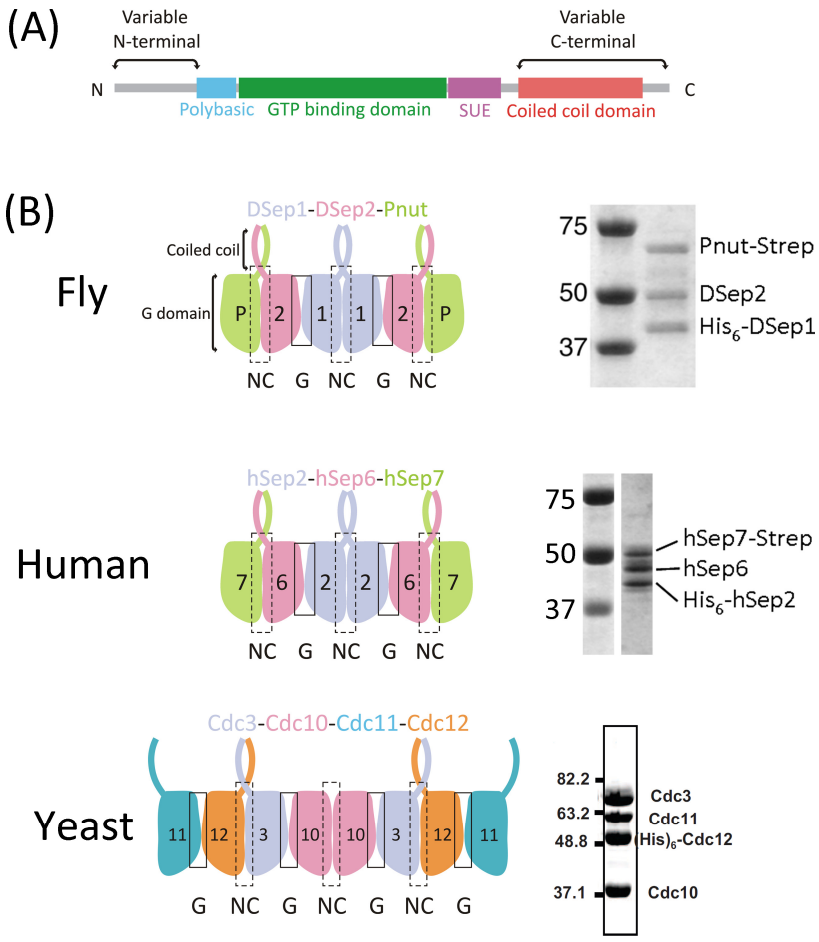

Figure 1. Septins and their assembly into hetero-oligomers. (A) Schematic depiction of prototypical domain structure of septins. Septins consist of three conserved domains: a phosphoinositide-binding polybasic region, a GTP-binding domain and the septin unique element (SUE) whose function is unknown. The amino-terminal (N-terminal) and carboxy-terminal (C-terminal) regions vary in length and amino acid composition. The C-terminus of most septins contains a predicted coiled coil domain. (B) *Left*: schematic depictions of septin complexes forming linear hexamers (fly and human septins) or octamers (yeast septins) with alternating G- (solid box) and NC-dimer (dashed box) interfaces. The G-dimer interface brings together the nucleotide-binding sites while the NC-dimer interface is stabilized by an interaction between the N- and C- terminal extensions. The putative coiled coil domains on the C-terminus further stabilize the NC-dimer interface. Septin complexes are hetero-oligomers with subunits from different homology groups arranged in a palindromic fashion. The color coding indicates homology groups 1 (pink), 2 (purple and green), 3 (cyan), and 4 (orange). Fly and human septin complexes, DSep1–Dsep2–Pnut and hSep2-hSep6-hSep7, respectively, form hexamers; budding yeast septin complexes, Cdc3-

Cdc10-Cdc11-Cdc12, form an octamer. *Right*: SDS-PAGE analysis of the corresponding recombinant septin complexes tagged with Strep- and His_6-tags as indicated. Recombinant septin complexes are obtained from an *E. coli* expression system. SDS-PAGE analysis is courtesy of M. Mavrakis (fly and human septins) and A. Bertin (yeast septin). Numbers on the left indicate expected molecular weights (in kiloDaltons).

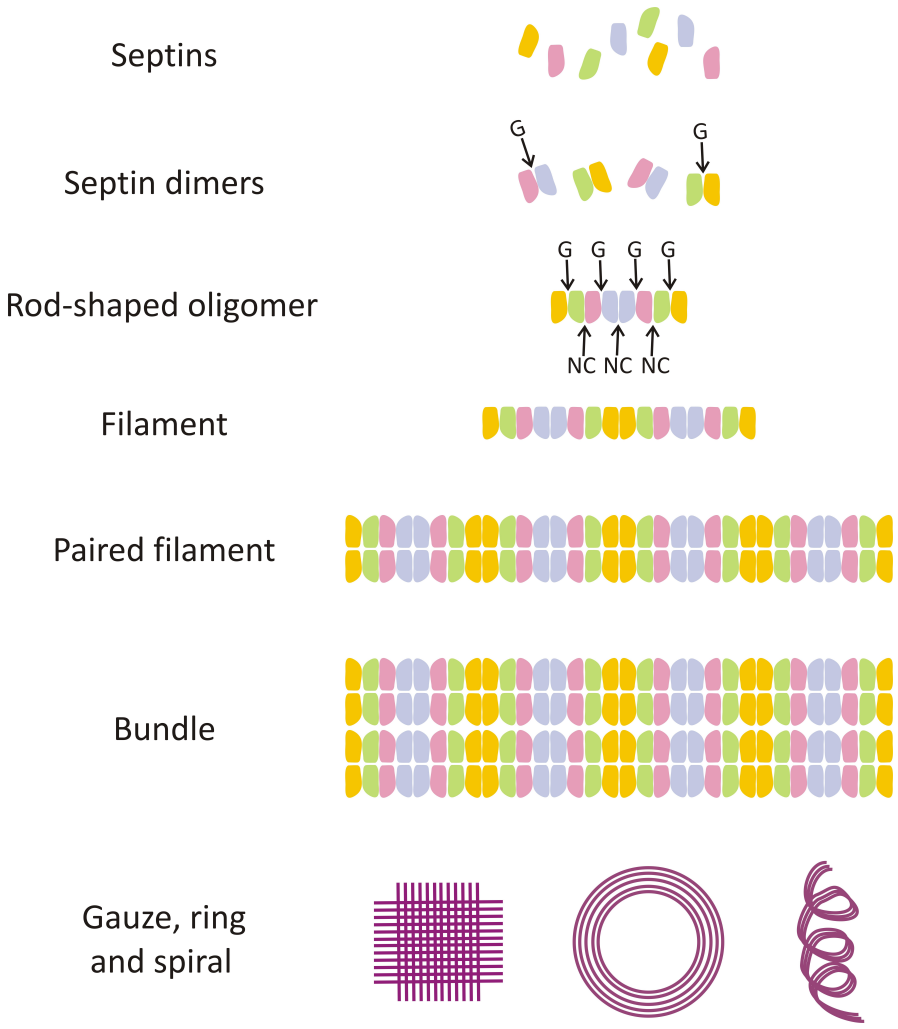

Figure 2. Schematic diagrams of hierarchical assembly of septins into dimers, filaments and higher-order structures. As exemplified here, human septins are represented by purple (hSep2), pink (hSep6), green (hSep7) and yellow (hSep9) blocks. Septins associate first through G interfaces, forming dimers. The dimers then interact at their NC interfaces to assemble into oligomers (octamers) arranged in a palindromic order hSep9-hSep7-

hSep6-hSep2-hSep2-hSep6-hSep7-hSep9. Septin oligomers can assemble end-to-end to form a non-polar filament. Septin filaments can further associate with each other through their coiled coil domains to form paired filaments. Finally, septin filaments can assemble laterally to form bundles. Bundles of septin filaments can form a flat "gauze", ring, or spiral.

septins that are each present in two copies, arranging in a palindromic order and forming a tetramer, hexamer or octamer, respectively [499] [500] [501] [502] [503]. Thus, septin core complexes are apolar. Along the long axis of the rod, septin subunits interact with each other at either G- or NC-interaction surfaces in an alternating manner [499] [504] [505] [502] [506]. The G interface brings together the GTP-binding domains, while at the NC-interface the interaction is mediated by intertwining of the N- and C-terminal alpha helical expansions. A phylogenetic analysis of the septin family among fungi, microsporidia and animals reveals that septins can be classified into five groups [477] and it has been shown that members of the same group can substitute each other within a complex [507]. *In vivo*, the expression of septins as well as the composition of septin oligomers varies in organ systems [507]. *In vitro*, four budding yeast septins Cdc3, Cdc10, Cdc11 (or Shs1) and Cdc12 form octamers with alternating G- and NC-interfaces arranged in the palindromic order of Cdc11-Cdc12-Cdc3-Cdc10-Cdc10-Cdc3-Cdc12-Cdc11 (Fig. 1B) [500] or Shs1-Cdc12-Cdc3-Cdc10-Cdc10-Cdc3-Cdc12-Shs1 where Cdc11 is replaced by Shs1 [508]. Human septins have been shown to form stable hexamers with three subunits, hSep2, hSept6 and hSept7, arranged in the palindromic order of hSep7-hSep6-hSep2-hSep2-hSep6-hSep7 (Fig. 1B) [499]. However, human septins also form octamers with hSep9 flanking the hexamers (Fig. 2) [502] [506]. An important but not yet fully understood question is how septin-septin interactions impact the temporal order of septin complex assembly. A recent study of the assembly of human septin octamers, hSep9-hSep7-hSep6-hSep2-hSep2-hSep6-hSep7-hSep9, demonstrated that the interaction at the G interface is much stronger than that at the NC interface [506]. It was suggested that septin subunits associate with one another in preferred pairs through dimerization at the G interface (forming dimers such as hSep2-hSep6 and hSep7-hSep9), followed by an NC interaction [506].

Several studies have addressed the question of how septin core complexes assemble into filaments and higher-order structures by *in vitro* reconstitution of purified septin complexes (see summary in Fig. 2 and Table 1). Native septins purified from *Drosophila* (fly) embryos, DSep1, DSep2 and Pnut, form filaments that are 7-9 nm in diameter and of variable length (up to 350 nm), or bundles composed of aligned filaments [509]. Native budding yeast septin complexes are able to form paired filaments as well as bundles [510]. Recombinant budding

yeast septins expressed in bacteria (Cdc3, Cdc10, Cdc11 and Cdc12) also form filaments and bundles [500] [511] [512]. Moreover, complexes containing Cdc3, Cdc10, Cdc12 and Shs1 have been demonstrated to form rings and spirals [508]. In addition, complex containing Cdc3, Cdc10, Cdc12 and a phosphomimetic mutant of Shs1 form gauzes [508]. Recombinant human septins (hSep2, hSep6 and hSep7) expressed in insect cells have likewise been shown to form filaments, bundles, rings and spirals [484]. Recombinant human septins expressed in bacteria have been shown to form filaments [513].

It is still unclear how septins assemble into complexes and higher-order structures *in vivo*, and how these septin structures and their dynamics are regulated [99] [96] [490]. In addition, septin interactions with other proteins and the roles of GTP binding and hydrolysis remain elusive. To our knowledge, most of the studies on septin assembly until now focused on budding yeast septins. Comparatively little work has been done on human septins and even less on fly septins. Given that septins are highly conserved [477], it is important to know whether their higher-order structures share a common organization at the molecular level.

Here, we purify recombinant fly, human, and budding yeast septins from *Escherichia coli* and investigate how these different septins assemble under different assembly conditions using electron and fluorescence microscopy. We show that both recombinant fly septins (specifically DSep1, DSep2 and Pnut) and their human counterparts (hSep2, hSep6 and hSep7) arrange into rod-shaped hexamers having two copies of each septin, and budding yeast septins form rod-shaped octamers containing four septins (Cdc3, Cdc10, Cdc11 and Cdc12), each of which is present in two copies. At the same assembly buffer condition, while budding yeast septins assemble into paired filaments, both fly and human septins form bundles of aligned filaments. By testing a broad range of septin concentrations, we estimate the critical concentrations for septin filament formation.

Origin	Purification	Septins	High salt condition and **the resulting septin structure**	Low salt condition and **the resulting septin structure**	Septin concentration	Assembly method	Reference
Fly	*Drosophila* embryo isolation	Pnut, DSep1, DSep2	75 mM KCl **filaments (26 – 350 nm long)**	75 mM KCl **bundles**	0.06 mg/mL	*	[509]
Human	Sf9 insect cell expression	hSep7, hSep6, hSep2	100-500 mM KCl 1 mM DTT	50 mM KCl** 2 mM $MgCl_2$ 1 mM DTT **bundles** (after 3hr dialysis), and **rings/spirals** (after 12-24 hr dialysis)	For the low salt condition: 0.1 mg/mL	dialysis (up to 48 hr)	[484]
Human	*E. coli* expression	hSep7, hSep6, hSep2	250 mM NaCl 5 mM $MgCl_2$ **filaments**	250 mM NaCl 5 mM $MgCl_2$ **filaments**	100 μg/mL	dilution	[513]
Xenopus	*E.coli* expression	*Xl* Sep2	Not available	20 mM NaCl 5 mM $MgCl_2$ **paired filaments**	3.3 ug/mL	dilution	[532]
Budding yeast	Budding yeast cell isolation	Cdc3, Cdc10, Cdc11, Cdc12	1M KCl **filaments (32 – 100 nm long)**	75 mM KCl **paired filaments and bundles**	0.07 mg/mL	dialysis	[510]
Budding yeast	*E.coli* expression	Cdc3, Cdc10, Cdc11, Cdc12	250 mM NaCl **straight, paired filaments**	50 mM KCl 2 mM $MgCl_2$ 1 mM DTT **bundles**	Not available	dialysis	[505]

Origin	Purification	Septins	High salt condition and **the resulting septin structure**	Low salt condition and **the resulting septin structure**	Septin concentration	Assembly method	Reference
Budding yeast	*E.coli* expression	Cdc3, Cdc10, Cdc11, Cdc12	250 mM NaCl **paired filament (200 – 2000 nm long)**	50 mM KCl 2 mM $MgCl_2$ 1 mM DTT **bundles**	Not available	dialysis	[511]
Budding yeast	*E.coli* expression	Cdc3, Cdc10, Cdc11, Cdc12	Not available	(1) the concentration of NaCl lower than 150 mM **paired filaments** (2) 100 - 150 mM NaCl **rings**	1 mg/mL***	dialysis (up to 16 hr)	[512]
Budding yeast	*E.coli* expression	Cdc3, Cdc10, Cdc11, Cdc12	250 - 300 mM KCl 2 mM $MgCl_2$	50 mM KCl, 2 mM $MgCl_2$ 1 mM DTT **paired filaments**	For the high salt condition: 0.01 mg/mL	dilution	[500]
Budding yeast	*E.coli* expression	Cdc3, Cdc10, Cdc11, Cdc12	250 - 300 mM KCl 2 mM $MgCl_2$	50 mM KCl, **paired filaments**	0.05 mg/mL	dilution	[517]
Budding yeast	*E.coli* expression	Cdc3, Cdc10, Cdc12, Shs1	300 mM NaCl 2 mM $MgCl_2$	10 mM NaCl 2 mM $MgCl_2$ **(1) no paired filaments but observed rings and spirals** **(2) gauze** (in the presence of phosphomimetic Shs1)	0.01 mg/mL	dilution	[508]

Table 1. Septin assembly in vitro.

* In this study, *Drosophila* embryo-purified septins were observed as they were after purification without further assembly procedure.

** Similar results were obtained in the absence of KCl.

*** It was mentioned that the critical concentration for septin filament formation is at 0.1 mg/mL.

5.2 Results

Recombinant fly septin core complexes are linear hexamers

Recombinant *Drosophila* septin complexes are purified by co-expressing DSep1, DSep2 and Pnut in *Escherichia coli* (*E. coli*), followed by a two tag purification scheme (a His_6 tag on DSep1 and a Strep tag on Pnut) including a size-exclusion chromatography step (Fig. 1B). Under high salt (300 mM KCl) conditions, the purified fly septins assemble into beaded rods as revealed by electron microscopy (EM) (Fig. 3, *top panel*), consistent with previously reported EM images of budding yeast octamers [500], human septin hexamers [499] and *C. elegans* tetramers [501]. The beads represent equally sized subunits organized in a linear fashion by hetero-oligomeric assembly. By averaging a large number of images of rods that are classified into different classes by their lengths, we obtain images of rods with an enhanced resolution. The class-averaged images reveal that the rods are 4 nm in width, which is consistent with dimensions observed for other GTP-binding domains [514], suggesting that the "beads" observed by EM reflect the conserved GTP binding (G-) domain of septins (Fig. 1) [515] [499] [500]. Different from human septin hexamers, which often appear kinked [499], we mostly observe straight rods (Fig. 3, *top panel*) and only rarely slightly bent ones (Fig. 3, *top panel*, indicated by a red squared box). The predominance of straight rods is similar to yeast septin octamers [500].

Based on phylogenetic analysis [477] [516], septins can be classified into five groups where there is a one-to-one correspondence between fly and human septins (Fig. 1). For instance, fly septins DSep1, DSep2 and Pnut are the homologs of human septins hSep2, hSep6 and hSep7, respectively. We therefore expect the fly septins to assemble in a similar fashion to the human septins, which form a hexamer arranged in a palindromic order, according to hSep7-hSep6-hSep2-hSep2-hSep6-hSep7 [499]. Thus, we expect fly septins to arrange in the order Pnut-DSep2-DSep1-DSep1-DSep2-Pnut and the resulting hexamers should therefore be nonpolar along the long axis. Analysis of EM images reveals that besides hexamers (43.8% of the total 2811 particles), there is an approximately equal amount of pentamers (48.5%) and a small population of tetramers (7%) together with very few trimers (0.7%). If the fly septins maintain the expected order of Pnut-DSep2-DSep1-DSep1-DSep2-Pnut, pentamers correspond to hexamers that lost one Pnut subunit from one end. The observation of almost equal fractions of hexamers and pentamers in this case implies that the NC interface of Pnut and DSep2 is less stable than the other interfaces. Our two-tag affinity purification with size-exclusion is expected to purify hexamers or pentamers, given that the two tags are on DSep1 and Pnut. Thus, it is intriguing that we detect some tetramers and trimers. One possibility is that these small

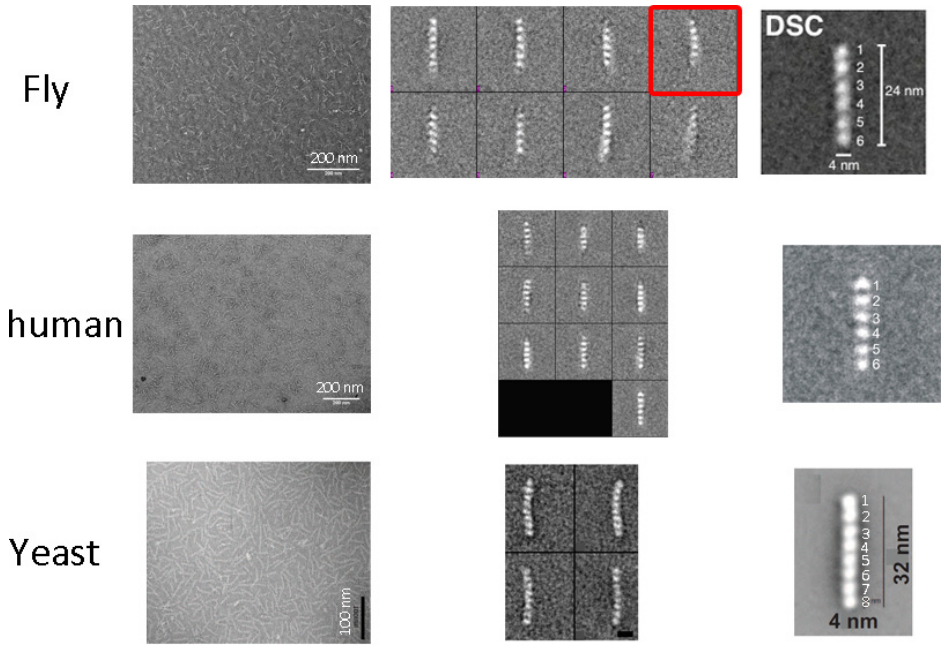

Figure 3. Characterization of recombinant fly (*top panel*), human (*middle panel*) and budding yeast (*bottom panel*) septin complexes purified from an *E. coli* expression system in a high salt (300 mM KCl for fly and human septins; 300 mM NaCl for budding yeast septins) buffer by electron microscopy. *Left column*: electron micrographs of purified septin complexes at low magnification. *Middle column*: representative two-dimensional class averages of septin complexes. *Right column*: high magnification views of two-dimensional class averages of septin complexes, showing Drosophila (fly) septin complexes (DSC) as well as human septin complexes assembled into hexamers, and budding yeast septin complexes assembled into octamers. The red box indicates a slightly bent fly septin pentamer. Budding yeast septin images are taken from Ref. [500] (data from A. Bertin).

structures are intermediate states of septin complex (dis)assembly, and that the fraction of different oligomeric states reflects the relative stability of septin complexes with different lengths. In a previous purification where a single tag purification scheme (a His_6 tag on Pnut) was performed, we detected a prominent degradation of Pnut due to high sensitivity to proteolysis of Pnut during bacterial expression (see Chapter 6, Fig. 1B). In that case, EM image analysis of a total 3707 particles shows a substantial population of tetramers (11%) and trimers (11%) together with a few dimers (3%), and a smaller population of pentamers (15%) compared to hexamers (60%). The two-tag affinity purification is associated with less Pnut degradation, and in this case we obtain a much smaller population of

tetramers (7%) and trimers (0.7%). Taken together, these results suggest the importance of the C-terminal extension (CTE) of the Pnut subunit for the stability of septin complex assembly through the interaction with the CTE of DSep2.

Morphology of fly septin bundles

It has been shown that septin complexes organize into higher order structures including filaments, rings, spirals and flat gauzes in a salt-dependent manner (see schematic depiction in Fig. 2 and overview in Table 1). Indeed, by directly diluting the purified fly septins into a low salt (50 mM KCl) buffer, we observe needle-like septin structures in the presence of 5 mole% AlexaFluor 488 labeled septins (AF488-septins) by total internal reflection fluorescence microscopy (TIRF) (Fig. 4). In the tested range of septin concentrations, from 0.1 μM to 1 μM, the septin structures are exclusively straight (Fig. 4A) and do not undergo thermal bending fluctuations (even though they are not stuck to the surface). This observation indicates that the septin structures are more rigid than actin filaments, which at similar contour lengths exhibit notable bending undulations [26]. The observed septin structures may correspond to bundles composed of several laterally associated septin filaments. The lengths are polydisperse, ranging from 2.2 μm to 20 μm with an average length of 7±4 μm (measured for 113 bundles at a septin concentration of 0.2 μM). We note that the length is likely underestimated due to the spot-like decoration of AF488-septins along the bundles, which is especially clear in enlarged regions (Fig. 4B).

To resolve the ultrastructure of the septin needles, we use transmission electron microscopy (EM). At a septin concentration of 0.2 μM, we detect thick bundles composed of aligned filaments, supporting the interpretation that the septin structures observed by TIRF are bundles. Most of the bundles are long (up to 5 μm long and with width from 8 nm to 90 nm) and straight, but some bundles are bent and curved (Fig. 5C-F). In the background of the bundles, there are mostly septin hexamers (with a length of 24±3 nm, 19 measurements in total). The appearance of the straight fly septin bundles is similar to that observed for native fly septins purified from fly embryos [509], both native [510] and bacterially expressed budding yeast septins [505] [511] [500], and human septins expressed in insect cells [484]. However, in contrast to those earlier observations, we do not observe other higher order structures such as rings [484] [508], spirals [484] or gauzes [508]. Also, we do not observe single or paired filaments as reported for bacteria expressed budding yeast septins [500] [505] [511] [512] [500] [517] and native septins purified from budding yeast [510]. We sometimes observe bundles that split into two parts either somewhere along the bundle or at the base (Fig. 5E, G), similar to previously reported bundles of budding yeast

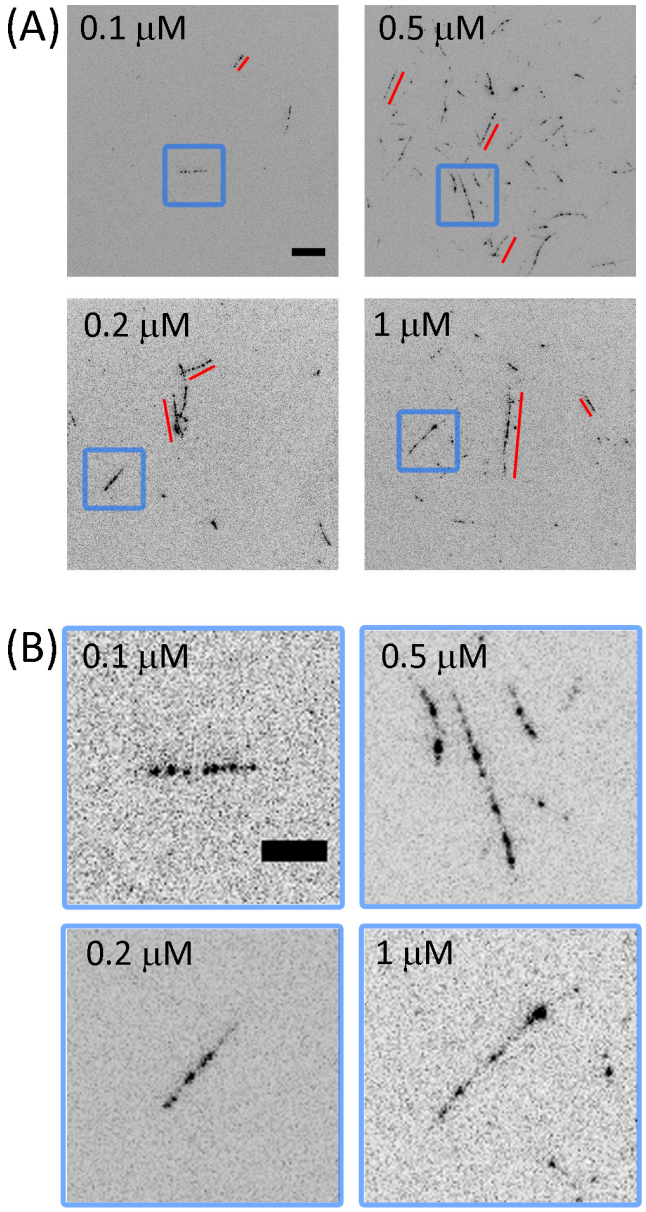

Figure 4. TIRF images of bundles of recombinant fly septins labeled with 5 mole% AF488-septin obtained by rapidly diluting septins into a low salt (50 mM KCl) buffer. The contrast of the images is inverted. The final concentration of septins where assembly takes place are indicated. For clarity, some bundles are highlighted by parallel red lines. In (B), enlarged regions from (A) indicated by the blue squares are shown. Scale bars: (A) 10 μm and (B) 5 μm.

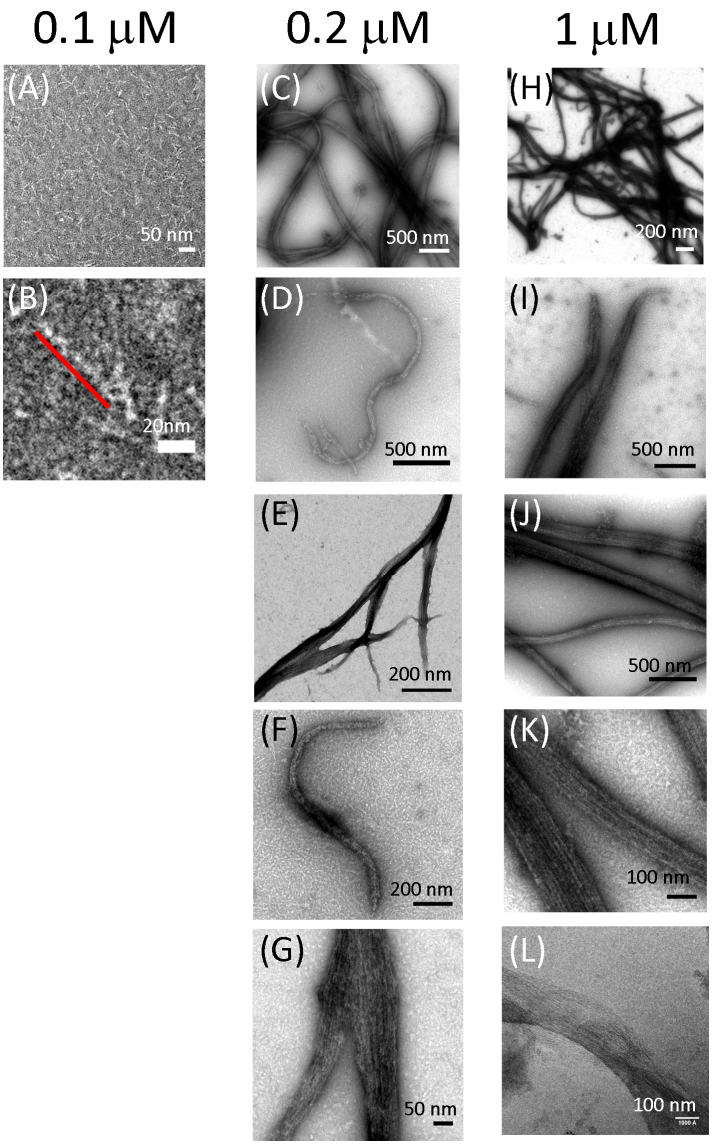

Figure 5. Electron micrographs of recombinant fly septins assembled by rapid dilution into a low salt (50 mM KCl) buffer at different septin concentrations. At a concentration of 0.1 μM (*left column*), most of the septins are isolated hexamers (A) and occasionally assemble into a dodecameric filament as indicated by a parallel red line in (B). At a concentration of 0.2 μM (*middle column*) and 1 μM (*right column*), septin filaments assemble into bundles that are sometimes slightly bent or curved. In each column, the graphs are arranged from low (*top*) to high (*bottom*) magnification (see scale bars). In all cases, septin complexes are present in the background surrounding the bundles.

septins [500]. At a higher septin concentration of 1 μM, we observe tightly packed thick bundles that are slightly bent or split (Fig. 5H-K), similar to those observed at a concentration of 0.2 μM. Interestingly, besides bundles composed of straight septin filaments, we sometimes observe twisted septin filaments along a bundle (Fig. 5L).

Formation of fly septin bundles depends on septin concentration

The assembly of bundles depends on the septin concentration. At a septin concentration of 0.1 μM, we observe mostly septin hexamers by EM (with a length of 26±2 nm, 29 measurement in total) (Fig. 5A) and only very few filaments with lengths ranging from 32 nm to 62 nm (Fig. 5B). Interestingly, as we increase the septin concentration to 0.2 or 1 μM, we do not observe any single filaments or paired filaments composed of two filaments aligned in parallel, which are expected intermediates in filament bundle formation. These intermediates were previously reported exclusively for budding septins [505] [511] [500] [512] (see Table 1). We observe a similar dependence of septin bundle formation on septin concentration by TIRF: at a septin concentration of 0.1 μM we rarely observe bundles, and the number of bundles increases with increasing concentration (Fig. 4). Taken together, our EM and TIRF observations allow us to estimate the critical concentration for fly septin filament formation (and thus bundle formation) to be around 0.1-0.2 μM.

Effect of assembly conditions on fly septin bundle formation

For some cytoskeletal filament-forming proteins, in particular muscle myosin II [518] and intermediate filaments [519], it has been shown that the filament length distribution and filament morphology is influenced by the assembly kinetics. For myosin II, it was shown that filaments formed by dialysis or slow dilution are longer than filaments formed by rapid dilution into a low-salt buffer [518]. For intermediate filaments, it was shown that filaments formed by dialysis are more uniform in terms of their mass to length ratio along the filament axis [519]. To test whether assembly kinetics also affect septin polymerization, we assemble septin bundles by dialysis and compare their morphology to that of bundles formed by rapid dilution. The morphology of septin bundles obtained by dialysis appears similar to bundles obtained by rapid dilution: bundles are needle-like and rigid with no detectable thermal undulations (Fig. 6, labeled as "*Tris+MgCl$_2$+DTT*" condition). Thus, qualitatively, we observe no influence of assembly kinetics on fly septin bundle formation. However, to substantiate this observation, more careful examination, including measurements of the length distribution of septin bundles, should be performed to compare the effect of dialysis versus rapid dilution on bundle formation in a quantitative manner.

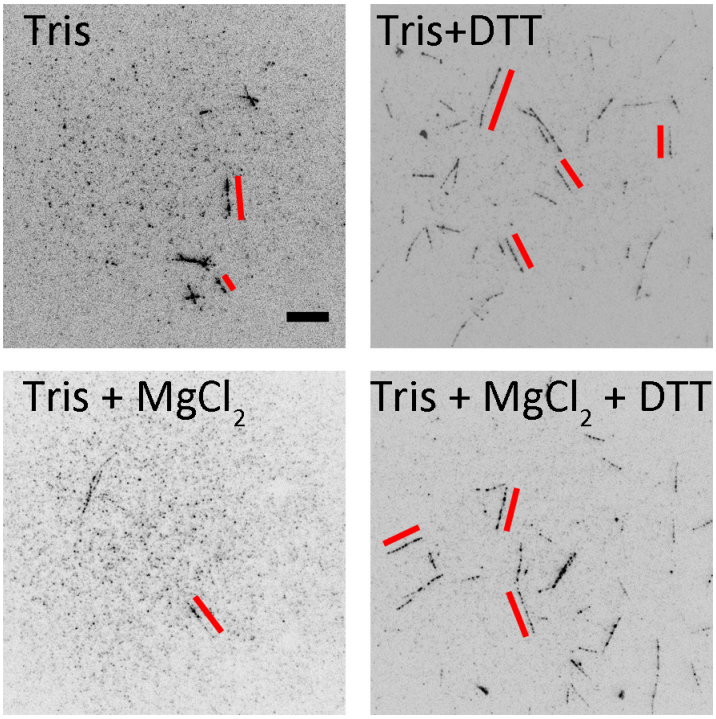

Figure 6. TIRF images of bundles of recombinant fly septins labeled with 5 mole% AF488-labeled septins (inverted contrast) obtained by dialyzing septins against a low salt buffer (20 mM Tris, pH 8 and 50 mM KCl) or against the same low-salt buffer also containing 2 mM $MgCl_2$ or/and 1 mM DTT, as indicated. The septin concentration after dialysis is 0.7 μM (*Tris*), 1.9 μM (*Tris + $MgCl_2$*), 1.7 μM (*Tris + DTT*), and 2.2 μM (*Tris + $MgCl_2$ + DTT*). For clarity, some bundles are highlighted by the parallel red lines. Scale bar: 10 μm.

Another factor that can potentially influence filament/bundle assembly is the crosslinking between septin hexamers through disulfide bonds derived from solvent-accessible cysteine residues (Cys). In the above experiments, dithiothreitol (DTT) is present to prevent disulfide bond formation between septin hexamers. To test the influence of disulfide bonds, we assemble septin bundles in the absence of dithiothreitol (DTT). Septin bundles formed in the absence of DTT appear morphologically similar to those formed in the presence of DTT, suggesting a weak, if any, influence of disulfide bonds on bundle formation (Fig. 6, panel labeled "*Tris + $MgCl_2$*"). However, we note that we found few bundles due to the low protein concentration after dialysis. Another factor that could influence septin bundle formation is the binding of cations. Cations play an important role for protein stability, functionality and protein-protein interactions [520] [521]. It is

known that GTPases bind tightly to GTP/GDP in the presence of magnesium cations (Mg^{2+}) [522]. The crystal structure of GDP-bound mammalian septins (mouse Sept2) in the presence of Mg^{2+} has been resolved [504]. Furthermore, it has been suggested that GTP binding or hydrolysis influences the stability of the G- and NC- interfaces involved in septin filament assembly [504]. Also, budding yeast septins of wild type Cdc3 and Cdc11, and GTP-binding defective Cdc10 (Cdc10(S46N)) and Cdc12 (Cdc12(T48N)) assemble into octamers that are less stable compared to those assembled by wild type septins Cdc3, Cdc10, Cdc11 and Cdc12 [500]. We thus test if septin bundle assembly is perturbed in the absence of Mg^{2+}. We observe no obvious difference in the morphology of septin bundles in the presence or absence of exogenously supplied Mg^{2+} (Fig. 6, panels "*Tris + DTT*" and "*Tris*"). These results may indicate that the magnesium that is already bound to septin hexamers during purification is strongly bound to the nucleotide-binding site and does not exchange.

Morphology of human septin bundles is similar to fly septin bundles

Mammalian septins, like fly septins, are known to form hexamers, although octamers have also been reported, with hSep9 at the two ends [502] [506]. To test whether mammalian septins form similar bundles as fly septins, we purify recombinant human septins, by co-expressing His_6-hSep2, hSep6 and Strep-hSep7 in *Escherichia coli* (Fig. 1). Under high salt conditions (300 mM KCl), the human septins assemble into linear rods composed of bead-like septin subunits (Fig. 3, *middle panel*), consistent with prior reports [513] [499]. The subunit sequence in these hexamers was earlier shown to be hSep7-hSep6-hSep2-hSep2-hSep6-hSep7 [499]. Image analysis of a total of 3299 particles shows that the rods are mainly hexamers (44.6%) and pentamers (36.6%), with a small population of tetramers (16.8%). Since two-tag purification together with size exclusion is performed, we expect to obtain only hexamers and pentamers. Thus, the presence of the substoichiometric septin complexes, the tetramers, reveals the disassembly of hexamers or pentamers. Similar to the purification of fly septin complexes, we obtain an almost equal stoichiometry of the hexamers and pentamers, which implies that the NC interface of hSep6 and hSep7 is less stable than the other interfaces.

When we dilute the recombinant human septins into a low salt (50 mM KCl) buffer, they form bundles (Fig. 7), which is consistent with prior studies [484] [513]. The bundles are formed across a wide range of septin concentrations, from 0.05 μM to 1 μM. Similar to fly septin bundles, human septin bundles are composed of aligned filaments, regardless of septin concentration (Fig. 7F, I, L). These bundles are usually straight (Fig. 7A, D, J) and only occasionally bent (Fig. 7G). Some of the bundles exhibit split ends (Fig. 7B, E, H, K). Notably, we do not detect ring-like bundles or spirals, which were observed for human septins

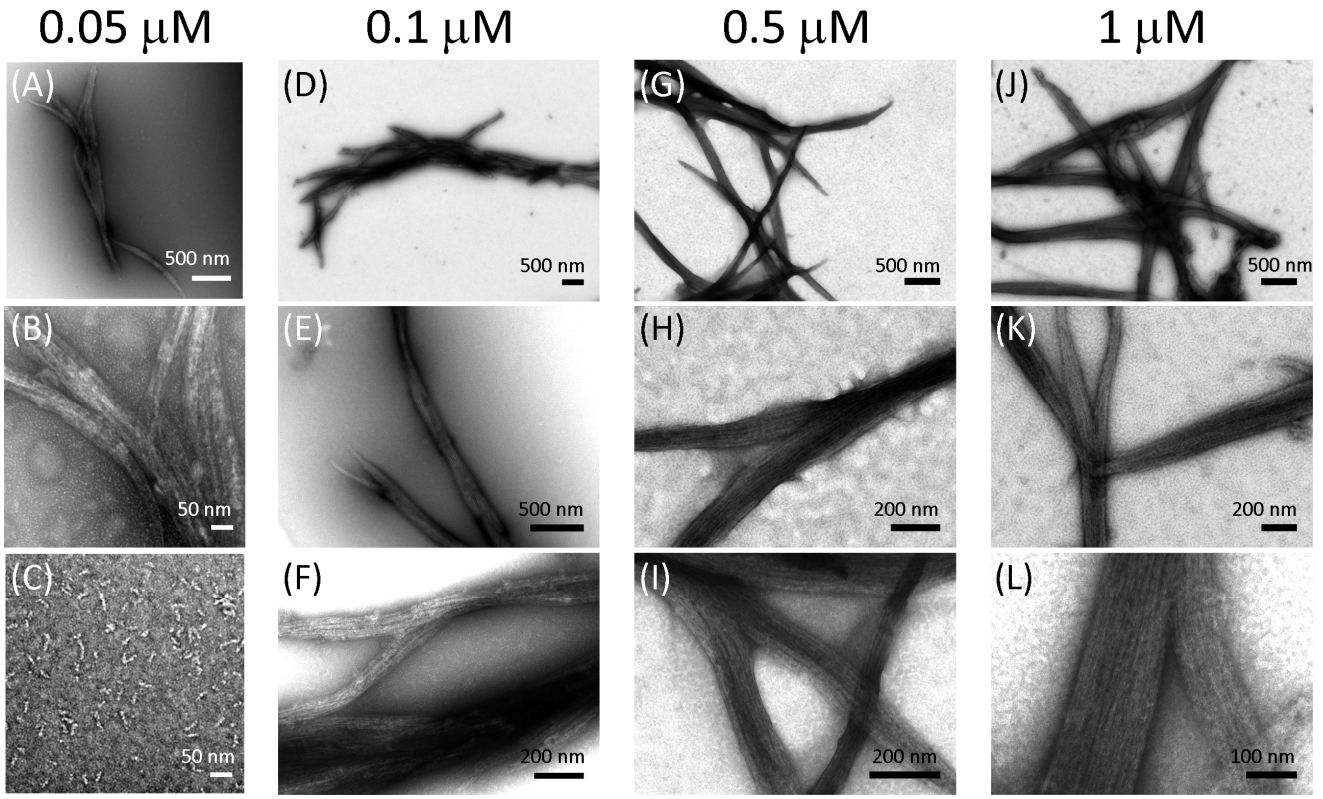

Figure 7. Electron micrographs of recombinant human septin bundles obtained by rapid dilution into a low salt (50 mM KCl) buffer at different septin concentrations as indicated. Bundles of human septins are found at all examined septin concentrations. The graphs in each column are arranged from low (*top*) to high (*bottom*) magnification. Septin oligomers are always present in the background.

expressed in insect cells [484]. At the lowest concentration tested (0.05 μM), we rarely find bundles but mainly observe short filaments with a length of 51±5 nm (in total 32 measurements) (Fig. 7C). Thus, we estimate that the critical concentration for human septin polymerization is around 0.05 μM.

Polymerization of budding yeast septin filaments

For comparison with the fly and human septins, we perform similar TIRF and EM studies of the assembly of recombinant budding yeast septin complexes that are purified by co-expressing Cdc3, Cdc10, Cdc11 and His_6 tagged Cdc12 in *Escherichia coli* as previously described (Fig. 1B) [500]. It has been shown that native septins isolated from budding yeast cells [510] as well as recombinant yeast septins purified from bacterial cells [505] [500] [512] [508] form stable complexes. In living budding yeast, both complexes and higher order structures such as filaments arrays [495] or gauzes [494] have been shown. The ability of septins to form filaments was shown to be essential for the survival of budding yeast cells [489].

Under high salt conditions (300 mM KCl), the yeast septins are assembled into octamers (Fig. 3, bottom panel). The septin subunits were earlier shown to be arranged in the palindromic sequence Cdc11-Cdc12-Cdc3-Cdc10-Cdc10-Cdc3-Cdc12-Cdc11 [500]. Under low salt conditions (50 - 60 mM KCl), the octamers polymerize end-to-end to form paired filaments, which consist of two long filaments aligned in parallel [500] [510] (Fig. 8). Little is known currently on how septin complexes assemble into paired filaments and higher-order structures. EM studies have so far focused mostly on the structure of yeast septin assemblies [500] [517] [508] [512] [510] [505] [511]. It was shown that budding yeast septin complexes Cdc3-Cdc10-Cdc11-Cdc12ΔCC in which Cdc12 lacks its coiled coil elements are able to assemble into short single filaments (two to three octamers long) but not paired filaments [517]. This observation supports a proposed pairing mechanism in which the pairing is mediated by lateral association of the Cdc3-Cdc12 coiled coil on one filament with the corresponding Cdc3-Cdc12 coiled coil on the other filament [500]. Some kinetic studies of yeast septin assembly were performed by light scattering experiments for the yeast septin complexes Cdc3-Cdc10-Cdc11-Cdc12 that assemble into paired filaments [517] and by EM for the yeast septin complexes Cdc3-Cdc10-Cdc12-Shs1 that assemble into rings [508].

To gain insight into the assembly kinetics, we perform time-lapse imaging by TIRF. To visualize the septin filaments, we utilize GFP-tagged septin complexes where GFP is appended to Cdc10 as described in [500]. At a septin concentration of 200 nM, approximately 1.5 hr after initiating polymerization by means of rapid dilution into low-salt buffer, we observe short and mobile septin structures (~ 1.5 – 6.5 μm in length) (Fig. 9, bottom-most panel labeled "*200 nM*"). By around 3.5 hr, longer septin structures with a length ranging from 3 to 13 μm appear. We

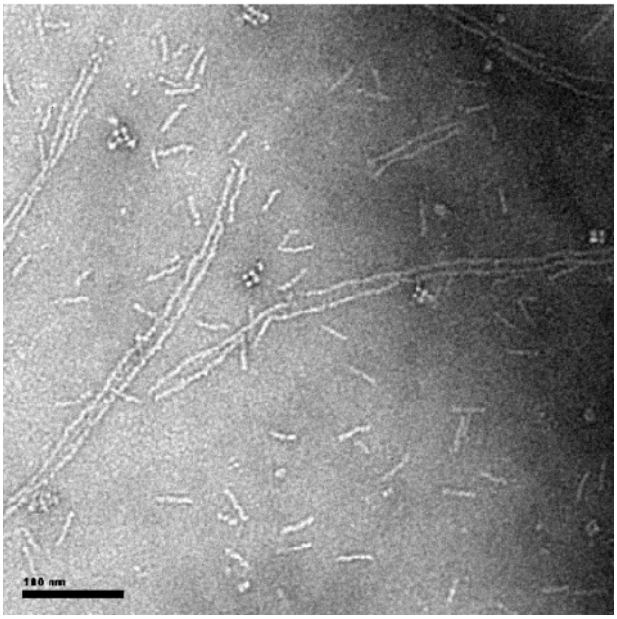

Figure 8. Electron micrograph showing paired filaments formed from recombinant budding yeast septin octamers in a low salt buffer (50 mM KCl). Scale bar: 100 nm. The image is taken from Ref. [500] (data from A. Bertin). Septin octamers are present in the background.

note that the estimated length is likely underestimated due to the thermal fluctuations of the filaments that cause ends or segments of the filaments to fluctuate out of the observing plane. After 10.5 hr, we observe more septin structures, but of similar morphological appearance as those observed at 3.5 hr. The observed filaments undergo observable thermal fluctuations (Fig. 10). We note that due to the optical diffraction limit ~ 0.2 μm, we are unable to determine whether the observed structures are paired filaments, single filaments or thin bundles. Interestingly, we observe a marked dependence of septin filament formation on septin concentration. When we lower the septin concentration to 5 or 10 nM, we observe much fewer septin filaments, even after 10.5 hr of incubation (Fig. 9, first and second panel). Increasing the septin concentration to 20, 50 or 100 nM, short filaments are present after 3.5 hr of incubation and longer ones are present after 10.5 hr of incubation. Thus, our results show a time-dependent growth of yeast septin filaments. Moreover, we observe that yeast septins form filaments already at a much lower concentration (5 nM, equivalent to 0.002 mg/mL) than where they were reported to form bundles (see Table 1).

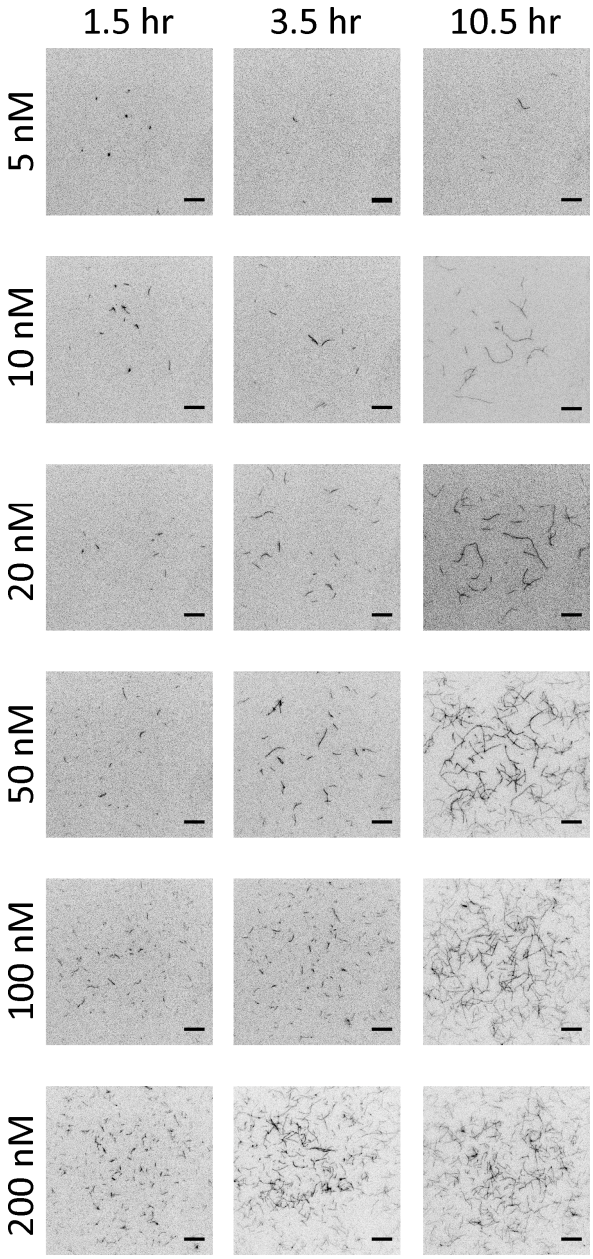

Figure 9. Kinetics of filament growth for recombinant budding yeast septins observed by TIRF imaging (inverted contrast images). Filament growth is examined at different septin concentrations and different time points, as indicated. Scale bars: 10 μm.

A previous EM study (A. Bertin, personal communication, 2013) reported the presence of filaments at concentrations above 0.005 mg/mL (13 nM), consistent with our observations. We thus estimate that the critical concentration for yeast septin filament formation is around, or even below, 5 nM.

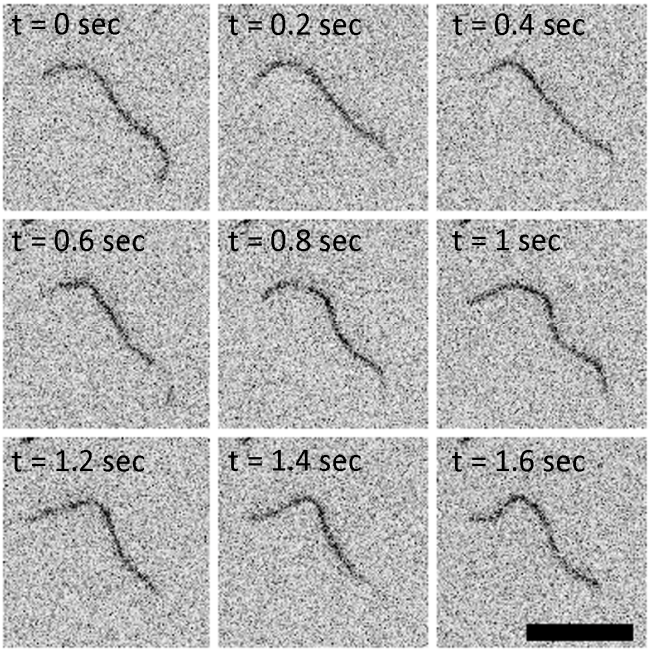

Figure 10. Snapshots from a time-lapse image series of a GFP-labeled budding yeast filament undergoing thermal bending undulations, observed by TIRF (inverted contrast images; exposure time: 100 ms; time difference between images: 200 ms). Scale bar: 10 μm.

The influence of assembly conditions on budding yeast septin assembly

A recent study showed that budding yeast septin complexes lacking solvent-exposed Cys have the ability to form filaments similar to the filaments formed by wild type yeast septins [523]. However, the critical concentration for filament formation was higher for the Cys-less septins [523]. It was suggested that the low concentration of Cys-less septins obtained after purification influenced the efficiency of filament formation [523], but it is also possible that the thiol group of the Cys influences filament assembly through the formation of disulfide bonds. To test this possibility, we assemble yeast septins in the absence of the reducing

agent DTT. Interestingly, we observe long, rigid filaments that exhibit no thermal undulations (Fig. 11), in strong contrast to the thermally fluctuating filaments observed in the presence of DTT. Thus, it is likely that these rigid filament structures are bundles composed of a few filaments (see enlarged regions in Fig. 11B). Interestingly, these bundles form locally ordered structures of aligned filaments (Fig. 11A), though there are also regions in the sample where there is no obvious formation of patterns. The spatial arrangement of the bundles is likely dependent on the local concentration of the bundles. In summary, our observation reveals that yeast septin filaments may potentially be crosslinked through disulfide bonds.

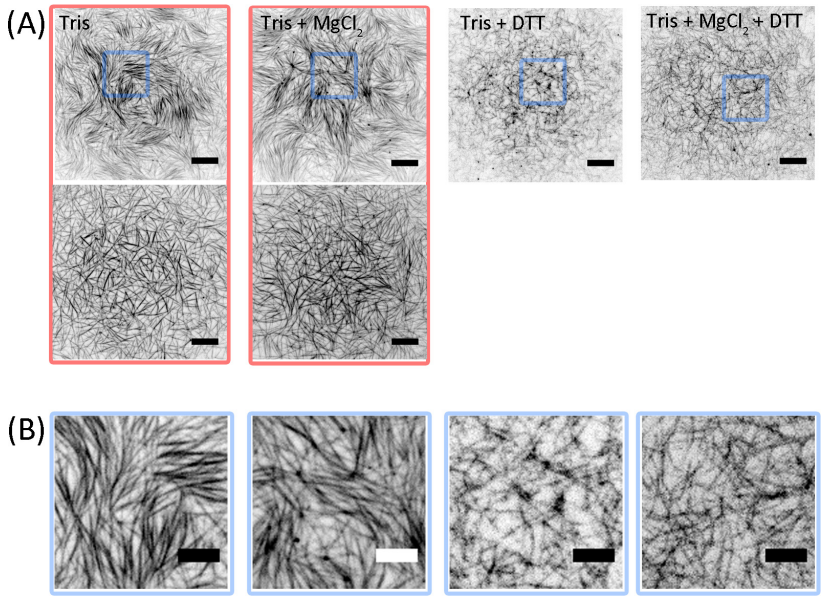

Figure 11. TIRF micrographs of bundles/filaments of GFP-labeled budding yeast septins (inverted contrast) obtained by rapid dilution in a low salt (20 mM Tris, pH 8 and 50 mM KCl) buffer. When present, $MgCl_2$ is 2 mM and DTT is 1 mM (see legends). The septin concentration is 0.4 μM. In (B), zoomed-in areas of the small rectangular areas indicated in (A) in the corresponding column. Scale bars: (A) 10 μm and (B) 5 μm.

It has been previously shown that the guanine nucleotide binding sites of budding yeast septin complexes are saturated and that the nucleotide exchange rate is slow [512] [524]. Since GTPases bind tightly to GTP/GDP in the presence of Mg^{2+} [522], and GTP/GDP-binding of yeast septins is crucial to obtain stable yeast

septin octamers [500], we test if exogenously added Mg^{2+} perturbs the assembly of yeast septins. In our hands, we do not observe an obvious morphological difference by TIRF imaging between yeast bundles (Fig. 11, panel "*Tris*" and "*Tris+Mg*$^{2+}$") or paired filaments (Fig. 11, panel "*Tris+DTT*" and "*Tris+DTT+Mg*$^{2+}$") prepared in the presence or absence of Mg^{2+}. Thus, similar to fly septin complexes, our observations may indicate that magnesium bound to yeast septin complexes is strongly bound to the nucleotide-binding site and does not exchange with the exogenously added Mg^{2+}.

Similar to what we observed for fly septin complexes, the filament assembly of yeast septin complexes does not appear to be influenced by the assembly process, i.e., rapid dilution or gentle dialysis (Fig. 12A, B, the "*Tris+MgCl*$_2$*+DTT*" condition on the far right). Furthermore, the observed dependence on DTT and the independence on exogenously supplied Mg^{2+} are robust: whether obtained by rapid dilution (Fig. 11) or by dialysis (Fig. 12) into a low salt (50 mM KCl) buffer, the detected bundles have a similar appearance.

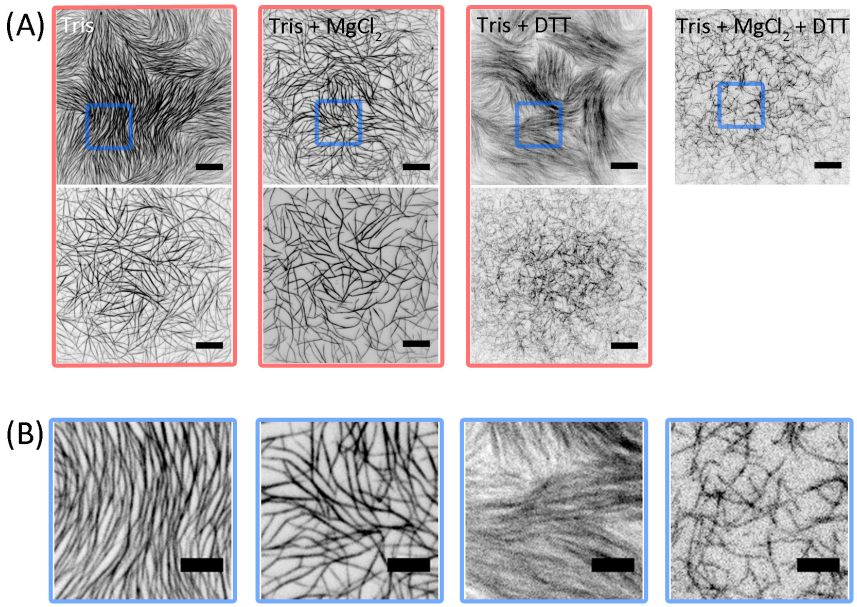

Figure 12. TIRF micrographs of bundles/filaments of GFP-labeled recombinant budding yeast septins (inverted contrast) obtained by dialyzing against a low salt (20 mM Tris, pH 8 and 50 mM KCl) buffer. If present, $MgCl_2$ is 2 mM and DTT is 1 mM (see legends). The septin concentration after dialysis is 1.25 μM (*Tris*), 0.3 μM (*Tris + MgCl*$_2$), 2 μM (*Tris + DTT*), and 1 μM (*Tris + MgCl*$_2$ *+ DTT*). In (B), zoomed-in areas of the small rectangular areas indicated in (A) in the corresponding column. Scale bars: (A) 10 μm and (B) 5 μm.

5.3 Discussion

Recombinant fly, human, and yeast septin hexamers organize into bundles

Septins have been implicated in many cellular functions, but it remains unclear whether these functions are mediated by septin complexes, filaments, or other higher order structures [525] [96] [490] [526] [480] [24]. Also, the mechanism of septin assembly *in vivo* remains elusive [99] [96] [490]. *In vitro*, it has been shown that native or bacteria-derived budding yeast and insect cell-derived human septin complexes assemble into filaments, and that these filaments can further organize into paired filaments [500] [517] [510] [512], bundles [484] [500] [510] [512] [511], rings [484] [508] [512], spirals [484] and gauzes [508]. Native fly septins purified from fly embryos were shown to be in filamentous form with various lengths (15 – 350 nm), and at a higher septin concentration (though not exactly specified in the paper [509]), bundles appeared [509]. However, less is known about higher order structures of fly septins. Here we purified recombinant fly septin complexes from *Escherichia coli* and showed that the septins assemble into hexamers and further into bundles composed of aligned filaments. These bundles resemble bundles observed previously [509]. Besides straight bundles, we also observe slightly curved and bent bundles. Furthermore, by testing a broad range of septin concentrations on septin assembly, we estimate that the critical concentration of fly septin filament formation is around 0.1-0.2 μM.

Parameters that influence higher order septin structures in vitro

For fly and human septins, we do not observe single or paired filaments. This is surprising given that single and paired filaments were previously reported for recombinant budding yeast septins expressed in bacteria [505] [511] [512] [500] [517] and native septins purified from budding yeast [510]. Furthermore, we do not detect higher-order septin filament structures such as rings or gauzes, which were observed for recombinant budding yeast septins from bacteria [508] [512] and recombinant human septins from insect cells [484]. The septin structures reported in the literature are summarized in Table 1. The variety in septin sources (recombinant versus endogenous, bacterial versus eukaryotic expression systems) and the variety of buffer conditions that have been used to assemble septin filaments and higher-order structures in different studies raise an important question: what parameters govern the assembly of septin structures?

(1) ionic strength, Mg^{2+} and septin concentration

Ionic strength greatly influences septin polymerization *in vitro*. Several studies have shown that recombinant septins assemble into filaments or bundles at low salt (10 mM to 250 mM NaCl/KCl) but not at high salt (>100 mM KCl/NaCl) conditions (see Table 1). For instance, at an ionic strength of 75 mM KCl, the

endogenous septins purified from budding yeast and fly embryos assemble into paired filaments and bundles, respectively [509] [510]. Consistent with the aforementioned studies, we find that recombinant fly/human septin hexamers and budding yeast septin octamers form bundles at a low ionic strength (50 mM KCl). For budding yeast as well as fly septins, there is no obvious difference in bundle appearance when the assembly is performed by rapid dilution or by dialysis. Furthermore, the presence or absence of exogenously supplied magnesium does not influence bundle assembly, consistent with prior studies where exogenous magnesium was absent (see Table 1).

A possible polymerization model has been suggested in which septin complexes form filaments by a nucleation-and-growth mechanism, similar to the polymerization mechanism of other GTPases such as tubulin and FtsZ, [527] [528] or ATPases such as actin [529] [530] [531]. Indeed, a light scattering study of the polymerization of a *Xenopus* septin, *Xl* Sept2, demonstrated nucleation-and-growth kinetics [532]. In case of a nucleation-and-growth process, septins only polymerize above a threshold concentration known as the critical concentration. Below this concentration, septin complexes remain as individual oligomers in solution, while above this concentration septin filaments coexist with oligomers at a constant oligomer concentration equal to the critical concentration. The critical concentration for septin filament polymerization has not been examined systematically, although the influence of septin concentration on the formation of filaments, bundles or rings has been mentioned [523] [517] [500] [509]. To our knowledge, the only reported critical concentration is 0.26 μM for filament formation of budding yeast septins [512]. However, in this study [512], the method used to determine the critical concentration was not described. To determine the concentration below which there is no filament assembly, we dilute septin complexes to different concentrations, and observed septins by TIRF or EM. In the range of examined concentrations, the critical concentration for fly septin is close to 0.1 μM, where we exclusively observe hexamers. For human septins, the estimated critical concentration is around 0.05 μM, where we detect mainly short filaments. The estimated critical concentration for yeast septins is around, or even below, the lowest tested concentration of 0.005 μM, where we observe that yeast filaments appeared after 10.5 hr incubation time.

To quantify time-dependent growth of septin filaments and determine the critical concentration for filament formation more precisely, there are two potential strategies. Pyrene labeled actin has been widely used to measure the critical concentration and polymerization rate of actin filaments [533] [534]. The thiol-reactive derivative of pyrene that attaches to a single solvent-exposed Cys of actin has a ~ 10-fold higher fluorescence intensity on polymerized actin than on monomers. It has been shown that *in vitro* recombinant Cys-less budding yeast

septins and Cys-less budding yeast septins with a single Cys introduced at a specific position display assembly properties indistinguishable from wild type septins [523]. It is thus conceivable to use pyrene-labeled septins in the future to assess assembly kinetics. Another convenient method to monitor septin polymerization would be to use a stopped-flow technique in combination with light scattering, where an increase of the scattering intensity corresponds to an increased mass fraction of filaments [517] [532]. In case of budding yeast septin assembly, EM images taken at different time points were shown to be consistent with light scattering measurements, showing that at a concentration of 0.05 mg/mL, septin filaments form within 5 sec and after ~ 1 min the scattering intensity reaches a plateau, indicating a steady state in filament polymerization [517].

(2) nucleotide binding

Like other GTPases, all septins bind guanine nucleotide and many of them hydrolyze GTP [509] [511] [513] [532] although GTPase activity is very low [509] [512] [513]. One important but elusive issue is whether the polymerization of septin complexes requires GTP binding. In budding yeast, purified wild type Cdc3 and Cdc11, and GTP-binding defective Cdc10 (Cdc10(S46N)) and Cdc12 (Cdc12(T48N)) still allowed formation of heteromeric octamers although less stable compared to those formed by the wild type septins (Cdc3, Cdc10, Cdc11 and Cdc12), and filament formation was inhibited [500] [511]. It was thus suggested that GTP binding possibly induces a conformational change of the septin complexes which stabilizes the septin octamers and would then facilitate filament formation [511]. Supporting this idea, GTP-induced conformational changes in mouse septins, Sept2, have been demonstrated [504]. A similar idea was raised based on the observation that GTP binding promoted the polymerization of a Xenopus septin (*XI* Sep2) [532]. However, it was suggested that the G domain of *XI* Sep2 purified from bacteria may be unfolded and that GTP binding triggered its folding, thus promoting GTP hydrolysis and septin filament formation [535]. This hypothesis was inspired by the folding of α-tubulin where GTP binding/hydrolysis is necessary [535] [536]. Although we observe bundles assembled from bacteria-expressed fly septin complexes in the absence of exogenous GTP, an examination of the GDP:GTP ratio in our septin complex and the effect of GTP-binding on filament assembly will be essential to fully understand the mechanism of fly septin filament formation.

(3) posttranslational modifications

Posttranslational modifications of septins including phosphorylation [537] [538] [539] [540] [537] [541], sumoylation [542] [543] and ubiquitylation [544] have been shown to contribute to the assembly of septin filaments and higher order

structures [545]. For instance, in budding yeast, the protein kinase Cla4 efficiently phosphorylates Cdc3, Cdc10 and Cdc11, and Cla4-mediated phosphorylation promotes septin filament formation and septin collar assembly at the mother-bud neck [511]. Furthermore, an *in vitro* study showed that the phosphorylation of the C-terminal extension of yeast septin Shs1 regulates the capacity of Shs1-containing octamers to form rings and gauzes [508]. Septins isolated from fly embryos have been shown to form single filaments and the phosphorylation of the fly septin Pnut was suggested to contribute to the regulation of septin polymerization [509]. Taken together, we hypothesize that recombinant fly/human septins purified from bacteria may be unable to form stable filaments due to the lack of phosphorylation. Given that the insect-cell derived and embryo-derived septins are likely phosphorylated during purification, it would be interesting to compare their assembly, in terms of the resulting septin structures and assembly kinetics, to that of bacteria-purified septins. Furthermore, it will be important to test the effect of phosphomimetic mutations of bacterially expressed purified septins on their assembly to understand the effect of phosphorylation.

(4) septin binding partners

Several septin binding partners have been suggested to regulate septin filament assembly [96]. Anillin recruits septins to the actomyosin ring during cell division [546] and its ability to influence actin-septin binding *in vitro* has been shown [484]. Though in this thesis we show that fly and mammalian septins can bind to actin directly (see Chapter 6), it is possible that anillin acts in synergy with this direct actin-septin interaction. Moreover, septins have been shown to bind to non-muscle myosin II and this interaction has been suggested to promote septin filament formation [486]. In addition to the association with actin, septins have been shown to interact with microtubules [480]. Although it is unclear what mediates the interaction of septins and microtubules, stabilizing microtubules by paclitaxel, an MT-stabilizing drug, has been shown to increase the number of septin filaments [483] and stabilize septin rings [547]. Furthermore, phosphatidylinositol-4,5-bisphosphate (PIP_2) containing lipid monolayers have been demonstrated to promote septin filament formation [517] and septin-mediated tubulation of liposomes containing PIP_2 has been shown [548]. All together, it will be important to assess septin assembly in the presence of all the aforementioned binding partners *in vitro* using controllable reconstituted model systems to elucidate how septin assembly is regulated *in vivo*.

(5) other factors: assembly kinetics and disulfide bonds

We observe by TIRF no obvious morphological difference between fly/budding yeast septins bundles/filaments obtained by dialysis and rapid dilution, in contrast

to intermediate filaments [519] and myosin II bipolar filaments [518], for which a marked dependence of filament length and morphology on assembly kinetics was reported. However, to draw firm conclusions, more detailed examination, such as measurements of the filament/bundle length distribution, should be performed to compare the effect of dialysis versus rapid dilution on filament/bundle formation in a quantitative manner.

The DTT-dependence of bundle formation for budding yeast septins raises the possibility that disulfide bonds contribute to septin-septin interactions and higher-order structure formation *in vitro*. Although it has been shown that yeast septin complexes lacking solvent-exposed Cys can still robustly form paired filaments [523], the potential of these filaments to form higher-order structures was not examined. Our observation that budding yeast septins form bundles in the absence of DTT suggests that the role of Cys in septin assembly (at least for higher-order structures) should be revisited. A similar observation has been shown in which disulfide bonds mediate bundling of actin filaments [549]. Interestingly, the Cys residues of fly septins does not seem to influence bundle formation. In the future, it will be interesting to test the role of Cys residues of the fly septin complex by purifying mutants lacking solvent-exposed Cys residues and assess their assembly properties.

Ring formation

The most commonly observed septin higher-order structures *in vivo* are rings [525]. Such rings are found at the division site of cells during cytokinesis, at the base of dendritic spines in hippocampal neurons, at the annulus of spermatozoa, and at the base of primary cilia. *In vitro*, recombinant septins have been reported to form rings composed of tightly packed filaments [512] [508] [484]. The structure of these rings appears to differ from the structure of the septin rings localized at the bud neck of budding yeast, in which filaments arrange into arrays with a 30 nm spacing [495] [97] [493]. Examples of rings observed *in vivo* and reconstituted septin rings *in vitro* are listed in Table 2. In our hands, we do not observe ring formation of fly/human septins. As discussed above, this could be due to the lack of posttranslational modifications such as phosphorylation, since our fly and human septins were purified from *E. coli*, unlike the insect cell-derived human septins in the literature [484]. Also, ring formation may require other fly septins such as DSept4 or DSept5, as reported for the ring formation of Shs1-yeast octamers (Shs1-Cdc12-Cdc3-Cdc10) [508]. However, yeast septins (Cdc11-Cdc12-Cdc3-Cdc10) at high concentration (1 mg/mL, equivalent to ~ 2.6 μM) assemble into rings after dialysis in a low salt buffer (100 -150 mM NaCl) for 16 hr [512]. This observation implies that ring formation probably requires a high septin concentration under an optimal ionic strength, and that the assembly process needs to be long and slow. Ring formation of bundles of human septins also

required dialysis and a long incubation time of 16 – 24 hr [484]. Thus, it will be important to test whether the fly/human septin complexes can also form rings under these conditions.

Ring diameter/μm	Origin	Reference
0.5 – 0.7 (outer diameter)	*in vitro*, Sf9 insect cell purified human septin hexamers hSept7, hSept6, hSept2	[484]
0.4 – 0.8 (outer diameter)	*in vitro*, *E.coli* purified budding yeast septins octamers Cdc3, Cdc10, Shs1, Cdc12	[508]
1	*in vitro*, *E.coli* purified budding yeast septin octamers Cdc3, Cdc10, Cdc11, Cdc12	[512]
0.42 – 0. 54	*In vivo*, bud neck of budding yeast cells	[493]
0.5	*In vivo*, intercellular bridge after cytokinesis in D-98S cells	[622]
~1 – 1.5	*In vivo*, ring canals in *Drosophila* spermatogenesis	[620]
~0.5	*In vivo*, stalks that connect *Drosophila* blastomeres to the yolk sac after cellularization	[621]
0.58	*In vivo*, at the annulus of spermatozoa	[107]
~ 0.8	*In vivo*, at the base of dendritic spines in hippocampal neurons	[106]

Table 2. Septin rings observed *in vitro* and *in vivo*.

5.4 Conclusion

We show by a combination of electron microscopy with time-lapse fluorescence imaging by total internal fluorescence microscopy that in the same assembly conditions, recombinant fly and human septin complexes purified from bacteria assemble into bundles composed of aligned filaments while bacteria-derived budding yeast septins assemble into paired filaments. We estimate the critical concentration for septin filament formation by testing a broad range of septin concentrations. We do not observe any formation of septin rings or spirals that are previously reported for bacteria-derived budding yeast septins and insect cell-derived human septins. It will be important to test whether factors such as posttranslational modifications or the presence of septin binding partners like PIP_2 lipids, anillin or non-muscle myosin II can promote the formation of these alternative, highly curved structures.

5.5 Materials and Methods

Observation chamber preparation

Microscope slides and cover slips were cleaned for 30 min in a base-piranha solution (5% hydrogen peroxide, 5% ammonium hydroxide, heated to 70°C) and stored in 100% isopropanol. Chambers were assembled by sandwiching strips of Parafilm between a slide and a cover slip, followed by melting the Parafilm at 120°C. The resulting chambers were then passivated by incubating for 15 min with 1 M potassium hydroxide, rinsing with Milli-Q water, blow-drying with nitrogen gas, incubating for 45 min with 0.2 mg/mL poly-L-lysine-polyethylene-glycol (Surface Solutions), rinsing with Milli-Q water, and blow-drying with nitrogen gas. Passivated chambers were used within 1 day. Solutions containing proteins were pipetted into the chamber and the chamber was hermetically sealed with VALAP (equal weights of vaseline**,** lanolin, and paraffin wax).

Total internal reflection fluorescence (TIRF) microscopy

Samples were imaged with a Nikon Apo TIRF 100x/1.49 NA oil objective mounted on an Eclipse Ti microscope (Nikon) using 491 nm and 561 nm laser lines. Images were acquired with a QuantEM 512SC EMCCD camera (Photometrics).

Transmission electron microscopy

Commercial carbon coated copper grids (CF300-Cu, Electron Microscopy Sciences) were glow discharged (EMS 500 sputter coater, Electron Microscopy Sciences) right before the protein solutions were pipetted onto the grids. Samples were incubated for at least 30 minutes on grids in a humid environment to make sure enough material was adsorbed onto the grids. The samples were stained with Nano-W, a 2% negative stain based on an organo-tungsten compound (Nanoprobes), or a 2% uranyl acetate solution (Nanoprobes). The samples were examined with either a JEOL 1400 (120 kV) electron microscope at Imagif (Gif sur Yvette, France) equipped with a SC100 Orius CCD camera or with a Philips CM12 (120 kV) electron microscope at Imagopole (Institut Pasteur, France), or a FEI Tecnai Spirit (120 kV) electron microscope (Institut Curie, France). Two dimensional image processing according to published procedures (SPIDER software [550]) was performed by Dr. A. Bertin [500].

Sample preparation

Recombinant fly (His_6-DSep1, DSep2 and Strep-Pnut) and human (His_6-hSep2, hSep6 and Strep-hSep7) septin complexes purified by using a HisTrap FF crude column (GE Healthcare) followed by a StrepTrap HP column (GE Healthcare) were provided by F. Iv and Dr. M. Mavrakis. Recombinant budding yeast septin complexes (Cdc3, Cdc10, Cdc11 and His_6-Cdc12) purified by using either a

nitrilotriacetic acid-agarose beads (Qiagen) or a HisTrap FPLC column (GE Healthcare) were provided by Dr. A. Bertin. Fly and human septins were stored in 50 mM Tris-HCl pH 8, 5 mM DTT, 300 mM KCl and 5 mM $MgCl_2$ at -80°C. Yeast septins were stored in 50 mM Tris-HCl pH 8 and 300 mM NaCl at -80°C. Protein concentrations were determined by optical absorption measurements at a wavelength of 280 nm, using extinction coefficients of 156320 $M^{-1} \cdot cm^{-1}$ for fly septins, 161423 $M^{-1} \cdot cm^{-1}$ for human septins, and 247080 $M^{-1} \cdot cm^{-1}$ for budding yeast septins. Septins were diluted to the desired concentration either in the corresponding storage buffer or to the polymerization buffer (20 mM Imidazole-HCl pH 7.4, 1 mM DTT, 0.1 mM MgATP, 50 mM KCl and 2 mM $MgCl_2$), followed by immediately adsorbing them on grids for EM sample preparation. To obtain higher-order septin structures by dialysis, septins at concentration of 2.5 μM (yeast septins) or 5 μM (fly/human septins) were dialyzed by using a cellulose membrane with a molecular weight cut-off 10,000 Dalton (Thermo Scientific, Etten-Leur, the Netherlands) overnight at 4°C against buffers containing 50 mM KCl and, when present, 20 mM Tris pH 8, 1 mM DTT and 2 mM $MgCl_2$. For TIRF microscopy samples, methylcellulose (0.1% w/v) was included to confine the filaments in a thin quasi-2D layer at the coverslip surface. Moreover, 1 mM trolox was included to prevent blinking, and an oxygen scavenging mixture of 2 mM protocatechuic acid and 0.1 μM protocatechuate 3,4-dioxygenase was included to minimize photobleaching [415].

5.6 Acknowledgements

Experiments were performed in collaboration with José Alvarado (AMOLF, Amsterdam), Manos Mavrakis (CNRS/Aix-Marseille University) and Aurélie Bertin (Institut Curie, Paris). We thank François Iv (Aix-Marseille University) and Marjolein Kuit-Vinkenoog (AMOLF, Amsterdam) for protein purification, and Magdalena Preciado López (AMOLF, Amsterdam) for insightful discussions and help with TIRF microscopy.

CHAPTER 6. Septins bind, bundle and curve actin filaments

During animal cell division, actin filaments and myosin II motors assemble into a contractile ring in the middle of the mitotic cell, which drives cell constriction. Despite the essential roles of actin and myosin motors in the contractile ring, the molecular mechanisms that regulate the assembly and constriction of the ring are unclear. Septins, a conserved component of the contractile ring, have been suggested to contribute structurally and mechanically to the stabilization and contraction of the ring. A close interplay between septins and the actin cytoskeleton has been proposed. However, the nature of this interplay remains elusive. Here, we reconstitute a cell-free model system based on purified actin and septins to study their interaction in the absence of additional binding partners. We show by co-sedimentation assays and fluorescence microscopy that septins bind to actin filaments directly. Strikingly, we find that septins bundle and curve actin filaments into rings and curved bundles. We find that the actin bundle morphology depends on the polymerization state of the septins. By time-lapse fluorescence imaging of septin-mediated actin bundle formation, we find that septins are capable of stabilizing bent segments of actin filaments and bundles. Our findings suggest that septins may stabilize and potentially contribute to the formation of the contractile ring during cell division.

The contents of this chapter are based on:

Mavrakis, M., Azou-Gros, Y., **Tsai, F.-C.***, Alvarado, J.*, Bertin, A.*, Iv, F., Kress, A., Brasselet, S., Koenderink, G. H. and Lecuit, T. (Manuscript under review)
Septins promote F-actin ring formation by cross-linking actin filaments into curved bundles. *authors contributed equally

Alvarado, J.*, **Tsai, F.-C.***, Bertin, A., Iv, F., Lecuit, T., Koenderink, G. H. and Mavrakis, M. (Manuscript in preparation)
Mechanistic insights into actin filament bending and bundling by septins. *authors contributed equally

6.1 Introduction

In animal cells, the actin cytoskeleton exhibits an astounding diversity of architectures with different biological functionalities [551]. Isotropic crosslinked networks of actin filaments form a thin (0.1 – 0.2 μm) cortical layer [46] [47] [48] that provides shape stability to the plasma membrane [49]. In cells crawling on flat substrates, branched actin networks in the front of the cell help push the plasma membrane forward [41] [40] [42]. Bundles of aligned actin filaments generate membrane protrusions known as filopodia that act as antennae to explore the extracellular environment [43] [45]. Also, contractile actin-myosin II bundles form in the cytoplasm known as stress fibers [92] [93], which contribute to mechanosensing [95], Moreover, during cytokinesis, actin filaments and myosin motors form a contractile ring at the cell equator that helps to divide the cell by contractile forces [90] [89]. All these diverse architectures are generated and dynamically regulated by a multitude of actin binding proteins (ABPs) that regulate actin filament length, control connectivity, or exert forces [52] [40] [35].

An important determinant of actin network architecture is the nature of the crosslinking proteins that are present. Crosslinking ABPs generally have two actin-binding domains that can connect two actin filaments together. Bottom-up approaches based on simplified cell-free model systems have shown that certain crosslinkers create preferentially bundles composed of aligned actin filaments whereas others generate preferentially isotropically crosslinked actin filament networks [231] [163]. However, it remains poorly understood how these actin network architectures emerge from the molecular properties of the crosslinker protein. One important factor appears to be the molecular geometry of the ABPs [552]. Small ABPs such as fascin [331], fimbrin [456] [553] or espin [458] tend to pack actin filaments into tight bundles, whereas larger ABPs such as α-actinin [454] [554], filamin [555] [556] or rigor-heavy meromyosin [457] prefer to crosslink actin filaments into networks composed of both single filaments and bundles. However, the molecular geometry of ABPs is not the only factor that determines the network architecture. The concentration of the ABPs for instance also strongly influences the morphology of the network: the very same crosslinker can form randomly crosslinked networks at low concentration, but composite or purely bundled networks at high concentration [454] [557] [558] [559] [458] [560] [333]. A third key factor is probably the crosslinker binding affinity [559] [561] [562] [563] [564]. It was shown that when modifying the binding affinity of α-actinin to actin by varying the temperature, an actin network can be driven from a randomly crosslinked architecture (at a higher temperature) to a bundled network (at a lower temperature) [559]. Also, the relative kinetics of actin polymerization and crosslink (un)binding influences the architecture of actin networks, as demonstrated for α-actinin [560] [558], filamin [565] and fascin [330].

Despite their relative simplicity, cell-free model systems have already provided important insights into the mechanistic basis of the formation of complex cellular structures such as actin bundles assembled by fascin in filopodia or branched actin networks organized by the actin-related protein 2 and 3 complex (Arp2/3) in lamellipodia [443] [43] [444] [445]] [165] [163]. However, one actin-based structure that so far has not been much studied via cell-free model systems is the contractile ring composed of actin and non-muscle myosin II, which drives cell division [566] [89] [90]. Similar contractile rings are found at the furrow canals in the early *Drosophila* embryos undergoing cellularization [567]. Multiple ABPs are associated with the contractile ring, such as formin, which nucleates actin, and cofilin, which severs actin filaments [568] [569] [90] [570] [89]. In addition, septins are a conserved component of the contractile ring [480] [96] [100].

Septins have been proposed to play a role in the structural and mechanical stabilization of the contractile ring [89] [90] [97] [102] [571] [572] [573] [574]. They can bind to acidic phosphatidylinositol phosphate (PIP) lipids [517] [575] as well as to the major contractile ring proteins anillin [484] and non-muscle myosin II [488] [486]. A study of Kinoshita and coworkers [484] showed no direct interaction of human septins with F-actin; therefore, it is generally thought that septins bind to actin indirectly through anillin and/or myosin II. However, septins are closely associated with various actin structures. Septins localize to stress fibers [487] [484] [485] [486] [576]. Depletion of septins by siRNA leads to loss of actin stress fibers, while disruption of actin filaments by cytochalasin D results in septin rings in the cytoplasm [484]. Septins are also part of the cortex underneath the plasma membrane, where they significantly contribute to cortical rigidity [577] and prevent bleb formation at the leading edge of migrating T-lymphocytes [481]. It remains unclear whether these roles at the cell cortex occur in synergy with the actin cytoskeleton. Thus, although co-localization of septins with actin bundles and the cell cortex has been documented, the question remains whether they have the ability to interact directly with actin.

Here we use a cell-free model system composed of purified actin and recombinant septins to resolve the question whether septins can bind actin filaments and control actin network architecture without the help of additional binding partners. We demonstrate by co-sedimentation assays and two-color fluorescence microscopy that recombinant fly septins bind actin filaments, with an affinity similar to that of more well-known actin crosslinkers. We furthermore show by fluorescence and electron microscopy that both recombinant fly and human septins mediate assembly of actin filaments into bundles with a comparable morphology, suggesting a conserved function of septins to interact with actin. Depending on septin concentration, the actin-septin bundles are curved, ring-like, or straight. The septin concentration dependence can be explained by the polymerization state of the septins, which form oligomers at low

concentration but assemble into rigid bundles at higher concentration (see Chapter 5). By time-lapse imaging of the formation of actin bundles and rings in the presence of septins, we observe that septins have the ability to stabilize curved actin filaments and bundles. Also, septins zipper actin filaments onto pre-existing actin rings, resulting in ring thickening. Our results suggest that septins may help stabilize the curved contractile actomyosin ring during cell division and *Drosophila* cellularization directly by bending and crosslinking actin filaments.

6.2 Results

Septins bind directly to actin filaments

To assess whether fly septins bind directly to actin filaments (F-actin), we perform an *in vitro* co-sedimentation assay. Recombinant *Drosophila melanogaster* (fly) DSep1-DSep2-Pnut septin complexes purified from *E.coli* are incubated in an actin polymerization buffer (containing 50 mM KCl and 2 mM $MgCl_2$) with a range of concentrations of rabbit skeletal muscle actin, followed by high speed (120,000g) centrifugation. With increasing actin concentration, we observe progressively more pelleting of the DSep2 subunit of the septin complex (*inset* of Fig. 1A). At actin concentrations above 10 μM, septin binding reaches a saturation level close to 100% (Fig. 1A). By fitting the binding curve to a quadratic function (see *Materials and Methods*) [578], we extract an equilibrium dissociation constant (or binding affinity), K_d, of 1.2 ± 0.5 μM. This affinity is comparable to that of other actin binding proteins, whose K_d values typically range from 0.1 μM to 3 μM, as shown for fascin [579] [580] [581], filamin [582], fimbrin [456], cortexillin [583], and α-actinin [584] [454] (Table 1).

Actin binding proteins	Dissociation constant (μM)	Reference
Human fascin	0.15	[580]
Human fascin	0.3	[581]
Vertebrate fascin 2b	0.37	[579]
Filamin	0.46*	[582]
Fission yeast fimbrin 1	0.65	[456]
Dictyostelium Cortexillin I	0.23	[583]
Acanthamoeba α-actinin	4.7	[454]
Acanthamoeba α-actinin	2.7**	[584]
Dictyostelium α-actinin	2.7**	[584]
Chicken gizzard α-actinin	1.2**	[584]

Table 1. Dissociation constants of actin binding proteins. *extracted from the ratio of association and dissociation rate constants. ** measured at 37°C.

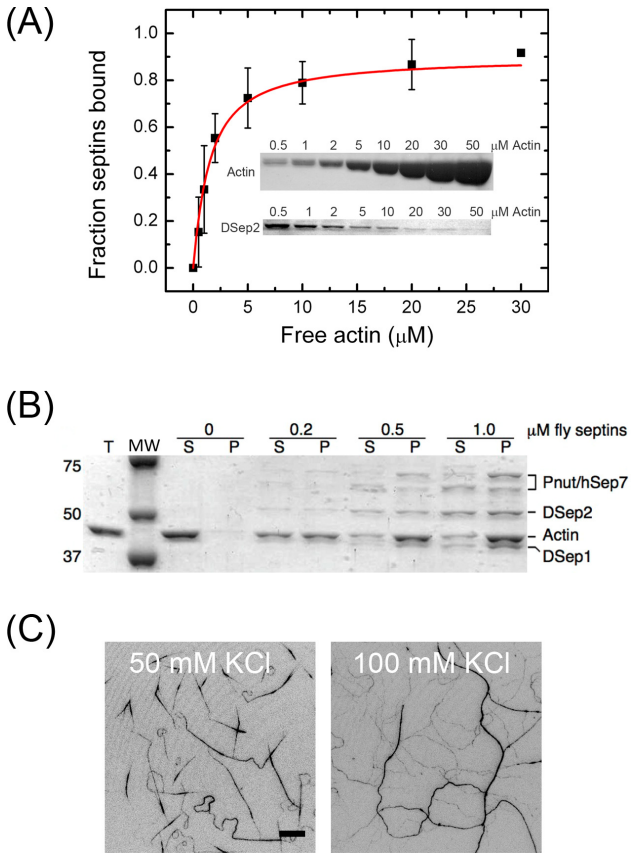

Figure 1. Recombinant fly septins bind to and bundle actin filaments. (A) Plot of the fraction of bound septins to actin filaments, measured using a high speed (120,000g) cosedimentation assay. The concentration of septins is fixed at 1 μM while actin is increased from 0.5 to 30 μM as indicated. The Coomassie-stained gels show actin filaments present in the pellets (*top panel*) and a progressive depletion of fly septin DSep2 in the supernatants (*bottom panel*) with increasing actin concentration. Each data point shows the mean ± standard deviation (3 independent experiments), except the data point of actin at 30 μM (2 experiments, no error bar shown). The equilibrium dissociation constant K_d of 1.2 ± 0.5 μM is extracted by fitting the data to a quadratic function (red line). (B) The Coomassie-stained gel shows supernatant (S) and pellet (P) fractions after low speed (12,000g) cosedimentation of 1 μM actin with increasing concentrations of fly septins (0.2, 0.5 and 1 μM, as indicated). Molecular weights are indicated on the left; the positions of actin and septin bands are shown on the right. T: total actin, MW: molecular weight marker. (C) Actin bundles generated by septins at different salt (KCl) concentrations observed by TIRF (contrast is inverted). Concentrations of septins and actin are 1 μM. To visualize actin, AlexaFluor 488 labeled actin at 10 mole% of the total actin concentration is included. Scale bar: 10 μm.

To test the crosslinking ability of fly septins to F-actin, we perform a low speed (12,000g) co-sedimentation assay. With increasing septin concentration, we observe progressively more F-actin in the pellet and less F-actin in the supernatant (Fig. 1B). Since single actin filaments are not pelleted at low speed (condition labeled *0 μM septin* on the gel), this result demonstrates that septins crosslink and/or bundle F-actin. Together, our results provide biochemical evidence that fly septins directly bind and crosslink F-actin in the absence of other proteins. We note that the faint band running below full-length Pnut is identified as Pnut by mass spectrometry, which reflects the proteolytic sensitivity of the C-terminus of Pnut when fly septin complexes are purified by a one tag (a His_6 tag on Pnut) purification scheme (Fig. 1B). In the high speed co-sedimentation assay and all the experiments described below, septins were purified by a two tag (a His_6 tag on DSep1 and a Strep tag on Pnut) purification scheme, which enriches for complexes with full-length Pnut and minimizes the isolation of substoichiometric septin complexes (see Chapter 5). The faint band just above full-length Pnut that consistently stays in the supernatant is the bacterial chaperone DnaK, identified by mass spectrometry (Fig. 1B).

Several actin binding proteins, such as fascin [585], α-actinin [586], dystrophin [587], calponin [588], tropomyosin [589] and myosin binding protein C [590], interact through positively charged residues with actin filaments, which are themselves negatively charged at neutral pH since their isoelectric point is 5.3 [115] [116]. It has been shown that a high ionic strength buffer (above 150 mM KCl) diminishes these electrostatic interactions [586] [587] [588]. To test whether the binding of septins to F-actin also depends on ionic strength, we observe F-actin in the presence of septins by total internal reflection fluorescence microscopy (TIRF). Note that in the following experiments, the actin concentration is fixed at 1 μM, unless specified otherwise. Consistent with the low speed co-sedimentation assays, we observe actin bundles at the standard ionic strength (50 mM KCl in the polymerization buffer), as shown in Fig. 1C. This observation directly confirms that septins are able to bind to and bundle F-actin. Interestingly, the bundling ability of septins seems somewhat weaker at a higher ionic strength (100 mM KCl), indicated by the presence of actin filaments in the background. Thus, these observations indicate that the septins bundle F-actin in a salt-dependent fashion, which indicates that the bundling ability of septins is determined at least in part by electrostatic interactions.

The morphology of septin-mediated actin bundles depends on septin concentration

It has been shown that the architecture of F-actin networks reconstituted in the presence of actin-binding crosslinking proteins is strongly influenced by the concentration of the crosslinker (α-actinin [560] [454] [559] [558], scruin [557],

espin [458], filamin [591] and fascin [333]). For example, in case of α-actinin, isotropic networks are formed at low crosslinker concentration, composite networks of coexisting bundles and single filaments at somewhat higher concentration [560] [454] [554], and clusters of actin bundles at an even higher concentration of α-actinin [560] [454] [554]. A similar transition from a crosslinked network of single actin filaments to a network of bundles with increasing crosslinker concentration has been observed in a coarse-grained theoretical model [563].

To test whether the fly septin concentration also impacts the morphology of actin bundles, we polymerize actin in the presence of fly septins at a wide range of septin concentrations: from 0.01 to 3.8 μM. To ensure that actin filaments are freely diffusible in the microscope chamber, we passivate the surfaces with poly-L-lysine-polyethylene-glycol. We use a dilute actin solution (1 μM) to ensure that there is limited overlap between the filaments (Fig. 2, *no septins*). When septin is present, we observe a remarkably wide range of actin bundle morphologies (Fig. 2). At the lowest septin concentrations of 0.01 and 0.02 μM, we mostly observe single actin filaments and rarely detect bundles. When increasing the septin concentration to 0.05 μM, we start to observe curved actin bundles interspersed with single actin filaments. These bundles often exhibit a frayed brush-like end composed of multiple actin filaments (better visible in Fig. 3A). At a septin concentration of 0.1 μM, actin bundles are interconnected and form a sparse bundle network with single actin filaments branched out from the bundles (Fig. 2 and 3A). Strikingly, we observe ring, loop and lasso structures, with diameters around 5 – 10 μm (Fig. 3B). These structures are either isolated, without any connections to other bundles, or they adhere to other bundles, rings or lassos. When the septin concentration is raised to 0.2 or 0.3 μM, we observe predominantly closed rings or lassos at the ends of bundles (Fig. 2 and 3C). These rings, with diameters around 1 – 1.5 μm, are smaller than those detected at the septin concentration of 0.1 μM (Fig.2 and 3B). Moreover, they are either isolated, connected with each other forming grape-like clusters, or are interconnected by bundles (Fig.2 and 3C). Further increasing the septin concentration to 0.5 – 1 μM, we observe mainly winding or zigzag bundles that interconnect with each other (Fig. 2 and 3D). At this septin concentration, much fewer ring-like structures are found (Fig. 3D). At septin concentrations above 1 μM, we observe straight, needle-like bundles with sharp kinks (Fig. 2 and 3E). Together, our observations demonstrate that the septin concentration strongly determines the morphology of actin bundles.

To resolve the ultrastructure of actin bundles assembled by septins, we observe them by transmission electron microscopy (EM). We detect the same range of actin bundle morphologies as seen by fluorescence microscopy (Fig. 4). At a septin

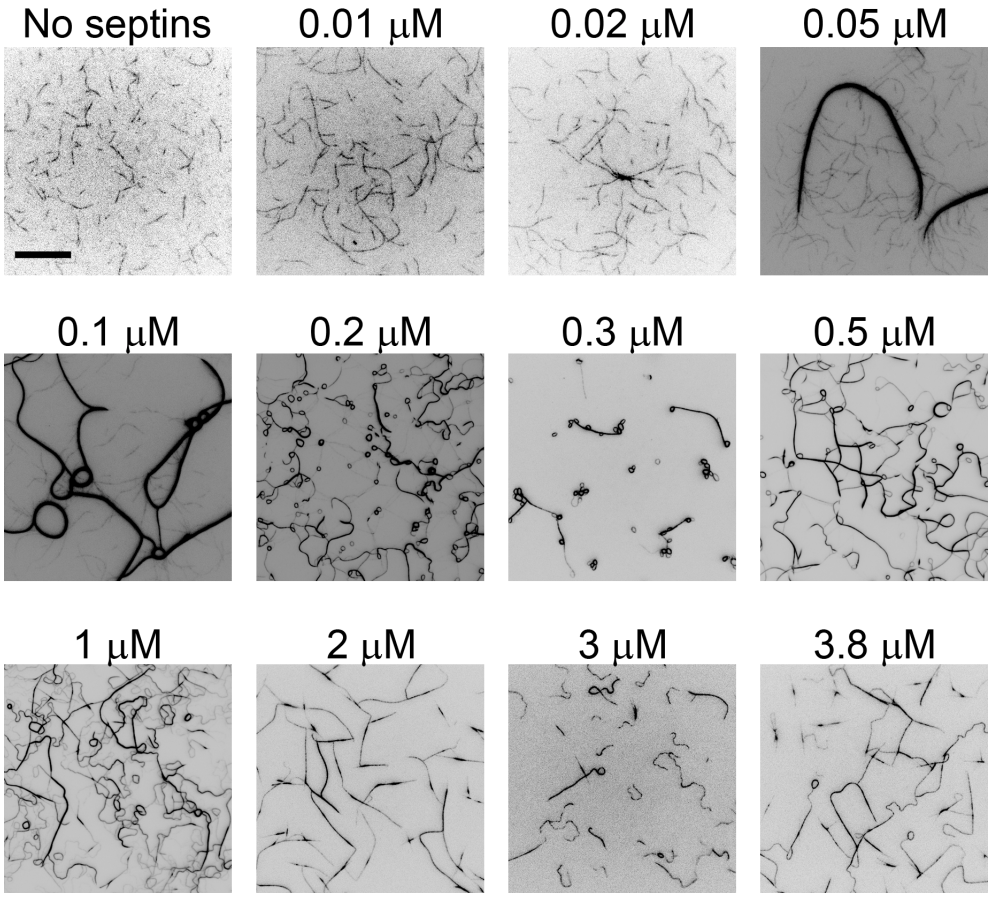

Figure 2. Morphology of actin bundles polymerized in the presence of fly septins. The concentrations of fly septins are indicated and the concentration of actin is fixed at 1 μM. The contrast of images obtained by TIRF is inverted. Scale bar: 20 μm.

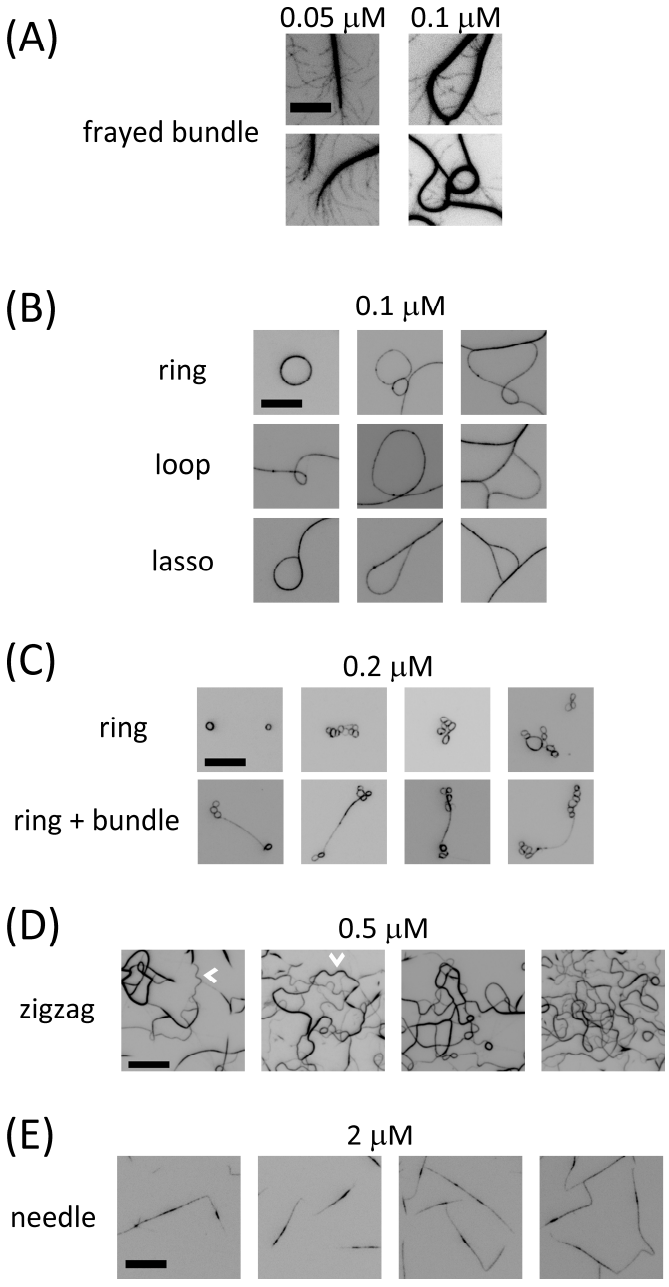

Figure 3. Gallery of actin structures assembled by fly septins (inverted contrast TIRF images). Septin concentrations are indicated. In (D), two examples of zigzag-like bundle structures are indicated by the white arrowheads. Scale bars: 10 μm.

concentration of 0.1 μM, we detect actin bundles embedded in a background full of septin hexamers (Fig. 4A-C). The bundles always appear loose and are composed of 2 - 22 actin filaments. Increasing the septin concentration to 0.2 μM, curved actin bundles, rings and lassos appear (Fig. 4D, E and G), with single actin filaments and septin hexamers present in the background. Besides actin bundles composed of densely packed actin filaments (Fig. 4F), we sometimes observe single actin filaments splaying out from a curved bundle or bundles that appear broken (Fig. 4 H and I). At a septin concentration of 0.5 μM, we observe actin bundles forming rings, entangled loops and lassos (Fig. 4J-M and P). All bundles are composed of densely packed, aligned actin filaments (Fig. 4N and O). Occasionally, we observe a ∞ shaped bundle (Fig. 4K). Sometimes, we detect a bundle that branches into one part that forms a straight bundle and another part that curves into a ∞ shape (Fig. 4J and M). Also, we sometimes observe actin bundles that are decorated by proteins that are presumably septins (Fig. 4 Q and R). We do not observe any periodic decoration patterns of these proteins on the actin bundles.

Septin polymerization influences the architecture of actin bundles

Unlike most actin crosslinking proteins that are either monomers having two actin-binding sites or dimers that present two actin-binding sites, septins have the ability to polymerize into filaments, bundles and rings (see Table 1, Chapter 5) [490] [96]. As presented in Chapter 5, we find that above a certain septin concentration, referred to as the critical concentration, fly and human septin complexes assemble into straight, rigid bundles in the absence of actin. In our actin polymerization buffer, the critical concentration for filament/bundle formation is around 0.1 - 0.2 μM for fly septins and 0.05 μM for human septins. It is conceivable that this concentration-dependent septin assembly contributes to the diversity of F-actin bundle morphologies that we observe. Indeed, we detect straight and needle-like actin bundles at high fly septin concentrations (> 0.5 μM), where septins form bundles, whereas we observe curved actin bundles, including rings and lassos, at low septin concentrations (< 0.2 μM) where septins are present as oligomers (observed by EM). We thus hypothesize that septin hexamers promote the assembly of curved actin bundles, whereas septin bundles facilitate the formation of straight actin bundles.

To test this hypothesis, we polymerize actin in the presence of pre-formed fly septin bundles (Fig. 5). Consistent with our hypothesis, we observe that straight actin bundles co-localize with straight septin bundles, whereas curved actin bundles, rings and lassos exhibit spotty decorations of septins. These septin spots likely correspond to septin hexamers or clusters thereof, though more detailed imaging (for instance by EM) will be needed to verify this. Nevertheless, our observations indicate that septin polymerization influences the morphology of

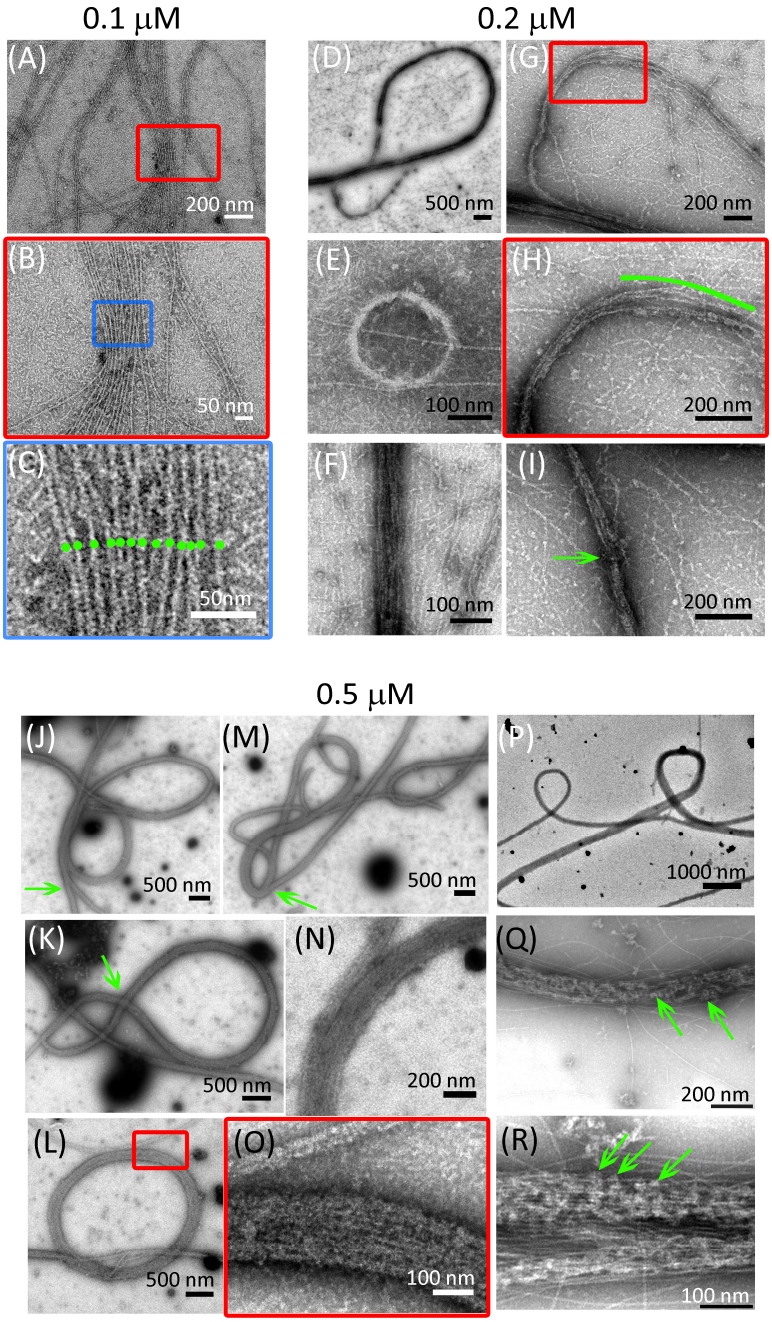

Figure 4. Electron micrographs of actin structures polymerized in the presence of fly septins. The concentration of actin is fixed at 3 μM, except for (Q) and (R) where the actin concentration is 1 μM. The concentrations of fly septins are indicated. Images (B), (C), (H),

and (O) are zoomed-in areas of the small rectangular areas indicated in (A), (B), (G), and (L), respectively. The green dots in (C) indicate single actin filaments (total 13 filaments) within an actin bundle. In (H), the green line indicates a segment of a bundle in which actin filaments are not tightly packed. In (I), the green arrow indicates a bundle that appears broken. In (J) and (M), the green arrows indicate actin bundles that appear to merge. In (K), the green arrow indicates an intersection of a curved actin bundle. In (Q) and (R), the green arrows indicate proteins, presumably septins, that decorate the actin bundles.

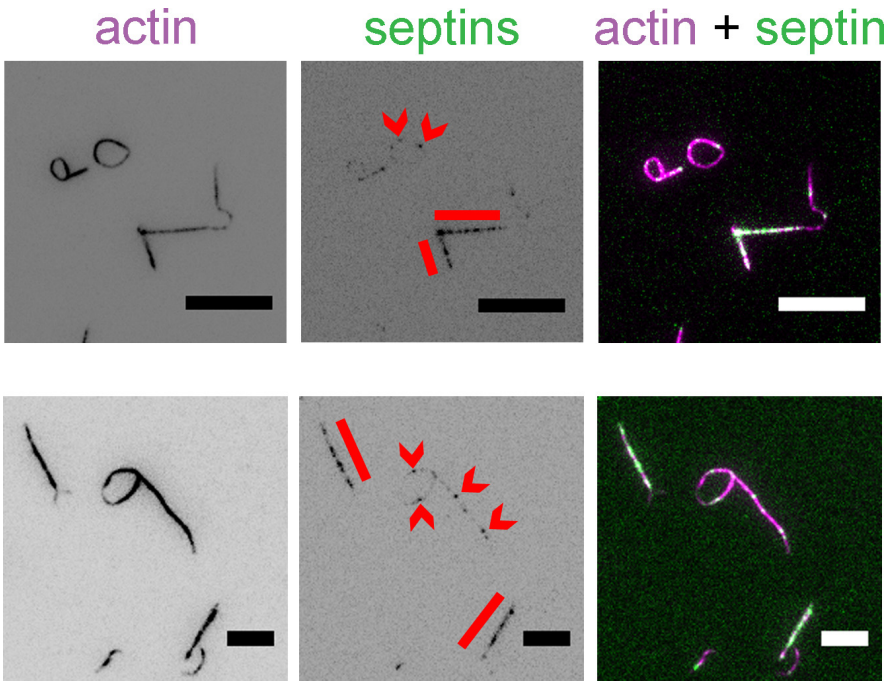

Figure 5. Localization of fly septins on actin bundles that are generated by polymerization in the presence of pre-polymerized fly septin bundles at a concentration of 2.2 μM. Images in the *third column* are merged images of the corresponding actin (*first column*, inverted contrast) and septin (*second column*, inverted contrast) fluorescence images. The red lines indicate straight septin bundles while the red arrowheads indicate the spotty decoration of septins on actin bundles. In the *third column*, actin is shown in purple and septins are shown in green. Scale bars: 10 μm (*top row*) and 5 μm (*bottom row*).

actin bundles: septin bundles are templates for the formation of straight actin bundles, whereas septin hexamers preferentially assemble curved actin structures.

Localization of fly septins on actin bundles

To resolve septin localization on the actin bundles, we polymerize actin filaments in the presence of fluorescent fly septins labeled with AlexaFluor 488. Fluorescent fly septins decorate actin bundles, again confirming that septins directly bind to and bundle actin filaments (Fig. 6). At a septin concentration of 0.1 μM, we observe curved actin bundles decorated with fluorescent septins in a

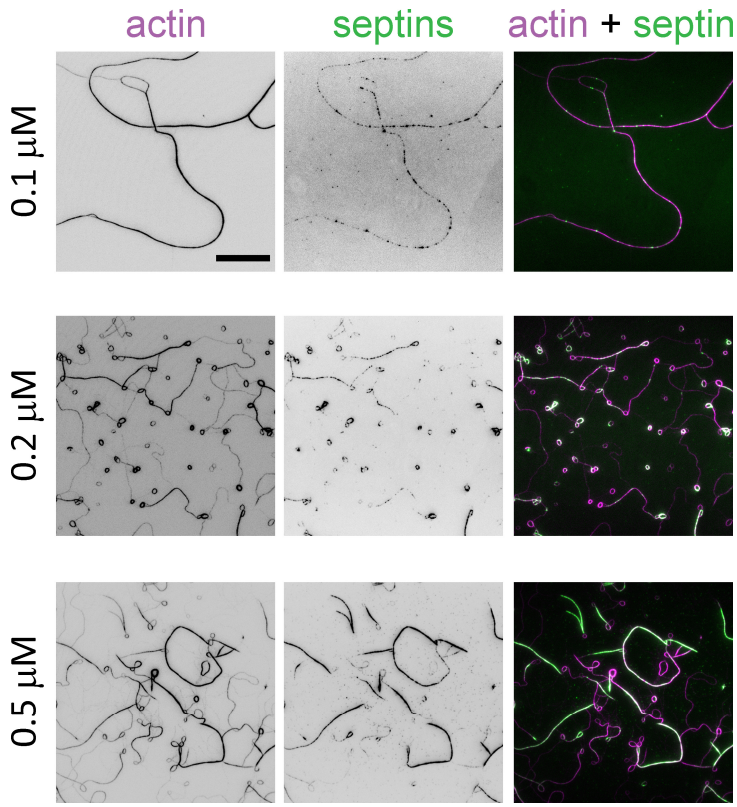

Figure 6. Localization of fly septins on actin bundles at increasing septin concentration, as indicated. Inverted contrast TIRF images of actin and septin fluorescence signals are shown in the *first and second column*, respectively. Images in the *third column* are merged from the corresponding actin and septin fluorescence images, with actin shown in purple and septins in green. Scale bar: 20 μm.

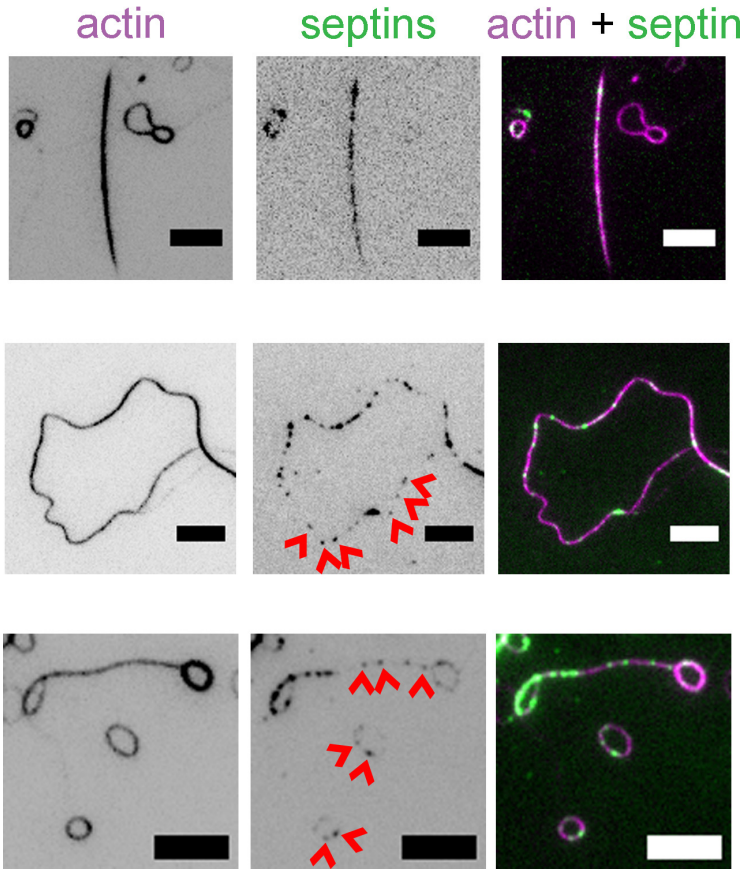

Figure 7. Localization of fly septins on actin bundles. The concentration of fly septins is 0.2 μM. Images in the *third column* are merged images of the corresponding actin (*first column*, inverted contrast) and septin (*second column*, inverted contrast) fluorescence images. The red arrowheads indicate the spotty decoration of septins on actin bundles. In the *third column*, actin is shown in purple and septins in green. Scale bars: 5 μm.

spotty or punctuate manner. Further increasing the septin concentration to 0.2 μM, we observe both straight and winding actin bundles that are decorated with spotty septin fluorescence signals (Fig. 6 and 7). On ring-like actin structures, we also observe a spotty decoration of septins (Fig. 7). At a septin concentration of 0.5 μM, we observe straight actin bundles and rings, with a much higher septin signal on the straight bundles (Fig. 6). This observation may indicate a strong bundling of septins. However, it is also possible that a higher septin signal simply reflects a thicker actin bundle.

In an attempt to resolve septin localization on actin bundles at a higher resolution, we tag septins with electron-dense nickel-gold particles that bind to the His-tagged fly septin complexes. We observe that the gold particles decorate septin bundles homogeneously across the bundle width and length (Fig. 8A and B). In septin-mediated actin bundles, gold particles decorate the bundle in a more random fashion (Fig. 8C-F). Based on these images, we suspect that the actin/septin filaments within these bundles may not organize in a repetitive and very well-structured pattern. Note that the accumulation of gold particles on the edges of bundles (Fig. 8A and B) is most likely due to a collapse of the bundles on the EM grid. Unfortunately, due to the comparable morphological appearance of septin and actin bundles, it is difficult to distinguish the localization of septin and actin filaments/bundles in the mixed bundles. To distinguish actin bundles from septin bundles by EM, we rely on either the helical structure of actin filaments, exemplified in Figure 4(C), or interpret ring-like structures as being actin rings because we do not observe ring-like structures of septins by themselves, as shown in Chapter 5, Figure 5. However, in the future, it will be important to distinguish actin and septin structures more directly in EM images by using GFP-tagged septins or antibodies that interact with septins [500].

Mechanism of septin-mediated actin bundle formation: zippering and bending

To obtain insight into the mechanism determining the formation of actin bundles, we directly visualize their assembly upon polymerization of actin in the presence of septins using time-lapse imaging by TIRF (Fig. 9). Approximately 30 s after initiating actin polymerization, we observe short and mobile bundles together with rings (Fig. 9, *t = 0 min*). After ~10 min, connections between bundles start to appear. Network development occurs progressively within an hour (Fig. 9). Afterwards, the appearance of the network architecture does not change. This time scale is similar to the time scales observed for assembly of actin bundles in the presence of α-actinin [560].

During network development, we observe that freely fluctuating single filaments often rapidly adhere to pre-existing actin bundles after coming in close proximity, an event which we will refer to as zippering (exemplified in Fig. 10). This zippering event is similar to observations reported for bundling by filamin [565] and fascin [592]. The speed of the zippering event shown in Figure 10 is around 50 μm/min, which is slower than reported speed in case of zippering of actin filaments by fascin (more than 100 μm/min) [592]. Zippering of adjacent filaments or bundles also causes the formation of branched actin structures, building up interconnections in the network. The formation of lassos can occur through zippering as well. Figure 11 shows an example where two actin filaments that grow from one end of a pre-existing winding bundle (the “mother bundle”)

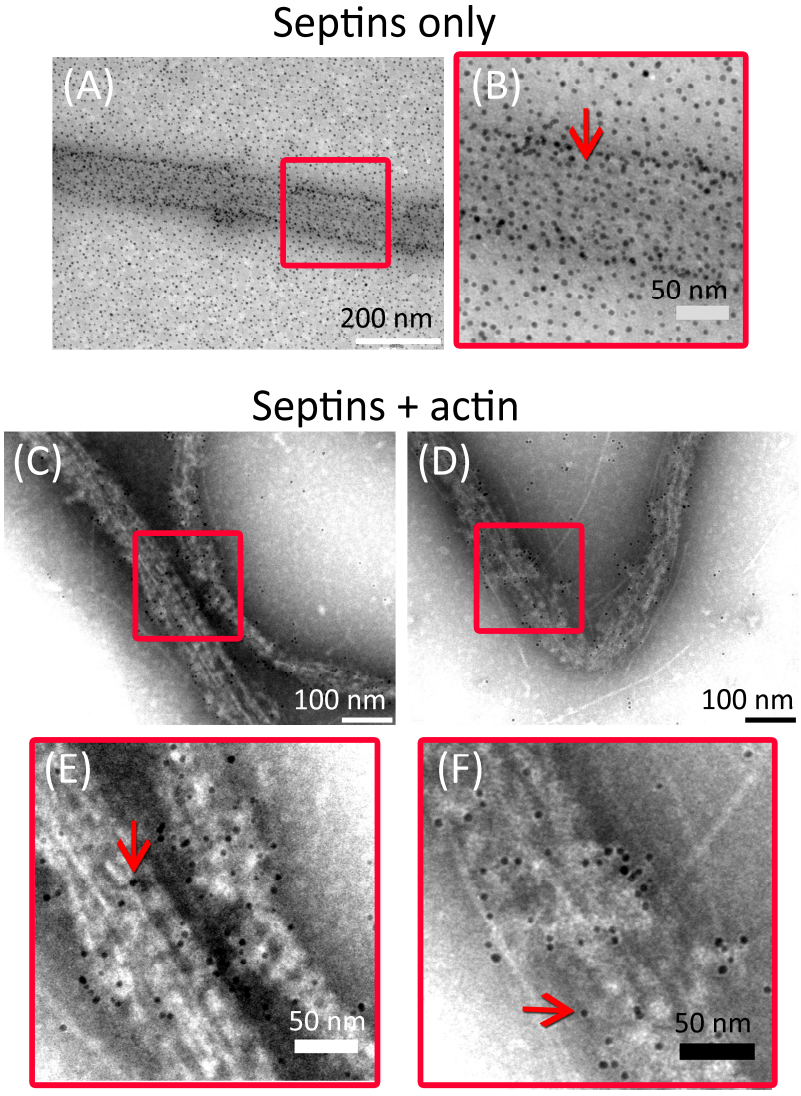

Figure 8. Electron micrographs of fly septin bundles ((A) and (B)) and actin filaments polymerized with septins ((C) - (F)) stained with Ni-NTA-Nanogold particles that bind to His-tagged DSep1. Images (B), (E) and (F) are zoomed-in areas of the small rectangular areas indicated in (A), (C) and (D), respectively. The red arrows indicate the Ni-NTA-Nanogold particles. In (A) and (B), the concentration of fly septins is 5 μM; in (C) - (F), the concentration of fly septins and actin is 0.5 μM and 2 μM, respectively

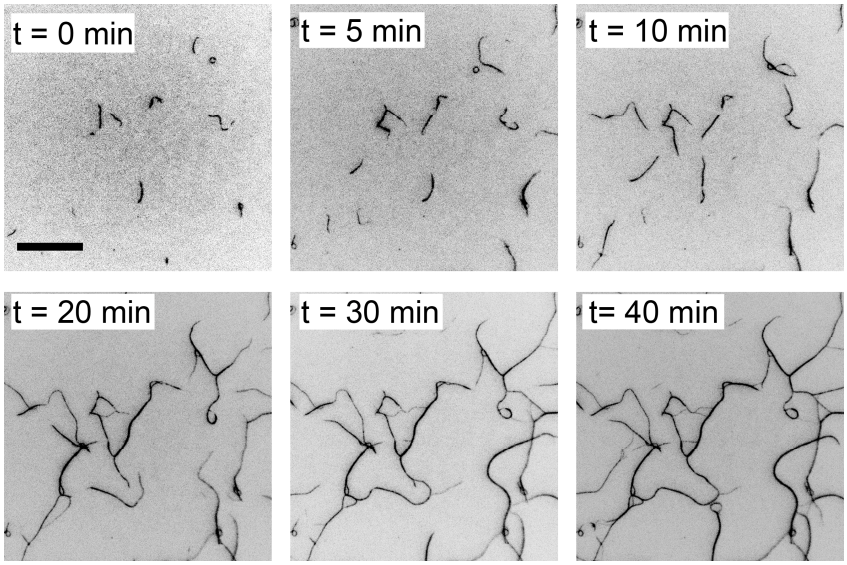

Figure 9. TIRF images (inverted contrast) of actin network formation (1 μM actin) in the presence of 0.5 μM fly septins. Time in minutes (min) is indicated. Actin polymerization is initiated approximately 30 sec before starting image recording (denoted as *t = 0 min*). Scale bar: 20 μm.

sequentially zip to it. Note that the lasso moves freely without adhering to the surface of the observation chamber.

Strikingly, septins can impose bends to growing actin bundles. Figure 12 shows an example where two thermally fluctuating filaments grow from one mother bundle. The filaments are zipped together (Fig. 12, blue arrow at *t = 1.02 min*), presumably by septins, followed by the stabilization of a bend (Fig. 12, blue arrow at *t = 4.53 min*) in the resulting bundle while the filaments are growing (Fig. 12, *t = 0 – 1.23 min*). Subsequently, another curving event occurs on the same actin bundle (Fig. 12, yellow arrow at *t = 24.87 min*). Interestingly, we observe that the first bend remains stable for approximately 25 min, but is then "smoothed out". The mechanism responsible for this smoothening event is unclear. It is possible that septin(s) at the bend unbinds, or that the formation of the second curved segment further along the bundle induces an internal stress that propagates along the bundle and stretches out the first curved segment. However, more careful investigation, preferably by two-color time-lapse imaging of both actin and septin, is needed to understand both the curvature-stabilizing and curvature-smoothening events.

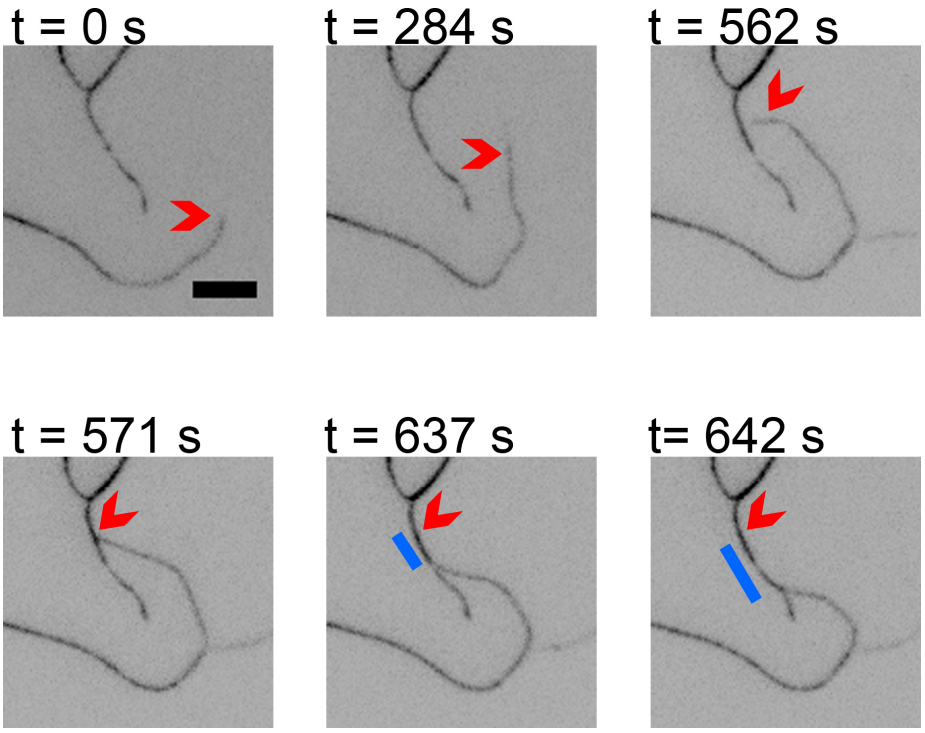

Figure 10. Zippering of actin bundles mediated by 0.5 μM fly septins. A freely fluctuating actin filament (indicated by the red arrowhead) zippers onto a pre-existing actin bundle. Note that the filament (indicated by the arrowheads at t = 0 s to t = 562 s) grows and thermally fluctuates before zippering onto the bundle (at t = 571 s). From t = 571 s to t = 642 s, the red arrowheads indicate the location where the filament initially binds to the bundle. The blue lines indicate the length over which filaments are zippered. The contrast of the TIRF images is inverted. Time in seconds (s) is indicated. Scale bar: 5 μm.

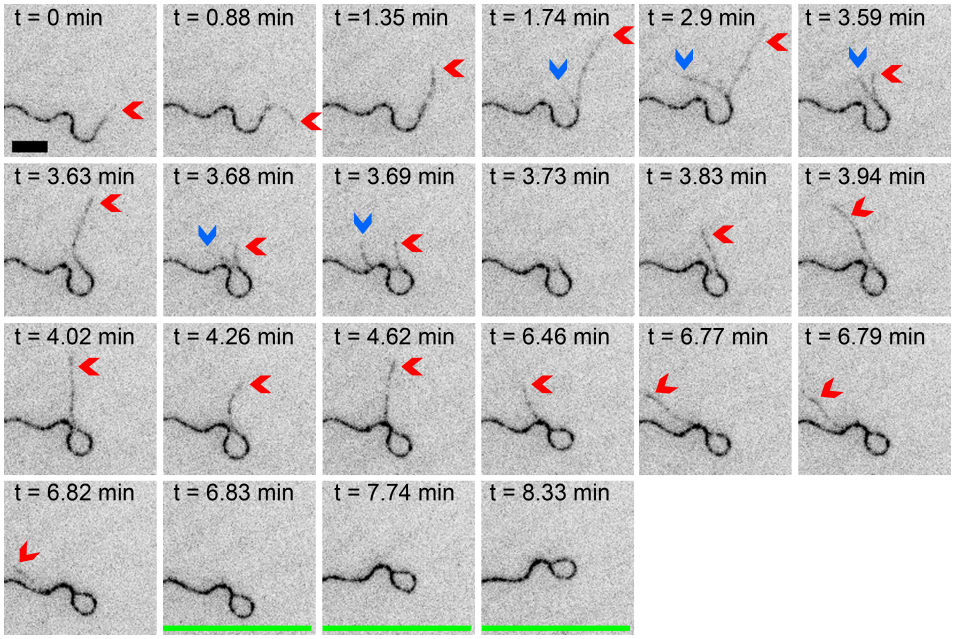

Figure 11. Time-lapse TIRF images (inverted contrast) of lasso formation in the presence of 0.1 μM fly septins. Two actin filaments (indicated by the red and blue arrowheads) grow from one end of a winding bundle and sequentially zipper onto the winding bundle. The green lines are drawn as a reference to show that the lasso moves freely (the field of view does not change during image recording). Time in minutes (min) is indicated. Scale bar: 5 μm.

The actin rings were often observed already within about 30 sec after initiating actin polymerization. It was thus impossible to resolve their formation mechanism. However, in some cases we observed that rings formed by zippering/wrapping of single actin filaments around a pre-existing lasso. Figure 13 shows an example where a lasso is first formed by a thermally fluctuating filament that curves sequentially, eventually resulting in an intersection with itself (Fig. 13, yellow arrow at *t = 4.85 min*). Since we do not observe disassembly of the intersection

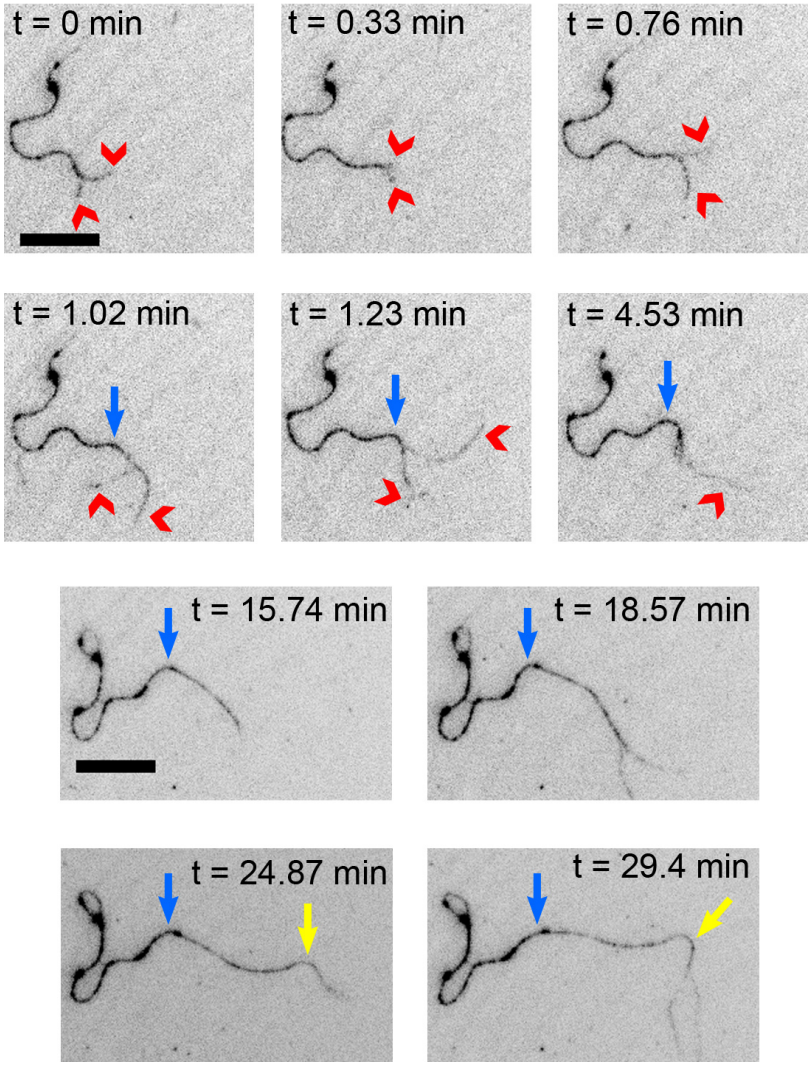

Figure 12. Time series showing bending of an actin bundle by fly septins. Two filaments growing from a winding actin bundle are indicated by the red arrowheads. The blue arrow at t = 1.02 min – 29.4 min indicates a bent actin bundle that appears first. A second bent segment of the same bundle is indicated by the yellow arrow at t = 24.87 min. After approximately 4.53 min of the formation of the second bent segment, the first bent segment, indicated by the blue arrow at t = 29.4 min, appears to "lose" its curvature. The concentration of septins is 0.1 μM. Time in minutes (min) is indicated. The contrast of all TIRF images is inverted. Scale bars: 10 μm.

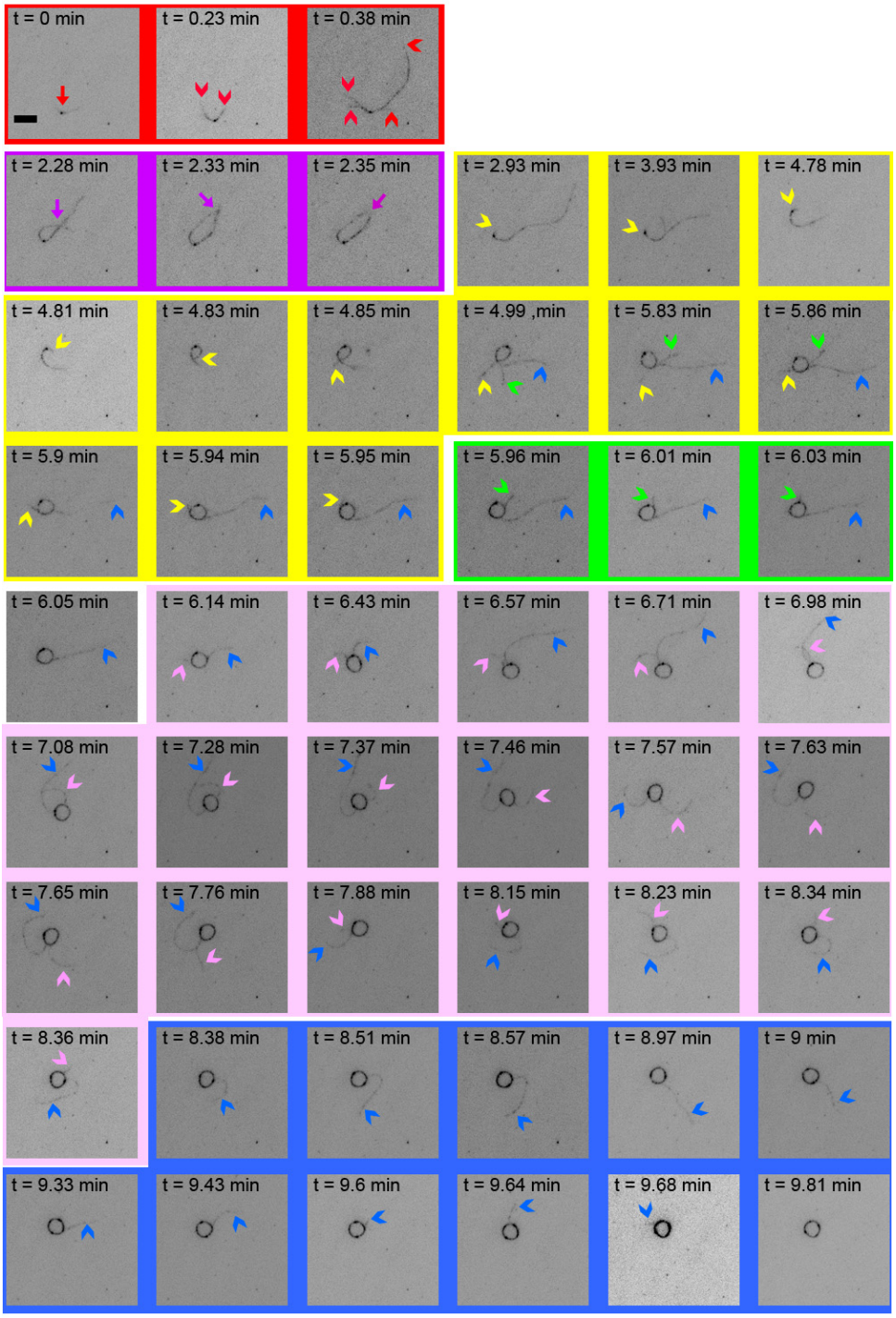
t = 0 min
t = 0.23 min
t = 0.38 min
t = 2.28 min
t = 2.33 min
t = 2.35 min
t = 2.93 min
t = 3.93 min
t = 4.78 min
t = 4.81 min
t = 4.83 min
t = 4.85 min
t = 4.99 ,min
t = 5.83 min
t = 5.86 min
t = 5.9 min
t = 5.94 min
t = 5.95 min
t = 5.96 min
t = 6.01 min
t = 6.03 min
t = 6.05 min
t = 6.14 min
t = 6.43 min
t = 6.57 min
t = 6.71 min
t = 6.98 min
t = 7.08 min
t = 7.28 min
t = 7.37 min
t = 7.46 min
t = 7.57 min
t = 7.63 min
t = 7.65 min
t = 7.76 min
t = 7.88 min
t = 8.15 min
t = 8.23 min
t = 8.34 min
t = 8.36 min
t = 8.38 min
t = 8.51 min
t = 8.57 min
t = 8.97 min
t = 9 min
t = 9.33 min
t = 9.43 min
t = 9.6 min
t = 9.64 min
t = 9.68 min
t = 9.81 min

Figure 13. Time-lapse micrographs of zippering and wrapping of actin filaments. At t = 0 min, actin filaments grow from the location indicated by the red arrow. From t = 0.23 min to t = 0.38 min, four filaments grow as indicated by red arrowheads. Note that due to the thermal fluctuations of the filaments it is difficult to distinguish them from one another. A strong fluctuation of the filaments can be seen from t = 2.28 min to 2.35 min, where a filament curves towards itself but returns to a relatively straight configuration, as indicated by the purple arrows. One filament as indicated by the yellow arrowhead (from t = 2.93 min to t = 4.85 min) curves in a clockwise manner to form a lasso. The same filament then wraps up to the lasso in a clockwise manner (from t = 4.99 min to t = 5.95 min) followed by the wrapping up of another three filaments in a clockwise manner (indicated by the pink arrowhead, from t = 6.14 min to t = 8.36 min) or a counterclockwise manner (indicated by the green (from t = 5.96 min to t = 6.03 min) and blue (from t = 8.38 min to t = 9.68 min) arrowheads). The septin concentration is 0.1 μM. Time in minutes (min) is indicated. The contrast of the TIRF images is inverted. Scale bar: 5 μm.

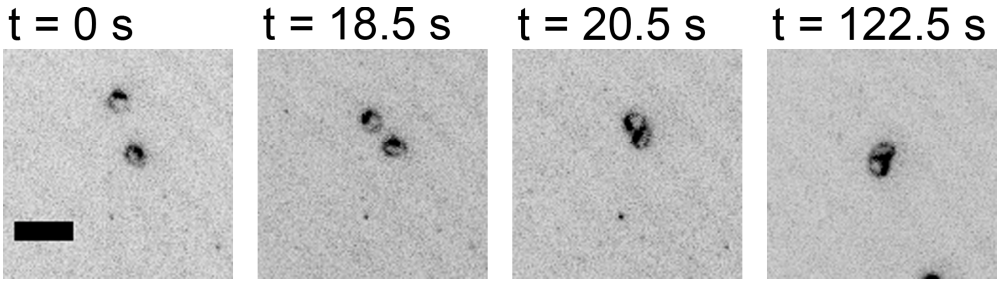

Figure 14. Formation of grape-like clusters of septin-mediated actin rings. The septin concentration is 0.2 μM. Time in seconds (s) is indicated. The contrast of the TIRF images is inverted. Scale bar: 5 μm.

point once formed, it is likely stabilized by septin crosslinking. The growing filament and other filaments that fluctuate around the lasso then sequentially wrap around the lasso either in a clockwise (Fig. 13, two events that are indicated by yellow and pink arrows) or counterclockwise (Fig. 13, two events that are indicated by green and blue arrows) manner to form a closed ring. We also frequently observe that isolated actin rings come together to form clusters. Figure 14 shows an example where two closed rings are stuck together to form a grape-like cluster.

Altogether, we conclude that septins assemble single actin filaments into straight or curved bundles, such as rings and lassos, by bending and zippering filaments/bundles together. Also, zippering events contribute to the formation of interconnected networks.

Septins crosslink parallel and anti-parallel actin filaments

It has been shown that many actin binding proteins such as α-actinin [454] [455] and fimbrin [456] interact with actin filaments in both parallel and anti-parallel orientations, whereas others associate exclusively with parallel actin filaments, like fascin [337] [455], or preferentially with anti-parallel filaments, like cortexillin [583]. From the time-lapse imaging of the process of septin-mediated actin bundle formation, we can conclude that septins are able to bundle actin filaments with mixed polarities. Figure 11 shows a zippering event of two filaments (indicated by the blue and red arrows) fusing in parallel into a bundle, which reveals the ability of septins to assemble parallel actin filaments. Figure 13 shows a wrapping event in which actin filaments growing from the same site fuse either in a clockwise (indicated by the yellow and pink arrows) or a counterclockwise manner (indicated by the green and blue arrows) into a pre-existing ring, which indicates an anti-parallel assembly. Thus, septins do not exhibit a polarity preference, perhaps on account of their (axially) nonpolar structure.

Mechanisms of septin-mediated actin bundle assembly

(1) Septins bend stiffer, phalloidin-decorated actin filaments

Considering the high energy penalty associated with bending a bundle composed of several actin filaments [340], it is striking that septins assemble actin filaments into curved bundles and rings. We hypothesize that the adhesion energy provided by septins can overcome the bending energy associated with the bent actin filaments. A similar energy balance between adhesion and bending energy has been shown to successfully account for actin ring and spiral formation induced by multivalent counterions [593] [594] [595], non-adsorbing polymers [596] [597], positively charged membranes [598], and biotin-streptavidin crosslinkers [594]. In support of this hypothesis, we observe an event where a

Figure 15. Actin bundles bent by fly septins (septin concentration 0.1 μM). The red arrows indicate a filament that crosses the neck of a winding bundle. The blue lines present as a reference to show the displacement of the winding bundle. We note that the filed of view does not change during image recording. Time in seconds (s) is indicated. The contrast of the TIRF images is inverted. Scale bar: 10 μm.

progressive adhesion of a filament across the neck of a winding bundle causes its neck to narrow (Fig. 15). This observation clearly shows a trade-off between adhesion and bending energy: the septin adhesion energy is "used" to bend the actin filament. The earlier example of wrapping of multiple actin filaments to form a curved actin structure (Fig. 13) similarly suggests that the adhesion energy is sufficient to overcome the energy associated with bending the filaments.

To gain more insight in the influence of the balance between bending and adhesion energy on bundle curvature, we co-polymerize fly septins and actin filaments in the presence of phalloidin, a small peptide that specifically binds to actin filaments and increases the persistence length of the filaments about two-fold, from ca. 9 μm to 18 μm [34]. Similar to the experiments performed in the absence of phalloidin, we observe that the septin concentration determines the morphology of actin bundles (Fig. 16). At low septin concentrations, 0.01 and 0.02 μM, we rarely observe actin bundles, while at a somewhat higher septin concentration of 0.05 μM we detect actin bundles with frayed ends. Interconnected actin bundle networks composed of curved actin bundles appear at septin concentrations of 0.1 – 0.5 μM. Intriguingly, rings and lassos occur much less often in the presence than in the absence of phalloidin. Further increasing the septin concentration to 1 – 3.8 μM, we observe winding and needle-like actin bundles similar to the bundles formed at high septin concentration in the absence of phalloidin. Our observations indicate that a two-fold stiffening of actin filaments does not prevent septins from assembling curved actin bundles, but it certainly inhibits ring and lasso formation.

The rings and lassos that do form in the presence of phalloidin have only a slightly reduced average curvature according to an automated image analysis of a total of 190 rings and lassos [599]. This rather modest effect suggests that a purely energetic argument based on a balance between bending and adhesion energy cannot fully account for the formation of the curved bundles.

(2) Curved actin bundles are not a result of non-equilibrium effects

To our knowledge, curved actin bundles have only been reported for filamin-mediated actin networks [565] [591] [600]. At actin concentrations of ~2.4 – 4.8 μM, where filaments/bundles entangle, it was shown that the bundles became curved due to build-up of local internal stress during actin polymerization [565] [591]. Schmoller and colleagues provided two lines of evidence to support that curvature was a result of kinetic frustration. First, bundle curvature relaxed upon laser ablation. Second, mixing pre-polymerized actin filaments with filamin resulted in a rather different network architecture, namely heterogeneous bundle clusters, thus confirming the presence of internal stress in networks formed by co-polymerization [565].

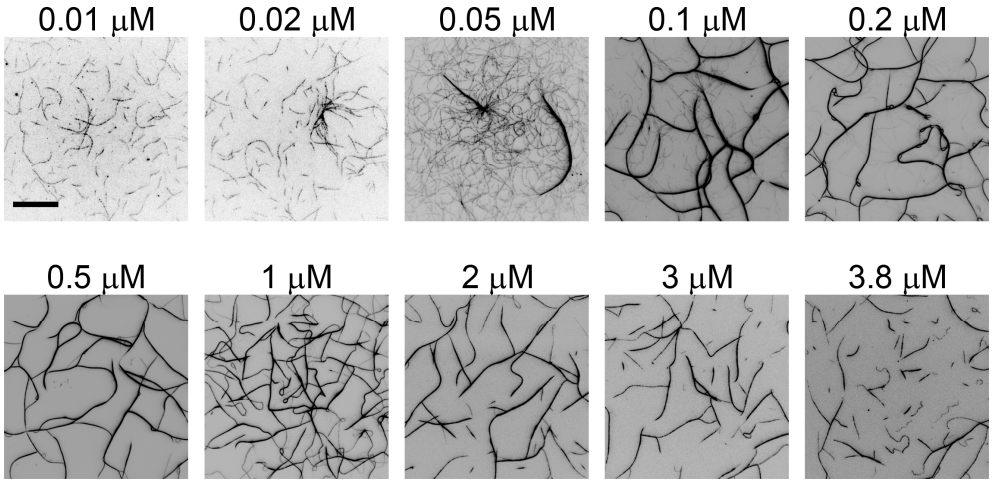

Figure 16. Morphology of actin bundles assembled by fly septins in the presence of phalloidin at an equimolar concentration with actin. The concentrations of fly septins are indicated and the concentration of actin is fixed at 1 μM. The contrast of images obtained by TIRF is inverted. Scale bar: 20 μm.

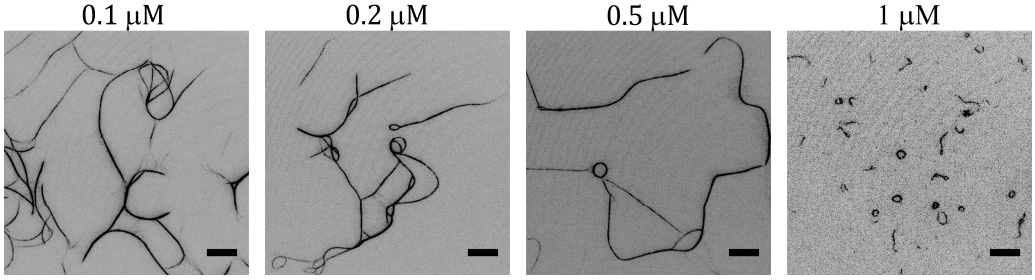

Figure 17. Actin bundles generated by pre-polymerized actin filaments (1 μM) in the presence of fly septins at increasing concentrations as indicated. The contrast of the TIRF images is inverted. Scale bars: 10 μm.

To test whether kinetic trapping contributes to the formation of curved septin-mediated actin bundles, such as rings and lassos, we pre-polymerize actin filaments and mix them with septins. We observe bundle architectures (Fig. 17) that are similar to the bundles observed by co-polymerization. At a septin concentration of 0.1 μM, we observe curved bundles forming an interconnected network. When raising the septin concentration to 0.2 – 1 μM, lassos and rings form. Although rings and lassos occur less often than in the co-polymerization experiments, the septin concentration still determines the architecture of actin bundles in a similar fashion.

To rule out the possibility that rings may form by shear-induced effects during mixing of pre-formed actin filaments and septins, we perform a control experiment by mixing actin filaments with another actin binding protein, fascin. We observe that fascin-mediated actin bundles are exclusively straight and needle-like (Supplementary Figure 1). All together, these observations indicate that the presence of curved septin-mediated actin bundles does not depend on actin assembly kinetics or shear-induced effects.

Human septins bundle actin filaments in a similar fashion as fly septins

To test if the actin bundling ability of septins is conserved among different species, we polymerize actin filaments in the presence of purified recombinant human septins (hSep2-hSep6-hSep7). We observe that human septins bundle actin filaments in a similar fashion as fly septins (Fig. 18). While at a human septin concentration of 0.02 μM, we do not observe actin bundles, at a higher concentration of 0.05 μM, we observe slightly curved actin bundles exhibiting frayed actin filaments. At septin concentrations of 0.1 – 0.3 μM, interconnected curved bundles appear together with lassos and rings. Further increasing the septin concentration to 0.5 – 2.2 μM leads to winding or zigzag structures. At a septin concentration of 1.7 μM, we observe needle-like actin bundles, similar to the fly septin-mediated actin bundles.

EM micrographs reveal the ultrastructure of the human septin-mediated actin bundles. At a septin concentration of 0.1 μM, we observe curved as well as straight bundles that are composed of 2 - 10 single actin filaments (Fig. 19A-D). Actin bundles with frayed brush-like ends are observed (Fig. 19E and F), consistent with the fluorescence microscopy observations. Further increasing the septin concentration to 0.2 μM, winding or zigzag bundles appear (Fig. 19G and I). We occasionally observe that two bundles appear to “meet” each other as indicated by the red arrow in Figure 19 (H). It is possible that these two bundles are coincidently juxtaposed, but it is also possible that this observation reflects a breakage of a longer bundle. The actin bundles are generally densely packed with closely aligned actin filaments (Fig. 19J). At a septin concentration of 0.5 μM,

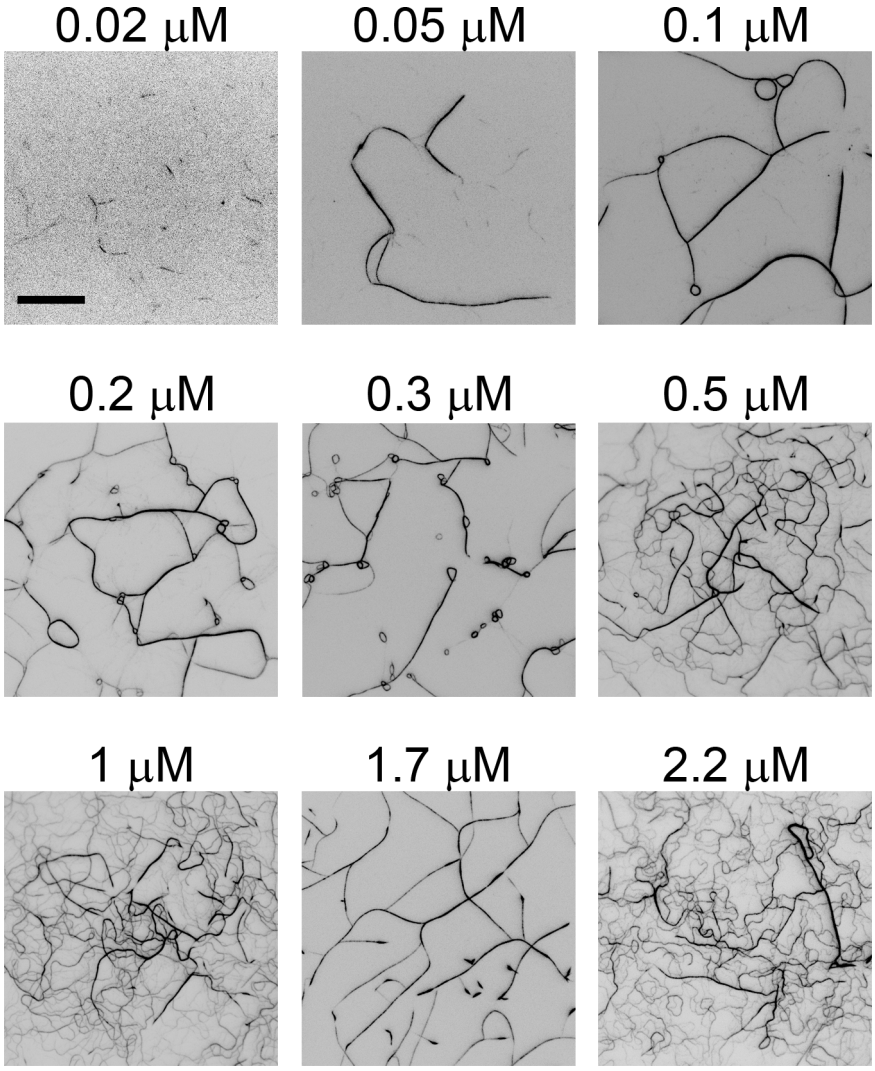

Figure 18. Morphology of actin bundles assembled by human septins. The concentrations of human septins are indicated while the concentration of actin is fixed at 1 μM. The contrast of images obtained by TIRF is inverted. Scale bar 20 μm.

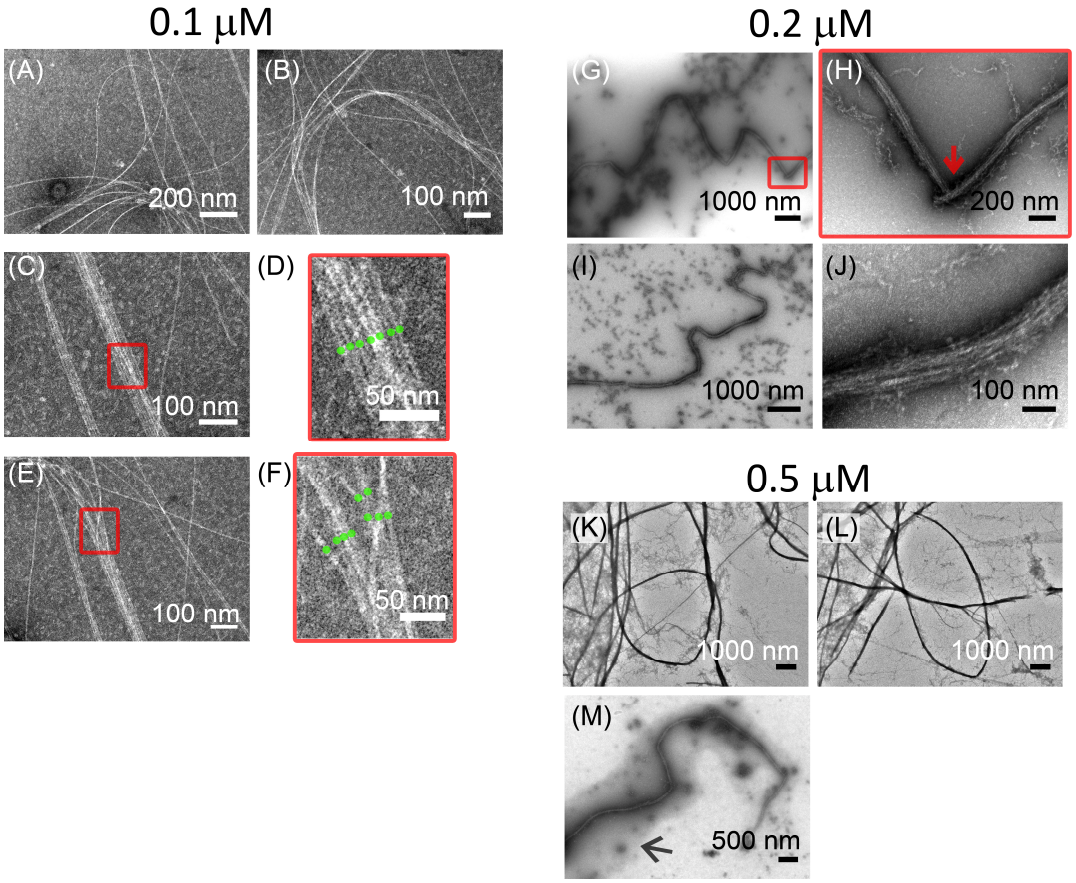

Figure 19. Electron micrographs of actin structures in the present of human septins. The concentration of actin is fixed at 3 μM and the concentrations of human septins are indicated. (D), (F) and (H) are zoomed-in areas of the small rectangular areas indicated in (C), (E) and (G), respectively. The green dots in (D) and (F) indicate 7 and 9 single actin filaments, respectively. In (H), the red arrow indicates the "meeting point" of two actin bundles, which may due to a broken bundle or two bundles may sit next to each other coincidently. In (M), the black arrow indicates a grayish area resulting from the staining procedure.

consistent with the fluorescence microscopy observations, we detect winding bundles, lassos and rings (Fig. 19K-M).

Budding yeast septins do not bundle actin filaments

Since septins are conserved among animal cells and fungi, we test if recombinant budding yeast septin complexes, Cdc3-Cdc10-Cdc11-Cdc12, have the same ability to bundle actin filaments as fly and human septins. We co-polymerize actin filaments at 1 μM with yeast septins at 0.05 μM and also perform tests where we mix pre-polymerized yeast septin filaments with pre-formed actin filaments at the same concentrations. In either case, we observe that actin filaments and yeast septin filaments do not colocalize (Fig. 20). Furthermore, there is no obvious bundling of actin filaments.

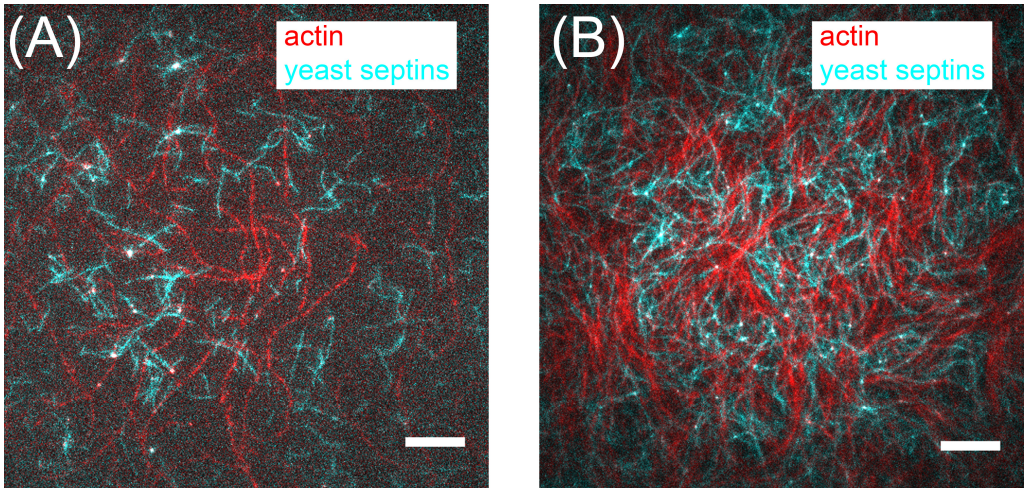

Figure 20. TIRF images of actin filaments in the presence of budding yeast septins. (A) Reconstituted actin filaments in the presence of budding yeast septins (Cdc3-Cdc10-Cdc11-Cdc12). (B) Reconstituted actin network assembled by mixing pre-polymerized yeast filaments and pre-polymerized actin filaments. The concentration of actin (shown as red) and budding yeast septins (shown as cyan) is 1 μM and 0.05 μM, respectively. Scale bars: 10 μm.

6.3 Discussions

Fly and human septins directly bind to and bundle actin filaments

We demonstrate that purified recombinant fly and human septins directly bind to and bundle actin filaments in the absence of other binding partners. This finding is striking given that no direct actin-septin interaction was reported before, although in mammalian cells septins have been shown to co-localize with actin filaments and bundles [485], to be responsible for actin bundling [484], and to contribute to cortical integrity [577] [109] and cell migration ability through intimate interactions with actomyosin networks [481] [601]. Previously, it was shown *in vitro* that human septins purified from insect cells do not bind to actin filaments unless anillin is present [484]. However, only one, rather low, septin concentration was tested (0.3 μM). Thus, it remains possible that binding and bundling could occur at higher septin concentration. With bacteria-purified septins, we find that bundling only occurs at septin concentration above ~0.1 μM. It is likely that the minimum amount of septins needed to bundle actin filaments is different for septins purified from insect cells.

As discussed in Chapter 5, bacteria-purified septins lack posttranslational modifications, such as phosphorylation, which are presumably present in septins purified from insect cells. It will be important to test the influence of posttranslational modifications on septin-actin interactions by comparing septins expressed in different systems (bacteria and eukaryotic cells such as insect cells [484] and mammalian cells [515]) and septins purified from intact organisms such as fly embryos [509]. SUMOylation [542] [543], ubiquitylation [544] and phosphorylation [508] [537] [538] [541] [511] of septins have all been reported, with likely implications for septin-septin as well as septin-actin interactions. Posttranslational modifications likely modulate the functions of septins during the cell cycle and during cell differentiation, as suggested by a recent study in budding yeast [508].

In contrast to fly and human septins, budding yeast septins do not appear to bind and bundle actin filaments. However, this tentative conclusion is based on observations at a low concentration of both actin and septin, so we plan further experiments scanning a range of actin and septin concentrations. Budding yeast septins differ from their human and fly counterparts in multiple ways. We observed a striking difference in polymerization behavior of yeast versus fly and human septins in Chapter 5: under the same buffer condition, yeast septins form thin, semiflexible paired filaments, whereas fly and human septins form straight, rigid bundles. It remains to be sorted out in detail how these differences affect actin binding and bundling.

The striking difference between the bundling ability of fly/human and yeast septins raises an important question of where the actin-binding domain is located in the septin complexes. The salt dependence of bundling (c.f. Fig. 1) points to a contribution from electrostatic interactions. It would certainly be interesting to test the assembly of actin bundles with mutant septins lacking the highly charged N-terminal polybasic domains. These domains are known to bind PIP lipids, so if they also turn out to bind actin, this will likely have implications for the ability of septins to act as an actin cortex-membrane linker. Another putative actin-binding region is provided by the C-terminal α–helical expansions. It has been shown that many actin binding proteins, including gelsolin, vitamin D-binding protein and Wiskott-Aldrich syndrome protein (WASP)-homology domain-2-related protein, share an actin-binding motif consisting of an α-helix with hydrophobic side chains that bind to the hydrophobic cleft of actin [602]. This hypothesis could be tested by assessing the ability of mutant septins lacking the C-terminal expansions to bind to and bundle actin filaments.

The difference between the actin bundling ability of fly/human and yeast septins may be related to the difference in septin function during animal and budding yeast cell cytokinesis. In animal cells, septins colocalize with the actomyosin ring throughout actomyosin contraction [573] [603] [572], whereas in budding yeast, septins and the actomyosin ring have distinct localizations [604]. In budding yeast cytokinesis, the septin ring splits into two and the actomyosin ring contracts between the septin rings [605]. A future investigation into the activity of non-muscle myosin motors mixed with actin networks/bundles assembled by fly/human versus budding yeast septins may shed light on this issue.

Septin polymerization and higher-order assembly impact actin bundling

In vivo, septin filaments have been proposed to function as diffusion barriers and as cortical organizers for the actin and microtubule cytoskeleton [480]. It remains poorly understood how important the ability of septins to polymerize and form higher-order assemblies is for these functions. To our knowledge, there is until now only evidence for budding yeast that the filamentous form of septins is critical for the survival of the budding yeast cells [489]. Septins form various types of higher-order structures in budding yeast, including rings and gauzes [493] [495] [494]. *In vitro*, ring and gauze formation of budding yeast septins has been reported [508] [512]. Our results demonstrate that fly/human septin hexamers and bundles both bind actin filaments, but result in different actin-septin bundle architectures. Specifically, we observe actin rings only in a narrow window of septin concentrations (0.2 – 0.3 μM) where septins are likely to function (mostly) as hexamers since these concentrations are close to the critical concentration of septin filament formation (~0.1-0.2 μM). At higher septin concentrations, we find coexistence of curved and straight actin bundles. Two-color labeling studies

suggest that the curved bundles are associated with septin hexamers whereas the straight bundles are associated with straight septin bundles. However, the spotty decoration of the AlexaFluor-labeled septin bundles (see Fig. 4B in Chapter 5) currently precludes a definitive conclusion. To clearly distinguish septin hexamers and filaments/bundles, it will be important to perform experiments with GFP-tagged septins, such that every complex is tagged. Another complicating factor is that septin bundles always coexist with septin hexamers above the critical concentration for septin polymerization; therefore we cannot cleanly distinguish their bundling abilities. To dissect this issue, it will be essential to reconstitute actin bundles using mutant septins that do not have the ability to polymerize. A good candidate would be septin complexes with Pnut bearing two point mutations that abolish G-interface dimerization and thus are predicted to impair septin polymerization [489] [499].

The interpretation of the salt-dependent effect on actin bundling is complicated by the fact that septins themselves polymerize in a salt-dependent fashion. It has been reported that high salt concentration (>200 mM NaCl [512]) impair septin polymerization [500] [512]. Thus, higher salt concentrations impair septin polymerization accompanied by a reduction of the binding affinity for actin. Conversely, lower salt concentrations promote septin polymerization and enhance the binding affinity for actin. Thus, using septin mutants that are unable to polymerize will help to distinguish between the contributions of septin polymerization and salt-dependent binding affinity to the bundle phenotype.

Septins crosslink both parallel and anti-parallel actin filaments

From time-lapse images of bundle formation we conclude that septins can crosslink both parallel and anti-parallel pairs of actin filaments. This conclusion has important implications for the role of septins in conjunction with contractile actomyosin arrays in cells. Septins have been shown to regulate actomyosin contractility in cytokinesis [571] [606] and to organize cortical actomyosin networks [486]. It has been suggested that the polarity of actin filaments impacts on the generation of myosin contractile force in motile cells [607] [61] [468]. *In vitro*, it has been shown that in the absence of other actin crosslinking proteins, myosin VI motors selectively contract and disassemble anti-parallel actin structures but not parallel actin filaments [459]. However, isotropic fascin-mediated actin networks can be contracted by myosin, despite fascin's preference for unipolar bundling [608] [283], leaving the question how bundle polarity precisely affects myosin contractility open. An *in vitro* study demonstrated that, at similar time scales, myosin II motors contract an actin network composed of cortexillin I mediated apolar actin bundles to a smaller area than an actin network composed of fascin mediated unipolar actin bundles [434]. This observation shows that the nature of the actin crosslinkers impacts myosin driven contractility

and may reflect their roles in living cells. For instance, the polar crosslinker fascin is usually found in stable, non-contractile structures such as filopodia [609], whereas the apolar crosslinker cortexillin I is enriched in the contracting equatorial region during cytokinesis [610]. Given septin's association with the actomyosin cortex in diverse cellular contexts, it will be interesting to test whether myosin motors have the ability to generate contractile force on septin-mediated actin bundles.

Actin-templated assembly of curved actin bundles, lassos and rings

The observation that fly and human septins organize actin filaments into closed rings and lassos is rather striking given that other actin crosslinking proteins usually assemble actin filaments into straight bundles (such as fascin [331] and scruin [557]). It has been shown that filamin can create curved bundles when co-polymerized with actin at concentrations where actin filaments are entangled, due to build-up of internal stress [591] [565]. We test whether kinetic trapping could account for the septin-mediated curved bundles and found no strong evidence of this. Instead, time-lapse imaging of bundle formation indicates that during actin filament elongation, septins progressively bend the filaments, resulting in a highly curved configuration of the actin filaments (c.f. Fig 12 and 13). This curved bundle acts as a template for further zippering up of single actin filaments to thicken the bundle. A similar "template assembly" mechanism has been suggested for toroidal DNA formation [611]. In support of a template-based formation mechanism, in which actin rings are thickened by zippering up single actin filaments, a quantitative analysis of curvatures in rings and lassos reveals that, while the curvatures of lassos and rings remain constant, the bundle thickness varies over two orders of magnitude in actin fluorescence intensity [599]. We furthermore observe that fewer rings and lassos are formed when septins are mixed with pre-polymerized actin filaments, which supports the idea that septins bend actin filaments progressively during their elongation to form a curved actin template. Potentially, the local density of actin filaments and their length distribution play a role in the formation of curved bundles. In living cells, these parameters are tightly regulated by a host of actin binding proteins to fulfill specific cellular functions. It will be interesting to assess the influence of actin regulatory proteins, such as gelsolin which controls actin filament length, on the occurrence of the curved bundles as well as on their curvatures.

Another possibility is that actin filaments utilize a pre-existing septin structure as a template for assembly, given that ring formation of purified budding yeast septins [512] [508] and human septins [484] has been shown. However, we do not observe ring formation for human or fly septins by EM (c.f. Chapter 5). This rules out the septin-template scenario under the conditions of our experiments, though it is still possible that under different conditions septin rings can act as templates.

It is possible that protein adsorption may not be 100% efficient on EM grids, which would cause us to miss some septin structures such as rings. Given that, in the absence of actin, the usage of AlexaFluor 488-labeled septins gives a spotty decoration on septin structures, it is also possible that ring-like septin structures are overlooked in TIRF. Thus, it will be important to perform experiments with GFP-tagged septins.

"Locked-in" curvature: septin binding stabilizes curved actin structures

We observe that winding actin bundles have frozen or "locked-in" configurations (c.f. Fig. 12). Note that the bent segments of the bundles do diffuse freely over the substrate, implying that they do not adhere nonspecifically to the substrate (c.f. Fig. 11, 15 and Supplementary Figure 2). This observation strongly suggests that septins stabilize the curvature of the bent actin filaments. It is possible that septins either impose a preferred curvature on the bound actin filaments/bundles or bind to actin filaments with a preferred curvature. The first hypothesis is inspired by the evidence that insect cell-derived human septins (hSep2, hSep6 and hSep7) and budding yeast septins (Cdc3, Cdc10, Cdc12 and Shs1) can accommodate highly curved structures such as rings and spirals [484] [508]. The second hypothesis is inspired by a recent study showing that the curvature of actin filaments biases the direction of branching by the actin nucleator Arp2/3 complex [612]. To test these hypotheses, one can measure septin binding/unbinding rates from straight or curved single actin filaments immobilized on a surface [612] or trapped by optical tweezers [613] [614] [455]. A third possibility is that septin induces structural changes in actin filaments that result in (local) changes in bending and/or torsional compliance. Such an effect has been demonstrated for cofilin. Cofilin was found to lower the bending rigidity of actin filaments, which facilitates cofilin-mediated filament severing [615] [616] [617]. Cryo-EM imaging showed that this effect could be explained in terms of structural plasticity of the actin filaments [618]. To test this possibility, it would be informative to measure the persistence length of actin filaments in the presence of different septin binding densities by observing thermal fluctuations of septin-decorated single actin filaments in quasi-2D chambers [615] [619] or septin-actin bundles confined in a 3D compartment such as a water-in-oil droplet [340]. Finally, it will be important to perform high resolution cryo-EM studies to determine the ultrastructure of the actin bundles mediated by septins.

6.4 Conclusion

Septins have been proposed to interact closely with the actin cytoskeleton in several cellular actin structures, such as the contractile ring in cytokinesis and the cell cortex that mechanically stabilizes the plasma membrane in some migrating

cells. However, the nature of this interaction is unclear. Here, we show that septins directly bind to and bundle actin filaments. Strikingly, we observe that septins are able to stabilize curved actin structure and mediate the formation of actin rings. This finding suggests that septins may stabilize the curved contractile ring in cell cytokinesis, and may even contribute to its assembly. Interestingly, we find that the polymerization state of septin strongly influences actin bundle morphology. Below the critical concentration for septin filament formation, where septins are mainly in oligomeric form, we observe mainly curved actin structures; above the critical concentration, where septins are in filamentous form, we observe mostly straight actin bundles. These observations suggest that cells may control the configuration of the actin cytoskeleton by varying the polymerization state of septins, which is determined by the local concentration of septins and perhaps also by posttranslational modifications or interactions with other binding partners such as anillin or plasma membrane lipids.

6.5 Supplementary Figures

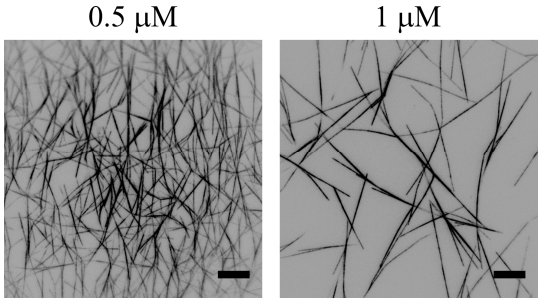

Supplementary Figure 1. Actin bundles assembled by pre-polymerized actin filaments in the presence of fascin at concentrations of 0.5 μM (*left panel*) and 1 μM (*right panel*). The contrast of the TIRF images is inverted. Scale bars: 10 μm.

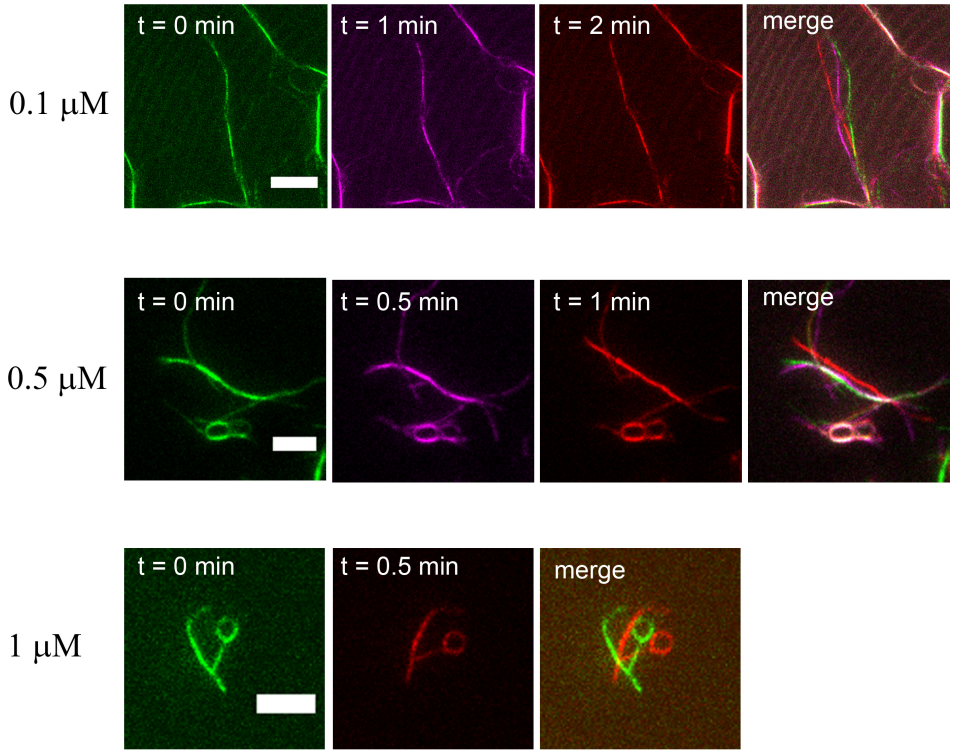

Supplementary Figure 2. Actin bundles assembled by fly septins do not adhere to the substrate. Actin filaments at a concentration of 1 μM are pre-polymerized before mixing with septins. The concentrations of fly septins are indicated. Note that in samples where the concentrations of fly septins are 0.5 μM and 1 μM, phalloidin at an equimolar concentration with actin is present. Time in minutes (min) is indicated. Scale bars: 10 μm (for fly septins at 0.1 μM) and 5 μm (for fly septins at concentration of 0.5 μM and 1 μM).

6.6 Materials and Methods

Protein preparation

Monomeric (G-)actin was purified by standard procedures including a gel filtration on a Sephacryl S-200 26/60 high-resolution column (GE Healthcare, Munich, Germany) to remove residual capping proteins, cross-linkers, and actin oligomers [295]. Fluorescent actin with a dye/protein molar ratio of 0.6 was prepared by labeling amine groups with AlexaFluor 488 or AlexaFluor 594 carboxylic acid succinimidyl ester [410]. G-actin was stored at -80^{o}C in G-buffer (2 mM Tris-HCl, 0.2 mM Na_2ATP, 0.2 mM $CaCl_2$, 2 mM dithiothreitol (DTT), pH 7.8).

Frozen aliquots were always quickly thawed and 4 mM DTT was added to reduce any oxidized sulfhydryl groups [411] [412]. Before use, the G-actin solution was centrifuged at 120,000g for 30 min to remove any aggregated proteins (Beckman Coulter Airfuge), followed by sonication for 5 min to disrupt actin dimers [413]. Recombinant mouse fascin was prepared from T7 pGEX *E. coli* as described in [410], with the only difference that gel filtration was performed on a high-resolution Superdex 200 column (GE Healthcare, Munich, Germany). Fascin was stored at -80^{o}C in 50 mM Tris-HCl pH 7.5, 150 mM KCl, 5 mM DTT, 10% (v/v) glycerol. Before use, fascin stock solutions were clarified by centrifuging at 120,000g for 5 min and used within a week. Recombinant fly and human septin complexes were provided by F. Iv and Dr. M. Mavrakis. Recombinant yeast septin complexes were provided by Dr. A. Bertin.

Reconstitution of actin-septin bundles

For co-polymerization experiments, G-actin was polymerized in the presence of fascin or septins for at least 45 min at room temperature in a polymerization buffer containing 20 mM Imidazole-HCl pH 7.4, 1 mM DTT, 0.1 mM MgATP, 50 mM KCl and 2 mM $MgCl_2$. Pre-polymerized septin filaments or bundles were prepared by either diluting septins at the desired concentration in the polymerization buffer or dialyzing septins (yeast septins at 2.5 μM and fly/human septins at 5μM) overnight at 4^{o}C against a buffer containing 20 mM Tris pH 8, 50 mM KCl, 1 mM DTT and 2 mM $MgCl_2$. Pre-polymerized actin filaments were obtained by polymerizing actin at a concentration of 24 or 12 μM for at least 1 hr at room temperature, followed by diluting to the desired concentration in the polymerization buffer. For TIRF microscopy samples, methylcellulose (0.1% w/v) was included to confine the filaments in a thin quasi-2D layer at the coverslip surface. Moreover, 1 mM trolox was included to prevent blinking, and an oxygen scavenging mixture of 2 mM protocatechuic acid and 0.1 μM protocatechuate 3,4-dioxygenase was included to minimize photobleaching [415]. Unless specified otherwise, the actin concentration was fixed at 1 μM for TIRF and 1 or 3 μM for EM. When present, AlexaFluor 488 or AlexaFluor 594 labeled actin was present at a 10% molar ratio to actin and phalloidin was present in an equimolar amount to actin.

High speed cosedimentation assay of septin-actin binding

G-actin at concentrations between 0.5 – 50 μM was polymerized in the presence of 1 μM septins for 2 hr at room temperature in the polymerization buffer. Samples (100 μL) were centrifuged at 120,000 g for 1 hr at room temperature (Airfuge, Beckman Coulter). Pellets were brought to the original volume in polymerization buffer. Proteins in pellets and supernatants were analyzed by standard SDS-PAGE (10% (w/v) acrylamide), stained with Coomassie

Brilliant blue (InstantBlue, Expedeon) and scanned by a commercial image scanner (Hewlett-Packard). To obtain the fractions of septins bound to actin from the band corresponding to DSep2 present in the supernatants, the scanned images were used to perform the gel quantification analysis in Fiji software [416]. The binding curve was obtained by plotting the fraction of bound septins versus the concentration of free actin filaments (Fig. 1A). Given that the concentration of the total septin used is in the range of the the dissociation equilibrium constant (K_d), K_d values were calculated by fitting the binding curve to a quadratic equation [578]:

$$[AS]/[S] = ([A]+[S]+K_d - (([A]+[S]+K_d)^2 - 4*[A]*[S])^{0.5})/2*[S],$$

where [AS] is the concentration of septins bound to actin, [A] is the total concentration of actin, [S] is the total concentration of septins and [AS]/[S] is the fraction of septins bound to actin. We note that septins pelleted by themselves in the absence of actin. Therefore, [AS]/[S] was corrected by subtracting the amount of septins pelleted in the absence of actin.

Low speed cosedimentation assay of bundling

G-actin was polymerized in the presence of septins for 30 – 45 min at room temperature in the polymerization buffer. Samples (100 μL) were sedimented for 15 min at 12,000 g at room temperature in an Eppendorf centrifuge. Pellets were brought to the original volume in polymerization buffer. Proteins in pellets and supernatants were analyzed by standard SDS-PAGE (10% (w/v) acrylamide) and stained with Coomassie Brilliant blue (InstantBlue, Expedeon).

Observation chamber preparation

Microscope slides and cover slips were cleaned for 30 min in a base-piranha solution (5% hydrogen peroxide, 5% ammonium hydroxide, heated to 70°C) and stored in 100% isopropanol. Chambers were assembled by sandwiching strips of Parafilm between the clean slide and cover slip, followed by melting at 120°C. The resulting chambers were then passivated by incubating for 15 min with 1 M potassium hydroxide, rinsing with Milli-Q water, blow-drying with nitrogen gas, incubating for 45 min with 0.2 mg/mL poly-L-lysine-polyethylene-glycol (Surface Solutions), rinsing with Milli-Q water, and blow-drying with nitrogen gas. Passivated chamber were used within 1 day. Solutions containing proteins were pipetted into the chamber and the chamber was hermetically sealed with VALAP (equal weights of vaseline**,** lanolin, and paraffin wax).

Total internal reflection fluorescence (TIRF) microscopy

Samples were imaged with a Nikon Apo TIRF 100x/1.49 NA oil objective mounted on an Eclipse Ti microscope (Nikon) using 491 nm and 561 nm laser lines. Images were acquired with a QuantEM 512SC EMCCD camera (Photometrics).

Transmission electron microscopy

Carbon coated copper grids (CF300-Cu, Electron Microscopy Sciences) were glow-discharged (EMS 500 sputter coater, Electron Microscopy Sciences) right before the protein solutions were pipetted onto the grids. After polymerizing in tubes for at least 45 min at room temperature, samples were incubated for at least 30 minutes on the grids in a humid environment to make sure enough protein was adsorbed onto the grids. The samples were stained with Nano-W, a 2% negative stain based on an organo-tungsten compound (Nanoprobes), or a 2% uranyl acetate solution (Nanoprobes) and examined with either a JEOL 1400 (120 kV) electron microscope at Imagif (Gif sur Yvette, France) equipped with a SC100 Orius CCD camera or with a Philips CM12 (120 kV) electron microscope at Imagopole (Institut Pasteur, France), or a FEI Tecnai Spirit (120 kV) electron microscope (Institut Curie, France). Two dimensional image processing according to published procedures was performed by Dr. A. Bertin [500]. For Ni-NTA-Nanogold particle (5nm, Nanoprobes) decoration, after incubating the sample on grid for 30 minutes in a humid environment, samples were washed with the polymerization buffer without DTT followed by incubating with the Ni-NTA-Nanogold particle for 30 minutes in a humid environment, washing 5 times with the polymerization without DTT and finally staining with either Nano-W or uranyl acetate solution as described above. We note that DTT reduces nickel ions on the Ni-NTA-Nanogold particle that would cause non-efficient binding of the his-tagged fly septins and the Ni-NTA-Nanogold particles.

6.7 Acknowledgements

Experiments were performed in collaboration with José Alvarado (AMOLF, Amsterdam), Manos Mavrakis (CNRS/Aix-Marseille University) and Aurélie Bertin (Institut Curie, Paris). We thank François Iv (Aix-Marseille University) and Marjolein Kuit-Vinkenoog (AMOLF, Amsterdam) for protein purification, and Magdalena Preciado López (AMOLF, Amsterdam) for insightful discussions and help with TIRF microscopy.

Bibliography

[1] R. Lipowsky and E. Sackmann, *Structure and Dynamics of Membranes: I. From Cells to Vesicles/II. Generic and Specific Interactions*, vol. 1. Access Online via Elsevier, 1995.

[2] G. Van Meer, D. R. Voelker, and G. W. Feigenson, "Membrane lipids: where they are and how they behave," *Nature reviews molecular cell biology*, vol. 9, no. 2, pp. 112–124, 2008.

[3] K. Larsson and K. Larsson, *Lipids: molecular organization, physical functions and technical applications*. Oily Press Dundee, 1994.

[4] G. Cevc and D. Marsh, *Phospholipid bilayers: physical principles and models*, vol. 5. Wiley, 1987.

[5] G. van Meer and A. de Kroon, "Lipid map of the mammalian cell," *Journal of Cell Science*, vol. 124, no. 1, pp. 5–8, 2011.

[6] M. Mondal, B. Mesmin, S. Mukherjee, and F. R. Maxfield, "Sterols are mainly in the cytoplasmic leaflet of the plasma membrane and the endocytic recycling compartment in cho cells," *Molecular biology of the cell*, vol. 20, no. 2, pp. 581–588, 2009.

[7] A. Zachowski, "Phospholipids in animal eukaryotic membranes: transverse asymmetry and movement," *BIOCHEMICAL JOURNAL-LONDON-*, vol. 294, pp. 1–1, 1993.

[8] S. J. Singer and G. L. Nicolson, "The fluid mosaic model of the structure of cell membranes," *Science*, vol. 175, no. 23, pp. 720–731, 1972.

[9] D. Brown and E. London, "Functions of lipid rafts in biological membranes," *Annual review of cell and developmental biology*, vol. 14, no. 1, pp. 111–136, 1998.

[10] M. Edidin, "The state of lipid rafts: from model membranes to cells," *Annual review of biophysics and biomolecular structure*, vol. 32, no. 1, pp. 257–283, 2003.

[11] K. Simons and D. Toomre, "Lipid rafts and signal transduction," *Nature reviews Molecular cell biology*, vol. 1, no. 1, pp. 31–39, 2000.

[12] B. Alberts, A. Johnson, J. Lewis, M. Raff, K. Roberts, and P. Walter, *Molecular Biology of the Cell, Fourth Edition*. Garland Science, 2002.

[13] A. Engel and H. E. Gaub, "Structure and mechanics of membrane proteins," *Annu. Rev. Biochem.*, vol. 77, pp. 127–148, 2008.

[14] K. Bacia and J. Schweizer, "Practical course: Giant unilamellar vesicles," *Institut für Biophysik Fachrichtung Physik, Dresden*, 2005.

[15] J. Zimmerberg and M. M. Kozlov, “How proteins produce cellular membrane curvature,” *Nature Reviews Molecular Cell Biology*, vol. 7, no. 1, pp. 9–19, 2005.
[16] B. Antonny, “Membrane deformation by protein coats,” *Current opinion in cell biology*, vol. 18, no. 4, pp. 386–394, 2006.
[17] T. Ryan, J. Myers, D. Holowka, B. Baird, and W. Webb, “Molecular crowding on the cell surface,” *Science*, vol. 239, no. 4835, pp. 61–64, 1988.
[18] M. Javanainen, H. Hammaren, L. Monticelli, J.-H. Jeon, M. S. Miettinen, H. Martinez-Seara, R. Metzler, and I. Vattulainen, “Anomalous and normal diffusion of proteins and lipids in crowded lipid membranes,” *Faraday Discussions*, vol. 161, pp. 397–417, 2013.
[19] M. Frick, K. Schmidt, and B. J. Nichols, “Modulation of lateral diffusion in the plasma membrane by protein density,” *Current biology*, vol. 17, no. 5, pp. 462–467, 2007.
[20] D. F. Kucik, E. L. Elson, and M. P. Sheetz, “Weak dependence of mobility of membrane protein aggregates on aggregate size supports a viscous model of retardation of diffusion,” *Biophysical journal*, vol. 76, no. 1, pp. 314–322, 1999.
[21] A. Kapus and P. Janmey, “Plasma membrane—cortical cytoskeleton interactions: A cell biology approach with biophysical considerations,” *Comprehensive Physiology*, 2013.
[22] A. Kusumi, C. Nakada, K. Ritchie, K. Murase, K. Suzuki, H. Murakoshi, R. S. Kasai, J. Kondo, and T. Fujiwara, “Paradigm shift of the plasma membrane concept from the two-dimensional continuum fluid to the partitioned fluid: high-speed single-molecule tracking of membrane molecules,” *Annu. Rev. Biophys. Biomol. Struct.*, vol. 34, pp. 351–378, 2005.
[23] Y. Barral and I. M. Mansuy, “Septins: cellular and functional barriers of neuronal activity,” *Current Biology*, vol. 17, no. 22, pp. R961–R963, 2007.
[24] F. Caudron and Y. Barral, “Septins and the lateral compartmentalization of eukaryotic membranes,” *Developmental cell*, vol. 16, no. 4, pp. 493–506, 2009.
[25] K. Schmidt and B. J. Nichols, “A barrier to lateral diffusion in the cleavage furrow of dividing mammalian cells,” *Current biology*, vol. 14, no. 11, pp. 1002–1006, 2004.
[26] F. Gittes, B. Mickey, J. Nettleton, and J. Howard, “Flexural rigidity of microtubules and actin filaments measured from thermal fluctuations in shape.,” *The Journal of cell biology*, vol. 120, no. 4, pp. 923–934, 1993.
[27] A. Burakov, E. Nadezhdina, B. Slepchenko, and V. Rodionov, “Centrosome positioning in interphase cells,” *The Journal of cell biology*, vol. 162, no. 6, pp. 963–969, 2003.
[28] F. J. McNally, “Mechanisms of spindle positioning,” *The Journal of cell biology*, vol. 200, no. 2, pp. 131–140, 2013.

[29] M. A. Welte, “Bidirectional transport along microtubules,” *Current Biology*, vol. 14, no. 13, pp. R525–R537, 2004.
[30] J. P. Caviston and E. L. Holzbaur, “Microtubule motors at the intersection of trafficking and transport,” *Trends in cell biology*, vol. 16, no. 10, pp. 530–537, 2006.
[31] S. P. Gross, “Hither and yon: a review of bi-directional microtubule-based transport,” *Physical Biology*, vol. 1, no. 2, p. R1, 2004.
[32] L. Kreplak and D. Fudge, “Biomechanical properties of intermediate filaments: from tissues to single filaments and back,” *Bioessays*, vol. 29, no. 1, pp. 26–35, 2007.
[33] H. Herrmann, H. Bär, L. Kreplak, S. V. Strelkov, and U. Aebi, “Intermediate filaments: from cell architecture to nanomechanics,” *Nature Reviews Molecular Cell Biology*, vol. 8, no. 7, pp. 562–573, 2007.
[34] H. Isambert, P. Venier, A. C. Maggs, A. Fattoum, R. Kassab, D. Pantaloni, and M.-F. Carlier, “Flexibility of actin filaments derived from thermal fluctuations. effect of bound nucleotide, phalloidin, and muscle regulatory proteins,” *Journal of Biological Chemistry*, vol. 270, no. 19, pp. 11437–11444, 1995.
[35] T. D. Pollard and J. A. Cooper, “Actin, a central player in cell shape and movement,” *Science*, vol. 326, no. 5957, pp. 1208–1212, 2009.
[36] A. Mogilner and K. Keren, “The shape of motile cells,” *Current Biology*, vol. 19, no. 17, pp. R762–R771, 2009.
[37] C. M. Field and P. Lénárt, “Bulk cytoplasmic actin and its functions in meiosis and mitosis,” *Current Biology*, vol. 21, no. 19, pp. R825–R830, 2011.
[38] S. A. Koestler, S. Auinger, M. Vinzenz, K. Rottner, and J. V. Small, “Differentially oriented populations of actin filaments generated in lamellipodia collaborate in pushing and pausing at the cell front,” *Nature cell biology*, vol. 10, no. 3, pp. 306–313, 2008.
[39] T. M. Svitkina and G. G. Borisy, “Arp2/3 complex and actin depolymerizing factor/cofilin in dendritic organization and treadmilling of actin filament array in lamellipodia,” *The Journal of cell biology*, vol. 145, no. 5, pp. 1009–1026, 1999.
[40] T. D. Pollard and G. G. Borisy, “Cellular motility driven by assembly and disassembly of actin filaments,” *Cell*, vol. 112, no. 4, pp. 453–465, 2003.
[41] T. M. Svitkina, “Ultrastructure of protrusive actin filament arrays,” *Current opinion in cell biology*, 2013.
[42] B. Bugyi and M.-F. Carlier, “Control of actin filament treadmilling in cell motility,” *Annual review of biophysics*, vol. 39, pp. 449–470, 2010.
[43] P. K. Mattila and P. Lappalainen, “Filopodia: molecular architecture and cellular functions,” *Nature Reviews Molecular Cell Biology*, vol. 9, no. 6, pp. 446–454, 2008.
[44] T. M. Svitkina, E. A. Bulanova, O. Y. Chaga, D. M. Vignjevic, S.-i. Kojima, J. M. Vasiliev, and G. G. Borisy, “Mechanism of filopodia initiation by

reorganization of a dendritic network," *The Journal of cell biology*, vol. 160, no. 3, pp. 409–421, 2003.
[45] J. Faix, D. Breitsprecher, T. E. Stradal, and K. Rottner, "Filopodia: Complex models for simple rods," *The international journal of biochemistry & cell biology*, vol. 41, no. 8, pp. 1656–1664, 2009.
[46] F. Hanakam, R. Albrecht, C. Eckerskorn, M. Matzner, and G. Gerisch, "Myristoylated and non-myristoylated forms of the ph sensor protein hisactophilin ii: intracellular shuttling to plasma membrane and nucleus monitored in real time by a fusion with green fluorescent protein.," *The EMBO journal*, vol. 15, no. 12, p. 2935, 1996.
[47] N. Morone, T. Fujiwara, K. Murase, R. S. Kasai, H. Ike, S. Yuasa, J. Usukura, and A. Kusumi, "Three-dimensional reconstruction of the membrane skeleton at the plasma membrane interface by electron tomography," *The Journal of cell biology*, vol. 174, no. 6, pp. 851–862, 2006.
[48] A. G. Clark, K. Dierkes, and E. K. Paluch, "Monitoring actin cortex thickness in live cells," *Biophysical journal*, vol. 105, no. 3, pp. 570–580, 2013.
[49] G. Salbreux, G. Charras, and E. Paluch, "Actin cortex mechanics and cellular morphogenesis," *Trends in Cell Biology*, 2012.
[50] A. Diz-Muñoz, D. A. Fletcher, and O. D. Weiner, "Use the force: membrane tension as an organizer of cell shape and motility," *Trends in cell biology*, 2012.
[51] G. G. Borisy and T. M. Svitkina, "Actin machinery: pushing the envelope," *Current opinion in cell biology*, vol. 12, no. 1, pp. 104–112, 2000.
[52] T. D. Pollard, L. Blanchoin, and R. D. Mullins, "Molecular mechanisms controlling actin filament dynamics in nonmuscle cells," *Annual review of biophysics and biomolecular structure*, vol. 29, no. 1, pp. 545–576, 2000.
[53] E. S. Chhabra and H. N. Higgs, "The many faces of actin: matching assembly factors with cellular structures," *nature cell biology*, vol. 9, no. 10, pp. 1110–1121, 2007.
[54] R. H. Insall and L. M. Machesky, "Actin dynamics at the leading edge: from simple machinery to complex networks," *Developmental cell*, vol. 17, no. 3, pp. 310–322, 2009.
[55] L. Blanchoin and A. Michelot, "Actin cytoskeleton: a team effort during actin assembly," *Current Biology*, vol. 22, no. 16, pp. R643–R645, 2012.
[56] T. D. Pollard, "Regulation of actin filament assembly by arp2/3 complex and formins," *Annu. Rev. Biophys. Biomol. Struct.*, vol. 36, pp. 451–477, 2007.
[57] E. D. Goley and M. D. Welch, "The arp2/3 complex: an actin nucleator comes of age," *Nature reviews Molecular cell biology*, vol. 7, no. 10, pp. 713–726, 2006.
[58] L. M. Machesky and K. L. Gould, "The arp2/3 complex: a multifunctional actin organizer," *Current opinion in cell biology*, vol. 11, no. 1, pp. 117–121, 1999.

[59] D. R. Kovar, “Molecular details of formin-mediated actin assembly,” *Current opinion in cell biology*, vol. 18, no. 1, pp. 11–17, 2006.
[60] B. Baum and P. Kunda, “Actin nucleation: spire—actin nucleator in a class of its own,” *Current biology*, vol. 15, no. 8, pp. R305–R308, 2005.
[61] T. M. Svitkina, A. B. Verkhovsky, K. M. McQuade, and G. G. Borisy, “Analysis of the actin–myosin ii system in fish epidermal keratocytes: mechanism of cell body translocation,” *The Journal of cell biology*, vol. 139, no. 2, pp. 397–415, 1997.
[62] T. Svitkina, “Electron microscopic analysis of the leading edge in migrating cells,” *Methods in cell biology*, vol. 79, pp. 295–319, 2007.
[63] R. D. Mullins, J. A. Heuser, and T. D. Pollard, “The interaction of arp2/3 complex with actin: nucleation, high affinity pointed end capping, and formation of branching networks of filaments,” *Proceedings of the National Academy of Sciences*, vol. 95, no. 11, pp. 6181–6186, 1998.
[64] L. Machesky, E. REEVES, F. WIENTJES, F. Mattheyse, A. GROGAN, N. Totty, A. BURLINGAME, J. Hsuan, and A. SEGAL, “Mammalian actin-related protein 2/3 complex localizes to regions of lamellipodial protrusion and is composed of evolutionarily conserved proteins,” *Biochem. J*, vol. 328, pp. 105–112, 1997.
[65] T. Takenawa and S. Suetsugu, “The wasp–wave protein network: connecting the membrane to the cytoskeleton,” *Nature reviews Molecular cell biology*, vol. 8, no. 1, pp. 37–48, 2007.
[66] E. Derivery and A. Gautreau, “Generation of branched actin networks: assembly and regulation of the n-wasp and wave molecular machines,” *Bioessays*, vol. 32, no. 2, pp. 119–131, 2010.
[67] S. Pellegrin and H. Mellor, “The rho family gtpase rif induces filopodia through mdia2,” *Current Biology*, vol. 15, no. 2, pp. 129–133, 2005.
[68] A. Schirenbeck, T. Bretschneider, R. Arasada, M. Schleicher, and J. Faix, “The diaphanous-related formin ddia2 is required for the formation and maintenance of filopodia,” *Nature cell biology*, vol. 7, no. 6, pp. 619–625, 2005.
[69] A. S. Paul and T. D. Pollard, “Review of the mechanism of processive actin filament elongation by formins,” *Cell motility and the cytoskeleton*, vol. 66, no. 8, pp. 606–617, 2009.
[70] H. Mellor, “The role of formins in filopodia formation,” *Biochimica et Biophysica Acta (BBA)-Molecular Cell Research*, vol. 1803, no. 2, pp. 191–200, 2010.
[71] C. Yang and T. Svitkina, “Filopodia initiation: focus on the arp2/3 complex and formins,” *Cell adhesion & migration*, vol. 5, no. 5, pp. 402–408, 2011.
[72] A. P. Liu, D. L. Richmond, L. Maibaum, S. Pronk, P. L. Geissler, and D. A. Fletcher, “Membrane-induced bundling of actin filaments,” *Nature physics*, vol. 4, no. 10, pp. 789–793, 2008.

[73] A. J. Ridley, “Rho gtpases and actin dynamics in membrane protrusions and vesicle trafficking,” *Trends in cell biology*, vol. 16, no. 10, pp. 522–529, 2006.
[74] R. Rose, M. Weyand, M. Lammers, T. Ishizaki, M. Ahmadian, and A. Wittinghofer, “Structural and mechanistic insights into the interaction between rho and mammalian dia,” *Nature*, vol. 435, no. 7041, pp. 513–518, 2005.
[75] T. Otomo, C. Otomo, D. R. Tomchick, M. Machius, and M. K. Rosen, “Structural basis of rho gtpase-mediated activation of the formin mdia1,” *Molecular cell*, vol. 18, no. 3, pp. 273–281, 2005.
[76] E. Paluch, M. Piel, J. Prost, M. Bornens, and C. Sykes, “Cortical actomyosin breakage triggers shape oscillations in cells and cell fragments,” *Biophysical journal*, vol. 89, no. 1, pp. 724–733, 2005.
[77] G. T. Charras, C.-K. Hu, M. Coughlin, and T. J. Mitchison, “Reassembly of contractile actin cortex in cell blebs,” *The Journal of cell biology*, vol. 175, no. 3, pp. 477–490, 2006.
[78] G. Charras, “A short history of blebbing,” *Journal of microscopy*, vol. 231, no. 3, pp. 466–478, 2008.
[79] S. Hannemann, R. Madrid, J. Stastna, T. Kitzing, J. Gasteier, A. Schönichen, J. Bouchet, A. Jimenez, M. Geyer, R. Grosse, *et al.*, “The diaphanous-related formin fhod1 associates with rock1 and promotes src-dependent plasma membrane blebbing,” *Journal of Biological Chemistry*, vol. 283, no. 41, pp. 27891–27903, 2008.
[80] K. M. Eisenmann, E. S. Harris, S. M. Kitchen, H. A. Holman, H. N. Higgs, and A. S. Alberts, “Dia-interacting protein modulates formin-mediated actin assembly at the cell cortex,” *Current Biology*, vol. 17, no. 7, pp. 579–591, 2007.
[81] Y. Han, E. Eppinger, I. G. Schuster, L. U. Weigand, X. Liang, E. Kremmer, C. Peschel, and A. M. Krackhardt, “Formin-like 1 (fmnl1) is regulated by n-terminal myristoylation and induces polarized membrane blebbing,” *Journal of Biological Chemistry*, vol. 284, no. 48, pp. 33409–33417, 2009.
[82] R. Levayer and T. Lecuit, “Biomechanical regulation of contractility: spatial control and dynamics,” *Trends in cell biology*, vol. 22, no. 2, pp. 61–81, 2012.
[83] C.-P. Heisenberg and Y. Bellache, “Forces in tissue morphogenesis and patterning,” *Cell*, vol. 153, no. 5, pp. 948–962, 2013.
[84] T. Lecuit, P.-F. Lenne, and E. Munro, “Force generation, transmission, and integration during cell and tissue morphogenesis,” *Annual review of cell and developmental biology*, vol. 27, pp. 157–184, 2011.
[85] E. Paluch, C. Sykes, J. Prost, and M. Bornens, “Dynamic modes of the cortical actomyosin gel during cell locomotion and division,” *Trends in cell biology*, vol. 16, no. 1, pp. 5–10, 2006.
[86] C. Roubinet, P. T. Tran, and M. Piel, “Common mechanisms regulating cell cortex properties during cell division and cell migration,” *Cytoskeleton*, vol. 69, no. 11, pp. 957–972, 2012.

[87] E. Paluch and C.-P. Heisenberg, “Biology and physics of cell shape changes in development,” *Current Biology*, vol. 19, no. 17, pp. R790–R799, 2009.
[88] A. G. Clark and E. Paluch, “Mechanics and regulation of cell shape during the cell cycle,” in *Cell Cycle in Development*, pp. 31–73, Springer, 2011.
[89] R. A. Green, E. Paluch, and K. Oegema, “Cytokinesis in animal cells,” *Annual review of cell and developmental biology*, vol. 28, pp. 29–58, 2012.
[90] U. S. Eggert, T. J. Mitchison, and C. M. Field, “Animal cytokinesis: from parts list to mechanisms,” *Annu. Rev. Biochem.*, vol. 75, pp. 543–566, 2006.
[91] L. P. Cramer, “Mechanism of cell rear retraction in migrating cells,” *Current Opinion in Cell Biology*, 2013.
[92] P. Naumanen, P. Lappalainen, and P. Hotulainen, “Mechanisms of actin stress fibre assembly,” *Journal of microscopy*, vol. 231, no. 3, pp. 446–454, 2008.
[93] S. Tojkander, G. Gateva, and P. Lappalainen, “Actin stress fibers–assembly, dynamics and biological roles,” *Journal of Cell Science*, vol. 125, no. 8, pp. 1855–1864, 2012.
[94] K. Burridge and E. S. Wittchen, “The tension mounts: Stress fibers as force-generating mechanotransducers,” *The Journal of cell biology*, vol. 200, no. 1, pp. 9–19, 2013.
[95] K. Hayakawa, H. Tatsumi, and M. Sokabe, “Mechano-sensing by actin filaments and focal adhesion proteins,” *Communicative & integrative biology*, vol. 5, no. 6, pp. 572–577, 2012.
[96] S. Mostowy and P. Cossart, “Septins: the fourth component of the cytoskeleton,” *Nature Reviews Molecular Cell Biology*, vol. 13, no. 3, pp. 183–194, 2012.
[97] A. S. Gladfelter, J. R. Pringle, and D. J. Lew, “The septin cortex at the yeast mother–bud neck,” *Current opinion in microbiology*, vol. 4, no. 6, pp. 681–689, 2001.
[98] M. A. McMurray, J. Thorner, *et al.*, “Septins: molecular partitioning and the generation of cellular asymmetry,” *Cell Div*, vol. 4, p. 18, 2009.
[99] M. Versele and J. Thorner, “Some assembly required: yeast septins provide the instruction manual,” *Trends in cell biology*, vol. 15, no. 8, pp. 414–424, 2005.
[100] M. Kinoshita and M. Noda, “Roles of septins in the mammalian cytokinesis machinery,” *Cell structure and function*, vol. 26, no. 6, pp. 667–670, 2001.
[101] E. Joo, C. W. Tsang, and W. S. Trimble, “Septins: traffic control at the cytokinesis intersection,” *Traffic*, vol. 6, no. 8, pp. 626–634, 2005.
[102] J. Dobbelaere and Y. Barral, “Spatial coordination of cytokinetic events by compartmentalization of the cell cortex,” *Science*, vol. 305, no. 5682, pp. 393–396, 2004.
[103] S. K. Kim, A. Shindo, T. J. Park, E. C. Oh, S. Ghosh, R. S. Gray, R. A. Lewis, C. A. Johnson, T. Attie-Bittach, N. Katsanis, *et al.*, “Planar cell polarity acts through

septins to control collective cell movement and ciliogenesis," *Science*, vol. 329, no. 5997, pp. 1337–1340, 2010.
[104] Q. Hu, L. Milenkovic, H. Jin, M. P. Scott, M. V. Nachury, E. T. Spiliotis, and W. J. Nelson, "A septin diffusion barrier at the base of the primary cilium maintains ciliary membrane protein distribution," *Science*, vol. 329, no. 5990, pp. 436–439, 2010.
[105] T. Tada, A. Simonetta, M. Batterton, M. Kinoshita, D. Edbauer, and M. Sheng, "Role of septin cytoskeleton in spine morphogenesis and dendrite development in neurons," *Current Biology*, vol. 17, no. 20, pp. 1752–1758, 2007.
[106] Y. Xie, J. P. Vessey, A. Konecna, R. Dahm, P. Macchi, and M. A. Kiebler, "The gtp-binding protein septin 7 is critical for dendrite branching and dendritic-spine morphology," *Current Biology*, vol. 17, no. 20, pp. 1746–1751, 2007.
[107] M. Ihara, A. Kinoshita, S. Yamada, H. Tanaka, A. Tanigaki, A. Kitano, M. Goto, K. Okubo, H. Nishiyama, O. Ogawa, *et al.*, "Cortical organization by the septin cytoskeleton is essential for structural and mechanical integrity of mammalian spermatozoa," *Developmental cell*, vol. 8, no. 3, pp. 343–352, 2005.
[108] S. Kwitny, A. V. Klaus, and G. R. Hunnicutt, "The annulus of the mouse sperm tail is required to establish a membrane diffusion barrier that is engaged during the late steps of spermiogenesis," *Biology of reproduction*, vol. 82, no. 4, pp. 669–678, 2010.
[109] J. Gilden and M. F. Krummel, "Control of cortical rigidity by the cytoskeleton: emerging roles for septins," *Cytoskeleton*, vol. 67, no. 8, pp. 477–486, 2010.
[110] P. Janmey, "Cell membranes and the cytoskeleton," *Handbook of Biological Physics*, vol. 1, pp. 805–849, 1995.
[111] A. S. Sechi and J. Wehland, "The actin cytoskeleton and plasma membrane connection: Ptdins(4, 5)P_2 influences cytoskeletal protein activity at the plasma membrane," *Journal of cell science*, vol. 113, no. 21, pp. 3685–3695, 2000.
[112] H. Zhao, A. Pykäläinen, and P. Lappalainen, "I-bar domain proteins: linking actin and plasma membrane dynamics," *Current opinion in cell biology*, vol. 23, no. 1, pp. 14–21, 2011.
[113] V. Bennett and J. Healy, "Membrane domains based on ankyrin and spectrin associated with cell–cell interactions," *Cold Spring Harbor perspectives in biology*, vol. 1, no. 6, 2009.
[114] A. Viel and D. Branton, "Spectrin: on the path from structure to function," *Current opinion in cell biology*, vol. 8, no. 1, pp. 49–55, 1996.
[115] D. Nowak, A. Kochman, and M. Malicka-Baszkiewicz, "Identification of actin from hepatoma morris 5123 cells.," *Acta biochimica Polonica*, vol. 46, no. 4, pp. 949–959, 1998.

[116] K. Zechel and K. Weber, “Actins from mammals, bird, fish and slime mold characterized by isoelectric focusing in polyacrylamide gels,” *European Journal of Biochemistry*, vol. 89, no. 1, pp. 105–112, 1978.
[117] R. Lipowsky, E. Sackmann, *et al.*, “Handbook of biological physics,” *Handbook of Biological Physics*, 1995.
[118] A. Laliberte and C. Gicquaud, “Polymerization of actin by positively charged liposomes.,” *The Journal of cell biology*, vol. 106, no. 4, pp. 1221–1227, 1988.
[119] A. Renault, P. Lenne, C. Zakri, A. Aradian, C. Vénien-Bryan, and F. Amblard, “Surface-induced polymerization of actin,” *Biophysical journal*, vol. 76, no. 3, pp. 1580–1590, 1999.
[120] R. Grimm, M. Bärmann, W. Häckl, D. Typke, E. Sackmann, and W. Baumeister, “Energy filtered electron tomography of ice-embedded actin and vesicles,” *Biophysical journal*, vol. 72, no. 1, pp. 482–489, 1997.
[121] C. Gicquaud, “Actin conformation is drastically altered by direct interaction with membrane lipids: a differential scanning calorimetry study,” *Biochemistry*, vol. 32, no. 44, pp. 11873–11877, 1993.
[122] C. Gicquaud and P. Wong, “Mechanism of interaction between actin and membrane lipids: a pressure-tuning infrared spectroscopy study.,” *Biochemical Journal*, vol. 303, no. Pt 3, p. 769, 1994.
[123] L. Limozin, M. Bärmann, and E. Sackmann, “On the organization of self-assembled actin networks in giant vesicles,” *The European Physical Journal E: Soft Matter and Biological Physics*, vol. 10, no. 4, pp. 319–330, 2003.
[124] M. Hase and K. Yoshikawa, “Structural transition of actin filament in a cell-sized water droplet with a phospholipid membrane,” *The Journal of Chemical Physics*, vol. 124, no. 10, p. 104903, 2006.
[125] D. St-Onge and C. Gicquaud, “Evidence of direct interaction between actin and membrane lipids,” *Biochemistry and Cell Biology*, vol. 67, no. 6, pp. 297–300, 1989.
[126] B. Demé, D. Hess, M. Tristl, L. Lee, and E. Sackmann, “Binding of actin filaments to charged lipid monolayers: Film balance experiments combined with neutron reflectivity,” *The European Physical Journal E: Soft Matter and Biological Physics*, vol. 2, no. 2, pp. 125–136, 2000.
[127] W. Häckl, M. Bärmann, and E. Sackmann, “Shape changes of self-assembled actin bilayer composite membranes,” *Physical review letters*, vol. 80, no. 8, pp. 1786–1789, 1998.
[128] S. Garg, J. Tang, J. Rühe, and C. Naumann, “Actin-induced perturbation of ps lipid–cholesterol interaction: a possible mechanism of cytoskeleton-based regulation of membrane organization,” *Journal of structural biology*, vol. 168, no. 1, pp. 11–20, 2009.

[129] A. P. Liu and D. A. Fletcher, “Actin polymerization serves as a membrane domain switch in model lipid bilayers,” *Biophysical journal*, vol. 91, no. 11, pp. 4064–4070, 2006.
[130] G. R. Chichili and W. Rodgers, “Cytoskeleton–membrane interactions in membrane raft structure,” *Cellular and molecular life sciences*, vol. 66, no. 14, pp. 2319–2328, 2009.
[131] A. Bretscher, K. Edwards, and R. G. Fehon, “Erm proteins and merlin: integrators at the cell cortex,” *Nature Reviews Molecular Cell Biology*, vol. 3, no. 8, pp. 586–599, 2002.
[132] J. Saarikangas, H. Zhao, and P. Lappalainen, “Regulation of the actin cytoskeleton-plasma membrane interplay by phosphoinositides,” *Physiological reviews*, vol. 90, no. 1, pp. 259–289, 2010.
[133] L. Zhang, Y. S. Mao, P. A. Janmey, and H. L. Yin, *Subcellular Biochemistry*. Springer-Verlag, Feb 2012.
[134] Y. S. Mao and H. L. Yin, “Regulation of the actin cytoskeleton by phosphatidylinositol 4-phosphate 5 kinases,” *Pflügers Archiv-European Journal of Physiology*, vol. 455, no. 1, pp. 5–18, 2007.
[135] H. L. Yin and P. A. Janmey, “Phosphoinositide regulation of the actin cytoskeleton,” *Annual review of physiology*, vol. 65, no. 1, pp. 761–789, 2003.
[136] K. Boesze-Battaglia and R. Schimmel, “Cell membrane lipid composition and distribution: implications for cell function and lessons learned from photoreceptors and platelets.,” *Journal of experimental biology*, vol. 200, no. 23, pp. 2927–2936, 1997.
[137] S. McLaughlin and D. Murray, “Plasma membrane phosphoinositide organization by protein electrostatics,” *Nature*, vol. 438, no. 7068, pp. 605–611, 2005.
[138] S. Takamori, M. Holt, K. Stenius, E. A. Lemke, M. Grønborg, D. Riedel, H. Urlaub, S. Schenck, B. Brügger, P. Ringler, *et al.*, “Molecular anatomy of a trafficking organelle,” *Cell*, vol. 127, no. 4, pp. 831–846, 2006.
[139] W. Kuo, D. Z. Herrick, and D. S. Cafiso, “Phosphatidylinositol 4, 5-bisphosphate alters synaptotagmin 1 membrane docking and drives opposing bilayers closer together,” *Biochemistry*, vol. 50, no. 13, pp. 2633–2641, 2011.
[140] M. P. Sheetz, J. E. Sable, and H.-G. Döbereiner, “Continuous membrane-cytoskeleton adhesion requires continuous accommodation to lipid and cytoskeleton dynamics,” *Annu. Rev. Biophys. Biomol. Struct.*, vol. 35, pp. 417–434, 2006.
[141] J. A. Brill, R. Wong, and A. Wilde, “Phosphoinositide function in cytokinesis,” *Current Biology*, vol. 21, no. 22, pp. R930–R934, 2011.
[142] A. Echard, “Phosphoinositides and cytokinesis: the “pip” of the iceberg,” *Cytoskeleton*, vol. 69, no. 11, pp. 893–912, 2012.

[143] M. R. Logan and C. A. Mandato, “Regulation of the actin cytoskeleton by pip2 in cytokinesis,” *Biology of the Cell*, vol. 98, no. 6, pp. 377–388, 2006.
[144] G. Isenberg, “Actin binding proteins—lipid interactions,” *Journal of muscle research and cell motility*, vol. 12, no. 2, pp. 136–144, 1991.
[145] P. Burn, A. Rotman, R. Meyer, and M. M. Burger, “Diacylglycerol in large α-actinin/actin complexes and in the cytoskeleton of activated platelets,” 1985.
[146] M. Fritz, R. Zimmermann, M. Bärmann, and H. Gaub, “Actin binding to lipid-inserted alpha-actinin.,” *Biophysical journal*, vol. 65, no. 5, p. 1878, 1993.
[147] H. Wolfenson, I. Lavelin, and B. Geiger, “Dynamic regulation of the structure and functions of integrin adhesions,” *Developmental cell*, vol. 24, no. 5, pp. 447–458, 2013.
[148] W. M. Brieher *et al.*, “Cadherin junctions and their cytoskeleton (s),” *Current opinion in cell biology*, 2012.
[149] A. L. Neisch and R. G. Fehon, “Ezrin, radixin and moesin: key regulators of membrane–cortex interactions and signaling,” *Current opinion in cell biology*, vol. 23, no. 4, pp. 377–382, 2011.
[150] R. G. Fehon, A. I. McClatchey, and A. Bretscher, “Organizing the cell cortex: the role of erm proteins,” *Nature Reviews Molecular Cell Biology*, vol. 11, no. 4, pp. 276–287, 2010.
[151] D. E. Ingber, “Tensegrity i. cell structure and hierarchical systems biology,” *Journal of Cell Science*, vol. 116, no. 7, pp. 1157–1173, 2003.
[152] D. E. Ingber, “The riddle of morphogenesis: a question of solution chemistry or molecular cell engineering?,” *Cell*, vol. 75, no. 7, pp. 1249–1252, 1993.
[153] B. D. Hoffman and J. C. Crocker, “Cell mechanics: dissecting the physical responses of cells to force,” *Annual review of biomedical engineering*, vol. 11, pp. 259–288, 2009.
[154] T. Lecuit and P.-F. Lenne, “Cell surface mechanics and the control of cell shape, tissue patterns and morphogenesis,” *Nature Reviews Molecular Cell Biology*, vol. 8, no. 8, pp. 633–644, 2007.
[155] R. Levayer, A. Pelissier-Monier, and T. Lecuit, “Spatial regulation of dia and myosin-ii by rhogef2 controls initiation of e-cadherin endocytosis during epithelial morphogenesis,” *Nature cell biology*, vol. 13, no. 5, pp. 529–540, 2011.
[156] A. P. Liu and D. A. Fletcher, “Biology under construction: in vitro reconstitution of cellular function,” *Nature Reviews Molecular Cell Biology*, vol. 10, no. 9, pp. 644–650, 2009.
[157] K. Rottner and T. E. Stradal, “Actin dynamics and turnover in cell motility,” *Current opinion in cell biology*, vol. 23, no. 5, pp. 569–578, 2011.
[158] K. Keren, “Cell motility: the integrating role of the plasma membrane,” *European Biophysics Journal*, vol. 40, no. 9, pp. 1013–1027, 2011.

[159] N. C. Gauthier, T. A. Masters, and M. P. Sheetz, “Mechanical feedback between membrane tension and dynamics,” *Trends in cell biology*, 2012.
[160] P. A. Janmey and C. A. McCulloch, “Cell mechanics: integrating cell responses to mechanical stimuli,” *Annu. Rev. Biomed. Eng.*, vol. 9, pp. 1–34, 2007.
[161] A.-S. Smith, “Physics challenged by cells,” *Nature Physics*, vol. 6, no. 10, pp. 726–729, 2010.
[162] S. K. Vogel and P. Schwille, “Minimal systems to study membrane–cytoskeleton interactions,” *Current Opinion in Biotechnology*, vol. 23, no. 5, pp. 758–765, 2012.
[163] D. A. Fletcher and R. D. Mullins, “Cell mechanics and the cytoskeleton,” *Nature*, vol. 463, no. 7280, pp. 485–492, 2010.
[164] S. K. Vogel, F. Heinemann, G. Chwastek, and P. Schwille, “The design of macs (minimal actin cortices),” *Cytoskeleton*, 2013.
[165] R. D. Mullins and S. D. Hansen, “In vitro studies of actin filament and network dynamics.,” *Current Opinion in Cell Biology*, vol. 25, pp. 6–13, 2013.
[166] J. Sedzinski, M. Biro, A. Oswald, J.-Y. Tinevez, G. Salbreux, and E. Paluch, “Polar actomyosin contractility destabilizes the position of the cytokinetic furrow,” *Nature*, vol. 476, no. 7361, pp. 462–466, 2011.
[167] E. Sackmann *et al.*, “Supported membranes: scientific and practical applications,” *Science-AAAS-Weekly Paper Edition*, vol. 271, no. 5245, pp. 43–48, 1996.
[168] A. S. Achalkumar, R. J. Bushby, and S. D. Evans, “Cholesterol-based anchors and tethers for phospholipid bilayers and for model biological membranes,” *Soft Matter*, vol. 6, no. 24, pp. 6036–6051, 2010.
[169] R. J. Barfoot, K. H. Sheikh, B. R. Johnson, J. Colyer, R. E. Miles, L. J. Jeuken, R. J. Bushby, and S. D. Evans, “Minimal f-actin cytoskeletal system for planar supported phospholipid bilayers,” *Langmuir*, vol. 24, no. 13, pp. 6827–6836, 2008.
[170] B. R. Johnson, R. J. Bushby, J. Colyer, and S. D. Evans, “Self-assembly of actin scaffolds at ponticulin-containing supported phospholipid bilayers,” *Biophysical journal*, vol. 90, no. 3, pp. L21–L23, 2006.
[171] S. Bosk, J. A. Braunger, V. Gerke, and C. Steinem, “Activation of f-actin binding capacity of ezrin: Synergism of PIP_2 interaction and phosphorylation,” *Biophysical journal*, vol. 100, no. 7, pp. 1708–1717, 2011.
[172] K. Lee, J. L. Gallop, K. Rambani, and M. W. Kirschner, “Self-assembly of filopodia-like structures on supported lipid bilayers,” *Science*, vol. 329, no. 5997, pp. 1341–1345, 2010.
[173] S. K. Vogel, Z. Petrasek, F. Heinemann, and P. Schwille, “Myosin motors fragment and compact membrane-bound actin filaments,” *Elife*, vol. 2, 2013.
[174] M. P. Murrell and M. L. Gardel, “F-actin buckling coordinates contractility and severing in a biomimetic actomyosin cortex,” *Proceedings of the National Academy of Sciences*, vol. 109, no. 51, pp. 20820–20825, 2012.

[175] T. P. Loisel, R. Boujemaa, D. Pantaloni, and M.-F. Carlier, “Reconstitution of actin-based motility of listeria and shigella using pure proteins,” *Nature*, vol. 401, no. 6753, pp. 613–616, 1999.
[176] C. Co, D. T. Wong, S. Gierke, V. Chang, and J. Taunton, “Mechanism of actin network attachment to moving membranes: barbed end capture by n-wasp wh2 domains,” *Cell*, vol. 128, no. 5, pp. 901–913, 2007.
[177] V. Koronakis, P. J. Hume, D. Humphreys, T. Liu, O. Hørning, O. N. Jensen, and E. J. McGhie, “Wave regulatory complex activation by cooperating gtpases arf and rac1,” *Proceedings of the National Academy of Sciences*, vol. 108, no. 35, pp. 14449–14454, 2011.
[178] H. Boukellal, O. Campás, J.-F. Joanny, J. Prost, and C. Sykes, “Soft listeria: actin-based propulsion of liquid drops,” *Physical Review E*, vol. 69, no. 6, p. 061906, 2004.
[179] D. Ershov, M. CohenáStuart, and J. der Gucht, “Mechanical properties of reconstituted actin networks at an oil–water interface determined by microrheology,” *Soft Matter*, vol. 8, no. 21, pp. 5896–5903, 2012.
[180] S. Isanta, G. Espinosa, R. Rodrguez-Garcá, P. Natale, I. López-Montero, D. Langevin, and F. Monroy, “Active membranes with bound f-actin: sliding vs. sticking conditions,” *Soft Matter*, vol. 7, no. 7, pp. 3100–3107, 2011.
[181] K. Carvalho, J. Lemière, F. Faqir, J. Manzi, L. Blanchoin, J. Plastino, T. Betz, and C. Sykes, “Actin polymerization or myosin contraction: two ways to build up cortical tension for symmetry breaking,” *Philosophical Transaction B*, vol. 368, p. 20130005, 2013.
[182] K. Carvalho, F.-C. Tsai, E. Lees, R. Voituriez, G. Koenderink, and C. Sykes, “Cell-sized liposomes reveal how actomyosin cortical tension drives shape change,” *Proceedings of the National Academy of Sciences*, vol. 110, pp. 16456–16461, 2013.
[183] E. Helfer, S. Harlepp, L. Bourdieu, J. Robert, F. MacKintosh, and D. Chatenay, “Microrheology of biopolymer-membrane complexes,” *Physical review letters*, vol. 85, no. 2, p. 457, 2000.
[184] V. Delatour, E. Helfer, D. Didry, K. H. D. Lê, J.-F. Gaucher, M.-F. Carlier, and G. Romet-Lemonne, “Arp2/3 controls the motile behavior of n-wasp-functionalized guvs and modulates n-wasp surface distribution by mediating transient links with actin filaments,” *Biophysical journal*, vol. 94, no. 12, pp. 4890–4905, 2008.
[185] P. A. Giardini, D. A. Fletcher, and J. A. Theriot, “Compression forces generated by actin comet tails on lipid vesicles,” *Proceedings of the National Academy of Sciences*, vol. 100, no. 11, pp. 6493–6498, 2003.
[186] A. Upadhyaya, J. R. Chabot, A. Andreeva, A. Samadani, and A. van Oudenaarden, “Probing polymerization forces by using actin-propelled lipid

vesicles," *Proceedings of the National Academy of Sciences*, vol. 100, no. 8, pp. 4521–4526, 2003.
[187] I. n. Lo pez Montero, R. Rodrguez-Garcá, and F. Monroy, "Artificial spectrin shells reconstituted on giant vesicles," *The Journal of Physical Chemistry Letters*, vol. 3, no. 12, pp. 1583–1588, 2012.
[188] J. Heuvingh, M. Franco, P. Chavrier, and C. Sykes, "Arf1-mediated actin polymerization produces movement of artificial vesicles," *Proceedings of the National Academy of Sciences*, vol. 104, no. 43, pp. 16928–16933, 2007.
[189] S. F. Fenz and K. Sengupta, "Giant vesicles as cell models," *Integrative Biology*, vol. 4, no. 9, pp. 982–995, 2012.
[190] T. Hamada and K. Yoshikawa, "Cell-sized liposomes and droplets: Real-world modeling of living cells," *Materials*, vol. 5, no. 11, pp. 2292–2305, 2012.
[191] P. Stano, E. D'Aguanno, P. Carrara, A. Fahr, and P. L. Luisi, "Recent advancements in synthetic cells research," in *Advances in Artificial Life, ECAL*, vol. 12, pp. 1160–1161, 2013.
[192] V. Noireaux, Y. T. Maeda, and A. Libchaber, "Development of an artificial cell, from self-organization to computation and self-reproduction," *Proceedings of the National Academy of Sciences*, vol. 108, no. 9, pp. 3473–3480, 2011.
[193] P. Stano, P. Carrara, Y. Kuruma, T. P. de Souza, and P. L. Luisi, "Compartmentalized reactions as a case of soft-matter biotechnology: synthesis of proteins and nucleic acids inside lipid vesicles," *Journal of Materials Chemistry*, vol. 21, no. 47, pp. 18887–18902, 2011.
[194] A. J. Dzieciol and S. Mann, "Designs for life: protocell models in the laboratory," *Chemical Society Reviews*, vol. 41, no. 1, pp. 79–85, 2012.
[195] P. Walde, K. Cosentino, H. Engel, and P. Stano, "Giant vesicles: preparations and applications," *ChemBioChem*, vol. 11, no. 7, pp. 848–865, 2010.
[196] H. Miyata and H. Hotani, "Morphological changes in liposomes caused by polymerization of encapsulated actin and spontaneous formation of actin bundles," *Proceedings of the National Academy of Sciences*, vol. 89, no. 23, pp. 11547–11551, 1992.
[197] H. Miyata and K. Kinosita Jr, "Transformation of actin-encapsulating liposomes induced by cytochalasin d," *Biophysical journal*, vol. 67, no. 2, pp. 922–928, 1994.
[198] H. Miyata, S. Nishiyama, K.-i. Akashi, and K. Kinosita Jr, "Protrusive growth from giant liposomes driven by actin polymerization," *Proceedings of the National Academy of Sciences*, vol. 96, no. 5, pp. 2048–2053, 1999.
[199] M. Honda, K. Takiguchi, S. Ishikawa, and H. Hotani, "Morphogenesis of liposomes encapsulating actin depends on the type of actin-crosslinking," *Journal of molecular biology*, vol. 287, no. 2, pp. 293–300, 1999.

[200] H. Maemichi, K. Shikinaka, A. Kakugo, H. Furukawa, Y. Osada, and J. P. Gong, “Morphogenesis of liposomes caused by polycation-induced actin assembly formation,” *Langmuir*, vol. 24, no. 20, pp. 11975–11981, 2008.
[201] D. Merkle, N. Kahya, and P. Schwille, “Reconstitution and anchoring of cytoskeleton inside giant unilamellar vesicles,” *ChemBioChem*, vol. 9, no. 16, pp. 2673–2681, 2008.
[202] L. Limozin and E. Sackmann, “Polymorphism of cross-linked actin networks in giant vesicles,” *Physical review letters*, vol. 89, no. 16, p. 168103, 2002.
[203] L.-L. Pontani, J. Van der Gucht, G. Salbreux, J. Heuvingh, J.-F. Joanny, and C. Sykes, “Reconstitution of an actin cortex inside a liposome,” *Biophysical journal*, vol. 96, no. 1, pp. 192–198, 2009.
[204] M. Murrell, L.-L. Pontani, K. Guevorkian, D. Cuvelier, P. Nassoy, and C. Sykes, “Spreading dynamics of biomimetic actin cortices,” *Biophysical journal*, vol. 100, no. 6, pp. 1400–1409, 2011.
[205] C. Campillo, P. Sens, D. Köster, L.-L. Pontani, D. Lévy, P. Bassereau, P. Nassoy, and C. Sykes, “Unexpected membrane dynamics unveiled by membrane nanotube extrusion,” *Biophysical journal*, vol. 104, no. 6, pp. 1248–1256, 2013.
[206] M. Abkarian, E. Loiseau, and G. Massiera, “Continuous droplet interface crossing encapsulation (cdice) for high throughput monodisperse vesicle design,” *Soft Matter*, vol. 7, no. 10, pp. 4610–4614, 2011.
[207] K. Takiguchi, M. Negishi, Y. Tanaka-Takiguchi, M. Homma, and K. Yoshikawa, “Transformation of actohmm assembly confined in cell-sized liposome,” *Langmuir*, vol. 27, no. 18, pp. 11528–11535, 2011.
[208] K. Takiguchi, A. Yamada, M. Negishi, M. Honda, Y. Tanaka-Takiguchi, and K. Yoshikawa, “Construction of cell-sized liposomes encapsulating actin and actin-cross-linking proteins,” *Methods in enzymology*, vol. 464, pp. 31–53, 2009.
[209] K. Takiguchi, M. Negishi, Y. Tanaka-Takiguchi, M. Homma, and K. Yoshikawa, “Reconstruction of motile actin networks in giant liposome,” in *Micro-NanoMechatronics and Human Science (MHS), 2010 International Symposium on*, pp. 150–155, IEEE, 2010.
[210] K. Takiguchi, A. Yamada, M. Negishi, Y. Tanaka-Takiguchi, and K. Yoshikawa, “Entrapping desired amounts of actin filaments and molecular motor proteins in giant liposomes,” *Langmuir*, vol. 24, no. 20, pp. 11323–11326, 2008.
[211] J. Reeves and R. Dowben, “Formation and properties of thin-walled phospholipid vesicles,” *Journal of cellular physiology*, vol. 73, no. 1, pp. 49–60, 1969.
[212] M. Angelova and D. Dimitrov, “Liposome electroformation,” *Faraday Discuss. Chem. Soc.*, vol. 81, pp. 303–311, 1986.

[213] P. M. Shaklee, S. Semrau, M. Malkus, S. Kubick, M. Dogterom, and T. Schmidt, “Protein incorporation in giant lipid vesicles under physiological conditions,” *ChemBioChem*, vol. 11, no. 2, pp. 175–179, 2010.
[214] L. Montes, A. Alonso, F. M. Goni, L. A. Bagatolli, *et al.*, “Giant unilamellar vesicles electroformed from native membranes and organic lipid mixtures under physiological conditions,” *Biophysical journal*, vol. 93, no. 10, pp. 3548–3554, 2007.
[215] T. Pott, H. Bouvrais, and P. Méléard, “Giant unilamellar vesicle formation under physiologically relevant conditions,” *Chemistry and physics of lipids*, vol. 154, no. 2, pp. 115–119, 2008.
[216] D. J. Estes and M. Mayer, “Giant liposomes in physiological buffer using electroformation in a flow chamber,” *Biochimica et Biophysica Acta (BBA)-Biomembranes*, vol. 1712, no. 2, pp. 152–160, 2005.
[217] K. Horger, D. Estes, R. Capone, and M. Mayer, “Films of agarose enable rapid formation of giant liposomes in solutions of physiologic ionic strength,” *Journal of the American Chemical Society*, vol. 131, no. 5, pp. 1810–1819, 2009.
[218] A. Weinberger, F.-C. Tsai, G. H. Koenderink, T. F. Schmidt, R. Itri, W. Meier, T. Schmatko, A. Schröder, and C. Marques, “Gel-assisted formation of giant unilamellar vesicles,” *Biophysical journal*, vol. 105, no. 1, pp. 154–164, 2013.
[219] F.-C. Tsai, B. Stuhrmann, and G. H. Koenderink, “Encapsulation of active cytoskeletal protein networks in cell-sized liposomes,” *Langmuir*, vol. 27, no. 16, pp. 10061–10071, 2011.
[220] S. Pautot, B. J. Frisken, and D. Weitz, “Engineering asymmetric vesicles,” *Proceedings of the National Academy of Sciences*, vol. 100, no. 19, pp. 10718–10721, 2003.
[221] D. van Swaay *et al.*, “Microfluidic methods for forming liposomes,” *Lab on a Chip*, vol. 13, no. 5, pp. 752–767, 2013.
[222] K. Nishimura, H. Suzuki, T. Toyota, and T. Yomo, “Size control of giant unilamellar vesicles prepared from inverted emulsion droplets,” *Journal of colloid and interface science*, vol. 376, no. 1, pp. 119–125, 2012.
[223] S. Matosevic, “Synthesizing artificial cells from giant unilamellar vesicles: State-of-the art in the development of microfluidic technology,” *Bioessays*, vol. 34, no. 11, pp. 992–1001, 2012.
[224] H. C. Shum, D. Lee, I. Yoon, T. Kodger, and D. A. Weitz, “Double emulsion templated monodisperse phospholipid vesicles,” *Langmuir*, vol. 24, pp. 7651–7653, Aug 2008.
[225] S. Teh, R. Khnouf, H. Fan, and A. Lee, “Stable, biocompatible lipid vesicle generation by solvent extraction-based droplet microfluidics,” *Biomicrofluidics*, vol. 5, no. 4, p. 044113, 2011.
[226] K. Funakoshi, H. Suzuki, and S. Takeuchi, “Formation of giant lipid vesiclelike compartments from a planar lipid membrane by a pulsed jet flow,” *Journal of the American Chemical Society*, vol. 129, no. 42, pp. 12608–12609, 2007.

[227] J. C. Stachowiak, D. L. Richmond, T. H. Li, A. P. Liu, S. H. Parekh, and D. A. Fletcher, "Unilamellar vesicle formation and encapsulation by microfluidic jetting," *Proceedings of the National Academy of Sciences*, vol. 105, no. 12, pp. 4697–4702, 2008.
[228] D. L. Richmond, E. M. Schmid, S. Martens, J. C. Stachowiak, N. Liska, and D. A. Fletcher, "Forming giant vesicles with controlled membrane composition, asymmetry, and contents," *Proceedings of the National Academy of Sciences*, vol. 108, no. 23, pp. 9431–9436, 2011.
[229] J. Howard, "Mechanics of motor proteins and the cytoskeleton. 2001," *Sunderland, MA: Sinauer*, 1985.
[230] G. J. Doherty and H. T. McMahon, "Mediation, modulation, and consequences of membrane-cytoskeleton interactions," *Annu. Rev. Biophys.*, vol. 37, pp. 65–95, 2008.
[231] O. Lieleg, M. M. Claessens, and A. R. Bausch, "Structure and dynamics of cross-linked actin networks," *Soft Matter*, vol. 6, no. 2, pp. 218–225, 2010.
[232] M. Tanaka and E. Sackmann, "Polymer-supported membranes as models of the cell surface," *Nature*, vol. 437, no. 7059, pp. 656–663, 2005.
[233] R. Walder, A. J. Levine, and M. Dennin, "Rheology of two-dimensional f-actin networks associated with a lipid interface," *Physical Review E*, vol. 77, no. 1, p. 011909, 2008.
[234] K. Sengupta, L. Limozin, M. Tristl, I. Haase, M. Fischer, and E. Sackmann, "Coupling artificial actin cortices to biofunctionalized lipid monolayers," *Langmuir*, vol. 22, no. 13, pp. 5776–5785, 2006.
[235] M. Angelova, S. Soleau, P. Méléard, F. Faucon, and P. Bothorel, "Preparation of giant vesicles by external ac electric fields. kinetics and applications," in *Trends in Colloid and Interface Science VI*, pp. 127–131, Springer, 1992.
[236] L. Bagatolli, T. Parasassi, and E. Gratton, "Giant phospholipid vesicles: comparison among the whole lipid sample characteristics using different preparation methods: a two photon fluorescence microscopy study," *Chemistry and physics of lipids*, vol. 105, no. 2, pp. 135–147, 2000.
[237] M. Mikelj, T. Praper, R. Demic, V. Hodnik, T. Turk, and G. Anderluh, "Electroformation of giant unilamellar vesicles from erythrocyte membranes under low-salt conditions," *Analytical biochemistry*, 2013.
[238] Y. Zhang, C.-m. Cheng, B. Cusick, and P. R. LeDuc, "Chemically encapsulated structural elements for probing the mechanical responses of biologically inspired systems," *Langmuir*, vol. 23, no. 15, pp. 8129–8134, 2007.
[239] J. D. Cortese, B. Schwab, C. Frieden, E. L. Elson, *et al.*, "Actin polymerization induces a shape change in actin-containing vesicles," *Proceedings of the National Academy of Sciences*, vol. 86, no. 15, pp. 5773–5777, 1989.

[240] E. Schäfer, T.-T. Kliesch, and A. Janshoff, “Mechanical properties of giant liposomes compressed between two parallel plates-impact of artificial actin shells,” *Langmuir*, 2013.
[241] Y. Zhou, C. K. Berry, P. A. Storer, and R. M. Raphael, “Peroxidation of polyunsaturated phosphatidyl-choline lipids during electroformation,” *Biomaterials*, vol. 28, no. 6, pp. 1298–1306, 2007.
[242] A. G. Ayuyan and F. S. Cohen, “Lipid peroxides promote large rafts: effects of excitation of probes in fluorescence microscopy and electrochemical reactions during vesicle formation,” *Biophysical journal*, vol. 91, no. 6, pp. 2172–2183, 2006.
[243] Y. Yamashita, M. Oka, T. Tanaka, and M. Yamazaki, “A new method for the preparation of giant liposomes in high salt concentrations and growth of protein microcrystals in them,” *Biochimica et Biophysica Acta (BBA)-Biomembranes*, vol. 1561, no. 2, pp. 129–134, 2002.
[244] K.-i. Akashi, H. Miyata, H. Itoh, and K. Kinosita Jr, “Preparation of giant liposomes in physiological conditions and their characterization under an optical microscope,” *Biophysical journal*, vol. 71, no. 6, pp. 3242–3250, 1996.
[245] J. D. Castile and K. M. Taylor, “Factors affecting the size distribution of liposomes produced by freeze–thaw extrusion,” *International journal of pharmaceutics*, vol. 188, no. 1, pp. 87–95, 1999.
[246] A. Moscho, O. Orwar, D. T. Chiu, B. P. Modi, and R. N. Zare, “Rapid preparation of giant unilamellar vesicles,” *Proceedings of the National Academy of Sciences*, vol. 93, no. 21, pp. 11443–11447, 1996.
[247] J. C. Stachowiak, D. L. Richmond, T. H. Li, F. Brochard-Wyart, and D. A. Fletcher, “Inkjet formation of unilamellar lipid vesicles for cell-like encapsulation,” *Lab on a Chip*, vol. 9, no. 14, pp. 2003–2009, 2009.
[248] S. Ota, S. Yoshizawa, and S. Takeuchi, “Microfluidic formation of monodisperse, cell-sized, and unilamellar vesicles,” *Angewandte Chemie International Edition*, vol. 48, no. 35, pp. 6533–6537, 2009.
[249] C. Billerit, G. D. Jeffries, O. Orwar, and A. Jesorka, “Formation of giant unilamellar vesicles from spin-coated lipid films by localized ir heating,” *Soft Matter*, vol. 8, no. 42, pp. 10823–10826, 2012.
[250] S. Pautot, B. J. Frisken, and D. Weitz, “Production of unilamellar vesicles using an inverted emulsion,” *Langmuir*, vol. 19, no. 7, pp. 2870–2879, 2003.
[251] S. Pautot, B. Frisken, J. Cheng, X. Xie, and D. Weitz, “Spontaneous formation of lipid structures at oil/water/lipid interfaces,” *Langmuir*, vol. 19, no. 24, pp. 10281–10287, 2003.
[252] O. Mertins, N. P. da Silveira, A. R. Pohlmann, A. P. Schröder, and C. M. Marques, “Electroformation of giant vesicles from an inverse phase precursor,” *Biophysical journal*, vol. 96, no. 7, pp. 2719–2726, 2009.
[253] H. Saito, Y. Kato, M. Le Berre, A. Yamada, T. Inoue, K. Yosikawa, and D. Baigl, “Time-resolved tracking of a minimum gene expression system

reconstituted in giant liposomes," *ChemBioChem*, vol. 10, no. 10, pp. 1640–1643, 2009.
[254] M. Angelova and D. Dimitrov, "A mechanism of liposome electroformation," in *Trends in colloid and interface science II*, pp. 59–67, Springer, 1988.
[255] J. W. Holland, C. Hui, P. R. Cullis, and T. D. Madden, "Poly (ethylene glycol)-lipid conjugates regulate the calcium-induced fusion of liposomes composed of phosphatidylethanolamine and phosphatidylserine," *Biochemistry*, vol. 35, no. 8, pp. 2618–2624, 1996.
[256] D. J. Estes and M. Mayer, "Electroformation of giant liposomes from spin-coated films of lipids," *Colloids and Surfaces B: Biointerfaces*, vol. 42, no. 2, pp. 115–123, 2005.
[257] J. Pécréaux, H.-G. Döbereiner, J. Prost, J.-F. Joanny, and P. Bassereau, "Refined contour analysis of giant unilamellar vesicles," *The European Physical Journal E*, vol. 13, no. 3, pp. 277–290, 2004.
[258] W. Helfrich, "Elastic properties of lipid bilayers: theory and possible experiments.," *Zeitschrift für Naturforschung. Teil C: Biochemie, Biophysik, Biologie, Virologie*, vol. 28, no. 11, p. 693, 1973.
[259] J. Faucon, M. Mitov, P. Méléard, I. Bivas, and P. Bothorel, "Bending elasticity and thermal fluctuations of lipid membranes. theoretical and experimental requirements," *Journal de Physique*, vol. 50, no. 17, pp. 2389–2414, 1989.
[260] W. Rawicz, K. Olbrich, T. McIntosh, D. Needham, and E. Evans, "Effect of chain length and unsaturation on elasticity of lipid bilayers," *Biophysical Journal*, vol. 79, no. 1, pp. 328–339, 2000.
[261] D. Marsh, "Elastic curvature constants of lipid monolayers and bilayers," *Chemistry and physics of lipids*, vol. 144, no. 2, pp. 146–159, 2006.
[262] S. Kaufmann, G. Papastavrou, K. Kumar, M. Textor, and E. Reimhult, "A detailed investigation of the formation kinetics and layer structure of poly (ethylene glycol) tether supported lipid bilayers," *Soft Matter*, vol. 5, no. 14, pp. 2804–2814, 2009.
[263] E. Evans and W. Rawicz, "Elasticity of"fuzzy"biomembranes," *Physical review letters*, vol. 79, no. 12, p. 2379, 1997.
[264] A. J. Levine and F. MacKintosh, "Dynamics of viscoelastic membranes," *Physical Review E*, vol. 66, no. 6, p. 061606, 2002.
[265] J.-B. Fournier, D. Lacoste, and E. Raphaël, "Fluctuation spectrum of fluid membranes coupled to an elastic meshwork: jump of the effective surface tension at the mesh size," *Physical review letters*, vol. 92, no. 1, p. 018102, 2004.
[266] N. Gov, A. Zilman, and S. Safran, "Cytoskeleton confinement and tension of red blood cell membranes," *Physical review letters*, vol. 90, no. 22, p. 228101, 2003.

[267] R. Shlomovitz and N. Gov, “Membrane waves driven by actin and myosin,” *Physical review letters*, vol. 98, no. 16, p. 168103, 2007.
[268] J.-P. Colletier, B. Chaize, M. Winterhalter, and D. Fournier, “Protein encapsulation in liposomes: efficiency depends on interactions between protein and phospholipid bilayer.,” *BMC biotechnology*, vol. 2, no. 1, p. 9, 2002.
[269] L. M. Dominak and C. D. Keating, “Polymer encapsulation within giant lipid vesicles,” *Langmuir*, vol. 23, no. 13, pp. 7148–7154, 2007.
[270] P. L. Luisi, M. Allegretti, T. Pereira de Souza, F. Steiniger, A. Fahr, and P. Stano, “Spontaneous protein crowding in liposomes: a new vista for the origin of cellular metabolism,” *ChemBioChem*, vol. 11, no. 14, pp. 1989–1992, 2010.
[271] T. Pereira de Souza, F. Steiniger, P. Stano, A. Fahr, and P. L. Luisi, “Spontaneous crowding of ribosomes and proteins inside vesicles: A possible mechanism for the origin of cell metabolism,” *ChemBioChem*, vol. 12, no. 15, pp. 2325–2330, 2011.
[272] P. L. Luisil, “Semi-synthetic minimal cells: Biochemical, physical, and technological aspects,” *Synthetic Biology: Tools and Applications*, 2013.
[273] L. M. Dominak and C. D. Keating, “Macromolecular crowding improves polymer encapsulation within giant lipid vesicles,” *Langmuir*, vol. 24, no. 23, pp. 13565–13571, 2008.
[274] L. M. Dominak, D. M. Omiatek, E. L. Gundermann, M. L. Heien, and C. D. Keating, “Polymeric crowding agents improve passive biomacromolecule encapsulation in lipid vesicles,” *Langmuir*, vol. 26, no. 16, pp. 13195–13200, 2010.
[275] C. I. Fisher and S. C. Kuo, “Filament rigidity causes f-actin depletion from nonbinding surfaces,” *Proceedings of the National Academy of Sciences*, vol. 106, no. 1, pp. 133–138, 2009.
[276] K. Takiguchi, M. Negishi, Y. Tanaka-Takiguchi, M. Homma, and K. Yoshikawa, “Real-world modeling of artificial motile cell,” in *Micro-NanoMechatronics and Human Science, 2009. MHS 2009. International Symposium on*, pp. 197–201, IEEE, 2009.
[277] J. T. Finer, R. M. Simmons, J. A. Spudich, *et al.*, “Single myosin molecule mechanics: piconewton forces and nanometre steps,” *Nature*, vol. 368, no. 6467, pp. 113–119, 1994.
[278] Y. Tanaka-Takiguchi, T. Kakei, A. Tanimura, A. Takagi, M. Honda, H. Hotani, and K. Takiguchi, “The elongation and contraction of actin bundles are induced by double-headed myosins in a motor concentration-dependent manner,” *Journal of molecular biology*, vol. 341, no. 2, pp. 467–476, 2004.
[279] A. B. Verkhovsky and G. G. Borisy, “Non-sarcomeric mode of myosin ii organization in the fibroblast lamellum.,” *The Journal of cell biology*, vol. 123, no. 3, pp. 637–652, 1993.
[280] M. S. e Silva, M. Depken, B. Stuhrmann, M. Korsten, F. C. MacKintosh, and G. H. Koenderink, “Active multistage coarsening of actin networks driven by

myosin motors," *Proceedings of the National Academy of Sciences*, vol. 108, no. 23, pp. 9408–9413, 2011.
[281] P. M. Bendix, G. H. Koenderink, D. Cuvelier, Z. Dogic, B. N. Koeleman, W. M. Brieher, C. M. Field, L. Mahadevan, and D. A. Weitz, "A quantitative analysis of contractility in active cytoskeletal protein networks," *Biophysical journal*, vol. 94, no. 8, pp. 3126–3136, 2008.
[282] G. H. Koenderink, Z. Dogic, F. Nakamura, P. M. Bendix, F. C. MacKintosh, J. H. Hartwig, T. P. Stossel, and D. A. Weitz, "An active biopolymer network controlled by molecular motors," *Proceedings of the National Academy of Sciences*, vol. 106, no. 36, pp. 15192–15197, 2009.
[283] J. Alvarado, M. Sheinman, A. Sharma, F. C. MacKintosh, and G. H. Koenderink, "Molecular motors robustly drive active gels to a critically connected state," *Nature physics*, vol. 9, pp. 591–597, 2013.
[284] T. J. Herbert and F. D. Carlson, "Spectroscopic study of the self-association of myosin," *Biopolymers*, vol. 10, no. 11, pp. 2231–2252, 1971.
[285] N. Kanzaki, T. Q. Uyeda, and K. Onuma, "Intermolecular interaction of actin revealed by a dynamic light scattering technique," *The Journal of Physical Chemistry B*, vol. 110, no. 6, pp. 2881–2887, 2006.
[286] S. F. Fenz, R. Merkel, and K. Sengupta, "Diffusion and intermembrane distance: case study of avidin and e-cadherin mediated adhesion," *Langmuir*, vol. 25, no. 2, pp. 1074–1085, 2008.
[287] E. Evans, "Probing the relation between force-lifetime-and chemistry in single molecular bonds," *Annual review of biophysics and biomolecular structure*, vol. 30, no. 1, pp. 105–128, 2001.
[288] Y. Loosli, R. Luginbuehl, and J. Snedeker, "Cytoskeleton reorganization of spreading cells on micro-patterned islands: a functional model," *Philosophical Transactions of the Royal Society A: Mathematical, Physical and Engineering Sciences*, vol. 368, no. 1920, pp. 2629–2652, 2010.
[289] G. T. Charras, J. C. Yarrow, M. A. Horton, L. Mahadevan, and T. Mitchison, "Non-equilibration of hydrostatic pressure in blebbing cells," *Nature*, vol. 435, no. 7040, pp. 365–369, 2005.
[290] S. A. Koestler, K. Rottner, F. Lai, J. Block, M. Vinzenz, and J. V. Small, "F- and g-actin concentrations in lamellipodia of moving cells," *PLoS One*, vol. 4, no. 3, p. e4810, 2009.
[291] L. W. Janson, J. Kolega, and D. L. Taylor, "Modulation of contraction by gelation/solation in a reconstituted motile model.," *The Journal of cell biology*, vol. 114, no. 5, pp. 1005–1015, 1991.
[292] T. D. Pollard, "Cytoplasmic contractile proteins.," *The Journal of cell biology*, vol. 91, no. 3, pp. 156s–165s, 1981.
[293] C. M. Hassan and N. A. Peppas, "Structure and applications of poly (vinyl alcohol) hydrogels produced by conventional crosslinking or by freezing/thawing

methods," in *Biopolymers PVA Hydrogels, Anionic Polymerisation Nanocomposites*, pp. 37–65, Springer, 2000.
[294] N. A. Peppas, J. Z. Hilt, A. Khademhosseini, and R. Langer, "Hydrogels in biology and medicine: from molecular principles to bionanotechnology," *Advanced Materials*, vol. 18, no. 11, pp. 1345–1360, 2006.
[295] J. D. Pardee, J. A. Spudich, *et al.*, "Purification of muscle actin," *Methods Cell Biol*, vol. 24, no. Pt A, pp. 271–289, 1982.
[296] S. S. Margossian and S. Lowey, "Preparation of myosin and its subfragments from rabbit skeletal muscle.," *Methods in enzymology*, vol. 85, p. 55, 1982.
[297] R. L. DeBiasio, L.-L. Wang, G. W. Fisher, D. L. Taylor, *et al.*, "The dynamic distribution of fluorescent analogues of actin and myosin in protrusions at the leading edge of migrating swiss 3t3 fibroblasts," *The Journal of cell biology*, vol. 107, no. 6, p. 2631, 1988.
[298] W. Dai and T. Barbari, "Characterization of mesh size asymmetry in hydrogel membranes using confocal microscopy," *Journal of Membrane Science*, vol. 171, no. 1, pp. 45–58, 2000.
[299] L. Wu and C. S. Brazel, "Modifying the release of proxyphylline from pva hydrogels using surface crosslinking," *International journal of pharmaceutics*, vol. 349, no. 1, pp. 144–151, 2008.
[300] R. C. Gonzalez, R. E. Woods, and S. L. Eddins, *Digital image processing using MATLAB*, vol. 2. Gatesmark Publishing Knoxville, 2009.
[301] R. O. Duda and P. E. Hart, "Use of the hough transformation to detect lines and curves in pictures," *Communications of the ACM*, vol. 15, no. 1, pp. 11–15, 1972.
[302] D. H. Ballard, "Generalizing the hough transform to detect arbitrary shapes," *Pattern recognition*, vol. 13, no. 2, pp. 111–122, 1981.
[303] R. Rodrguez-Garcá, M. Mell, I. López-Montero, and F. Monroy, "Subdiffusive fluctuation dynamics of rigid membranes as resolved by ultrafast videomicroscopy," *EPL (Europhysics Letters)*, vol. 94, no. 2, p. 28009, 2011.
[304] P. Méléard, T. Pott, H. Bouvrais, and J. H. Ipsen, "Advantages of statistical analysis of giant vesicle flickering for bending elasticity measurements," *The European Physical Journal E*, vol. 34, no. 10, pp. 1–14, 2011.
[305] R. S. Gracià, N. Bezlyepkina, R. L. Knorr, R. Lipowsky, and R. Dimova, "Effect of cholesterol on the rigidity of saturated and unsaturated membranes: fluctuation and electrodeformation analysis of giant vesicles," *Soft Matter*, vol. 6, no. 7, pp. 1472–1482, 2010.
[306] Y.-Z. Yoon, H. Hong, A. Brown, D. C. Kim, D. J. Kang, V. L. Lew, and P. Cicuta, "Flickering analysis of erythrocyte mechanical properties: dependence on oxygenation level, cell shape, and hydration level," *Biophysical journal*, vol. 97, no. 6, pp. 1606–1615, 2009.

[307] J. A. Theriot and T. J. Mitchison, “Actin microfilament dynamics in locomoting cells,” *Nature*, vol. 352, no. 6331, pp. 126–131, 1991.
[308] A. Mallavarapu and T. Mitchison, “Regulated actin cytoskeleton assembly at filopodium tips controls their extension and retraction,” *The Journal of cell biology*, vol. 146, no. 5, pp. 1097–1106, 1999.
[309] Y.-L. Wang, “Exchange of actin subunits at the leading edge of living fibroblasts: possible role of treadmilling.,” *The Journal of cell biology*, vol. 101, no. 2, pp. 597–602, 1985.
[310] K. Keren, Z. Pincus, G. M. Allen, E. L. Barnhart, G. Marriott, A. Mogilner, and J. A. Theriot, “Mechanism of shape determination in motile cells,” *Nature*, vol. 453, no. 7194, pp. 475–480, 2008.
[311] C. Yang, M. Hoelzle, A. Disanza, G. Scita, and T. Svitkina, “Coordination of membrane and actin cytoskeleton dynamics during filopodia protrusion,” *PloS one*, vol. 4, no. 5, p. e5678, 2009.
[312] P. A. Janmey, C. C. Cunningham, G. F. Oster, and T. P. Stossel, “Cytoskeletal networks and osmotic pressure in relation to cell structure and motility,” *NATO ASI SERIES H CELL BIOLOGY*, pp. 333–333, 1992.
[313] M. Pinot, F. Chesnel, J. Z. Kubiak, I. Arnal, F. J. Nedelec, and Z. Gueroui, “Effects of confinement on the self-organization of microtubules and motors,” *Current Biology*, vol. 19, no. 11, pp. 954–960, 2009.
[314] D. K. Fygenson, M. Elbaum, B. Shraiman, and A. Libchaber, “Microtubules and vesicles under controlled tension,” *Physical Review E*, vol. 55, no. 1, p. 850, 1997.
[315] D. K. Fygenson, J. F. Marko, and A. Libchaber, “Mechanics of microtubule-based membrane extension,” *Physical review letters*, vol. 79, no. 22, pp. 4497–4500, 1997.
[316] M. Elbaum, D. Kuchnir Fygenson, and A. Libchaber, “Buckling microtubules in vesicles,” *Physical review letters*, vol. 76, no. 21, pp. 4078–4081, 1996.
[317] V. Emsellem, O. Cardoso, and P. Tabeling, “Vesicle deformation by microtubules: A phase diagram,” *Physical Review E*, vol. 58, pp. 4807–4810, 1998.
[318] T. Kaneko, T. J. Itoh, and H. Hotani, “Morphological transformation of liposomes caused by assembly of encapsulated tubulin and determination of shape by microtubule-associated proteins (maps),” *Journal of molecular biology*, vol. 284, no. 5, pp. 1671–1681, 1998.
[319] H. Hotani and H. Miyamoto, “Dynamic features of microtubules as visualized by dark-field microscopy,” *Advances in biophysics*, vol. 26, pp. 135–156, 1990.
[320] M. S. e Silva, J. Alvarado, J. Nguyen, N. Georgoulia, B. M. Mulder, and G. H. Koenderink, “Self-organized patterns of actin filaments in cell-sized confinement,” *Soft Matter*, vol. 7, no. 22, pp. 10631–10641, 2011.

[321] M. J. Footer, J. W. Kerssemakers, J. A. Theriot, and M. Dogterom, “Direct measurement of force generation by actin filament polymerization using an optical trap,” *Proceedings of the National Academy of Sciences*, vol. 104, no. 7, pp. 2181–2186, 2007.
[322] E. Atilgan, D. Wirtz, and S. X. Sun, “Mechanics and dynamics of actin-driven thin membrane protrusions,” *Biophysical journal*, vol. 90, no. 1, pp. 65–76, 2006.
[323] S. Pronk, P. L. Geissler, and D. A. Fletcher, “Limits of filopodium stability,” *Physical review letters*, vol. 100, no. 25, p. 258102, 2008.
[324] A. Mogilner and B. Rubinstein, “The physics of filopodial protrusion,” *Biophysical journal*, vol. 89, no. 2, pp. 782–795, 2005.
[325] M. P. Sheetz and J. Dai, “Modulation of membrane dynamics and cell motility by membrane tension,” *Trends in cell biology*, vol. 6, no. 3, pp. 85–89, 1996.
[326] E. L. Batchelder, G. Hollopeter, C. Campillo, X. Mezanges, E. M. Jorgensen, P. Nassoy, P. Sens, and J. Plastino, “Membrane tension regulates motility by controlling lamellipodium organization,” *Proceedings of the National Academy of Sciences*, vol. 108, no. 28, pp. 11429–11434, 2011.
[327] E. Abu Shah and K. Keren, “Mechanical forces and feedbacks in cell motility,” *Current opinion in cell biology*, 2013.
[328] Y. Hashimoto, D. J. Kim, and J. C. Adams, “The roles of fascins in health and disease,” *The Journal of pathology*, vol. 224, no. 3, pp. 289–300, 2011.
[329] D. Vignjevic, S.-i. Kojima, Y. Aratyn, O. Danciu, T. Svitkina, and G. G. Borisy, “Role of fascin in filopodial protrusion,” *The Journal of cell biology*, vol. 174, no. 6, pp. 863–875, 2006.
[330] O. Lieleg, J. Kayser, G. Brambilla, L. Cipelletti, and A. Bausch, “Slow dynamics and internal stress relaxation in bundled cytoskeletal networks,” *Nature materials*, vol. 10, no. 3, pp. 236–242, 2011.
[331] M. Claessens, C. Semmrich, L. Ramos, and A. Bausch, “Helical twist controls the thickness of f-actin bundles,” *Proceedings of the National Academy of Sciences*, vol. 105, no. 26, pp. 8819–8822, 2008.
[332] C. F. Schmidt, M. Baermann, G. Isenberg, and E. Sackmann, “Chain dynamics, mesh size, and diffusive transport in networks of polymerized actin: a quasielastic light scattering and microfluorescence study,” *Macromolecules*, vol. 22, no. 9, pp. 3638–3649, 1989.
[333] O. Lieleg, M. M. Claessens, C. Heussinger, E. Frey, and A. R. Bausch, “Mechanics of bundled semiflexible polymer networks,” *Physical review letters*, vol. 99, no. 8, p. 088102, 2007.
[334] S. Yamashiro-Matsumura and F. Matsumura, “Purification and characterization of an f-actin-bundling 55-kilodalton protein from hela cells.,” *Journal of Biological Chemistry*, vol. 260, no. 8, pp. 5087–5097, 1985.

[335] J. C. Adams, “Roles of fascin in cell adhesion and motility,” *Current opinion in cell biology*, vol. 16, no. 5, pp. 590–596, 2004.
[336] N. Kureishy, V. Sapountzi, S. Prag, N. Anilkumar, and J. C. Adams, “Fascins, and their roles in cell structure and function,” *Bioessays*, vol. 24, no. 4, pp. 350–361, 2002.
[337] R. Ishikawa, T. Sakamoto, T. Ando, S. Higashi-Fujime, and K. Kohama, “Polarized actin bundles formed by human fascin-1: their sliding and disassembly on myosin ii and myosin v in vitro,” *Journal of neurochemistry*, vol. 87, no. 3, pp. 676–685, 2003.
[338] M. Yang, K. Kpalma, J. Ronsin, *et al.*, “A survey of shape feature extraction techniques,” *Pattern recognition*, pp. 43–90, 2008.
[339] Y. Tseng, E. Fedorov, J. M. McCaffery, S. C. Almo, and D. Wirtz, “Micromechanics and ultrastructure of actin filament networks crosslinked by human fascin: a comparison with α-actinin,” *Journal of molecular biology*, vol. 310, no. 2, pp. 351–366, 2001.
[340] M. M. Claessens, M. Bathe, E. Frey, and A. R. Bausch, “Actin-binding proteins sensitively mediate f-actin bundle stiffness,” *Nature materials*, vol. 5, no. 9, pp. 748–753, 2006.
[341] L. Landau and E. Lifshitz, “Theory of elasticity, 3rd,” 1986.
[342] M. Claessens, F. Leermakers, F. Hoekstra, and M. Stuart, “Osmotic shrinkage and reswelling of giant vesicles composed of dioleoylphosphatidylglycerol and cholesterol,” *Biochimica et Biophysica Acta (BBA)-Biomembranes*, vol. 1778, no. 4, pp. 890–895, 2008.
[343] P. Peterlin and V. Arrigler, “Electroformation in a flow chamber with solution exchange as a means of preparation of flaccid giant vesicles,” *Colloids and Surfaces B: Biointerfaces*, vol. 64, no. 1, pp. 77–87, 2008.
[344] E. Karatekin, O. Sandre, H. Guitouni, N. Borghi, P.-H. Puech, and F. Brochard-Wyart, “Cascades of transient pores in giant vesicles: line tension and transport,” *Biophysical journal*, vol. 84, no. 3, pp. 1734–1749, 2003.
[345] S. Dieluweit, A. Csisza r, W. Rubner, J. Fleischhauer, S. Houben, and R. Merkel, “Mechanical properties of bare and protein-coated giant unilamellar phospholipid vesicles. a comparative study of micropipet aspiration and atomic force microscopy,” *Langmuir*, vol. 26, no. 13, pp. 11041–11049, 2010.
[346] V. Heinrich, B. Božic, S. Svetina, and B. Žekš, “Vesicle deformation by an axial load: from elongated shapes to tethered vesicles,” *Biophysical journal*, vol. 76, no. 4, pp. 2056–2071, 1999.
[347] R. E. Waugh and R. M. Hochmuth, “Mechanical equilibrium of thick, hollow, liquid membrane cylinders,” *Biophysical journal*, vol. 52, no. 3, pp. 391–400, 1987.

[348] F. Brochard-Wyart, N. Borghi, D. Cuvelier, and P. Nassoy, “Hydrodynamic narrowing of tubes extruded from cells,” *Proceedings of the National Academy of Sciences*, vol. 103, no. 20, pp. 7660–7663, 2006.
[349] E. Evans and A. Yeung, “Hidden dynamics in rapid changes of bilayer shape,” *Chemistry and Physics of Lipids*, vol. 73, no. 1, pp. 39–56, 1994.
[350] R. Hochmuth, H. Wiles, E. Evans, and J. McCown, “Extensional flow of erythrocyte membrane from cell body to elastic tether. ii. experiment,” *Biophysical journal*, vol. 39, no. 1, pp. 83–89, 1982.
[351] S. Khurana and S. P. George, “The role of actin bundling proteins in the assembly of filopodia in epithelial cells,” *Cell adhesion & migration*, vol. 5, no. 5, pp. 409–420, 2011.
[352] R. Nambiar, R. E. McConnell, and M. J. Tyska, “Myosin motor function: the ins and outs of actin-based membrane protrusions,” *Cellular and molecular life sciences*, vol. 67, no. 8, pp. 1239–1254, 2010.
[353] E. Evans, “Minimum energy analysis of membrane deformation applied to pipet aspiration and surface adhesion of red blood cells,” *Biophysical journal*, vol. 30, no. 2, pp. 265–284, 1980.
[354] F. Hochmuth, J.-Y. Shao, J. Dai, and M. P. Sheetz, “Deformation and flow of membrane into tethers extracted from neuronal growth cones,” *Biophysical journal*, vol. 70, no. 1, pp. 358–369, 1996.
[355] J. Dai and M. P. Sheetz, “Mechanical properties of neuronal growth cone membranes studied by tether formation with laser optical tweezers,” *Biophysical journal*, vol. 68, no. 3, pp. 988–996, 1995.
[356] G. Morrison and D. Thirumalai, “Semiflexible chains in confined spaces,” *Physical Review E*, vol. 79, no. 1, p. 011924, 2009.
[357] K. Ostermeir, K. Alim, and E. Frey, “Buckling of stiff polymer rings in weak spherical confinement,” *Physical Review E*, vol. 81, no. 6, p. 061802, 2010.
[358] K. Ostermeir, K. Alim, and E. Frey, “Confinement induces conformational transition of semiflexible polymer rings to figure eight form,” *Soft Matter*, vol. 6, no. 15, pp. 3467–3471, 2010.
[359] M. Fošnaric, A. Iglic, D. M. Kroll, and S. May, “Monte carlo simulations of a polymer confined within a fluid vesicle,” *Šoft Matter*, 2013.
[360] D. Marenduzzo and E. Orlandini, “Dynamics of fibers growing inside soft vesicles,” *EPL (Europhysics Letters)*, vol. 80, no. 4, p. 48004, 2007.
[361] C. S. Peskin, G. M. Odell, and G. F. Oster, “Cellular motions and thermal fluctuations: the brownian ratchet,” *Biophysical Journal*, vol. 65, no. 1, pp. 316–324, 1993.
[362] G. Oster and A. S. Perelson, “Cell protrusions,” in *Frontiers in Mathematical Biology*, pp. 53–78, Springer, 1994.

[363] P. Girard, J. Pécréaux, G. Lenoir, P. Falson, J.-L. Rigaud, and P. Bassereau, "A new method for the reconstitution of membrane proteins into giant unilamellar vesicles," *Biophysical journal*, vol. 87, no. 1, pp. 419–429, 2004.
[364] R. Furukawa, R. Kundra, and M. Fechheimer, "Formation of liquid crystals from actin filaments," *Biochemistry*, vol. 32, no. 46, pp. 12346–12352, 1993.
[365] T. R. Powers, G. Huber, and R. E. Goldstein, "Fluid-membrane tethers: minimal surfaces and elastic boundary layers," *Physical Review E*, vol. 65, no. 4, p. 041901, 2002.
[366] A. Roux, "The physics of membrane tubes: soft templates for studying cellular membranes.," *Soft Matter*, 2013.
[367] I. Derényi, F. Jülicher, and J. Prost, "Formation and interaction of membrane tubes," *Physical review letters*, vol. 88, no. 23, p. 238101, 2002.
[368] G. Koster, A. Cacciuto, I. Derényi, D. Frenkel, and M. Dogterom, "Force barriers for membrane tube formation," *Physical review letters*, vol. 94, no. 6, p. 068101, 2005.
[369] T. Inaba, A. Ishijima, M. Honda, F. Nomura, K. Takiguchi, and H. Hotani, "Formation and maintenance of tubular membrane projections require mechanical force, but their elongation and shortening do not require additional force," *Journal of molecular biology*, vol. 348, no. 2, pp. 325–333, 2005.
[370] B. Pontes, N. B. Viana, L. Campanati, M. Farina, V. M. Neto, and H. M. Nussenzveig, "Structure and elastic properties of tunneling nanotubes," *European Biophysics Journal*, vol. 37, no. 2, pp. 121–129, 2008.
[371] B. Pontes, N. Viana, L. Salgado, M. Farina, V. M. Neto, and H. Nussenzveig, "Cell cytoskeleton and tether extraction," *Biophysical journal*, vol. 101, no. 1, pp. 43–52, 2011.
[372] T. L. Hill, "Microfilament or microtubule assembly or disassembly against a force," *Proceedings of the National Academy of Sciences*, vol. 78, no. 9, pp. 5613–5617, 1981.
[373] T. D. Pollard, "Rate constants for the reactions of atp-and adp-actin with the ends of actin filaments.," *The Journal of cell biology*, vol. 103, no. 6, pp. 2747–2754, 1986.
[374] C. S. Heacock and J. R. Bamburg, "The quantitation of g-and f-actin in cultured cells," *Analytical biochemistry*, vol. 135, no. 1, pp. 22–36, 1983.
[375] G. M. Grason, "Frustration and packing in curved-filament assemblies: from isometric to isomorphic bundles," *Soft Matter*, 2013.
[376] G. M. Grason, "Topological defects in twisted bundles of two-dimensionally ordered filaments," *Physical review letters*, vol. 105, no. 4, p. 045502, 2010.
[377] O. Medalia, M. Beck, M. Ecke, I. Weber, R. Neujahr, W. Baumeister, and G. Gerisch, "Organization of actin networks in intact filopodia," *Current biology*, vol. 17, no. 1, pp. 79–84, 2007.

[378] D. R. Daniels and M. S. Turner, “Islands of conformational stability for filopodia,” *PloS one*, vol. 8, no. 3, p. e59010, 2013.
[379] A. Husainy, A. Morrow, T. Perkins, and J. Lee, “Robust patterns in the stochastic organization of filopodia,” *BMC cell biology*, vol. 11, no. 1, p. 86, 2010.
[380] W. Wood and P. Martin, “Structures in focus—filopodia,” *The international journal of biochemistry & cell biology*, vol. 34, no. 7, pp. 726–730, 2002.
[381] T. Gustafson and L. Wolpert, “Studies on the cellular basis of morphogenesis in the sea urchin embryo: directed movements of primary mesenchyme cells in normal and vegetalized larvae,” *Experimental cell research*, vol. 24, no. 1, pp. 64–79, 1961.
[382] Y. Lan and G. A. Papoian, “The stochastic dynamics of filopodial growth,” *Biophysical journal*, vol. 94, no. 10, pp. 3839–3852, 2008.
[383] T. Oberholzer and A. Fischer, “Microinjection of macromolecules in giant vesicles prepared by electroformation,” *Perspectives in Supramolecular Chemistry: Giant Vesicles, Volume 6*, pp. 285–295, 2000.
[384] R. Wick, M. I. Angelova, P. Walde, and P. L. Luisi, “Microinjection into giant vesicles and light microscopy investigation of enzyme-mediated vesicle transformations,” *Chemistry & biology*, vol. 3, no. 2, pp. 105–111, 1996.
[385] P. Bucher, A. Fischer, P. L. Luisi, T. Oberholzer, and P. Walde, “Giant vesicles as biochemical compartments: the use of microinjection techniques,” *Langmuir*, vol. 14, no. 10, pp. 2712–2721, 1998.
[386] P. I. Zhuravlev and G. A. Papoian, “Molecular noise of capping protein binding induces macroscopic instability in filopodial dynamics,” *Proceedings of the National Academy of Sciences*, vol. 106, no. 28, pp. 11570–11575, 2009.
[387] H. Tokuo and M. Ikebe, “Myosin x transports mena/vasp to the tip of filopodia,” *Biochemical and biophysical research communications*, vol. 319, no. 1, pp. 214–220, 2004.
[388] P. I. Zhuravlev, B. S. Der, and G. A. Papoian, “Design of active transport must be highly intricate: a possible role of myosin and ena/vasp for g-actin transport in filopodia,” *Biophysical journal*, vol. 98, no. 8, pp. 1439–1448, 2010.
[389] T. Umeda, H. Nakajima, and H. Hotani, “Theoretical analysis of shape transformations of liposomes caused by microtubule assembly,” *Journal of the Physics Society Japan*, vol. 67, no. 2, pp. 682–688, 1998.
[390] R. Morikawa, Y. Saito, and H. Hyuga, “Monte carlo study of a vesicle morphology caused by microtubule assembly,” *Journal of the Physical Society of Japan*, vol. 68, no. 5, pp. 1760–1768, 1999.
[391] B. Bozic, S. Svetina, and B. Zeks, “Theoretical analysis of the formation of membrane microtubes on axially strained vesicles,” *Physical Review E*, vol. 55, no. 5, p. 5834, 1997.

[392] A. Iglic, P. Veranic, U. Batista, and V. Kralj-Iglic, “Theoretical analysis of shape transformation of v-79 cells after treatment with cytochalasin b,” *Journal of Biomechanics*, vol. 34, no. 6, pp. 765–772, 2001.
[393] M. R. Kasschau, T. D. Ngo, L. M. Sperber, and K. L. Tran, “Formation of filopodia in earthworm (lumbricus terrestris) coelomocytes in response to osmotic stress,” *Zoology*, vol. 110, no. 1, pp. 66–76, 2007.
[394] A. Mogilner and G. Oster, “Cell motility driven by actin polymerization,” *Biophysical journal*, vol. 71, no. 6, pp. 3030–3045, 1996.
[395] D. Raucher and M. P. Sheetz, “Cell spreading and lamellipodial extension rate is regulated by membrane tension,” *The Journal of cell biology*, vol. 148, no. 1, pp. 127–136, 2000.
[396] J. G. White and J. J. Sauk, “Microtubule coils in spread blood platelets,” *Blood*, vol. 64, no. 2, pp. 470–478, 1984.
[397] S. Patel-Hett, J. L. Richardson, H. Schulze, K. Drabek, N. A. Isaac, K. Hoffmeister, R. A. Shivdasani, J. C. Bulinski, N. Galjart, J. H. Hartwig, *et al.*, “Visualization of microtubule growth in living platelets reveals a dynamic marginal band with multiple microtubules,” *Blood*, vol. 111, no. 9, pp. 4605–4616, 2008.
[398] I. Nemhauser, J. Joseph-Silverstein, and W. D. Cohen, “Centriole as microtubule-organizing centers for marginal bands of molluscan erythrocytes,” *The Journal of cell biology*, vol. 96, no. 4, pp. 979–989, 1983.
[399] O. Maniti, K. Carvalho, and C. Picart, “Model membranes to shed light on the biochemical and physical properties of ezrin/radixin/moesin,” *Biochimie*, 2012.
[400] R. M. Hochmuth, N. Mohandas, and P. Blackshear Jr, “Measurement of the elastic modulus for red cell membrane using a fluid mechanical technique,” *Biophysical journal*, vol. 13, no. 8, pp. 747–762, 1973.
[401] N. C. Gauthier, M. A. Fardin, P. Roca-Cusachs, and M. P. Sheetz, “Temporary increase in plasma membrane tension coordinates the activation of exocytosis and contraction during cell spreading,” *Proceedings of the National Academy of Sciences*, vol. 108, no. 35, pp. 14467–14472, 2011.
[402] C. Le Clainche and M.-F. Carlier, “Regulation of actin assembly associated with protrusion and adhesion in cell migration,” *Physiological reviews*, vol. 88, no. 2, pp. 489–513, 2008.
[403] D. Raucher, T. Stauffer, W. Chen, K. Shen, S. Guo, J. D. York, M. P. Sheetz, and T. Meyer, “Phosphatidylinositol 4, 5-bisphosphate functions as a second messenger that regulates cytoskeleton–plasma membrane adhesion,” *Cell*, vol. 100, no. 2, pp. 221–228, 2000.
[404] B. L. Goode and M. J. Eck, “Mechanism and function of formins in the control of actin assembly,” *Annu. Rev. Biochem.*, vol. 76, pp. 593–627, 2007.
[405] K. Rottner, B. Behrendt, J. V. Small, and J. Wehland, “Vasp dynamics during lamellipodia protrusion,” *Nature Cell Biology*, vol. 1, no. 5, pp. 321–322, 1999.

[406] M. Krause, E. W. Dent, J. E. Bear, J. J. Loureiro, and F. B. Gertler, "Ena/vasp proteins: regulators of the actin cytoskeleton and cell migration," *Annual review of cell and developmental biology*, vol. 19, no. 1, pp. 541–564, 2003.
[407] A. Schirenbeck, R. Arasada, T. Bretschneider, T. E. Stradal, M. Schleicher, and J. Faix, "The bundling activity of vasodilator-stimulated phosphoprotein is required for filopodium formation," *Proceedings of the National Academy of Sciences*, vol. 103, no. 20, pp. 7694–7699, 2006.
[408] A. B. Bohil, B. W. Robertson, and R. E. Cheney, "Myosin-x is a molecular motor that functions in filopodia formation," *Proceedings of the National Academy of Sciences*, vol. 103, no. 33, pp. 12411–12416, 2006.
[409] H. Tokuo, K. Mabuchi, and M. Ikebe, "The motor activity of myosin-x promotes actin fiber convergence at the cell periphery to initiate filopodia formation," *The Journal of cell biology*, vol. 179, no. 2, pp. 229–238, 2007.
[410] B. S. Gentry, S. van der Meulen, P. Noguera, B. Alonso-Latorre, J. Plastino, and G. H. Koenderink, "Multiple actin binding domains of ena/vasp proteins determine actin network stiffening," *European Biophysics Journal*, vol. 41, no. 11, pp. 979–990, 2012.
[411] S. Ishiwata, "Freezing of actin. reversible oxidation of a sulfhydryl group and structural change," *Journal of biochemistry*, vol. 80, no. 3, pp. 595–609, 1976.
[412] J. X. Tang, P. A. Janmey, T. P. Stossel, and T. Ito, "Thiol oxidation of actin produces dimers that enhance the elasticity of the f-actin network," *Biophysical journal*, vol. 76, no. 4, pp. 2208–2215, 1999.
[413] M. Carlier, D. Pantaloni, and E. D. Korn, "Polymerization of adp-actin and atp-actin under sonication and characteristics of the atp-actin equilibrium polymer.," *Journal of Biological Chemistry*, vol. 260, no. 11, pp. 6565–6571, 1985.
[414] P. Artimo, M. Jonnalagedda, K. Arnold, D. Baratin, G. Csardi, E. De Castro, S. Duvaud, V. Flegel, A. Fortier, E. Gasteiger, *et al.*, "Expasy: Sib bioinformatics resource portal," *Nucleic acids research*, vol. 40, no. W1, pp. W597–W603, 2012.
[415] C. E. Aitken, R. A. Marshall, and J. D. Puglisi, "An oxygen scavenging system for improvement of dye stability in single-molecule fluorescence experiments," *Biophysical journal*, vol. 94, no. 5, pp. 1826–1835, 2008.
[416] J. Schindelin, I. Arganda-Carreras, E. Frise, V. Kaynig, M. Longair, T. Pietzsch, S. Preibisch, C. Rueden, S. Saalfeld, B. Schmid, *et al.*, "Fiji: an open-source platform for biological-image analysis," *Nature methods*, vol. 9, no. 7, pp. 676–682, 2012.
[417] R. McGill, J. W. Tukey, and W. A. Larsen, "Variations of box plots," *The American Statistician*, vol. 32, no. 1, pp. 12–16, 1978.
[418] I. Mabuchi and M. Okuno, "The effect of myosin antibody on the division of starfish blastomeres," *The Journal of cell biology*, vol. 74, no. 1, pp. 251–263, 1977.
[419] H. Huxley, "Muscular contraction and cell motility," 1973.

[420] J. Howard, “Mechanics of motor proteins and the cytoskeleton,” 2001.
[421] P. Kunda, A. E. Pelling, T. Liu, and B. Baum, “Moesin controls cortical rigidity, cell rounding, and spindle morphogenesis during mitosis,” *Current Biology*, vol. 18, no. 2, pp. 91–101, 2008.
[422] O. M. Lancaster, M. Le Berre, A. Dimitracopoulos, D. Bonazzi, E. Zlotek-Zlotkiewicz, R. Picone, T. Duke, M. Piel, and B. Baum, “Mitotic rounding alters cell geometry to ensure efficient bipolar spindle formation,” *Developmental cell*, 2013.
[423] A. S. Maddox and K. Burridge, “Rhoa is required for cortical retraction and rigidity during mitotic cell rounding,” *The Journal of cell biology*, vol. 160, no. 2, pp. 255–265, 2003.
[424] D. Bray and J. White, “Cortical flow in animal cells,” *Science*, vol. 239, no. 4842, pp. 883–888, 1988.
[425] M. Kapustina, T. C. Elston, and K. Jacobson, “Compression and dilation of the membrane-cortex layer generates rapid changes in cell shape,” *The Journal of cell biology*, vol. 200, no. 1, pp. 95–108, 2013.
[426] A. Gautreau, P. Poullet, D. Louvard, and M. Arpin, “Ezrin, a plasma membrane–microfilament linker, signals cell survival through the phosphatidylinositol 3-kinase/akt pathway,” *Proceedings of the National Academy of Sciences*, vol. 96, no. 13, pp. 7300–7305, 1999.
[427] J. Rosenblatt, “Mitosis: moesin and the importance of being round,” *Current Biology*, vol. 18, no. 7, pp. R292–R293, 2008.
[428] M. Tsujioka, S. Yumura, K. Inouye, H. Patel, M. Ueda, and S. Yonemura, “Talin couples the actomyosin cortex to the plasma membrane during rear retraction and cytokinesis,” *Proceedings of the National Academy of Sciences*, vol. 109, no. 32, pp. 12992–12997, 2012.
[429] M. Rauzi, P.-F. Lenne, and T. Lecuit, “Planar polarized actomyosin contractile flows control epithelial junction remodelling,” *Nature*, vol. 468, no. 7327, pp. 1110–1114, 2010.
[430] M. Schuh and J. Ellenberg, “A new model for asymmetric spindle positioning in mouse oocytes,” *Current Biology*, vol. 18, no. 24, pp. 1986–1992, 2008.
[431] G. R. Plaza and T. Q. Uyeda, “Contraction speed of the actomyosin cytoskeleton in the absence of the cell membrane,” *Soft Matter*, 2013.
[432] C. M. Field, M. Wühr, G. A. Anderson, H. Y. Kueh, D. Strickland, and T. J. Mitchison, “Actin behavior in bulk cytoplasm is cell cycle regulated in early vertebrate embryos,” *Journal of Cell Science*, vol. 124, no. 12, pp. 2086–2095, 2011.
[433] M. Pinot, V. Steiner, B. Dehapiot, B.-K. Yoo, F. Chesnel, L. Blanchoin, C. Kervrann, and Z. Gueroui, “Confinement induces actin flow in a meiotic cytoplasm,” *Proceedings of the National Academy of Sciences*, vol. 109, no. 29, pp. 11705–11710, 2012.

[434] S. Köhler and A. R. Bausch, “Contraction mechanisms in composite active actin networks,” *PloS one*, vol. 7, no. 7, p. e39869, 2012.
[435] M. Lenz, T. Thoresen, M. L. Gardel, and A. R. Dinner, “Contractile units in disordered actomyosin bundles arise from f-actin buckling,” *Physical Review Letters*, vol. 108, no. 23, p. 238107, 2012.
[436] T. Thoresen, M. Lenz, and M. L. Gardel, “Reconstitution of contractile actomyosin bundles,” *Biophysical journal*, vol. 100, no. 11, pp. 2698–2705, 2011.
[437] R. Kane, “Interconversion of structural and contractile actin gels by insertion of myosin during assembly.,” *The Journal of cell biology*, vol. 97, no. 6, pp. 1745–1752, 1983.
[438] A. E. Carlsson, “Contractile stress generation by actomyosin gels,” *Physical Review E*, vol. 74, no. 5, p. 051912, 2006.
[439] S. Wang and P. G. Wolynes, “Active contractility in actomyosin networks,” *Proceedings of the National Academy of Sciences*, vol. 109, no. 17, pp. 6446–6451, 2012.
[440] N. L. Dasanayake, P. J. Michalski, and A. E. Carlsson, “General mechanism of actomyosin contractility,” *Physical review letters*, vol. 107, no. 11, p. 118101, 2011.
[441] K. Kruse, J. Joanny, F. Jülicher, J. Prost, and K. Sekimoto, “Asters, vortices, and rotating spirals in active gels of polar filaments,” *Physical review letters*, vol. 92, no. 7, p. 078101, 2004.
[442] F. C. MacKintosh and A. J. Levine, “Nonequilibrium mechanics and dynamics of motor-activated gels,” *Physical review letters*, vol. 100, no. 1, p. 018104, 2008.
[443] C. Revenu, R. Athman, S. Robine, and D. Louvard, “The co-workers of actin filaments: from cell structures to signals,” *Nature Reviews Molecular Cell Biology*, vol. 5, no. 8, pp. 635–646, 2004.
[444] A. J. Ridley, “Life at the leading edge,” *Cell*, vol. 145, no. 7, pp. 1012–1022, 2011.
[445] L. A. Flanagan, J. Chou, H. Falet, R. Neujahr, J. H. Hartwig, and T. P. Stossel, “Filamin a, the arp2/3 complex, and the morphology and function of cortical actin filaments in human melanoma cells,” *The Journal of cell biology*, vol. 155, no. 4, pp. 511–518, 2001.
[446] A. I. McClatchey and R. G. Fehon, “Merlin and the erm proteins–regulators of receptor distribution and signaling at the cell cortex,” *Trends in cell biology*, vol. 19, no. 5, pp. 198–206, 2009.
[447] M. P. Stewart, J. Helenius, Y. Toyoda, S. P. Ramanathan, D. J. Muller, and A. A. Hyman, “Hydrostatic pressure and the actomyosin cortex drive mitotic cell rounding,” *Nature*, vol. 469, no. 7329, pp. 226–230, 2011.

[448] N. W. Goehring, P. K. Trong, J. S. Bois, D. Chowdhury, E. M. Nicola, A. A. Hyman, and S. W. Grill, "Polarization of par proteins by advective triggering of a pattern-forming system," *Science*, vol. 334, no. 6059, pp. 1137–1141, 2011.
[449] M. Mayer, M. Depken, J. S. Bois, F. Jülicher, and S. W. Grill, "Anisotropies in cortical tension reveal the physical basis of polarizing cortical flows," *Nature*, vol. 467, no. 7315, pp. 617–621, 2010.
[450] A. B. Verkhovsky, T. M. Svitkina, G. G. Borisy, *et al.*, "Myosin ii filament assemblies in the active lamella of fibroblasts: their morphogenesis and role in the formation of actin filament bundles," *Journal of Cell Biology*, vol. 131, no. 4, pp. 989–1002, 1995.
[451] M. Vicente-Manzanares, X. Ma, R. S. Adelstein, and A. R. Horwitz, "Non-muscle myosin ii takes centre stage in cell adhesion and migration," *Nature reviews Molecular cell biology*, vol. 10, no. 11, pp. 778–790, 2009.
[452] M. Bárány, "Atpase activity of myosin correlated with speed of muscle shortening," *The Journal of General Physiology*, vol. 50, no. 6, pp. 197–218, 1967.
[453] P. Licht, "The temperature dependence of myosin-adenosinetriphosphatase and alkaline phosphatase in lizards," *Comparative Biochemistry and Physiology*, vol. 12, no. 3, pp. 331–340, 1964.
[454] D. H. Wachsstock, W. Schwartz, and T. D. Pollard, "Affinity of alpha-actinin for actin determines the structure and mechanical properties of actin filament gels," *Biophysical journal*, vol. 65, no. 1, pp. 205–214, 1993.
[455] D. S. Courson and R. S. Rock, "Actin cross-link assembly and disassembly mechanics for α-actinin and fascin," *Journal of Biological Chemistry*, vol. 285, no. 34, pp. 26350–26357, 2010.
[456] C. T. Skau, D. S. Courson, A. J. Bestul, J. D. Winkelman, R. S. Rock, V. Sirotkin, and D. R. Kovar, "Actin filament bundling by fimbrin is important for endocytosis, cytokinesis, and polarization in fission yeast," *Journal of Biological Chemistry*, vol. 286, no. 30, pp. 26964–26977, 2011.
[457] Y. Luan, O. Lieleg, B. Wagner, and A. R. Bausch, "Micro-and macrorheological properties of isotropically cross-linked actin networks," *Biophysical journal*, vol. 94, no. 2, pp. 688–693, 2008.
[458] K. R. Purdy, J. R. Bartles, and G. C. Wong, "Structural polymorphism of the actin-espin system: a prototypical system of filaments and linkers in stereocilia," *Physical review letters*, vol. 98, no. 5, p. 058105, 2007.
[459] A.-C. Reymann, R. Boujemaa-Paterski, J.-L. Martiel, C. Guérin, W. Cao, H. F. Chin, M. Enrique, M. Théry, and L. Blanchoin, "Actin network architecture can determine myosin motor activity," *Science*, vol. 336, no. 6086, pp. 1310–1314, 2012.
[460] L. Haviv, D. Gillo, F. Backouche, and A. Bernheim-Groswasser, "A cytoskeletal demolition worker: myosin ii acts as an actin depolymerization agent," *Journal of molecular biology*, vol. 375, no. 2, pp. 325–330, 2008.

[461] M. Mori, N. Monnier, N. Daigle, M. Bathe, J. Ellenberg, and P. Lénárt, "Intracellular transport by an anchored homogeneously contracting f-actin meshwork," *Current Biology*, vol. 21, no. 7, pp. 606–611, 2011.
[462] P. Lénárt, C. P. Bacher, N. Daigle, A. R. Hand, R. Eils, M. Terasaki, and J. Ellenberg, "A contractile nuclear actin network drives chromosome congression in oocytes," *Nature*, vol. 436, no. 7052, pp. 812–818, 2005.
[463] K. Yi, B. Rubinstein, J. R. Unruh, F. Guo, B. D. Slaughter, and R. Li, "Sequential actin-based pushing forces drive meiosis i chromosome migration and symmetry breaking in oocytes," *The Journal of cell biology*, vol. 200, no. 5, pp. 567–576, 2013.
[464] J. Azoury, K. W. Lee, V. Georget, P. Rassinier, B. Leader, and M.-H. Verlhac, "Spindle positioning in mouse oocytes relies on a dynamic meshwork of actin filaments," *Current Biology*, vol. 18, no. 19, pp. 1514–1519, 2008.
[465] K. Yi, J. R. Unruh, M. Deng, B. D. Slaughter, B. Rubinstein, and R. Li, "Dynamic maintenance of asymmetric meiotic spindle position through arp2/3-complex-driven cytoplasmic streaming in mouse oocytes," *Nature cell biology*, vol. 13, no. 10, pp. 1252–1258, 2011.
[466] E. K. Paluch and E. Raz, "The role and regulation of blebs in cell migration," *Current Opinion in Cell Biology*, 2013.
[467] G. Charras and E. Paluch, "Blebs lead the way: how to migrate without lamellipodia," *Nature Reviews Molecular Cell Biology*, vol. 9, no. 9, pp. 730–736, 2008.
[468] C. A. Wilson, M. A. Tsuchida, G. M. Allen, E. L. Barnhart, K. T. Applegate, P. T. Yam, L. Ji, K. Keren, G. Danuser, and J. A. Theriot, "Myosin ii contributes to cell-scale actin network treadmilling through network disassembly," *Nature*, vol. 465, no. 7296, pp. 373–377, 2010.
[469] N. A. Medeiros, D. T. Burnette, and P. Forscher, "Myosin ii functions in actin-bundle turnover in neuronal growth cones," *Nature Cell Biology*, vol. 8, no. 3, pp. 216–226, 2006.
[470] K. Shiroguchi, H. F. Chin, D. E. Hannemann, E. Muneyuki, M. Enrique, and K. Kinosita Jr, "Direct observation of the myosin va recovery stroke that contributes to unidirectional stepping along actin," *PLoS biology*, vol. 9, no. 4, p. e1001031, 2011.
[471] B. Stuhrmann, M. S. e Silva, M. Depken, F. C. MacKintosh, and G. H. Koenderink, "Nonequilibrium fluctuations of a remodeling in vitro cytoskeleton," *Physical Review E*, vol. 86, no. 2, p. 020901, 2012.
[472] N. Gal, D. Lechtman-Goldstein, and D. Weihs, "Particle tracking in living cells: a review of the mean square displacement method and beyond," *Rheologica Acta*, pp. 1–19, 2013.

[473] C. Vézy, G. Massiera, and A. Viallat, “Adhesion induced non-planar and asynchronous flow of a giant vesicle membrane in an external shear flow,” *Soft Matter*, vol. 3, no. 7, pp. 844–851, 2007.
[474] A. R. Honerkamp-Smith, F. G. Woodhouse, V. Kantsler, and R. E. Goldstein, “Membrane viscosity determined from shear-driven flow in giant vesicles,” *Physical review letters*, vol. 111, no. 3, p. 038103, 2013.
[475] A.-S. Smith and E. Sackmann, “Progress in mimetic studies of cell adhesion and the mechanosensing,” *ChemPhysChem*, vol. 10, no. 1, pp. 66–78, 2009.
[476] I. Kusters, N. Mukherjee, M. R. de Jong, S. Tans, A. Koçer, and A. J. Driessen, “Taming membranes: functional immobilization of biological membranes in hydrogels,” *PloS one*, vol. 6, no. 5, p. e20435, 2011.
[477] F. Pan, R. L. Malmberg, and M. Momany, “Analysis of septins across kingdoms reveals orthology and new motifs,” *BMC evolutionary biology*, vol. 7, no. 1, p. 103, 2007.
[478] L. Hartwell, “Genetic control of the cell division cycle in yeast: Iv. genes controlling bud emergence and cytokinesis,” *Experimental cell research*, vol. 69, no. 2, pp. 265–276, 1971.
[479] L. H. Hartwell, J. Culotti, J. R. Pringle, B. J. Reid, *et al.*, “Genetic control of the cell division cycle in yeast,” *Science*, vol. 183, no. 4120, pp. 46–51, 1974.
[480] J. Saarikangas and Y. Barral, “The emerging functions of septins in metazoans,” *EMBO reports*, vol. 12, no. 11, pp. 1118–1126, 2011.
[481] A. J. Tooley, J. Gilden, J. Jacobelli, P. Beemiller, W. S. Trimble, M. Kinoshita, and M. F. Krummel, “Amoeboid t lymphocytes require the septin cytoskeleton for cortical integrity and persistent motility,” *Nature cell biology*, vol. 11, no. 1, pp. 17–26, 2008.
[482] R. Silverman-Gavrila and L. Silverman-Gavrila, “Septins: new microtubule interacting partners,” *The Scientific World Journal*, vol. 8, pp. 611–620, 2008.
[483] J. R. Bowen, D. Hwang, X. Bai, D. Roy, and E. T. Spiliotis, “Septin gtpases spatially guide microtubule organization and plus end dynamics in polarizing epithelia,” *The Journal of cell biology*, vol. 194, no. 2, pp. 187–197, 2011.
[484] M. Kinoshita, C. M. Field, M. L. Coughlin, A. F. Straight, and T. J. Mitchison, “Self-and actin-templated assembly of mammalian septins,” *Developmental cell*, vol. 3, no. 6, pp. 791–802, 2002.
[485] M. Kinoshita, S. Kumar, A. Mizoguchi, C. Ide, A. Kinoshita, T. Haraguchi, Y. Hiraoka, and M. Noda, “Nedd5, a mammalian septin, is a novel cytoskeletal component interacting with actin-based structures.,” *Genes & development*, vol. 11, no. 12, pp. 1535–1547, 1997.
[486] E. Joo, M. C. Surka, and W. S. Trimble, “Mammalian sept2 is required for scaffolding nonmuscle myosin ii and its kinases,” *Developmental cell*, vol. 13, no. 5, pp. 677–690, 2007.

[487] M. C. Surka, C. W. Tsang, and W. S. Trimble, “The mammalian septin msf localizes with microtubules and is required for completion of cytokinesis,” *Molecular biology of the cell*, vol. 13, no. 10, pp. 3532–3545, 2002.
[488] S. Mostowy, M. Bonazzi, M. A. Hamon, T. N. Tham, A. Mallet, M. Lelek, E. Gouin, C. Demangel, R. Brosch, C. Zimmer, *et al.*, “Entrapment of intracytosolic bacteria by septin cage-like structures,” *Cell host & microbe*, vol. 8, no. 5, pp. 433–444, 2010.
[489] M. A. McMurray, A. Bertin, G. Garcia III, L. Lam, E. Nogales, and J. Thorner, “Septin filament formation is essential in budding yeast,” *Developmental cell*, vol. 20, no. 4, pp. 540–549, 2011.
[490] C. S. Weirich, J. P. Erzberger, and Y. Barral, “The septin family of gtpases: architecture and dynamics,” *Nature Reviews Molecular Cell Biology*, vol. 9, no. 6, pp. 478–489, 2008.
[491] A. M. Vrabioiu and T. J. Mitchison, “Structural insights into yeast septin organization from polarized fluorescence microscopy,” *Nature*, vol. 443, no. 7110, pp. 466–469, 2006.
[492] B. S. DeMay, X. Bai, L. Howard, P. Occhipinti, R. A. Meseroll, E. T. Spiliotis, R. Oldenbourg, and A. S. Gladfelter, “Septin filaments exhibit a dynamic, paired organization that is conserved from yeast to mammals,” *The Journal of cell biology*, vol. 193, no. 6, pp. 1065–1081, 2011.
[493] B. Byers and L. Goetsch, “A highly ordered ring of membrane-associated filaments in budding yeast.,” *The Journal of Cell Biology*, vol. 69, no. 3, pp. 717–721, 1976.
[494] A. A. Rodal, L. Kozubowski, B. L. Goode, D. G. Drubin, and J. H. Hartwig, “Actin and septin ultrastructures at the budding yeast cell cortex,” *Molecular biology of the cell*, vol. 16, no. 1, pp. 372–384, 2005.
[495] A. Bertin, M. A. McMurray, J. Pierson, L. Thai, K. L. McDonald, E. A. Zehr, G. Garcá, P. Peters, J. Thorner, and E. Nogales, “Three-dimensional ultrastructure of the septin filament network in saccharomyces cerevisiae,” *Molecular biology of the cell*, vol. 23, no. 3, pp. 423–432, 2012.
[496] D. R. Soll and L. H. Mitchell, “Filament ring formation in the dimorphic yeast candida albicans.,” *The Journal of cell biology*, vol. 96, no. 2, pp. 486–493, 1983.
[497] D. N. Woolfson and T. Alber, “Predicting oligomerization states of coiled coils,” *Protein Science*, vol. 4, no. 8, pp. 1596–1607, 1995.
[498] P. S. Kim, B. Berger, and E. Wolf, “Multicoil: A program for predicting two- and three-stranded coiled coils,” *Protein Science*, vol. 6, no. 6, pp. 1179–1189, 1997.
[499] M. Sirajuddin, M. Farkasovsky, F. Hauer, D. Kühlmann, I. G. Macara, M. Weyand, H. Stark, and A. Wittinghofer, “Structural insight into filament formation by mammalian septins,” *Nature*, vol. 449, no. 7160, pp. 311–315, 2007.

[500] A. Bertin, M. A. McMurray, P. Grob, S.-S. Park, G. Garcia, I. Patanwala, H.-l. Ng, T. Alber, J. Thorner, and E. Nogales, "Saccharomyces cerevisiae septins: supramolecular organization of heterooligomers and the mechanism of filament assembly," *Proceedings of the National Academy of Sciences*, vol. 105, no. 24, pp. 8274–8279, 2008.
[501] C. M. John, R. K. Hite, C. S. Weirich, D. J. Fitzgerald, H. Jawhari, M. Faty, D. Schläpfer, R. Kroschewski, F. K. Winkler, T. Walz, *et al.*, "The caenorhabditis elegans septin complex is nonpolar," *The EMBO journal*, vol. 26, no. 14, pp. 3296–3307, 2007.
[502] M. E. Sellin, L. Sandblad, S. Stenmark, and M. Gullberg, "Deciphering the rules governing assembly order of mammalian septin complexes," *Molecular biology of the cell*, vol. 22, no. 17, pp. 3152–3164, 2011.
[503] N. Lukoyanova, S. A. Baldwin, and J. Trinick, "3d reconstruction of mammalian septin filaments," *Journal of molecular biology*, vol. 376, no. 1, pp. 1–7, 2008.
[504] M. Sirajuddin, M. Farkasovsky, E. Zent, and A. Wittinghofer, "Gtp-induced conformational changes in septins and implications for function," *Proceedings of the National Academy of Sciences*, vol. 106, no. 39, pp. 16592–16597, 2009.
[505] M. Versele, B. Gullbrand, M. J. Shulewitz, V. J. Cid, S. Bahmanyar, R. E. Chen, P. Barth, T. Alber, and J. Thorner, "Protein–protein interactions governing septin heteropentamer assembly and septin filament organization in saccharomyces cerevisiae," *Molecular biology of the cell*, vol. 15, no. 10, pp. 4568–4583, 2004.
[506] M. S. Kim, C. D. Froese, H. Xie, and W. S. Trimble, "Uncovering principles that control septin-septin interactions," *Journal of Biological Chemistry*, vol. 287, no. 36, pp. 30406–30413, 2012.
[507] L. Dolat, Q. Hu, and E. T. Spiliotis, "Septin functions in organ system physiology and pathology," *Biological chemistry*, vol. in press, 2013.
[508] G. Garcia, A. Bertin, Z. Li, Y. Song, M. A. McMurray, J. Thorner, and E. Nogales, "Subunit-dependent modulation of septin assembly: budding yeast septin shs1 promotes ring and gauze formation," *The Journal of cell biology*, vol. 195, no. 6, pp. 993–1004, 2011.
[509] C. M. Field, O. Al-Awar, J. Rosenblatt, M. L. Wong, B. Alberts, and T. J. Mitchison, "A purified drosophila septin complex forms filaments and exhibits gtpase activity.," *The Journal of cell biology*, vol. 133, no. 3, pp. 605–616, 1996.
[510] J. A. Frazier, M. L. Wong, M. S. Longtine, J. R. Pringle, M. Mann, T. J. Mitchison, and C. Field, "Polymerization of purified yeast septins: evidence that organized filament arrays may not be required for septin function," *The Journal of cell biology*, vol. 143, no. 3, pp. 737–749, 1998.

[511] M. Versele and J. Thorner, “Septin collar formation in budding yeast requires gtp binding and direct phosphorylation by the pak, cla4,” *The Journal of cell biology*, vol. 164, no. 5, pp. 701–715, 2004.
[512] M. Farkasovsky, P. Herter, B. Voß, and A. Wittinghofer, “Nucleotide binding and filament assembly of recombinant yeast septin complexes,” *Biological chemistry*, vol. 386, no. 7, pp. 643–656, 2005.
[513] P. J. Sheffield, C. J. Oliver, B. E. Kremer, S. Sheng, Z. Shao, and I. G. Macara, “Borg/septin interactions and the assembly of mammalian septin heterodimers, trimers, and filaments,” *Journal of Biological Chemistry*, vol. 278, no. 5, pp. 3483–3488, 2003.
[514] M. Stewart, H. M. Kent, and A. J. McCoy, “The structure of the q69l mutant of gdp-ran shows a major conformational change in the switch ii loop that accounts for its failure to bind nuclear transport factor 2 (ntf2),” *Journal of molecular biology*, vol. 284, no. 5, pp. 1517–1527, 1998.
[515] S.-C. Hsu, C. D. Hazuka, R. Roth, D. L. Foletti, J. Heuser, and R. H. Scheller, “Subunit composition, protein interactions, and structures of the mammalian brain sec6/8 complex and septin filaments,” *Neuron*, vol. 20, no. 6, pp. 1111–1122, 1998.
[516] M. Kinoshita *et al.*, “The septins,” *Genome biology*, vol. 4, no. 11, pp. 236–236, 2003.
[517] A. Bertin, M. A. McMurray, L. Thai, G. Garcia III, V. Votin, P. Grob, T. Allyn, J. Thorner, and E. Nogales, “Phosphatidylinositol-4, 5- bis phosphate promotes budding yeast septin filament assembly and organization,” *Journal of molecular biology*, vol. 404, no. 4, pp. 711–731, 2010.
[518] J. Koretz, L. Coluccio, and A. Bertasso, “The aggregation characteristics of column-purified rabbit skeletal myosin in the presence and absence of c-protein at ph 7.0,” *Biophysical journal*, vol. 37, no. 2, pp. 433–440, 1982.
[519] H. Herrmann, M. Häner, M. Brettel, S. A. Müller, K. N. Goldie, B. Fedtke, A. Lustig, W. W. Franke, and U. Aebi, “Structure and assembly properties of the intermediate filament protein vimentin: the role of its head, rod and tail domains,” *Journal of molecular biology*, vol. 264, no. 5, pp. 933–953, 1996.
[520] H. Kang, M. J. Bradley, B. R. McCullough, A. Pierre, E. E. Grintsevich, E. Reisler, and M. Enrique, “Identification of cation-binding sites on actin that drive polymerization and modulate bending stiffness,” *Proceedings of the National Academy of Sciences*, vol. 109, no. 42, pp. 16923–16927, 2012.
[521] X. Arias-Moreno, O. Abian, S. Vega, J. Sancho, and A. Velazquez-Campoy, “Protein-cation interactions: Structural and thermodynamic aspects,” *Current Protein and Peptide Science*, vol. 12, no. 4, pp. 325–338, 2011.
[522] S. R. Sprang and D. E. Coleman, “Invasion of the nucleotide snatchers: structural insights into the mechanism of g protein gefs,” *Cell*, vol. 95, no. 2, pp. 155–158, 1998.

[523] N. de Val, M. A. McMurray, L. H. Lam, C. C.-S. Hsiung, A. Bertin, E. Nogales, and J. Thorner, "Native cysteine residues are dispensable for the structure and function of all five yeast mitotic septins," *Proteins: Structure, Function, and Bioinformatics*, 2013.
[524] A. M. Vrabioiu, S. A. Gerber, S. P. Gygi, C. M. Field, and T. J. Mitchison, "The majority of the saccharomyces cerevisiae septin complexes do not exchange guanine nucleotides," *Journal of Biological Chemistry*, vol. 279, no. 4, pp. 3111–3118, 2004.
[525] Y. Oh and E. Bi, "Septin structure and function in yeast and beyond," *Trends in cell biology*, vol. 21, no. 3, pp. 141–148, 2011.
[526] M. P. Estey, M. S. Kim, and W. S. Trimble, "Septins," *Current Biology*, vol. 21, no. 10, pp. R384–R387, 2011.
[527] L. Romberg, M. Simon, and H. P. Erickson, "Polymerization of ftsz, a bacterial homolog of tubulin is assembly cooperative?," *Journal of Biological Chemistry*, vol. 276, no. 15, pp. 11743–11753, 2001.
[528] M.-F. Carlier, "Guanosine-5 -triphosphate hydrolysis and tubulin polymerization," *Molecular and cellular biochemistry*, vol. 47, no. 2, pp. 97–113, 1982.
[529] H. Schüler, R. Karlsson, C. E. Schutt, and U. Lindberg, "The connection between actin atpase and polymerization," *Advances in Molecular and Cell Biology*, vol. 37, pp. 49–66, 2006.
[530] D. Gordon, Y. Yang, and E. Korn, "Polymerization of acanthamoeba actin. kinetics, thermodynamics, and co-polymerization with muscle actin.," *Journal of Biological Chemistry*, vol. 251, no. 23, pp. 7474–7479, 1976.
[531] P. Janmey, J. Tang, and C. Schmidt, "Actin filaments. biophys. textb. online (btol)." Biophysics Textbook online, 1999.
[532] M. Mendoza, A. A. Hyman, and M. Glotzer, "Gtp binding induces filament assembly of a recombinant septin," *Current biology*, vol. 12, no. 21, pp. 1858–1863, 2002.
[533] T. Kouyama and K. Mihashi, "Fluorimetry study of n-(1-pyrenyl) iodoacetamide-labelled f-actin," *European Journal of Biochemistry*, vol. 114, no. 1, pp. 33–38, 1981.
[534] J. A. Cooper, S. B. Walker, and T. D. Pollard, "Pyrene actin: documentation of the validity of a sensitive assay for actin polymerization," *Journal of Muscle Research & Cell Motility*, vol. 4, no. 2, pp. 253–262, 1983.
[535] T. J. Mitchison and C. M. Field, "Cytoskeleton: what does gtp do for septins?," *Current biology*, vol. 12, no. 22, pp. R788–R790, 2002.
[536] G. Tian, A. Bhamidipati, N. J. Cowan, and S. A. Lewis, "Tubulin folding cofactors as gtpase-activating proteins gtp hydrolysis and the assembly of the α/β-tubulin heterodimer," *Journal of Biological Chemistry*, vol. 274, no. 34, pp. 24054–24058, 1999.

[537] J. Dobbelaere, M. S. Gentry, R. L. Hallberg, and Y. Barral, "Phosphorylation-dependent regulation of septin dynamics during the cell cycle," *Developmental cell*, vol. 4, no. 3, pp. 345–357, 2003.
[538] Y. Barral, M. Parra, S. Bidlingmaier, and M. Snyder, "Nim1-related kinases coordinate cell cycle progression with the organization of the peripheral cytoskeleton in yeast," *Genes & Development*, vol. 13, no. 2, pp. 176–187, 1999.
[539] D. Fiedler, H. Braberg, M. Mehta, G. Chechik, G. Cagney, P. Mukherjee, A. C. Silva, M. Shales, S. R. Collins, S. van Wageningen, *et al.*, "Functional organization of the s. cerevisiae phosphorylation network," *Cell*, vol. 136, no. 5, pp. 952–963, 2009.
[540] C. Tang and S. Reed, "Phosphorylation of the septin cdc3 in g1 by the cdc28 kinase is essential for efficient septin ring disassembly.," *Cell cycle (Georgetown, Tex.)*, vol. 1, no. 1, pp. 42–49, 2002.
[541] E. M. Mortensen, H. McDonald, J. Yates, and D. R. Kellogg, "Cell cycle-dependent assembly of a gin4-septin complex," *Molecular biology of the cell*, vol. 13, no. 6, pp. 2091–2105, 2002.
[542] E. S. Johnson and G. Blobel, "Cell cycle–regulated attachment of the ubiquitin-related protein sumo to the yeast septins," *The Journal of cell biology*, vol. 147, no. 5, pp. 981–994, 1999.
[543] E. S. Johnson and A. A. Gupta, "An e3-like factor that promotes sumo conjugation to the yeast septins," *Cell*, vol. 106, no. 6, pp. 735–744, 2001.
[544] Y. Zhang, J. Gao, K. K. Chung, H. Huang, V. L. Dawson, and T. M. Dawson, "Parkin functions as an e2-dependent ubiquitin–protein ligase and promotes the degradation of the synaptic vesicle-associated protein, cdcrel-1," *Proceedings of the National Academy of Sciences*, vol. 97, no. 24, pp. 13354–13359, 2000.
[545] Y. Hernández-Rodrguez and M. Momany, "Posttranslational modifications and assembly of septin heteropolymers and higher-order structures," *Current opinion in microbiology*, 2012.
[546] K. Oegema, M. S. Savoian, T. J. Mitchison, and C. M. Field, "Functional analysis of a human homologue of the drosophila actin binding protein anillin suggests a role in cytokinesis," *The Journal of cell biology*, vol. 150, no. 3, pp. 539–552, 2000.
[547] M. E. Sellin, P. Holmfeldt, S. Stenmark, and M. Gullberg, "Microtubules support a disk-like septin arrangement at the plasma membrane of mammalian cells," *Molecular biology of the cell*, vol. 22, no. 23, pp. 4588–4601, 2011.
[548] Y. Tanaka-Takiguchi, M. Kinoshita, and K. Takiguchi, "Septin-mediated uniform bracing of phospholipid membranes," *Current Biology*, vol. 19, no. 2, pp. 140–145, 2009.
[549] J. Goverman, L. A. Schick, and J. Newman, "The bundling of actin with polyethylene glycol 8000 in the presence and absence of gelsolin," *Biophysical journal*, vol. 71, no. 3, pp. 1485–1492, 1996.

[550] T. R. Shaikh, H. Gao, W. T. Baxter, F. J. Asturias, N. Boisset, A. Leith, and J. Frank, "Spider image processing for single-particle reconstruction of biological macromolecules from electron micrographs," *Nature protocols*, vol. 3, no. 12, pp. 1941–1974, 2008.
[551] B. Alberts, A. Johnson, J. Lewis, M. Raff, K. Roberts, and P. Walter, "Molecular biology of the cell. new york: Garland science; 2008," *Classic textbook now in its 5th Edition*, 2010.
[552] Y. A. Puius, N. M. Mahoney, and S. C. Almo, "The modular structure of actin-regulatory proteins," *Current opinion in cell biology*, vol. 10, no. 1, pp. 23–34, 1998.
[553] N. Volkmann, D. DeRosier, P. Matsudaira, and D. Hanein, "An atomic model of actin filaments cross-linked by fimbrin and its implications for bundle assembly and function," *The Journal of cell biology*, vol. 153, no. 5, pp. 947–956, 2001.
[554] O. Pelletier, E. Pokidysheva, L. S. Hirst, N. Bouxsein, Y. Li, and C. R. Safinya, "Structure of actin cross-linked with α-actinin: a network of bundles," *Physical review letters*, vol. 91, no. 14, p. 148102, 2003.
[555] B. Wagner, R. Tharmann, I. Haase, M. Fischer, and A. Bausch, "Cytoskeletal polymer networks: the molecular structure of cross-linkers determines macroscopic properties," *Proceedings of the National Academy of Sciences*, vol. 103, no. 38, pp. 13974–13978, 2006.
[556] W. H. Goldmann, M. Tempel, I. Sprenger, G. Isenberg, and R. M. Ezzell, "Viscoelasticity of actin-gelsolin networks in the presence of filamin," *European Journal of Biochemistry*, vol. 246, no. 2, pp. 373–379, 1997.
[557] J. Shin, M. Gardel, L. Mahadevan, P. Matsudaira, and D. Weitz, "Relating microstructure to rheology of a bundled and cross-linked f-actin network in vitro," *Proceedings of the National Academy of Sciences of the United States of America*, vol. 101, no. 26, pp. 9636–9641, 2004.
[558] O. Lieleg, K. M. Schmoller, C. J. Cyron, Y. Luan, W. A. Wall, and A. R. Bausch, "Structural polymorphism in heterogeneous cytoskeletal networks," *Soft Matter*, vol. 5, no. 9, pp. 1796–1803, 2009.
[559] M. Tempel, G. Isenberg, and E. Sackmann, "Temperature-induced sol-gel transition and microgel formation in α-actinin cross-linked actin networks: a rheological study," *Physical Review E*, vol. 54, no. 2, p. 1802, 1996.
[560] T. T. Falzone, M. Lenz, D. R. Kovar, and M. L. Gardel, "Assembly kinetics determine the architecture of α-actinin crosslinked f-actin networks," *Nature communications*, vol. 3, p. 861, 2012.
[561] C. Cyron, K. Müller, K. Schmoller, A. Bausch, W. Wall, and R. Bruinsma, "Equilibrium phase diagram of semi-flexible polymer networks with linkers," *EPL (Europhysics Letters)*, vol. 102, no. 3, p. 38003, 2013.

[562] R. Chelakkot, R. Lipowsky, and T. Gruhn, “Self-assembling network and bundle structures in systems of rods and crosslinkers–a monte carlo study,” *Soft Matter*, vol. 5, no. 7, pp. 1504–1513, 2009.
[563] L. T. Nguyen, W. Yang, Q. Wang, and L. S. Hirst, “Molecular dynamics simulation of f-actin reveals the role of cross-linkers in semi-flexible filament assembly,” *Soft Matter*, vol. 5, no. 10, pp. 2033–2036, 2009.
[564] I. Borukhov, R. F. Bruinsma, W. M. Gelbart, and A. J. Liu, “Structural polymorphism of the cytoskeleton: A model of linker-assisted filament aggregation,” *Proceedings of the National Academy of Sciences of the United States of America*, vol. 102, no. 10, pp. 3673–3678, 2005.
[565] K. M. Schmoller, O. Lieleg, and A. R. Bausch, “Internal stress in kinetically trapped actin bundle networks,” *Soft Matter*, vol. 4, no. 12, pp. 2365–2367, 2008.
[566] M. Glotzer, “The molecular requirements for cytokinesis,” *Science*, vol. 307, no. 5716, pp. 1735–1739, 2005.
[567] E. Schejter and E. Wieschaus, “Functional elements of the cytoskeleton in the early drosophila embryo,” *Annual review of cell biology*, vol. 9, no. 1, pp. 67–99, 1993.
[568] N. Tolliday, L. VerPlank, and R. Li, “Rho1 directs formin-mediated actin ring assembly during budding yeast cytokinesis,” *Current biology*, vol. 12, no. 21, pp. 1864–1870, 2002.
[569] T. M. Huckaba and L. A. Pon, “Cytokinesis: rho and formins are the ringleaders,” *Current biology*, vol. 12, no. 23, pp. R813–R814, 2002.
[570] B. Lacroix and A. S. Maddox, “Cytokinesis, ploidy and aneuploidy,” *The Journal of pathology*, vol. 226, no. 2, pp. 338–351, 2012.
[571] N. Founounou, N. Loyer, and R. Le Borgne, “Septins regulate the contractility of the actomyosin ring to enable adherens junction remodeling during cytokinesis of epithelial cells,” *Developmental cell*, vol. 24, no. 3, pp. 242–255, 2013.
[572] A. S. Maddox, L. Lewellyn, A. Desai, and K. Oegema, “Anillin and the septins promote asymmetric ingression of the cytokinetic furrow,” *Developmental cell*, vol. 12, no. 5, pp. 827–835, 2007.
[573] M. P. Estey, C. Di Ciano-Oliveira, C. D. Froese, M. T. Bejide, and W. S. Trimble, “Distinct roles of septins in cytokinesis: Sept9 mediates midbody abscission,” *The Journal of cell biology*, vol. 191, no. 4, pp. 741–749, 2010.
[574] T. P. Neufeld and G. M. Rubin, “The drosophila peanut gene is required for cytokinesis and encodes a protein similar to yeast putative bud neck filament proteins,” *Cell*, vol. 77, no. 3, pp. 371–379, 1994.
[575] J. Zhang, C. Kong, H. Xie, P. S. McPherson, S. Grinstein, and W. S. Trimble, “Phosphatidylinositol polyphosphate binding to the mammalian septin h5 is modulated by gtp,” *Current Biology*, vol. 9, no. 24, pp. 1458–1467, 1999.

[576] B. E. Kremer, L. A. Adang, and I. G. Macara, “Septins regulate actin organization and cell-cycle arrest through nuclear accumulation of nck mediated by socs7,” *Cell*, vol. 130, no. 5, pp. 837–850, 2007.
[577] S. Mostowy, S. Janel, C. Forestier, C. Roduit, S. Kasas, J. Pizarro-Cerdá, P. Cossart, and F. Lafont, “A role for septins in the interaction between the listeria monocytogenes invasion protein inlb and the met receptor,” *Biophysical journal*, vol. 100, no. 8, pp. 1949–1959, 2011.
[578] T. D. Pollard, “A guide to simple and informative binding assays,” *Molecular biology of the cell*, vol. 21, no. 23, pp. 4061–4067, 2010.
[579] S.-W. Chou, P. Hwang, G. Gomez, C. A. Fernando, M. C. West, L. M. Pollock, J. Lin-Jones, B. Burnside, and B. M. McDermott Jr, “Fascin 2b is a component of stereocilia that lengthens actin-based protrusions,” *PloS one*, vol. 6, no. 4, p. e14807, 2011.
[580] Y. Yamakita, S. Ono, F. Matsumura, and S. Yamashiro, “Phosphorylation of human fascin inhibits its actin binding and bundling activities,” *Journal of Biological Chemistry*, vol. 271, no. 21, pp. 12632–12638, 1996.
[581] S. Ono, Y. Yamakita, S. Yamashiro, P. T. Matsudaira, J. R. Gnarra, T. Obinata, and F. Matsumura, “Identification of an actin binding region and a protein kinase c phosphorylation site on human fascin,” *Journal of Biological Chemistry*, vol. 272, no. 4, pp. 2527–2533, 1997.
[582] W. Goldmann and G. Isenberg, “Analysis of filamin and α-actinin binding to actin by the stopped flow method,” *FEBS letters*, vol. 336, no. 3, pp. 408–410, 1993.
[583] J. Faix, M. Steinmetz, H. Boves, R. A. Kammerer, F. Lottspeich, U. Mintert, J. Murphy, A. Stock, U. Aebi, and G. Gerisch, “Cortexillins, major determinants of cell shape and size, are actin-bundling proteins with a parallel coiled-coil tail,” *Cell*, vol. 86, no. 4, pp. 631–642, 1996.
[584] R. K. Meyer and U. Aebi, “Bundling of actin filaments by alpha-actinin depends on its molecular length.,” *The Journal of cell biology*, vol. 110, no. 6, pp. 2013–2024, 1990.
[585] S. Jansen, A. Collins, C. Yang, G. Rebowski, T. Svitkina, and R. Dominguez, “Mechanism of actin filament bundling by fascin,” *Journal of Biological Chemistry*, vol. 286, no. 34, pp. 30087–30096, 2011.
[586] S. Rosenberg, A. Stracher, and K. Burridge, “Isolation and characterization of a calcium-sensitive alpha-actinin-like protein from human platelet cytoskeletons.,” *Journal of Biological Chemistry*, vol. 256, no. 24, pp. 12986–12991, 1981.
[587] K. J. Amann, B. A. Renley, and J. M. Ervasti, “A cluster of basic repeats in the dystrophin rod domain binds f-actin through an electrostatic interaction,” *Journal of Biological Chemistry*, vol. 273, no. 43, pp. 28419–28423, 1998.

[588] J. X. Tang, P. T. Szymanski, P. A. Janmey, and T. Tao, “Electrostatic effects of smooth muscle calponin on actin assembly,” *European Journal of Biochemistry*, vol. 247, no. 1, pp. 432–440, 1997.
[589] M. Lorenz, K. J. Poole, D. Popp, G. Rosenbaum, and K. C. Holmes, “An atomic model of the unregulated thin filament obtained by x-ray fiber diffraction on oriented actin-tropomyosin gels,” *Journal of molecular biology*, vol. 246, no. 1, pp. 108–119, 1995.
[590] I. N. Rybakova, M. L. Greaser, and R. L. Moss, “Myosin binding protein c interaction with actin characterization and mapping of the binding site,” *Journal of Biological Chemistry*, vol. 286, no. 3, pp. 2008–2016, 2011.
[591] K. Schmoller, O. Lieleg, and A. Bausch, “Structural and viscoelastic properties of actin/filamin networks: cross-linked versus bundled networks,” *Biophysical journal*, vol. 97, no. 1, pp. 83–89, 2009.
[592] D. Breitsprecher, S. A. Koestler, I. Chizhov, M. Nemethova, J. Mueller, B. L. Goode, J. V. Small, K. Rottner, and J. Faix, “Cofilin cooperates with fascin to disassemble filopodial actin filaments,” *Journal of cell science*, vol. 124, no. 19, pp. 3305–3318, 2011.
[593] A. Cebers, Z. Dogic, and P. Janmey, “Counterion-mediated attraction and kinks on loops of semiflexible polyelectrolyte bundles,” *Physical review letters*, vol. 96, no. 24, p. 247801, 2006.
[594] J. X. Tang, J. A. KaÈs, J. V. Shah, and P. A. Janmey, “Counterion-induced actin ring formation,” *European Biophysics Journal*, vol. 30, no. 7, pp. 477–484, 2001.
[595] H. Kaur, S. Kumar, K. Singh, and L. M. Bharadwaj, “Divalent cation induced actin ring formation,” *International journal of biological macromolecules*, vol. 48, no. 5, pp. 793–797, 2011.
[596] A. Lau, A. Prasad, and Z. Dogic, “Condensation of isolated semi-flexible filaments driven by depletion interactions,” *EPL (Europhysics Letters)*, vol. 87, no. 4, p. 48006, 2009.
[597] T. Sanchez, I. Kulic, and Z. Dogic, “Circularization, photomechanical switching, and a supercoiling transition of actin filaments,” *Physical review letters*, vol. 104, no. 9, p. 098103, 2010.
[598] K. A. Taylor, D. W. Taylor, and F. Schachat, “Isoforms of α-actinin from cardiac, smooth, and skeletal muscle form polar arrays of actin filaments,” *The Journal of cell biology*, vol. 149, no. 3, pp. 635–646, 2000.
[599] J. Alvarado, *Biological polymers: confined, bent and driven*. VU University Amsterdam, 2013.
[600] K. Schmoller, O. Lieleg, and A. Bausch, “Cross-linking molecules modify composite actin networks independently,” *Physical review letters*, vol. 101, no. 11, p. 118102, 2008.

[601] J. K. Gilden, S. Peck, Y.-C. M. Chen, and M. F. Krummel, “The septin cytoskeleton facilitates membrane retraction during motility and blebbing,” *The Journal of cell biology*, vol. 196, no. 1, pp. 103–114, 2012.
[602] R. Dominguez, “Actin-binding proteins–a unifying hypothesis,” *Trends in biochemical sciences*, vol. 29, no. 11, pp. 572–578, 2004.
[603] H. Fares, M. Peifer, and J. R. Pringle, “Localization and possible functions of drosophila septins.,” *Molecular biology of the cell*, vol. 6, no. 12, p. 1843, 1995.
[604] N. Tolliday, N. Bouquin, and R. Li, “Assembly and regulation of the cytokinetic apparatus in budding yeast,” *Current opinion in microbiology*, vol. 4, no. 6, pp. 690–695, 2001.
[605] J. Lippincott, K. B. Shannon, W. Shou, R. J. Deshaies, and R. Li, “The tem1 small gtpase controls actomyosin and septin dynamics during cytokinesis,” *Journal of Cell Science*, vol. 114, no. 7, pp. 1379–1386, 2001.
[606] C. Guillot and T. Lecuit, “Adhesion disengagement uncouples intrinsic and extrinsic forces to drive cytokinesis in epithelial tissues,” *Developmental cell*, vol. 24, no. 3, pp. 227–241, 2013.
[607] L. P. Cramer, M. Siebert, and T. J. Mitchison, “Identification of novel graded polarity actin filament bundles in locomoting heart fibroblasts: implications for the generation of motile force,” *The Journal of cell biology*, vol. 136, no. 6, pp. 1287–1305, 1997.
[608] S. Köhler, V. Schaller, and A. R. Bausch, “Structure formation in active networks,” *Nature materials*, vol. 10, no. 6, pp. 462–468, 2011.
[609] J. R. Bartles, “Parallel actin bundles and their multiple actin-bundling proteins,” *Current opinion in cell biology*, vol. 12, no. 1, pp. 72–78, 2000.
[610] E. M. Reichl, Y. Ren, M. K. Morphew, M. Delannoy, J. C. Effler, K. D. Girard, S. Divi, P. A. Iglesias, S. C. Kuo, and D. N. Robinson, “Interactions between myosin and actin crosslinkers control cytokinesis contractility dynamics and mechanics,” *Current Biology*, vol. 18, no. 7, pp. 471–480, 2008.
[611] N. V. Hud and I. D. Vilfan, “Toroidal dna condensates: unraveling the fine structure and the role of nucleation in determining size,” *Annu. Rev. Biophys. Biomol. Struct.*, vol. 34, pp. 295–318, 2005.
[612] V. I. Risca, E. B. Wang, O. Chaudhuri, J. J. Chia, P. L. Geissler, and D. A. Fletcher, “Actin filament curvature biases branching direction,” *Proceedings of the National Academy of Sciences*, vol. 109, no. 8, pp. 2913–2918, 2012.
[613] H. Miyata, R. Yasuda, and K. Kinosita Jr, “Strength and lifetime of the bond between actin and skeletal muscle α-actinin studied with an optical trapping technique,” *Biochimica et Biophysica Acta (BBA)-General Subjects*, vol. 1290, no. 1, pp. 83–88, 1996.
[614] J. M. Ferrer, H. Lee, J. Chen, B. Pelz, F. Nakamura, R. D. Kamm, and M. J. Lang, “Measuring molecular rupture forces between single actin filaments and

actin-binding proteins," *Proceedings of the National Academy of Sciences*, vol. 105, no. 27, pp. 9221–9226, 2008.
[615] B. R. McCullough, L. Blanchoin, J.-L. Martiel, and E. M. De La Cruz, "Cofilin increases the bending flexibility of actin filaments: implications for severing and cell mechanics," *Journal of molecular biology*, vol. 381, no. 3, pp. 550–558, 2008.
[616] J. Pfaendtner, M. Enrique, and G. A. Voth, "Actin filament remodeling by actin depolymerization factor/cofilin," *Proceedings of the National Academy of Sciences*, vol. 107, no. 16, pp. 7299–7304, 2010.
[617] J. Fan, M. G. Saunders, E. J. Haddadian, K. F. Freed, E. M. De La Cruz, and G. A. Voth, "Molecular origins of cofilin-linked changes in actin filament mechanics," *Journal of molecular biology*, 2013.
[618] V. E. Galkin, A. Orlova, D. S. Kudryashov, A. Solodukhin, E. Reisler, G. F. Schröder, and E. H. Egelman, "Remodeling of actin filaments by adf/cofilin proteins," *Proceedings of the National Academy of Sciences*, vol. 108, no. 51, pp. 20568–20572, 2011.
[619] B. R. McCullough, E. E. Grintsevich, C. K. Chen, H. Kang, A. L. Hutchison, A. Henn, W. Cao, C. Suarez, J.-L. Martiel, L. Blanchoin, *et al.*, "Cofilin-linked changes in actin filament flexibility promote severing," *Biophysical journal*, vol. 101, no. 1, pp. 151–159, 2011.
[620] G. R. Hime, J. A. Brill, and M. T. Fuller, "Assembly of ring canals in the male germ line from structural components of the contractile ring," *Journal of cell science*, vol. 109, no. 12, pp. 2779–2788, 1996.
[621] D. N. Robinson and L. Cooley, "Stable intercellular bridges in development: the cytoskeleton lining the tunnel," *Trends in cell biology*, vol. 6, no. 12, pp. 474–479, 1996.
[622] J. Mullins and J. J. Biesele, "Terminal phase of cytokinesis in d-98s cells," *The Journal of cell biology*, vol. 73, no. 3, pp. 672–684, 1977.

Summary

Cytoskeletal organization in biomimetic liposomes

Animal cells have the striking ability to undergo dramatic changes in shape during cell division, growth and movement. These cell shape changes are essential for normal embryonic development and throughout adult life. Understanding how a cell regulates its molecular components to achieve precise cell shape control is thus an important task. Animal cells use cytoskeletal proteins to actively control the shape of the plasma membrane, which envelopes them and defines a cell's autonomy. The main cytoskeletal system that determines cell shape change is the actin cytoskeleton. The actin cytoskeleton exhibits a vast variety of architectures to fulfill special functions. For instance, actin filaments assemble into bundles that deform the plasma membrane, forming cylindrical protrusions, called filopodia. These filopodia enable cells to sense the surrounding environment and determine the direction in which they need to move. In the front of a motile cell, branched actin networks push the plasma membrane out, forming thin and flat protrusions known as lamellipodia, which facilitate cell movement. In addition, actin filaments form a dense mesh-like network right underneath the plasma membrane, known as the actin cortex. The actin cortex helps to physically maintain a stable cell shape by providing mechanical rigidity. However, at the same time the actin cortex also has the remarkable ability to actively deform the plasma membrane by exerting pulling forces through the action of myosin II motor proteins. Myosins are molecular motors that are able to transform chemical energy (ATP) into mechanical pulling forces on actin filaments. Cell shape thus depends on a balance between active forces from myosin contractility and from actin filament polymerization with the passive forces arising from actin-membrane anchoring and from the elastic properties of the plasma membrane and the associated actin cortex. During animal cell division, actin filaments and myosin II motors transiently form a contractile ring at the equator that physically constricts the membrane to form two daughter cells. It has been proposed that stable anchoring of the contractile ring to the plasma membrane is facilitated by septins, which are GTPase proteins that intimately interact with the actin cytoskeleton as well as the plasma membrane.

The goal of this thesis is to understand the physical mechanisms by which the actin cytoskeleton and the plasma membrane may jointly determine cell shape. To achieve this goal, we use a bottom-up approach using simplified model

systems based on cell-sized liposomes encapsulating purified cytoskeletal proteins, actin and myosin II motors. In Chapter 2, I demonstrate that active actin-myosin networks can be encapsulated in liposomes with cell-like diameters of 10 to 20 μm by swelling lipid layers dried on top of an agarose or polyvinyl alcohol hydrogel in an aqueous protein solution. The actin encapsulation efficiency is high and rather uniform, and the majority of liposomes are unilamellar. I also show that actin-membrane anchors can be introduced at a controlled surface density by combining the swelling technique with an inverse phase precursor method to prepare lipid micelles containing neutravidin. Partially biotinylated actin filaments can thus be specifically bound to the inner surface of the liposomes. The liposome-based model system thus allows us to study the minimal, physical requirements for cell shape control by cytoskeletal filaments inside a cell-sized compartment.

In Chapter 3, to understand how the reciprocal interplay of the actin cytoskeleton and the plasma membrane determines cell shape, I investigate liposomes that encapsulate rigid actin-fascin bundles. I show that actin bundles are able to deform the membrane of flaccid liposomes into thin protrusions reminiscent of filopodia. These protrusions can reach impressive lengths of up to 60 μm, confirming recent theoretical predictions that actin bundles enclosed in narrow membrane tubes are stabilized against buckling due to the elasticity of the membrane. In contrast, when the liposome membrane is under tension or has a large bending rigidity, the membrane remains undeformed and the actin bundles are forced to bend. In this case, membrane confinement forces the actin bundles to form cortical rings underneath the membrane, an arrangement which minimizes the energy cost associated with filament bending. Thus, the membrane and the bundles influence each other's configuration and the mechanical properties of the membrane and of the actin bundles jointly determine liposome shape. Our results highlight the importance of taking into account the physical characteristics of the cytoskeleton and the plasma membrane besides factors such as biochemical signaling to understand cell shape control.

In chapter 4, I study liposomes encapsulating active actin-myosin networks to elucidate how myosin-driven contractile forces and actin-membrane anchors jointly control actin network remodeling. I show that when the actin networks are crosslinked, myosin motors assemble into a single dense cluster surrounded by a compacted actin network, a signature of myosin contraction. I further show that actin-membrane anchoring in the form of biotin-neutravidin crosslinkers between the actin filaments and the membrane governs the directionality of myosin contraction. When anchors are present, myosin motors contract the actin network towards the liposome membrane, while in the absence of anchors, myosin motors contract the actin network away from the membrane. When fascin is added to create actin bundles, the liposomes are less protrusive in the presence

of myosin motors than in their absence, suggesting that the myosin motors may disassemble the bundles. Taken together, these findings show how actin-membrane anchors and actin network connectivity physically regulate actin network remodeling, which is relevant for understanding how the actin cortex may drive cell polarization. Unfortunately it turns out to be difficult to study the kinetics of myosin-driven contraction inside liposomes, because the contraction happens in less than 1 minute. To overcome this practical problem, future experiments could make use of methods to control the timing of actin polymerization and myosin activity. For instance, one could use membrane channels for influx of salts or ATP from the external buffer, or caged compounds that release ATP or salts upon localized UV light illumination.

Given that in cells, actin-membrane anchors are spatiotemporally regulated to allow cell shape change while at the same time maintaining cortical integrity, it is important to eventually study physiological actin-membrane anchors such as the ERM proteins or septins. In chapter 5 and 6, I investigate the ability of septins to reorganize architectures of the actin cytoskeleton. Septins form hetero-oligomeric complexes which, unlike well-known actin crosslinkers such as fascin, can assemble into filaments and other higher order structures, including bundles and rings. In chapter 5, I study the assembly of recombinant fly, human and budding yeast septins, all expressed and purified from *Escherichia coli* bacteria, under different assembly conditions. By a combination of electron microscopy with time-lapse fluorescence microscopy, I find that recombinant fly and human septin complexes assemble into bundles composed of aligned filaments, whereas in the same assembly condition budding yeast septins assemble into paired filaments. I estimate the critical concentration for septin filament formation by testing a broad range of septin concentrations. We do not observe any formation of septin rings or spirals, in contrast to previous findings for bacteria-derived budding yeast septins and insect cell-derived human septins. It will be important to test whether factors such as posttranslational modifications or the presence of septin binding partners such as phosphatidylinositol lipids or filamentous actin, can promote the formation of these alternative, highly curved structures. Septins have been proposed to closely interact with the actin cytoskeleton in cells, but the nature of this interaction remains elusive. In chapter 6, I report that both fly and human septins directly bind to actin filaments in the absence of other actin binding partners, such as anillin or myosin motors. Septin bundles assemble actin filaments into thick straight bundles, whereas septin oligomers preferentially assemble actin filaments into curved bundles and even highly curved rings. Time-lapse fluorescence imaging of actin filament growth and bundling in the presence of septins reveals that septins are capable of stabilizing bent segments of actin filaments and bundles. These findings suggest that septins may directly contribute to the formation and the stabilization of the actin-myosin ring that powers cell

division. Moreover, our observations suggest that cells may control the configuration of the actin cytoskeleton by varying the polymerization state of septins, which is determined by the local concentration of septins and perhaps also by posttranslational modifications or interactions with other binding partners such as anillin or plasma membrane lipids.

The work presented in this thesis provides a starting point to build more realistic model systems to further resolve how the actin-myosin cytoskeleton and the plasma membrane jointly determine cell shape. Given that actin nucleation in cells occurs mostly, perhaps even exclusively, adjacent to the plasma membrane, it will be crucial to introduce actin nucleators such as the Arp2/3 complex or formins on the inner surface of the liposomes. Moreover, it will be important to control the turnover of actin and the filament length by regulatory proteins such as ADF/cofilin. Another important step towards a more physiologically relevant model system will be to introduce physiological actin-membrane anchors such as the septins and also members of the ERM family. Unlike biotin-neutravidin bonds, these proteins provide transient bonds between actin filaments and phosphatidylinositol lipids. It will be interesting to test how dynamic actin-membrane anchoring will influence myosin-driven contractility of cortical actin networks.

Samenvatting

Organisatie van het cytoskelet in biomimetische cellen

Dierlijke cellen hebben het opvallende vermogen om dramatische veranderingen in vorm te ondergaan. Deze celvormveranderingen zijn essentieel om allerlei cellulaire processen normaal te laten verlopen, zoals celdeling, groei en beweging. Deze processen zijn op hun beurt essentieel voor embryonale ontwikkeling en ook tijdens het volwassen leven. Het is dus belangrijk om te begrijpen hoe een cel zijn moleculaire componenten reguleert om zijn vorm precies te controleren. Dierlijke cellen zijn omsloten door een dunne (~5nm) dubbellaag van lipiden, het zogenaamde plasma membraan, dat de cel afbakent van zijn omgeving. Dit membraan is uiterst flexibel en is van zichzelf vormeloos. De cel geeft dit membraan vorm door een intern netwerk van eiwitdraden, het zogenaamde cytoskelet. Het belangrijkste onderdeel van dit cytoskelet voor celvorm is het actine cytoskelet dat opgebouwd is uit actine filamenten. Deze filamenten worden door allerlei hulpeiwitten zoals crosslinks and motoren georganiseerd in allerlei architecturen die erop gericht zijn om speciale functies te vervullen. Nabij het celmembraan groeperen actine filamenten zich bijvoorbeeld in stijve rechte bundels, die het plasmamembraan vervormen. Zo ontstaan cilindrische uitsteeksels, zogenaamde filopodia, die de cel in staat stellen om de omgeving te voelen en te bepalen in welke richting de cel moet bewegen. Aan de voorkant van cel die zich voortbeweegt over een substraat duwen vertakte netwerken van actine filamenten het plasmamembraan actief naar buiten. Zo vormen zich dunne en vlakke uitstulpsels van het plasma membraan. Deze zogenaamde lamellipodia helpen de cel om zich voort te bewegen. Direct onder het plasmamembraan vormen actine filamenten een fijnmazig netwerk dat bekend is als de actine cortex. De actine cortex helpt een cel om een stabiele vorm te behouden door mechanische stijfheid te verlenen aan het membraan. Daarnaast heeft de actine cortex ook het opmerkelijke vermogen om het plasmamembraan actief te vervormen door het uitoefenen van trekkrachten met behulp van myosine II eiwitten. Myosines zijn moleculaire motoren die chemische energie (ATP) kunnen omzetten in minieme (picoNewton) mechanische trekkrachten op actine filamenten. Tijdens de deling van dierlijke cellen vormen de myosine motoren samen met actine filamenten tijdelijk een ring in het midden van de cel, die het membraan actief insnoert om zo twee dochtercellen te vormen. Er wordt momenteel gedacht dat stabiele verankering van deze ring aan het

plasmamembraan mede wordt mogelijk gemaakt door septines, een speciale klasse van GTPase eiwitten. De precieze rol en functie van septines tijdens celdeling is echter nog onbekend.

Al met al is de vorm van een cel dus afhankelijk van een balans tussen actieve trekkrachten uitgeoefend door myosine motoren en door polymerisatie van actine filamenten, tegenover passieve tegenkrachten die voortvloeien uit actine/membraan verankering en de elastische weerstand van het plasmamembraan en de bijbehorende actine cortex tegen vervorming.

Het doel van dit proefschrift is om de fysische mechanismen te begrijpen die celvorm door het actine cytoskelet en het plasmamembraan bepalen. Om dit te bereiken maak ik gebruik van een bottom-up experimentele benadering gebaseerd op vereenvoudigde modelsystemen. Deze modelsystemen baseer ik op zogenaamde “reuzen-liposomen” die een soortelijke grootte hebben als een typische dierlijke cel. Binnenin deze liposomen sluit ik een versimpeld cytoskelet op bestaande uit opgezuiverde cytoskeleteiwitten: actine filamenten, myosine II motoren, crosslink eiwitten, en membraan-actine linkers. In hoofdstuk 2 toon ik aan dat actieve actine/myosine netwerken kunnen worden ingekapseld in liposomen met diameters van 10 tot 20 micrometer, vergelijkbaar met de grootte van een cel, door lipiden die eerst gedroogd zijn bovenop een agarose- of polyvinyl alcohol hydrogel weer te hydrateren in een waterige eiwitoplossing. De efficiëntie van actine inkapseling is hoog en redelijk vergelijkbaar tussen liposomen onderling, en de meerderheid van de liposomen is unilamellair, hetgeen wil zeggen dat ze een enkele lipide dubbellaag hebben net als het plasmamembraan van een cel. Ik laat verder zien dat actine/membraanankers met een gecontroleerde oppervlaktedichtheid kunnen worden toegevoegd door de zwelling techniek te combineren met een "inverse fase precursor methode" waarbij lipide micellen worden gevormd met een waterige oplossing van neutravidine in de kern. Op deze manier kunnen gebiotinyleerde actine filamenten specifiek aan het membraan aan de binnenzijde van de liposomen worden gebonden. Het modelsysteem dat we op deze manier maken is uiterst geschikt om de minimale fysieke vereisten te bestuderen die nodig zijn voor celvorm controle door actine filamenten in een compartiment ter grootte van een cel.

In hoofdstuk 3 richt ik mij op de vraag hoe de onderlinge wisselwerking van het actine cytoskelet en het plasmamembraan de vorm van een cel kan bepalen. Hiervoor gebruik ik als modelsysteem liposomen die stijve actine-fascine bundels bevatten. Ik laat zien dat actine bundels in staat zijn om het membraan van slappe liposomen te vervormen tot dunne uitsteeksels die doen denken aan cellulaire filopodia. Deze uitsteeksels kunnen indrukwekkende lengtes bereiken tot 60 micrometer, hetgeen recente theoretische voorspellingen bevestigt dat actine bundels ingesloten in nauwe membraanbuizen worden gestabiliseerd tegen

knikken door de elasticiteit van het membraan. Wanneer daarentegen het liposoommembraan onder spanning staat of een grote buigstijfheid heeft, blijft het membraan onvervormd. In dit geval dwingt de opsluiting door het membraan de actine bundels om te buigen en corticale ringen te vormen onder het membraan, dit om de energiekosten verbonden aan het buigen van de filamenten te minimaliseren. Het membraan en de bundels beïnvloeden dus elkaars configuratie en de mechanische eigenschappen van zowel het membraan als de actine bundels spelen een rol in celvorm. Onze resultaten benadrukken het belang van de rol van fysische kenmerken van het cytoskelet en het plasmamembraan in celvorm controle, naast factoren zoals biochemische regulatie.

In hoofdstuk 4 bestudeer ik liposomen die actieve actine/myosine netwerken bevatten om de balans tussen myosine-gedreven trekkrachten enerzijds en actine/membraan verankering anderzijds in organisatie van het actine cytoskelet op te helderen. Ik laat zien dat wanneer actine netwerken worden gecrosslinkt, myosine motoren samenkomen tot één enkel compact cluster, omringd door een verdicht actine netwerk. Dit is een duidelijk teken dat motoren het actine netwerk samentrekken. Ik laat verder zien dat actine/membraan verankering in de vorm van biotine-neutravidine crosslinkers tussen de actine filamenten en het membraan de richting van de myosine contractie beinvloeden. Wanneer ankers aanwezig zijn trekken de myosine motoren het actine netwerk naar het liposoommembraan toe, terwijl in de afwezigheid van ankers de myosine motoren het actine netwerk van het membraan aftrekken. In aanwezigheid van het eiwit fascine, dat actine filamenten bundelt zijn de liposomen minder geneigd uitsteeksels te vormen als myosine aanwezig is dan in de afwezigheid van myosine. Dit wijst erop dat de myosine motoren de bundels kunnen ontbinden. Tezamen tonen deze bevindingen aan hoe contractie van het actine netwerk wordt gereguleerd door actine/membraanankers en door de connectiviteit van het actine netwerk zelf. Dit is relevant om te begrijpen hoe de actine cortex de polarisatie van een cel kan bepalen. Helaas blijkt het moeilijk om contractie van actine netwerken door myosine binnenin liposomen in de tijd te volgen, omdat de samentrekking in minder dan 1 minuut al over is. Om dit praktische probleem te overwinnen is het in de toekomst interessant om methodes te gebruiken om de timing van actine polymerisatie en myosine activiteit te beheersen. Zo zouden bijvoorbeeld membraan kanalen voor de instroom van zouten of ATP uit de externe buffer gebruikt kunnen worden, of chemische verbindingen die ATP vrijlaten onder belichting met gefocusseerd UV licht.

In cellen zijn actine/membraanankers veel dynamischer dan de biotine-neutravidine ankers die ik in mijn proefschrift gebruikt heb. Om de modelsystemen meer op het levende systeem te laten lijken is het daarom belangrijk om uiteindelijk fysiologische actine/membraanankers zoals de ERM eiwitten of septines te bestuderen. In hoofdstuk 5 en 6 onderzoek ik de

mogelijkheden van septines om actine structuren te reorganiseren. Septines vormen hetero-oligomere complexen, die, in tegenstelling tot bekende actine crosslinkers zoals fascine, zelf filamenten en andere hogere orde structuren, zoals bundels en ringen, kunnen vormen. In hoofdstuk 5 bestudeer ik de assemblage van recombinant vliegen septine, menselijk septine en gist septine, allen tot expressie gebracht en opgezuiverd uit Escherichia coli bacteriën. Door een combinatie van elektronenmicroscopie met time-lapse fluorescentie microscopie constateer ik dat recombinant vliegen en menselijk septine allebei dikke bundels vormen, samengesteld uit uitgelijnde filamenten, terwijl onder dezelfde assemblage omstandigheden gist septine dunne, dubbele filamenten vormen. Door assemblage over een breed spectrum van septine concentraties te bekijken kan ik de kritische concentratie afschatten die nodig is voor septine polymerisatie. Ik heb geen septine ringen of spiralen gevonden, in tegenstelling tot eerdere bevindingen voor gist septines geproduceerd door bacteriën en menselijke septines afkomstig uit insecten cellen. Het is in de toekomst belangrijk om te onderzoeken of factoren zoals post-translationele modificaties of de aanwezigheid van septine bindende moleculen zoals phosphatidylinositol lipiden de vorming van deze dergelijke gekromde structuren kan bevorderen. Op basis van allerlei studies van septines in levende cellen wordt gedacht dat septines nauw contact hebben met het actine cytoskelet. Het is echter onduidelijk of septines direkt of indirekt aan actine filamenten binden. In hoofdstuk 6 rapporteer ik dat zowel vliegen als menselijke septines rechtstreeks binden aan actine filamenten in de afwezigheid van andere bindingspartners, zoals aniline of myosine motoren. Septine bundels brengen actine filamenten samen tot dikke rechte bundels, terwijl septine oligomeren actine filamenten samenvoegen tot gekromde bundels en zelfs sterk gebogen ringen. Uit time-lapse fluorescentie opnames van actine filamentvorming in aanwezigheid van septines blijkt dat septines gebogen segmenten van actine filamenten en bundels kunnen stabiliseren. Deze bevindingen suggereren dat septines rechtstreeks kunnen bijdragen tot de vorming en stabilisering van de actine-myosine ring die voor celdeling nodig is. Bovendien suggereren mijn waarnemingen dat cellen de configuratie van het actine cytoskelet kunnen regelen door variaties in de polymerisatie toestand van septines, die afhangt van de lokale concentratie van septines, en misschien ook van posttranslationele modificaties of interacties met andere bindingspartners zoals aniline of specifieke lipiden.

Het werk gepresenteerd in dit proefschrift biedt een startpunt om meer realistische modelsystemen te bouwen die gebruikt kunnen worden om verder te onderzoeken hoe het actine/myosine cytoskelet en het plasmamembraan samen de vorm van een cel bepalen. Aangezien actine nucleatie in cellen meestal, zoniet uitsluitend, gebeurt vlakbij het plasmamembraan, zal het cruciaal zijn om actine nucleatoren zoals het Arp2/3 complex of formines op het binnenoppervlak van de

liposomen te introduceren. Bovendien zal het belangrijk zijn om de lengte en dynamica van de actine filamenten te beheersen door regulerende eiwitten zoals ADF/cofiline. Een andere belangrijke stap naar een meer fysiologisch relevant modelsysteem zal zijn om fysiologische actine/membraanankers zoals septines en tevens leden van de ERM familie te introduceren. Anders dan biotine-neutravidine bindingen bieden deze eiwitten kortstondige bindingen tussen actine filamenten en phosphatidylinositol lipiden. Het zal interessant zijn om te testen hoe dynamische actine/membraan verankering de samentrekking van corticale actine netwerken door myosine motoren zal beïnvloeden.

Acknowledgements

These years have been an unforgettable and enjoyable time for me. This would never have happened if my supervisor Gijsje had not given me the opportunity to join her group. Gijsje, thank you for always being supportive and considerate. Your warm encouragement and high motivation for our projects have been the driving forces to keep me going. Especially, I would like to thank you for your invaluable guidance that made me grow as a researcher. I will miss these times we shared together. Also, I very much appreciate the opportunities you gave me to collaborate with many great scientists.

I would like to take this opportunity to thank my committee members, Yves, Armağan, Gijs, Cécile and Thomas, who carefully read my dissertation and gave valuable advice to improve it.

I am enormously grateful to my collaborators who not only assisted and coached me in these years, but also brought a lot of fun and great traveling trips.

Manos, it was an invaluable experience to work side by side with you. I will never forget those seemingly endless but exciting times (days and nights) of our experiments. Your fruitful insights and enthusiasm for research inspire me to this day and have had a significant impact on me. François, thank you for sharing your experience on protein purification with me.

Aurélie, it was a great pleasure working with you. I am grateful for your teaching of the basics of EM. I will not forget the crazily huge number of EM samples that we prepared. The career advice you gave me is very much appreciated. Gerard, thank you for your help with the EM imaging. I enjoyed a lot our French style lunch time in Institut Pasteur.

Cécile and Kévin, it was an invaluable experience to collaborate with you. Thank you for all the insightful discussions. Especially, I am thankful for your constant patience and understanding during our collaboration.

Armağan and Duygu, thank you for giving me the opportunity to work in Groningen on the MscL-liposome project. It was a lot of fun and I learned a lot from you two. Thank you for sharing your experience with me and always taking time to answer all my naive questions.

Balázs and Kinga, it was a great pleasure working with you. Thank you for sharing your knowledge and experience with me. The visit of Pécs and your university was one of my greatest trips of these years.

Carlos, thank you for giving me the great opportunity to work in your lab. Thank you for your fruitful insights (as well as crazy ideas ;)) and advice during our discussions. Fabrice, thank you for arranging my stay in Strasbourg and for the

bike renting. André, Omar, Andreas and Georges, thank you for sharing your experience with me and assisting me to setup things in Carlos' lab in a very short period of time.

Yves, thank you for sharing your experience of the purification of transmembrane proteins with me. The discussions we had were very useful and increased my understanding of the project.

During my PhD, I was very lucky to work with four great students, Guido, Said, Liselotte and Leffert. Thank you for your excellent inputs during the projects. Guido, thank you for teaching me the biochemistry behind protein purification. I have to say that I learned more from you than that I could teach you. Said, it was nice seeing you become more independent and come up with your own ideas for the project. Liselotte, your enthusiasm for research was impressive and contagious. Leffert, it was your persistence that made the project work and I enjoyed very much our discussions to conquer the difficulties of our experiments.

There are so many people at AMOLF who assisted me in my projects and also made my life during these years greatly colorful and enjoyable. Björn, thank you for teaching me so many things in the lab. Especially, I would like to thank you for your always warm support, not only in research but also life-wise. Thank you for being very considerate and always finding time to discuss things with me, giving me directions when it was most needed. Nils, my officemate, it was always very helpful to discuss my work with you. Thank you for providing humor for what could sometimes be difficult/stressful situations. I will not forget our cool martini/tea party. Milena, thank you for being supportive and always being there for me. I am still inspired by your enthusiasm and experimental mind, not only in your research but also in the kitchen. I will never forget our precious memories together. Svenja and Gábor, thank you for always welcoming me to your house and treating me with nice home-made food. Svenja, I especially would like to thank you for your warm support. Cho-Shuen, my life in Europe would not be as great without our trips together. Thank you for organizing these. Brian, thank you for sharing your experience with me. I especially want to thank you for letting me spend times with your family. It made me feel at home and I enjoyed very much being with Bella and Isha. Sophie and Jeanette, thank for joining me in my defense. Sophie, thank you for always finding time to listen to me and giving me helpful advice, not only for the research but also for my life. The philosophy you taught me will be carried. Jeanette, you always know how to cheer me up. I enjoyed very much all our girl's talk. It was your sense of humor that kept me motivated. Ioana, thank you for listening to me when times were difficult and always giving me your support. I will miss our gossiping times. José, your positive energy motivated me and your warm support kept me going. Thank you for bringing so much fun in the lab. Nuria, thank you for always cheering me up when I was "a bit" down. Mark, thank you for being tolerant of my messy office desk and areas surrounding me. It

was great to have someone to talk to in Chinese. Martin, thank you for bringing so much fun during lunch time. Baldo, Magdalena and Florian, thank you for your help and insightful ideas in the lab. Vanda, I am grateful for your encouragements and advice. Marina, Iza, Marijn, Martijn, Corianne, Karin, Nicholas, Bart and Amira thank you for sharing your valuable ideas/inputs in our meetings and giving support in the lab. Marjolein, thank you for helping me with the protein purification. Especially, thank you for making my thesis cover. Simone, thank you for your assistance in the lab. Bela, thank you for your good ideas in our confinement meetings. Lutz (as well as your nice hair ;)) and Stefanie, thank you for bringing so much fun to the parties. Laurens, Ana, Daan, Paige, Nienke, Wiet, Sarah, Alireza, Marjon, Alexandre, Chris, Pierre, Filipe, Philippe, François, Gesa, Narjes, Stef, Bob, Georges, Sebastian, Noreen, Joris, Eva, Tomek, Martijn, Andrew, Stephen, Jacopo, Katja, Nicola, Sergey, Arif, David, Fatemeh, Kim and Aditya, thank you for all the help, chatting, laughing and partying that made my life here very enjoyable.

I would like to thank the support facilities at AMOLF. My stay in the Netherlands and my PhD would not have gone so well without your tremendous help. Especially, I would like to thank Wouter and Anouk for helping me with my working permit. Arnelli, thank you for helping me deal with all financial applications. Tatiana and Andre, thank you for taking care of my package sending and ordering. Jan and Rutger, thank you for helping me with computer related issues. Juanita and Lenny, thank you for helping to arrange housing for me. Erik, Henk-Jan, Wim and Iliya, thank you for helping to design, make and further teach me how to use the equipment for my experiments. Silvia, thank you for helping me gather literatures. Finally, I would like to thank Roland for helping me on so many things in the lab. A big part of my work would not be possible without your help. I would like to thank Hermine who made a very beautiful glass art work at the AMOLF canteen and permitted me to use it for my thesis cover. Harry, I am grateful for your guidance to become a more positive thinker.

It would not be possible to study my PhD degree here without the help from my two mentors in Taiwan. Chau-Hwang, thank you for your kind help and encouragement before as well as during my PhD time. Hsuan-Yi, thank you for your warm support, scientifically and life-wise, that guided and motivated me.

I wish to thank the members of the Miedema family. It was your warm and kind support during the last few years that made me feel at home. I would like to thank my friends from Taiwan, Ya Ching, Doris, Chia-yun, Daisy, En Hung, Chienhong, Hsiu Yuan, Chien Yi, Snow, Pocute and MJ who encouraged and supported me whenever I needed it. I would like to send special thanks to my family, particularly my parents. It would not have been possible to accomplish my PhD without your faith, invaluable support and encouragement. Finally, I express my biggest thanks

to Thomie (Thomas). Thank you for your tremendous support, encouragement, patience and always being there for me.